Imaging and fast features extraction of two-phase flows using electrical impedance tomography

Chuihui Dang

CENTRALE MARSEILLE

École Doctorale : Physique et Sciences de la Matière (ED352)

Institut Fresnel & LTHC/CEA Cadarache

THÈSE DE DOCTORAT

pour obtenir le grade de

DOCTEUR de l'ÉCOLE CENTRALE de MARSEILLE

Discipline : Physique (Instrumentation)

IMAGING AND FAST FEATURES EXTRACTION OF TWO-PHASE FLOWS USING ELECTRICAL IMPEDANCE TOMOGRAPHY

par

DANG Chunhui

Directeurs de thèse : BOURENNANE Salah, RICCIARDI Guillaume, BELLIS Cédric

Soutenue le 01 Octobre 2020

devant le jury composé de :

U. Hampel	Professeur, Helmholtz-Zentrum Dresden-Rossendorf	Rapporteur
N. Polydorides	Professeur, University of Edinburgh	Rapporteur
M. de Buhan	Chargé de Recherche, CNRS - Université Paris Descartes	Examinatrice
S. Mylvaganam	Professeur, University College of Southeast Norway	Examinateur
H-M. Prasser	Professeur, ETH Zürich	Examinateur
H. Schmidt	Head of PKL and INKA, Framatome GmbH	Invité
S. Bourennane	Professeur, Ecole Centrale Marseille	Directeur de thèse
G. Ricciardi	Expert senior, CEA	Co-directeur
C. Bellis	Chargé de Recherche, LMA CNRS	Encadrant

Declaration of Authorship

I, Chunhui DANG, declare that this thesis titled,“IMAGING AND FAST FEATURES EXTRACTION OF TWO-PHASE FLOWS USING ELECTRICAL IMPEDANCE TOMOGRAPHY” and the work presented in it are my own. I confirm that:

- This work was done wholly or mainly while in candidature for a research degree at this University.
- Where any part of this thesis has previously been submitted for a degree or any other qualification at this University or any other institution, this has been clearly stated.
- Where I have consulted the published work of others, this is always clearly attributed.
- Where I have quoted from the work of others, the source is always given. With the exception of such quotations, this thesis is entirely my own work.
- I have acknowledged all main sources of help.
- Where the thesis is based on work done by myself jointly with others, I have made clear exactly what was done by others and what I have contributed myself.

Signed:

Date:

"*I know that new situations can be intimidating. You're lookin' around and it's all scary and different, but y'know... meeting them head-on, charging into 'em like a bull - that's how we grow as people.*"

Rick Sanchez

"*The most precious things in one's life are: curiosity about knowledge, pursuit of beauty, kindness to the world, and sympathy for others.*"

My former teacher

Abstract

With the advantages of non-intrusiveness, high acquisition rate and low-cost, Electrical Impedance Tomography (EIT) has been successfully applied in several cases in multi-phase flow instrumentation and clinical imaging. Most EIT systems currently in use rely on a sequential excitation at neighboring electrodes with measurements at the remaining ones, i.e. the adjacent strategy, while some alternative excitation strategies have proven to be effective and easy to implement using modern hardwares. Amongst the so-called full-scan strategy shows certain advantages in terms of the robustness to measurement noise and the quality of reconstructed image. The objective of this thesis is to assess the applicability of an EIT system implementing full-scan strategy at a high acquisition rate in two-phase flow measurements. The first stage consists of evaluating the four excitation strategies, namely the adjacent, opposite, full-scan and trigonometric strategies, on a number of practical criteria and quality of the reconstructed images, and assessing the influences of electrode size on the performance of an EIT system. The results are worthwhile to the design of practical EIT systems and the associated test sections. The second stage develops a novel eigenvalue-based approach for phase fraction estimation leveraging the redundant measurements from full-scan strategy, the ill-posed EIT image reconstruction is circumvented. The third stage reviews and evaluates various image reconstruction methods for high contrast and fast evolving conductivity profiles, several feasible reconstruction strategies, namely one-step 2.5D method, iterative 2D methods, and GREIT method, are selected to make benchmark reconstructions for a set of static experiments. Finally, the comprehensive EIT measurement mode comprised by the developed EIT system, the image reconstruction procedure and the proposed eigenvalue-based approach, is applied to horizontal two-phase flow measurements under both laboratory and industrial environments. The analysis of the measurement data provides insights on the merits and deficiencies of the measurement mode.

Key words: Electrical Impedance Tomography, full-scan strategy, two-phase flow, void fraction, eigenvalues

Résumé

Avec les avantages de la non-intrusion, d'un taux d'acquisition èlevé et d'un faible coût, la tomographie par impédance électrique (EIT) a été appliquée avec succès dans plusieurs cas d'instrumentation de flux polyphasique et d'imagerie clinique. La plupart des systèmes EIT actuellement utilisés reposent sur une excitation séquentielle aux électrodes voisines avec des mesures sur les autres, c'est-à-dire la stratégie adjacente, tandis que certaines stratégies d'excitation alternatives se sont révélées efficaces et faciles à mettre en œuvre en utilisant des matériels modernes. Parmi elles, la stratégie <full-scan> présente certains avantages en termes de robustesse au bruit de mesure et de qualité de l'image reconstruite. L'objectif de cette thèse est d'évaluer l'applicabilité d'un système EIT mettant en œuvre une stratégie de balayage complet à un taux d'acquisition élevé dans les mesures de débit diphasiques. La première étape consiste à évaluer les quatre stratégies d'excitation, à savoir les stratégies adjacentes, opposées, full-scan et trigonométriques, sur un certain nombre de critères pratiques et de qualité des images reconstruites, et à évaluer les influences de la taille des électrodes sur les performances d'un système EIT. Les résultats sont utiles à la conception de systèmes EIT et aux sections de test associées. La deuxième étape développe une nouvelle approche basée sur les valeurs propres pour l'estimation du taux de vide tirant parti des mesures redondantes de la stratégie de balayage complet : la reconstruction d'image EIT mal conditionnée est ainsi contournée. La troisième étape passe en revue et évalue diverses méthodes de reconstruction d'images pour les profils de conductivité à contraste élevé et à évolution rapide. Plusieurs stratégies de reconstruction réalisables, à savoir la méthode 2.5D en une itération, les méthodes 2D itératives et la méthode GREIT, sont sélectionnées pour effectuer des reconstructions de référence pour un ensemble d'expériences statiques. Enfin, le mode de mesure EIT complet, composé du système EIT développé, de la procédure de reconstruction d'image et de l'approche basée sur les valeurs propres, est appliqué aux mesures de débit en deux phases horizontales en laboratoire et environnements industriels. L'analyse des données donne un aperçu des avantages et des inconvénients de ces méthodes de mesure.

Mots clés: Tomographie d'impédance électrique, la stratégie full-scan, valeurs propres, écoulement diphasique, taux de vide

Acknowledgements

Foremost, I would like to express my sincere gratitude to my supervisor Guillaume Ricciardi for the continuous support of my Ph.D study and research, for his motivation, encouragement, and immense knowledge. His guidance helped me in all the time of research and writing of this thesis. I am also grateful to my co-supervisor Cédric Bellis for his valuable supervision and inspiration, I learned a lot from him on rigorous thinking and scientific writing. And I appreciate the help from my thesis director Salah Bourennane. I could not have imagined having better supervisors and mentors for my Ph.D study.

Besides my superviosors, I would like to thank Schmidt Holger from Framatome GmbH and Saba Mylvaganam from USN, for their help in paper revisions and performing experiments that are essential to my Ph.D study. My sincere thanks also go to my colleagues in LTHC of CEA Cadarache, for offering a professional and warmful environment for my study and work, their diverse exciting projects broadened my horizons. Amongst, I'd like to give special thanks to my Ph.D-mate Mathieu Darnajou, for the stimulating discussions as well as for the pleasing work trips, skiing, climbing, and music, oh, plus our first and probably last international conference on EIT held in CHALET with Antoine Dupré.

I thank my fellow workmates in the lab: Naz Turankok, Lorenzo Longo, Roberto Capanna, Samy Mokhtari, Louise Bernadou, Benjamin Jourdy, for the countless delightful small talks, cafe breaks and lunches. Also I thank my colleagues in CEA Chinese Ph.D team: Jianwei Shi, Fang Chen, Hui Guo, Shengli Chen, Weifeng Zhou, Xiaoshu Ma, Guangze Yang, Shuo Li, Congjin Ding and others, and my friends in Aix en Provence: Siyun Wang, Chaowei Xu, for the afterwork activities, short hiking, and enjoyable chatting.

Last but not the least, I would like to thank my parents Dianjun Dang and Xiuli Zhi, my sister Jiaojiao Dang and my girlfriend Xuan Guo, for supporting me spiritually and bringing happiness to my daily life.

Contents

List of Figures

List of Tables

List of Abbreviations

AI	Analogue Input
AO	Analogue Output
AT3NA	Algorithme de Tomographie en 3D NOSER et Aplanissement (French)
BNC	Bayonet Neill-Concelman connector
CEA	French Alternative Energies and Atomic Energy Commission
CT	Computed Tomography
DIM	Differential Impedance Matrix
DO	Digital Output
DtN	Dirichlet-to-Neumann
ECT	Electrical Capacitance Tomography
EIDORS	Electrical Impedance Tomography and Diffuse Optical Tomography Reconstruction Software
EIT	Electrical Impedance Tomography
ES1	Electrode Set 1
ES2	Electrode Set 2
FBP	Filtered Back-Projection
FDM	Frequency Division Multiplexing
FEM	Finite Element Method
FFT	Fast Fourier Transform
FPGA	Field Programmable Gate Array
fps	frames per second
GREIT	Graz consensus Reconstruction algorithm for EIT
GRM	Gamma-Ray Meter
LTHC	Laboratory of analytical Thermo-hydraulics and Hydromechanics of Core and Circuits
MAP	Maximum *A Posteriori*
MUSIC	MUltiple-SIgnal-Classification
NIM	Normalized Impedance Matrix
NOSER	Newton's one-step error reconstruction
NtD	Neumann-to-Dirichlet
ONE-SHOT	ONe Excitation for Simultaneous High-speed Operation Tomography (French)
PCB	Printed Circuit Board
PDIPM	Primal Dual-Interior Point Methods
PKL	PWR Integral System Test Facility
PMMA	Polymethylmethacrylate
ProME-T	Prototype pour Mesures Electriques par Tomographie
PWR	Pressurized Water Reactor
RE	Relative Error
SNR	Signal to Noise Ratio
TDM	Time Division Multiplexing
TV	Total Variation
USN	University College of Southeast Norway

List of Symbols

A	area of water segment
A_{id}	area of the object(s) in the segmented reconstruction
A_{true}	area of the object(s) in the true image
$\boldsymbol{A}$	a matrix representation of the Galerkin projection
C_e	double layer capacitance
d	distance of the single bubble to the domain center
d_{id}	distance of the the objects barycenter to the origin in the reconstructed image
d_{true}	distance of the the objects barycenter to the origin in the true image
D	internal diameter of the test section
$D_z(x)$	dipole function
$\boldsymbol{d}$	an arbitrary unit vector
f	boundary current density
f_{exc}	frequency of the excitation signal
$\boldsymbol{f}$	an orthogonal basis formed by $\boldsymbol{f}_i$
$\boldsymbol{f}_i$	i-th boundary excitations of trigonometric strategy
$G(x,s)$	Green's function in $\mathbb{R}^2$
$G_\Omega(\cdot,z)$	Green's function in the domain Ω
h	height of the bubble segment
h_w	height of the water segment
I_0	a fixed amplitude
I_e	a given current excitation
$I_{k,j}$	boundary excitation at electrode k in j-th excitation pattern of trigonometric strategy
I_Z	current passing through the system in an excitation pattern
$\boldsymbol{I}$	identity matrix
$\mathscr{J}_2(\boldsymbol{\sigma}_{\varepsilon;a})$	topological derivative associated with $\boldsymbol{\sigma}_{\varepsilon;a}$
$J(\boldsymbol{\sigma})$	an objective function for EIT problem
$J(\varepsilon;a)$	an objective function associated with $\Omega_\varepsilon(a)$
$\boldsymbol{J}$	Jacobian matrix
ℓ	number of electrodes
L_d	distance between the guarding and main electrode planes
L_{dis}	distance between the dual planes
L_e	length of the electrodes
L_{EIT}	total length of the dual-plane test section
L_{iso}	distance between the electrodes and the grounded pipe
ℓ_{max}	theoretical limit to ℓ for a finite accuracy acquisition system
$\boldsymbol{L}$	regularization matrix
m_0	the number of eigenvalues and eigenvectors considered in factorization method
$\dot{m}$	water mass flow rate
n_0	index corresponding to the minimum eigenvalue over the noise level
n_{bub}	number of uniformly distributed bubbles
n_c	number of repeating frames
n_e	index of the element in the finite element model

N_d	number of sampling points for one frame of ONE-SHOT
N_e	number of excitation patterns
N_{el}	number of elements in the finite element model
N_m	number of measurements
N_m^i	number of independent measurements
N_p	number of periods per excitation pattern
N_{sp}	number of samples per period
$\boldsymbol{n}$	unit outward normal vector on the boundary
p	exponent coefficient of generalized Tikhonov regularization
$P(x\|b)$	conditional probability of x given b
$\boldsymbol{P}$	an orthonormal projector onto the basis $\boldsymbol{f}$
$Q(\boldsymbol{\sigma})$	regularization term
r	radius of a single bubble
r_0	radius of the simulation geometry
r_{dis}	radius of uniformly distributed bubbles
r_e	equivalent radius of the uniformly distributed bubbles
R_0	constant resistor
R_e	charge transfer resistance
$\mathscr{R}$	contrast between the high and low conductivity
$\mathscr{R}_f$	rank of a matrix or operator
$\boldsymbol{R}$	inverse matrix
$\mathbb{R}^2$	infinite two-dimensional real coordinate space
$\mathbb{R}^\ell_\diamond$	ℓ-dimensional vector space
$s_{(i,k)j}$	sensitivity of V_{ik} to a local conductivity perturbation in j-th element
S_j	overall sensitivity in the j-th element
t_z	trace of T_z
t_{frame}	acquisition time for one frame
T_z	test function for factorization method
u	electrical field
u_0	electrical field of reference case
u_{adj}	adjoint electrical field
u_{ref}	reference electrical field
u_i	voltage field associated with i-th current pattern
u_k	voltage field computed using the k-th voltage measurement as an excitation current
$u\|_{\partial\Omega}$	boundary potential of image case
$u_0\|_{\partial\Omega}$	boundary potential of reference case
$\boldsymbol{U}(\boldsymbol{\sigma})$	a set of simulated boundary measurements associated with $\boldsymbol{\sigma}$
v_{ideal}	ideal velocity estimation
v_{real}	real velocity estimation
v_z	a harmonic function of D_z
$\boldsymbol{v}^{(i)}$	i-th eigenvector of the impedance matrix
V_0	amplitude of the excitation voltage
V_R	voltage measurement across R_0
V_{ik}	a measurement at electrode pair k with excitation at electrode pair i
$V_{i,j}$	voltage difference between source i and drain j
$\boldsymbol{V}$	a set of boundary measurements
$\boldsymbol{V}_h$	reference measurements with homogeneous profile
$\boldsymbol{V}_i$	image measurements with extra object(s) inside
x_i^{FFT}	discrete amplitude at frequency i after FFT
Z^{source}	contact impedance at the source electrode
Z^{drain}	contact impedance at the drain electrode

Z^{tot}	total impedance
$Z_{i,j}$	bulk impedance between source i and drain j
$\hat{Z}_{i,j}$	normalized bulk impedance between source i and drain j
$\boldsymbol{Z}$	impedance matrix
$\boldsymbol{Z}^0$	impedance matrix of reference case
$\Delta\boldsymbol{Z}$	difference impedance matrix between $\boldsymbol{Z}$ and $\boldsymbol{Z}^0$
$\hat{\boldsymbol{Z}}$	normalized impedance matrix
$\hat{\boldsymbol{Z}}_m$	impedance matrix of m-th frame
$\hat{\boldsymbol{Z}}_{\boldsymbol{mean}}$	mean impedance matrix of consecutive frames
α	hyper-parameter
γ	electric admittivity
δ	Dirac's delta function
δ_d	distinguishability
ϵ	electric permittivity
ϵ_{id}	global identification error
ϵ_{A}	geometrical area error
ϵ_{p}	positioning error
$\varepsilon_0 r_i$	radius of Ω_i assumed in MUSIC method
η	void fraction
η_l	liquid volume fraction
θ_z	the angle between t_z and $\mathscr{R}(\Lambda_\sigma - \Lambda_0)^{1/2}$
κ	condition number of a matrix
$\lambda^{(16)}_{noisy}$	leading eigenvalue of the noisy data
$\lambda^{(i)}$	i-th eigenvalue of the impedance matrix
$\lambda^{(\ell)}$	leading eigenvalue
$\sum_{\lvert\lambda\rvert}^{15}$	sum of the absolute value of the first 15 eigenvalues
$\lambda^{(16)}_{mean}$	leading eigenvalue of $\hat{\boldsymbol{Z}}_{\boldsymbol{mean}}$
Λ_0	NtD map of reference case
Λ_σ	NtD map of image case
ξ	relative error of the eigenvalues
Π	relative NtD map
σ	electric conductivity
σ_j	local conductivity in the j-th element
$\delta\sigma_j$	a conductivity perturbation to σ_j
$\boldsymbol{\sigma}_{\mathrm{id}}$	approximated conductivity profile that minimizes the cost function
$\tilde{\boldsymbol{\sigma}}_{\mathrm{id}}$	segmented profile of $\boldsymbol{\sigma}_{\mathrm{id}}$
$\boldsymbol{\sigma}^{\mathrm{k}}$	conductivity estimation at step k
$\boldsymbol{\sigma}^{\mathrm{k+1}}$	conductivity estimation at step k+1
$\delta\boldsymbol{\sigma}^{\mathrm{k}}$	update of conductivity approximation at step k
$\boldsymbol{\sigma}_{\mathrm{ref}}$	reference conductivity profile
$\boldsymbol{\sigma}_{\mathrm{true}}$	true conductivity profile
$\boldsymbol{\sigma}_{\varepsilon;a}$	conductivity profile with the object $\Omega_\varepsilon(a)$
ς	relative error of the estimated velocity
τ_{ideal}	ideal time delay between the two electrode planes
τ_{real}	real time delay between the two electrode planes
$\Phi(\boldsymbol{\sigma})$	cost function used in the least squares methods
Φ''	Hessian matrix
χ	steam quality
ω	excitation frequency

ω_j	angular frequency of trigonometric excitation
Ω	a two- or three-dimensional domain
$\partial\Omega$	boundary of the domain Ω
$\Omega_\varepsilon(a)$	a small object with a characteristic radius ε at location a
Ω_i	a set of non-conductive inclusions
$\partial\Omega_\mathrm{i}$	boundary of the inclusions Ω_i

Dedicated to my beloved family, for
their endless love, support and
inspiration during my Ph.D. . .

Chapter 1

Context

Tomography means imaging sections or by sectioning, through exerting penetrating waves and receiving resulting waves. Usually images are obtained through tomographic reconstructions, such as the X-ray computed tomography. The principle has been applied to many research fields: geophysics, material science, plasma physics, archaeology, to cite but a few. Different types of penetrating waves have been used, including radiation beams (X-ray, γ-ray), pressure waves (ultrasounds), electromagnetic waves, and so on. Among which low frequency electrical current shows plausible features favoring the applications in process monitoring and medical imaging.

Electrical Impedance Tomography (EIT) is a non-intrusive tomography technique using low-frequency electrical current to probe a domain, the material distribution is determined from the electrical boundary measurements. This technique is based on the electrical properties of materials, *i.e.* the electric admittivity (conductivity and permittivity). In early 1980s, the EIT technique was firstly developed for medical use. Afterwards, intensive researches have been carried out on its mathematic basis, system modeling and optimization, hardware designing, reconstruction algorithms, among others.

Meanwhile, gas-water two-phase flows are encountered in various industrial processes. For example in nuclear power industry, the phase change, heat transfer and flow instability in reactor thermal-hydraulics are critical to nuclear safety. While the interactions between phases make it difficult to understand the flow behaviors numerically. Non-intrusive instrumentation techniques for two-phase flow measurements are in great need, to provide valuable information about the flow features, *e.g.* the void fraction, flow pattern and phase distribution. With the advantages of non-intrusion and low cost, EIT technique seems to be a good choice for dynamic two-phase flow measurements.

For dynamic flow imaging, the spatial and temporal resolutions of EIT should match the characteristic time and length scales of the flow, a high frame rate and spatial resolution are always desirable. Recently developed EIT systems usually have high temporal resolutions, hundreds or even thousands of frames can be acquired per second. While the main drawback of EIT technique is its low spatial resolution caused by: i) the limited number of measurements restricted by the number of electrodes; ii) the *soft-field* nature of the electrical current. Numerous researches have been done on the development of EIT systems with large number of electrodes and high speed, as well as on advanced reconstruction methods handling the *ill-posed* EIT inverse problems. Meanwhile, studies on image reconstructions and features extraction methods bypassing the EIT inverse problems, *e.g.* convolutional neural network, principal component analysis, are arising.

Motivation of the project

The present thesis work is under a joint research project between the Laboratory of analytical Thermo-hydraulics and Hydromechanics of Core and Circuits (LTHC) of French Alternative Energies and Atomic Energy Commission (CEA) and the Erlangen technical centre of Framatome GmbH, Germany. Both groups are international leaders in nuclear energy industry and research, carrying out researches and designs on advanced nuclear systems and equipments. Erlangen technical centre operates a number of experimental facilities, test rigs and laboratories, several of which are unique worldwide, for example, the Pressurized Water Reactor (PWR) Integral System Test Facility (PKL facility in brief).

The PKL facility conducts experiments on the thermal-hydraulic behavior of PWRs during operational transients and accidents with respect to systems testing and separate effects using parameter studies and tests. It contributes to the solutions of PWR safety issues insufficiently replicated by thermal-hydraulic system codes. The main components of PKL are shown in Figure 1.1, it simulates the thermal-hydraulic systems of a 1300 MW PWR plant with four steam generators, the height scale is 1:1, the volume scale is 1:145. The core is simulated by electrically heated rods with a power capacity of 20 MW. The pressure limits in the primary and secondary loop are 50 bar and 60 bar, separately.

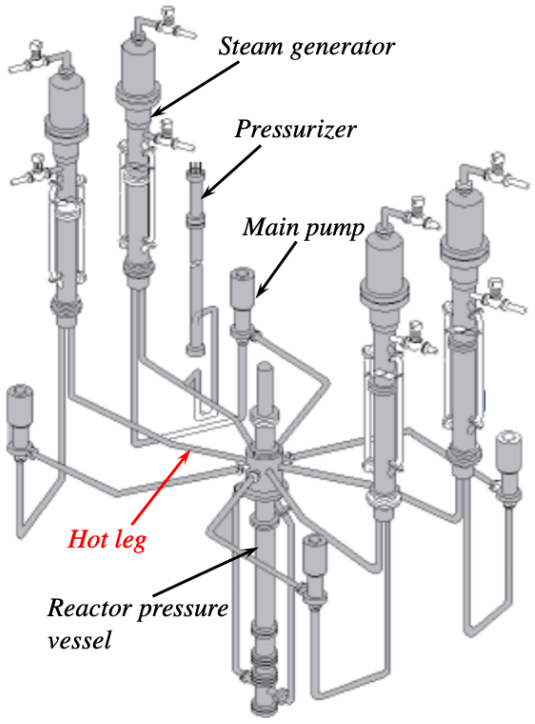

FIGURE 1.1: The main components of PKL facility, the developed EIT sensor would be mounted on one of the four hot legs.

During the integral tests in PKL simulating the loss of coolant accident, transient behaviors have been observed in the hot leg, with drastic changes of void fraction and flow velocities, sometimes even the flow direction changed. A wire-mesh sensor was developed to study the phenomena, however, the impurities in the water blocked the intrusive mesh grid of the sensor, the measurements were severely disturbed and could not provide meaningful information. Therefore, a non-intrusive measurement system is demanded to study the two-phase flows in the hot leg.

The current thesis work has been conducted in parallel with the thesis work of Mathieu Darnajou, and both works follow the studies of a former Ph.D student Antoine Dupré (defensed in October 2017). Dupré initiated the research on EIT in our laboratory and developed a high speed EIT system with satisfying performances, although only preliminary image reconstructions were implemented using static experiment data. Darnajou's work puts emphasis on the development of novel ultra-high speed EIT systems (several thousands of images per second) using multi-frequency strategies. The main efforts of my thesis work focus on the software of EIT, *i.e.* the online and offline image reconstruction methods feasible for two-phase flow imaging, and the comprehensive data post-processing procedures for fast flow features extraction, including void fraction estimation and flow regime identification. The ultimate goal of our work is to develop an ultra-high speed EIT system dedicated to two-phase flow measurements under high temperature high pressure environments.

The main contributions of my thesis work include:

- Investigate the influences of electrode size on the performance of an EIT system with respect to the impedance response, noise level, and residual error induced by multiplexing;
- Propose a novel eigenvalue-based approach to estimate the phase fraction bypassing image reconstruction;
- Implement and compare some conventional and non-conventional image reconstruction methods to decide the proper methods feasible for high contrasted two-phase flow imaging;
- Compare the four excitation strategies, *i.e.* adjacent, opposite, full-scan and trigonometric strategy, concerning several practical implementation criteria;
- Evaluate quantitatively the role of the excitation strategy itself on the reconstructed images, the preeminence of full-scan and trigonometric strategy is evidenced;
- Design a dual-plane EIT test section for industrial two-phase flow measurements under practical constraints, *e.g.* limited workspace, electrically conductive pipelines;
- Propose a comprehensive EIT measurement mode comprised by the developed EIT system, the image reconstruction procedure and the eigenvalue-based approach, and characterize its merits and deficiencies in dynamic two-phase flow measurements under laboratory and industrial environments.

Outline of the thesis

This first introductory chapter introduces the general backgrounds of tomographic techniques and present thesis work, the motivations and objectives are described.

The second chapter reviews various intrusive and non-intrusive tomographic techniques applied to two-phase flow measurements. Their advantages and disadvantages are stressed regarding the flow measurements under harsh environment. Then, the attention is put on the EIT technique, particularly, the mathematic basis, electrode models, excitation strategies and 3D nature of EIT are presented.

The third chapter focuses on the practical aspects of EIT system design. The EIT systems developed in LTHC and applied in the present thesis work, namely the Prototype

pour Mesures Electriques par Tomographie (ProME-T) system and the ONe Excitation for Simultaneous High-speed Operation Tomography (ONE-SHOT) system, are introduced respectively with their system configurations. The four excitation strategies commonly used in EIT, namely the adjacent, opposite, full-scan and trigonometric strategies, have been compared concerning several practical implementation criteria, the results are presented. Besides, the influences of electrode size on the performance of an EIT system have been studied using the ProME-T system as a prototype, the results are considered in the dual-plane test section design for PKL, the electrode size and arrangement are decided optimizing the EIT system performance under the practical constraints of the working environment.

The fourth chapter describes a novel eigenvalue-based approach to estimate the phase fraction from the so-called normalized impedance matrix. An impedance matrix can be derived from the raw EIT measurement directly and further normalized by the impedance matrix of a reference case. The resulting normalized impedance matrix contains the full information about the phase distribution inside the domain, from which some metrics could be derived to estimate the phase fraction bypassing image reconstruction. Here, the eigenvalues are the chosen metrics, their correlations to the phase fractions have been investigated by numerical simulations of various phase distribution patterns, then validated by static experiments.

The fifth chapter concerns the image reconstruction methods feasible for two-phase flow imaging. An extensive review of conventional and non-conventional EIT reconstruction methods is presented, their implementation procedures are demonstrated and compared using numerical simulations. Benchmark reconstructions are made for several static experiments using several selected methods, *i.e.* 2.5D one-step method, 2D iterative methods and GREIT method. In parallel, the role of the excitation strategy itself on the reconstructed images is evaluated, the reconstructed images from the four excitations are compared quantitively, the preeminence of full-scan and trigonometric strategy is evidenced.

The sixth chapter presents the procedures and results of the two sets of dynamic experiments performed in different horizontal flow loops. The first set was performed in October 2019 in the multiphase flow loop of University College of Southeast Norway (USN), the loop is designed for experiments at room temperature with a polymethylmethacrylate (PMMA) pipeline. A total of 80 experimental series were performed at various water and air mass flow rates, the EIT measurement results are compared to the reference measurements from other meters in the loop. The second set was performed in July 2019 in the BENSON loop of Erlangen center. The BENSON loop is an industrial research loop with metal pipelines withstanding high temperature and high pressure. The possible origins of measurement noises are identified through frequency domain analysis of the measured signal. The EIT data analysis provides insights on the merits and deficiencies of the proposed measurement mode, its applicability to two-phase flow measurements is evaluated.

The final concluding chapter summaries the findings of present thesis work and proposes some perspectives for the continuation of the study.

Notes and publications

The interdisciplinary nature of current thesis work allows to communicate the findings to the scientific research communities in both sensor development area and nuclear thermal-hydraulics area. The journal papers and proceeding papers are listed separately as follows.

Articles in referred journal:

- C. Dang, C. Bellis, M. Darnajou, G. Ricciardi, S. Mylvaganam, and S. Bourennane. Practical Comparisons of EIT Excitation Protocols with Applications in High Contrast Imaging. *Instrumentation Science and Technology*, Submitted
- C. Dang, M. Darnajou, C. Bellis, G. Ricciardi, S. Mylvaganam, and S. Bourennane. Improving EIT-based visualizations of two-phase flows using an eigenvalue correlation method. *IEEE Transactions on Instrumentation and Measurement*, Submitted
- M. Darnajou, A. Dupré, C. Dang, G. Ricciardi, S. Bourennane, C. Bellis, and S. Mylvaganam. High Speed EIT with Multifrequency Excitation using FPGA and Response Analysis using FDM. *IEEE Sensors Journal*, 2020
- C. Dang, M. Darnajou, C. Bellis, G. Ricciardi, H. Schmidt, and S. Bourennane. Numerical and experimental analysis of the correlation between EIT data eigenvalues and two-phase flow phase fraction. *Measurement Science and Technology*, 31(1): 015302, 2019a
- M. Darnajou, A. Dupré, C. Dang, G. Ricciardi, S. Bourennane, and C. Bellis. On the Implementation of Simultaneous Multi-Frequency Excitations and Measurements for Electrical Impedance Tomography. *Sensors*, 19(17):3679, 2019

Conference proceedings:

- C. Dang, M. Darnajou, G. Ricciardi, L. Rossi, S. Bourennane, C. Bellis, and H. Schmidt. Spectral And Eigenvalues Analysis of Electrical Impedance Tomography Data For Flow Regime Identification. *Proc. SWINTH (Livorno, Italy)*, 2019b
- C. Dang, M. Darnajou, G. Ricciardi, L. Rossi, S. Bourennane, C. Bellis, and H. Schmidt. Two-phase flow void fraction estimation from the raw data of electrical impedance tomography sensor. *Proc. ICAPP (Juan-les-Pins, France)*, 2018b
- C. Dang, M. Darnajou, G. Ricciardi, A. Beisiegel, S. Bourennane, and C. Bellis. Performance analysis of an electrical impedance tomography sensor with two sets of electrodes of different sizes. *Proc. WCIPT-9 (Bath, UK)*, 2018a
- M. Darnajou, C. Dang, G. Ricciardi, S. Bourennane, C. Bellis, and H. Schmidt. The Design of Electrical Impedance Tomography Detectors in Nuclear Industry. *Proc. WCIPT-9 (Bath, UK)*, 2018

The eigenvalue-based approach for phase fraction estimation has been published in the journal *Measurement Science and Technology* (Dang et al., 2019a), the content is reproduced in Chapter 4. The practical comparisons of the four excitation strategies have been submitted to the journal *Measurement* (Dang et al., Submitted), the qualitative comparisons part is included in Chapter 3, the quantitive part in Chapter 5.3. The results of the dynamic two-phase flow experiments in USN have been submitted to the journal *Flow Measurement and Instrumentation* (Dang et al., Submitted), and reproduced in Chapter 6.2. In the journal papers published in *IEEE Sensors* (Darnajou et al., 2020) and *Sensors* (Darnajou et al., 2019), my contributions are on conceptualization, image reconstruction using experimental data, manuscript writing and revision, while the contents are not included in the present thesis manuscript.

As to the proceedings, the results of flow regime identification based on the spectral and eigenvalues analysis of EIT raw data were presented at the Specialists Workshop on Advanced Instrumentation and Measurement Techniques for Nuclear Reactor Thermal Hydraulics (Livorno, Italy, October 2019) (Dang et al., 2019b). At the 9-th World Congress on Industrial Process Tomography (Bath, UK, September 2018), the results concerning the influences of electrode size on the EIT system performance were presented (Dang et al., 2018a). At the International Congress on Advances in Nuclear Power Plants (Juan-les-Pins, France, May 2019), the results of phase fraction estimation using eigenvalues analysis of EIT raw data were presented (Dang et al., 2018b).

Chapter 2

Introduction

Gas-water two phase flows play a vital role in various industrial processes, for example in the power generation industry, the flow heat transfer takes the heat from the core to the turbine for power generation. It is crucial to optimize the performance of the processes by detecting the flow regimes and gas build-ups with potential escalations compromising the safe and secure operations. Especially in nuclear power industry, the heat transfer and flow instability involving different phases in reactor thermal-hydraulics are critical to nuclear safety (Ricciardi et al., 2011). There is a great need of non-intrusive imaging techniques for online monitoring of the gas-water two-phase flows in many industrial sectors including the nuclear power industries. Various techniques have been developed for this purpose, and evaluated in terms of the accuracy of void fraction estimation and the complexity of practical implementation. A brief review of intrusive and non-intrusive imaging techniques is given in this chapter. Particularly, the EIT technique is presented in detail, including its mathematic basis, electrode models, excitation strategies and 3D nature.

2.1 Flow imaging techniques

Two-phase flow imaging techniques can be classified into several categories according to the penetrating waves used, including: i) the Computed Tomography (CT) using radiation beams, *e.g.* X-ray, γ-ray and neutron tomography; ii) the acoustic tomography based on the interaction between the sound wave and object, *e.g.* ultrasonic tomography; iii) the techniques exploiting electrical properties of materials, *e.g.* wire-mesh sensor, electrical tomography. Imaging techniques based on the nucleus properties, *i.e.* magnetic resonance imaging and positron emission tomography, are commonly used in medical radiology hence not discussed in current topic review. Besides, there are several other intrusive techniques exist providing local information of the flows. For example, the optical and electrical probes are sensitive to interfacial passages enabling to measure local void fraction with a high precision (Enrique Julia et al., 2005; Jones Jr and Delhaye, 1976), while they are not able to perform flow imaging.

2.1.1 Radiation tomography

Radiation tomography is a *hard-field* tomographic technique relying on the high frequency beams passing through the imaging domain. The beams used can be radiative X-ray and γ-ray, or high energy neutron beams, which has several advantages, *e.g.* high penetration ability, high time and spatial resolutions. In radiation tomography, the beams pass through the domain along a straight line, featuring the *hard-field* nature, the informations of the material properties are condensed along the traveling path of the beam, giving one

projection. The attenuations of X-ray and γ-ray depend on the material's density, denser materials have stronger attenuation effect. While the attenuations of neutron beam are related to the atom-specific neutron capture cross-section, which is unnecessarily relevant to the density, making it suitable for different instances than the X-ray or γ-ray tomography.

Mathematically, the radiation tomography is to recover a non-negative attenuation function from a collection of line integrals (projections). The so-called Radon transform and central slice theorem give direct reconstruction approach for radiation tomography, namely, the Filtered Back-Projection (FBP). High resolution images can be obtained with full-angle and sufficient number of projections. Morden X-ray tomography uses multiple receivers and cone beam sources rotating around the imaging object to have a full-angle scanning at a high speed. The state-of-the-art CT techniques feature a high speed up to 10000 frames per second (fps) with a spatial resolution in the order of 1 mm. Figure 2.1 shows a fast X-ray scanner developed in Salgado et al. (2010) with three cone beam sources, two arrays of receivers are associated to each source. Several researches used CT to perform fast measurements of multiphase flows, giving promising results, see Heindel (2011) and Mudde (2011). However, the high acceleration voltage (hundreds of kV) and radiation protection required by radiation tomography are a heavy burden. Moreover, under harsh environment steel pipelines are commonly used to withstand the high temperature high pressure flows, which have strong attenuation effects on the radiation beams, hence reducing the sensitivity to the flows inside. Neutron beams may avoid this problem due to the low neutron capture cross-section of steel, while it is even more costly than X-ray and γ-ray tomography.

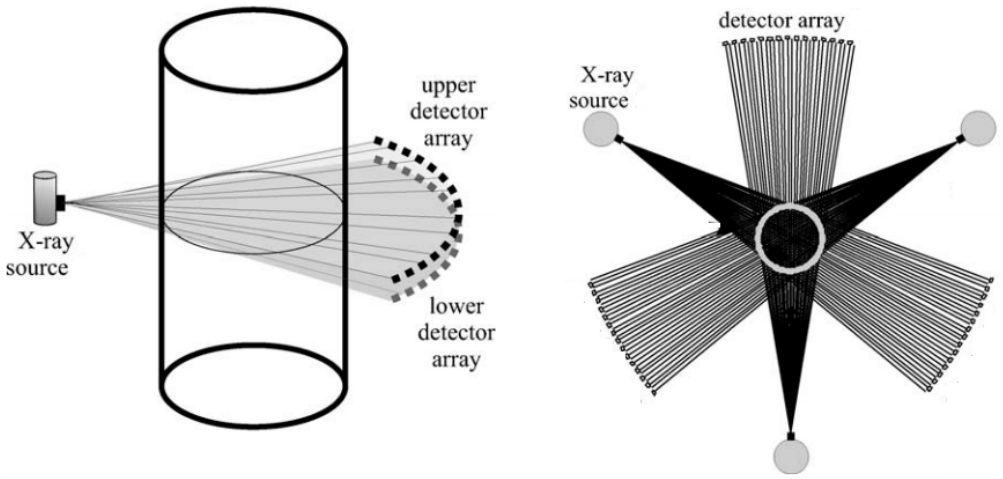

FIGURE 2.1: Schematic of a fast X-ray scanner with three X-ray sources, adapted from Salgado et al. (2010). Left: side view showing only one source with its two detector arrays, right: top view showing three sources and their corresponding detectors.

Additionally, the limited angle or sparse X-ray tomography seems favorable to two-phase flow measurements. Generally, they takes much fewer (1/10 to 1/100 times) projections for imaging than conventional X-ray tomography, making it possible to use very high energy beams while not reducing the frame rate significantly. On the opposite, the limited number of projections define an *ill-posed* reconstruction problem, to which the FBP gives very poor image reconstructions. The regularized reconstruction methods are favored in such applications, which will be introduced in Chapter 5. Currently, the limited angle

or sparse X-ray tomography has been applied in some cases where the working space is limited or low resolution image is sufficient, for example, the dental implanting case (Kolehmainen et al., 2003).

2.1.2 Ultrasonic tomography

Ultrasonic waves sent into the domain would interact with the object, which can be sensed by transducers and used to extract information about the object. Ultrasound waves contain multiple information affected by the object, including the attenuation of wave pressure, the time-of-flight, the scattered or refracted waves. Based on these information, various sensing modes exist, *i.e.* transmission-mode, reflection-mode, and diffraction-mode (Khairi et al., 2019). Their schematics are shown in Figure 2.2 using a 32 transducers system as an example, the object is square-shaped to facilitate the prensentation.

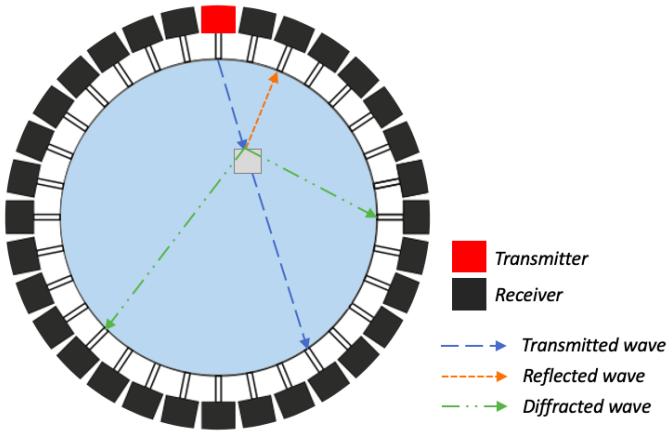

FIGURE 2.2: Schematic of the three ultrasonic sensing modes, using a 32 transducers system as example and a square-shaped object.

In transmission-mode, the object presents in the wave propagation path between the transmitter and receiver, the transmitted waves are attenuated, the time-of-flight is disturbed. The reflection-mode considers the reflected wave after hitting the object, the receiver is located at the same side with the transmitter. The diffraction-mode is based on the spread of waves after being transmitted through the object, the receiver placement should be carefully designed to measure a precise signal. Different sensing modes can be combined in a practical measurement system. Researches using ultrasonic sensors in two-phase flow measurements are extensive, an up-to-date review is given in Goh et al. (2017). Since the interaction between the ultrasonic waves and the object is closely related to the object's density, this technique is favorable to significant density variations, such as micro-bubbles and low void fraction cases, while shows limitations in high void fraction cases.

Ultrasonic technique has the potential for dual-modality measurement in combination with other sensing modules. For example, in Pusppanathan et al. (2017) an ultrasonic tomography sensor is integrated with an Electrical Capacitance Tomography (ECT) sensor, composing a dual-modality tomography system for water-oil-gas three-phase flow imaging. In biomedical imaging, the photo-acoustic tomography leverages the coupling between optical absorption of light sources and ultrasound emission to obtain high contrast and high resolution images (Bal and Uhlmann, 2010; Bal and Ren, 2012).

2.1.3 Electrical tomography

Electrical tomography techniques probe the domain based on the electrical properties of materials. Unlike the radiation beams and the ultrasonic waves, the transmission path of low frequency electric current evolves with the internal material distribution, featuring a *soft-field* nature. Various electrical tomography techniques have been developed and applied for two-phase flow measurements, including the intrusive wire-mesh sensors, non-invasive ECT sensors, and non-intrusive EIT sensors.

Wire-mesh sensor

Wire-mesh sensor, by its name, uses a grid of wires to measure the flows in the studied domain, it was firstly introduced in the pioneer work of Prasser et al. (1998). The principle is to use two sets of wires stretching along the pipe transverse section, which have small axial separation in between and are perpendicular to each other, giving a grid of measurement points at their crossing points. During the measurement, the transmitters are activated sequentially through multiplexing, the receivers are parallel sampled simultaneously. A wire-mesh sensor with 24×24 mesh grid is shown in Figure 2.3, the two sets of wires are transmitters and receivers, respectively.

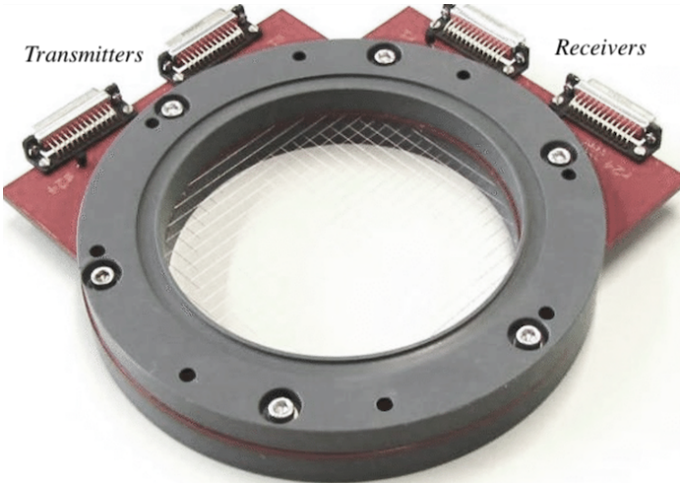

FIGURE 2.3: A wire-mesh sensor with a 24×24 measurement grid, adapted from Nedeltchev et al. (2016).

Wire-mesh sensor allows to investigate multiphase flows at high spatial and temporal resolutions, recently developed sensors feature an acquisition rate up to 10 kHz with a spatial resolution of around 3 mm (Wiedemann et al., 2019). It can provide information about local, cross-sectional or in-situ volume profiles and distributions of phases, however, it has disruptive effects on the flows. Yet, its application under harsh environment is challenging, thicker wires are needed to ensure the robustness, which would in turn reinforce the disruptive effects. Additionally, the fine grid of wires restricts the applications in flows with solid particles or impurities, for example the flows in the hot leg of the PKL facility. A good review of wire-mesh sensors applying into flow measurements under various environments can be found in Peña and Rodriguez (2015).

Electrical capacitance tomography

Unlike the wire-mesh sensors, the EIT/ECT techniques determine the conductivity or permittivity distribution in the probed domain from the measurements at the boundary. The material distribution can be retrieved from a set of boundary excitations and measurements solving the so-called Calderon's inverse problem (Calderón, 2006). The image reconstructions of *soft-field* electrical tomography are challenging, numerous researches have been done on this topic.

ECT uses a finite number of electrodes mounted on the exterior of an insulating pipe. The scheme of an ECT sensor with 8 electrodes is shown in Figure 2.4. All electrodes are excited sequentially, the capacitances between the excitation electrode and all the other electrodes are measured simultaneously, giving a full set of measurements. Since the electrodes are not in direct contact with the medium, the ECT measurement signals are extremely weak, although a high potential (usually in kV) is exerted for excitation, the signal amplification and conditioning are crucial.

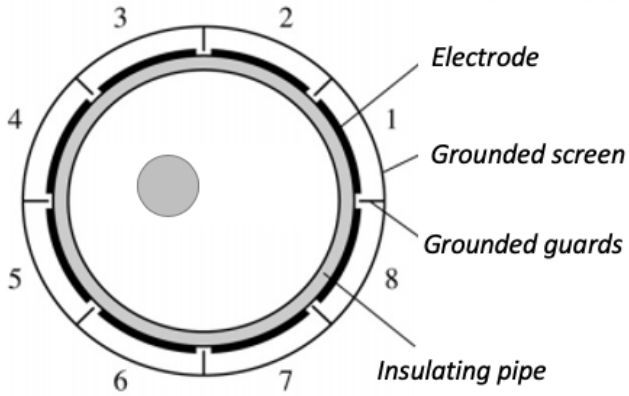

FIGURE 2.4: The schematic of an ECT sensor, with 8 electrodes mounted on the insulated pipe exterior.

The spatial resolution of ECT image reconstructions is restricted by the number of independent measurements, a higher resolution can be achieved by increasing the number of electrodes. However, this would in turn reduce the periphery size of the electrodes hence the measurement amplitudes, making the system more sensitive to noise. Typically, the number of electrodes used in ECT is between 8 and 16, allowing a very low spatial resolution. The acquisition rate of ECT is normally lower than 100 fps due to its high excitation amplitude (Gamio et al., 2005).

ECT sensors are suitable for dielectric components imaging in pipelines or vessels. Huang et al. (2003) used ECT technique to estimate the void fraction from the reconstructed image, a satisfactory accuracy was presented. Recent researches on the dual-modality EIT/ECT sensors give appealing results on the phase fraction estimations and flow imaging of multiphase flows (Sun and Yang, 2015; Wang et al., 2017), the oil-water-gas phases can be discriminated in the image reconstruction. However, the dielectric pipeline required by ECT is not applicable for harsh environments, where metal pipelines are commonly used to withstand the high temperature high pressure loads.

Electrical impedance tomography

EIT uses a finite number of electrodes installed on the interior boundary of a studied domain, making it an invasive but non-intrusive technique. Since the electrodes are in direct contact with the materials, a low excitation signal (several mA or V) is sufficient to give precise measurements, featuring a safe and low cost system. Usually, alternating current or voltage at a given frequency is used for excitation. The low excitation amplitude allows a high excitation frequency and high speed multiplexing, hence a high frame rate. Recently developed EIT systems can achieve up to hundreds or even thousands of fps using excitation frequencies from several to tens of kHz (Jia et al., 2017; Darnajou et al., 2020). With these advantages, EIT technique has been successfully applied in some cases of multiphase flow monitoring and clinical imaging, among others.

A number of EIT systems dedicated to multiphase flow measurements have been developed in the last two decades. A comprehensive review of EIT applications to various media and purposes in chemical engineering can be found in Sharifi and Young (2013). Specifically for two-phase flow measurements, George et al. (2000) presented an EIT system applied to solid-liquid and gas-liquid flows, the phase fractions within a circular cross-section were determined and compared with nominal values. Jia et al. (2017) developed a voltage source EIT system for highly conductive water-oil two-phase flow measurements, the cross-sectional tomographic images and axially stacked images were obtained, the total phase fractions were estimated and compared to the reference values. Dupré (2017) developed an EIT system for void fraction estimation of two-phase flows, in which the so-called full-scan strategy was implemented, however, only static tests were carried out for system validation in their research.

Up to now, the main imaging techniques for multiphase flow measurements are presented, most of which show certain limitations for applications under harsh environments, where metal pipelines are inevitably used and impurities may present in the flows. In this context, EIT technique seems to bear encouraging features for flow measurements in such cases.

2.2 Electrical impedance tomography

EIT technique determines the material distribution inside a 2D or 3D domain based on their constitutive electric properties, *i.e.* the electric admittivity (conductivity and permittivity). Certain current or voltage excitations and the resulting voltage or current measurements are performed on the boundary. In this section, the EIT mathematical basis and electrode models are introduced, some practical aspects considered in implementation, *e.g.* excitation strategies and 3D effect, are discussed.

2.2.1 Forward model

Considering the electric field in a two- or three-dimensional domain Ω, from Maxwell's equation, the electric potential u inside is governed by,

$$\nabla \cdot \big(\gamma(x)\nabla u(x)\big) = 0, \quad x \text{ in } \Omega, \tag{2.1}$$

where $\gamma(x) = \sigma(x) + i\omega\epsilon(x)$ is the isotropic admittivity distribution in Ω, in which σ is the electric conductivity, ϵ is the electric permittivity, ω is the excitation frequency. In multiphase flow measurements, usually only the conductivity σ is considered, because the electric permittivity ϵ of liquid phase can be neglected in the chosen working frequency range of EIT sensors (Dang et al., 2018a).

EIT forward problem is to compute the electrical field u inside the domain Ω and the associated boundary measurements from the knowledge of the conductivity distribution σ and the injecting current or voltage on the boundary. While the inverse problem is to estimate the conductivity profile σ in Ω knowing the injecting current/voltage and the resulting boundary measurements. Mathematically, infinite boundary excitations and measurements can be made on the boundary, determining a unique solution of the internal conductivity profile. In practice, the excitations and measurements can only be made on a finite set of electrodes on the boundary $\partial\Omega$ of the domain, defining a solution of finite resolution. The EIT forward and inverse problems are commonly solved using Finite Element Method (FEM).

Figure 2.5 shows an EIT sensor with 16 evenly separated electrodes located on $\partial\Omega$. Here, the excitation currents are exerted on the electrodes i, j, the corresponding difference voltages are measured at all the other electrodes simultaneously. Conventionally, the excitation signal is routed to one selected pair of electrodes at a given time (namely, one excitation pattern), then switched to the next pair, until all excitation patterns in one strategy are sequentially traversed (Cheney et al., 1999), forming a frame of measurement data.

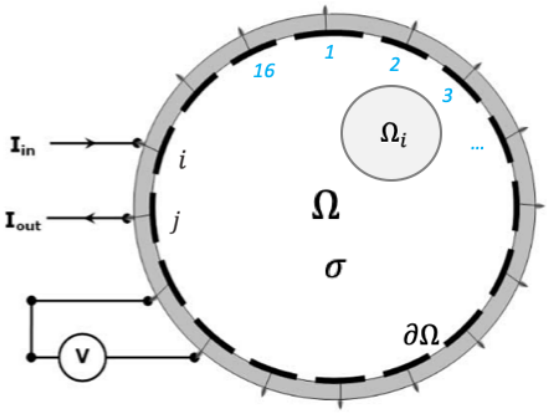

FIGURE 2.5: Schematic of an EIT sensor with 16 electrodes (electrode index is given from 1 to 16). The excitation currents are injected at electrodes (i, j), difference voltage is measured at neighboring electrodes.

The EIT problem is associated with an elliptic boundary-value problem prescribing Neumann boundary conditions, the Dirichlet boundary measurements depend on the internal conductivity distribution. It aims at recovering the information on the admittivity distribution inside a domain of interest from boundary measurements. The mathematical basis of EIT is introduced with the Neumann-to-Dirichlet (NtD) operator in the following section. Applying voltage excitation on the boundary defines the Dirichlet boundary conditions, the associated forward problem gives the Dirichlet-to-Neumann (DtN) map, mathematically it is equivalent to the NtD map.

Neumann-to-Dirichlet map

The domain Ω is assumed to be homogeneous except for a number of inclusions (or objects), which are denoted as Ω_i. These inclusions have a conductivity different with the background, and they are assumed to be simply connected domains contained in Ω. Specifically for two-phase flows, the conductivity of the water phase is within 10^{-4} – $10^{-2} S/m$, and that of gas is around $10^{-15} - 10^{-9} S/m$, *i.e.*,

$$\sigma = \begin{cases} \sim 0 & \text{in } \Omega_i, \\ 1 & \text{in } \Omega \setminus \Omega_i, \end{cases} \tag{2.2}$$

with σ of the water phase normalized to 1.

Denoting as $\boldsymbol{n}$ the unit outward normal vector on the boundary $\partial\Omega$, which is assumed to be smooth, we have the Neumann boundary conditions

$$\sigma \nabla u \cdot \boldsymbol{n} = f \quad \text{on } \partial\Omega, \tag{2.3}$$

in which $f \in L^2(\partial\Omega)$ represents the boundary current density that satisfies $\int_{\partial\Omega} f \, \mathrm{d}S = 0$. Note that the model Eqn. (2.2) entails that $\sigma \nabla u \cdot \boldsymbol{n} \approx 0$ on the boundary $\partial\Omega_i$ of the inclusions.

Introducing the functional space $H^1_\diamond(\Omega) = \{\varphi \in H^1(\Omega) : \int_{\partial\Omega} \varphi \, \mathrm{d}S = 0\}$, the Neumann boundary value problem is as follows: find $u \in H^1_\diamond(\Omega)$ that satisfies

$$\int_\Omega \sigma \nabla u \cdot \nabla \varphi \, \mathrm{d}V = \int_{\partial\Omega} f \varphi \, \mathrm{d}S, \qquad \forall \varphi \in H^1_\diamond(\Omega). \tag{2.4}$$

On denoting $L^2_\diamond(\partial\Omega) = \{\varphi \in L^2(\Omega) : \int_{\partial\Omega} \varphi \, \mathrm{d}S = 0\}$, the Neumann-to-Dirichlet (NtD) map, or the so-called *forward operator*, is introduced as $\Lambda_\sigma : L^2_\diamond(\partial\Omega) \to L^2_\diamond(\partial\Omega)$ so that the boundary potential can be written as $\Lambda_\sigma f = u|_{\partial\Omega}$, where $u \in H^1_\diamond(\Omega)$ is the solution to Eqn. (2.4). The boundary potential can be measured and compared with the boundary potential $\Lambda_0 f = u_0|_{\partial\Omega}$ for the same f and Ω but without inclusions, *i.e.* $\Omega_i = \emptyset$, with $u_0 \in H^1_\diamond(\Omega)$ being the solution of:

$$\int_\Omega \nabla u_0 \cdot \nabla \varphi \, \mathrm{d}V = \int_{\partial\Omega} f \varphi \, \mathrm{d}S, \qquad \forall \varphi \in H^1_\diamond(\Omega), \tag{2.5}$$

which corresponds to the reference problem with a homogeneous conductivity distribution inside the domain Ω. The relative NtD map is denoted as $\Pi = \Lambda_\sigma - \Lambda_0$. In the study by Hanke and Brühl (2003), the eigenvalues of Π are used to locate the inhomogeneities non-iteratively.

Electrode models

In practical implementation, the boundary current density f cannot be measured, only the current or voltage at discrete electrodes could be obtained. There are various electrode models available depending on their assumptions on current density, *i.e.* the gap model, the shunt model and the complete model (Cheng et al., 1989; Wang, 2005).

The gap model assumes that the current density is constant over electrodes, while the shunt model considers that the integral of the current density over the electrode equals to the total current flowing through that electrode. Furthermore, the complete model

is based on the shunt model, but takes into account the electrochemical effect at the interface between the electrode and the probed medium, which is called the 'contact impedance'. Compared to the gap model, the shunt and complete models are closer to reality (Cheney et al., 1999).

In the shunt model, considering a number ℓ of identical electrodes placed on $\partial\Omega$ equally spaced, the integral of the current density over the electrode is equal to the current through this electrode, while the current density at the isolated gaps between electrodes is zero, *i.e.*

$$\int_{e_k} \sigma \nabla u \cdot \boldsymbol{n} \, \mathrm{d}s = I_k \qquad \text{for } k = 1, \ldots, \ell \tag{2.6}$$

$$\sigma \nabla u \cdot \boldsymbol{n} = 0 \qquad \text{on } \partial\Omega \setminus \bigcup_k e_k, \tag{2.7}$$

where I_k is the current passing through the k^{th} electrode and e_k is the surface of the k^{th} electrode. Besides, the electrodes are assumed to be perfectly conducting so that the electrostatic potential $u|_{e_k}$ is constant at each electrode.

EIDORS code

In current study, the MATLAB based Electrical Impedance Tomography Diffusion based Optical Tomography (EIDORS) (Polydorides and Lionheart, 2002) code is employed to solve both the EIT forward and inverse problems using FEM. The goal of EIDORS is providing free software algorithms for forward and inverse modeling for EIT in medical and industrial settings, and to share data and promote collaboration between groups working on these fields. A number of pre-defined functions are available in EIDORS to solve the EIT forward and inverse problems conveniently (Adler and Lionheart, 2006).

Typically, the procedures to solve an EIT forward problem are as follows: i) define a 2D or 3D studied domain using certain geometry parameters, as well as the excitation and measurement strategies; ii) generate a finite element mesh with proper parameters, possibly refine the mesh near the boundary of the domain especially the electrodes; iii) assign the conductivity profile to the mesh; iv) solve Eqn. (2.1) with the associated boundary excitations using FEM, the potential field and boundary measurements can be obtained. EIDORS has a bunch of pre-defined forward models incorporated in the function *mk_common_model*. User-defined forward models and electrode configurations can be realized conveniently by calling external codes, *e.g.* the Netgen or Gmsh, to generate mesh on complex geometries. The excitation and measurement strategies are designated with the function *mk_stim_patterns*, commonly applied strategies are pre-defined. The electrode contact impedance can be modified easily, making it possible to apply different electrode models. The conductivity profile is assigned simply setting a value to the corresponding mesh element. Finally, the prescribed forward model is saved in a MATLAB object, the electrical field in the domain and the boundary measurements are computed using FEM solvers provided by *fwd_solve* function, both the first-order and the second-order solvers are available.

For EIT inverse problem, EIDORS facilitates 2D and 3D image reconstructions with built-in functions implementing various iterative and non-iterative methods, mainly in least squares sense. Various image reconstruction methods and their implementations in EIDORS will be further discussed in Chapter 5.

Furthermore, EIDORS provides several functions for model visualization. The *show_fem* function allows to visualize a 2D or 3D finite element model with the values in the mesh elements, the *show_slice* function gives a slice of the model at a given plane. The potential and current fields, as well as the sensitivity distributions can be easily superimposed on the finite element model for visualization.

2.2.2 Excitation strategy

Considering the conditions to be imposed on the currents/voltages fed into the electrodes and their measurement counterparts, they may be chosen arbitrarily and can be classified into pair and multiple drive systems depending on the number of excitation carrying electrodes that are active at a given time. In a pair drive system, the excitation is applied through a pair of source and drain electrodes. In a multiple drive system, all of the electrodes are active simultaneously. In any case, the specific form of the boundary condition considered defines an excitation pattern. A given series of excitation patterns is applied sequentially, forming an excitation strategy, which is ultimately used to compute a tomographic image.

Among the preeminent excitation strategies available and easily implementable with up-to-date hardware, the adjacent, opposite, full-scan (Dupré et al., 2017a), and trigonometric strategies (Cheney and Isaacson, 1992) have shown satisfying performances and been studied further in the present work. Their schematics are shown in Figure 2.6, the detailed introduction is presented hereafter.

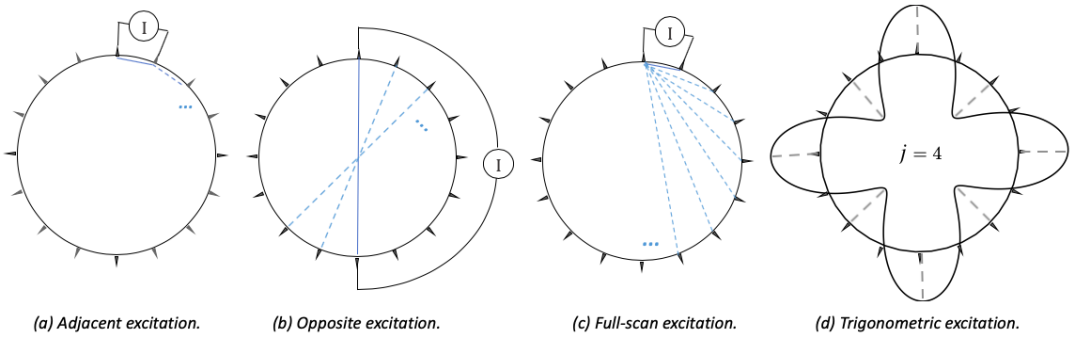

FIGURE 2.6: Schematics of the four excitation strategies, the blue dotted lines in (a) to (c) indicate the following electrode pairs for excitation. In (d) the trigonometric function with a frequency $j = 4$ is plotted, giving the excitation amplitude at each electrode.

Pair drive systems

Adjacent strategy. It is defined by the pattern where the excitation current is injected at two neighboring electrodes. In the adjacent strategy, the current is switched to the next pair of neighboring electrodes until all the possible neighboring pair have been considered. The number N_e of excitation patterns is equal to the number of electrodes, *i.e.* $N_e = \ell$, yielding a number of measurements $N_m = \ell^2$. The main drawback of the adjacent strategy is the expected non-uniformity of the current distribution within the domain, with the current density being maximized in a neighborhood of the excitation electrodes and much lower at distant electrodes, thus leading to measurements of low amplitude at the latter, which would therefore be more susceptible to noise pollution.

Opposite strategy. It considers current injection at pairs of opposite electrodes, with $N_e = \ell/2$ possible excitation patterns, which gives $N_m = \ell^2/2$ measurements. The latter value is half this associated with the adjacent strategy, which can be expected to be detrimental to the images to be reconstructed. Nonetheless, the signal amplitudes acquired at distant electrodes can be expected to be larger in the opposite strategy compared to the adjacent one, as the maximal distance between excitation and measurement electrodes being approximately reduced by a factor $\sqrt{2}$ for the former.

Full-scan strategy. Here, all electrodes are sequentially selected to be source and drain until all possible pairs of electrodes have been formed, giving $N_e = \ell(\ell-1)/2$ and $N_m = \ell^2(\ell-1)/2$. This strategy includes the excitation patterns of the adjacent and opposite strategies, among others, thus leading to comparatively longer acquisition times. Indeed, it respectively involves $(\ell-1)/2$ and $(\ell-1)$ times more patterns than the latter.

Multiple drive systems

Among the possible excitation strategies applicable to multiple drive EIT systems, we only focus here on the following one which seems to be favored by previous studies.

Trigonometric strategy. This strategy has been introduced in the search for an optimal excitation pattern and it has been shown to maximize a *distinguishability* criterion, see Cheney and Isaacson (1992). In each excitation pattern, the current at the electrodes e_k, for $k = 1,\dots,\ell$, is constructed from a cosine or sine function of varying angular frequency $\omega_j = 2\pi j/\ell$, as

$$I_{k,j} = \begin{cases} I_0 \cos(k\omega_j) & \text{with } 1 \le j \le \ell/2, \\ (-1)^{k+1} I_0 \sin(k\omega_j) & \text{with } \ell/2 < j \le (\ell-1), \end{cases} \tag{2.8}$$

where I_0 is a fixed amplitude. The definition (2.8) of $I_{k,j}$ is to be used in the boundary condition (2.6) and it can be adapted to the case of voltage excitations. This defines $N_e = (\ell-1)$ different patterns that lead to $N_m = \ell(\ell-1)$ measurements overall. Compared to the other strategies, the trigonometric one requires simultaneous excitation of multiple sources, which is more demanding in practice and increases the complexity of the EIT system.

For conciseness, the latter will only be described in terms of current excitation and voltage measurement, alternative operating modes available are shown in Figure 2.7. The current-based operating mode can easily be transformed into a voltage-based mode for both excitations and measurements. With the resistor having fixed value R_0 connected to the electrode, the excitation or measurement current can be calculated from the voltage measurement across the resistor. The operating mode (b) has been applied in several EIT systems, such as the ProME-T system (Dupré et al., 2017a), and the system developed in Jia et al. (2017) for highly conductive oil-water two-phase flow measurement. The ONE-SHOT EIT system reported recently in Darnajou et al. (2020) applies the operating mode (c). Both the ProME-T and ONE-SHOT systems have been used in the present thesis work for static and dynamic experiments, separately.

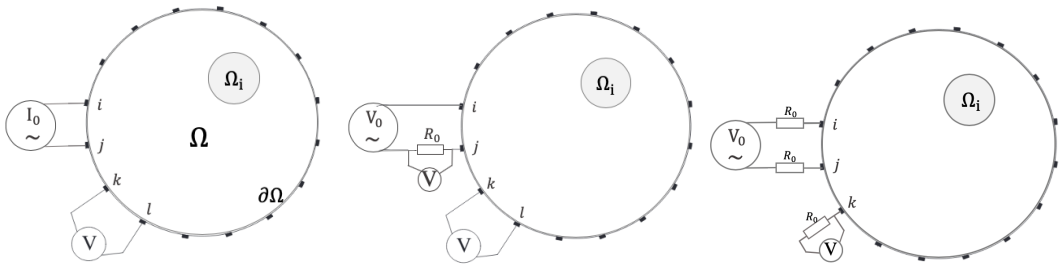

FIGURE 2.7: Schemes of EIT operating modes: (a) Current excitation at electrodes (i, j) with difference voltage measurements at neighboring electrodes; (b) Voltage excitation at electrodes (i, j) with difference voltage measurements at neighboring electrodes; (c) Voltage excitation at electrodes (i, j) with voltage measurement across R_0 at each electrode.

Number of independent measurements

The number N_m^i of independent measurements accessible in each strategy is vital, as it determines the spatial resolution of the reconstructed images produced and might not be necessarily equal to the number N_m of measurements. Since source and drain are essentially the same for pair drive strategies, the measurements would be reciprocal for a specific pair of electrodes. For an EIT system with ℓ electrodes, Breckon and Pidcock (1988) showed that, for any pair drive strategy, the number N_m^i of independent measurement is at most equal to $\ell(\ell-1)/2$. Yet, the opposite strategy is such that $N_m^i = \ell(3\ell-2)/8$ because it makes use of a relatively limited number of excitation patterns.

Particularizing for an EIT system with $\ell = 16$ electrodes, Table 2.1 provides the number N_m^i of independent measurements and the ratio with the number N_m of measurements for the various excitation strategies considered. This ratio is called the redundancy ratio, as it quantifies the redundancies in the measurements, with the value 1 being attained if they are all independent. Conversely, a small ratio characterizes large measurements redundancies, which may be a factor to be considered if memory and computational power are an issue.

TABLE 2.1: Number N_m^i of independent measurements and redundancy ratio relatively to the number N_m of measurements for the various strategies, considering an EIT system with 16 electrodes.

Strategies	**Adjacent**	**Opposite**	**Full-scan**	**Trigonometric**
N_m^i	120	92	120	240
N_m^i/N_m	0.47	0.72	0.06	1

Up to now, most of the practical EIT systems in use applied the adjacent excitation strategy due to its simplicity in implementation, only requiring a pair of sources and a few multiplexing operations. While the other excitation strategies have proven to be effective and easy to implement using modern hardwares. Some studies involving physical modelings and numerical simulations have been done on these excitation strategies before. In the present thesis work, the four excitation strategies considered here have been assessed on a number of criteria in terms of practical implementation and quality of reconstructed images, aims at confronting some of the predominant EIT excitation protocols on practical systems that is dedicated to the imaging of media with highly contrasted material

components, for example, two-phase flows. The results will be shown in Section 3.2 and 5.3.

2.2.3 3D effect

Due to the *soft-field* nature of electrical current and the finite length of electrodes, the electric field in the studied domain spreads far beyond the electrode plane, leading to a 3D sensing region for a 2D sensor. The objects outside of the electrode plane would have effects on the measurements hence on the reconstructed images, which is known as the 3D effect of EIT. Also, severe distortions of the electric field appear on both ends of the electrodes, giving the so-called 'fringe effect' (Sun and Yang, 2014).

2D simulations have been carried out to explain the geometrical spreading effect of EIT. The open source code FreeFem++ (Hecht, 2012) is used to solve the EIT forward problem. FreeFem++ is a partial differential equation solver for multi-physics non linear systems in 2D and 3D. Here, the simulation model is set to be a rectangular with unit height and a width of 2. A pair of electrodes on the opposite boundaries are considered, the rest of the boundaries are insulating, *i.e.* zero current density. The generated finite element mesh is refined on the electrodes, an example mesh for the case with $L_e = 1.2$ is shown in Figure 2.8. Voltage sources with amplitudes of ± 1 V are exerted on the two electrodes respectively, the potential and current fields inside the domain are computed for various lengths L_e of the two electrodes.

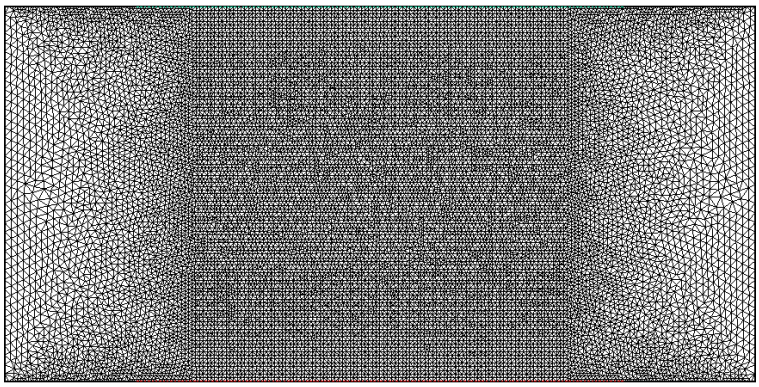

FIGURE 2.8: An example finite element mesh for the case with $L_e = 1.2$.

Figure 2.9 shows the current streamlines and equipotential lines in the domain for cases with electrode length $L_e = 0.02$, 0.2, 0.7, and 1.2, separately. The vectors in blue represent the current streamlines, and the contours with different colors for equipotential lines. As we can see, in all cases the current streamlines concentrate in the middle of the domain, and the axial extends of the high concentration region is similar for different L_e. Considering the case $L_e = 0.02$, the current streamlines spread out far beyond the electrode plane, the geometrical spreading effect of EIT is clearly shown. Noting that the current streamlines are computed from local potential gradient, intensive streamlines indicate a high potential gradient, where a small conductivity change can have strong effect on the potential field. As L_e increases the current streamlines between the two electrodes become more homogeneous, indicating a smoother potential field, which may give a more homogeneous sensitivity distribution. In addition, the fringe effect is presented by the extraordinarily uneven current streamlines at the ends of the electrodes, see Figure 2.10.

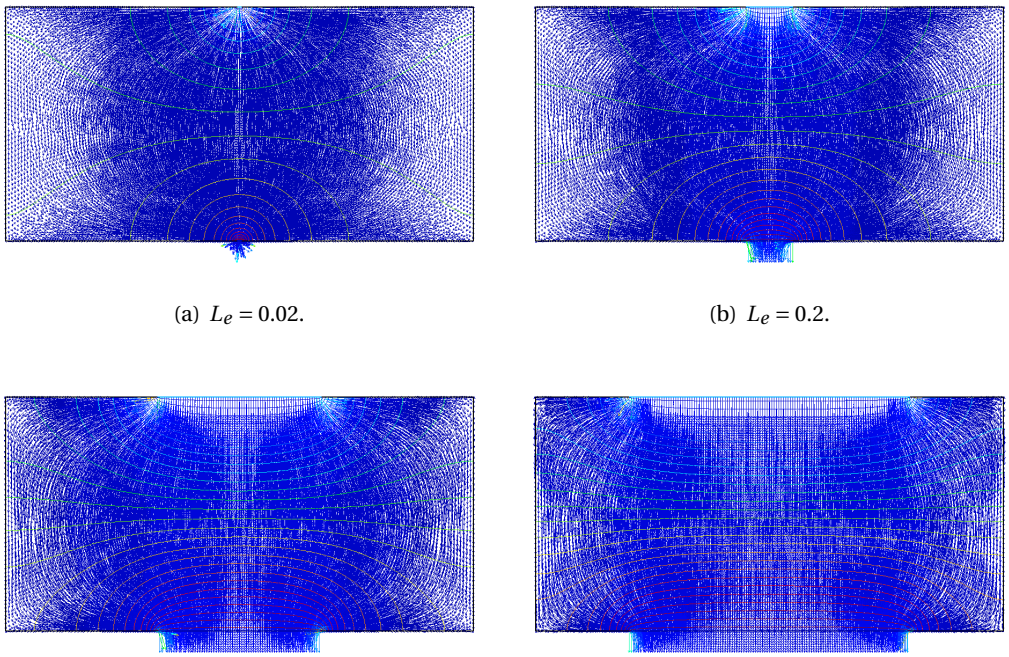

(a) $L_e = 0.02$. (b) $L_e = 0.2$.

(c) $L_e = 0.7$. (d) $L_e = 1.2$.

FIGURE 2.9: The current streamlines and equipotential lines in the domain with varying electrode lengths $L_e = 0.02, 0.2, 0.7, 1.2$.

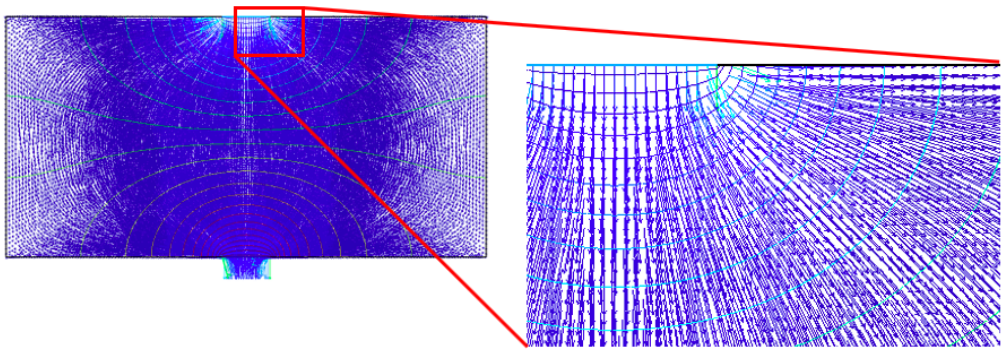

FIGURE 2.10: Zoom-in plot of the current streamlines at the ends of the electrode for $L_e = 0.2$.

Besides, a number of researches have been done studying the effects of guarding electrodes on the potential and current fields inside the domain (Ma et al., 1997; Plonsey and Collin, 1977). This approach employs extra planes of electrodes aside the main plane, take Figure 2.11(a) as an example, the pair of electrodes in the middle represent the main plane, while the other two pairs of electrodes are called the 'guarding electrodes', they can be either grounded or excited by the same voltage sources as the main plane electrodes (Ma et al., 1997).

A series of simulations have been performed with different distances L_d between the guarding electrode plane and the main plane. The electrode length is fixed as $L_e = 0.2$, the current streamlines inside the domain for $L_d = 0.3$ and $L_d = 0.7$ are computed and plotted.

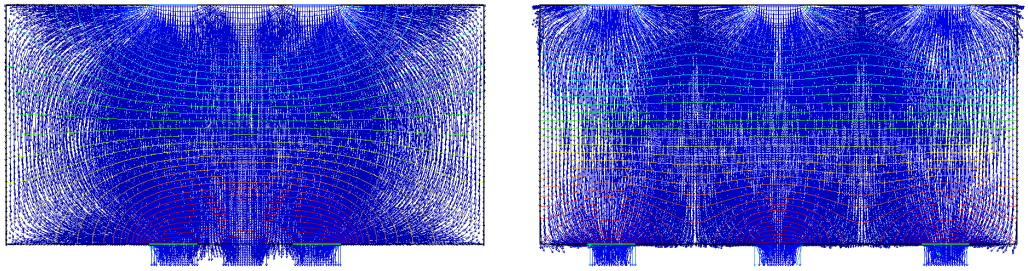

(a) $L_d = 0.3$. (b) $L_d = 0.7$.

FIGURE 2.11: The current streamlines and equipotential lines in the domain for $L_e = 0.2$ and $L_d = 0.3, 0.7$, the guarding electrodes are excited with the same voltages as the main plane electrodes.

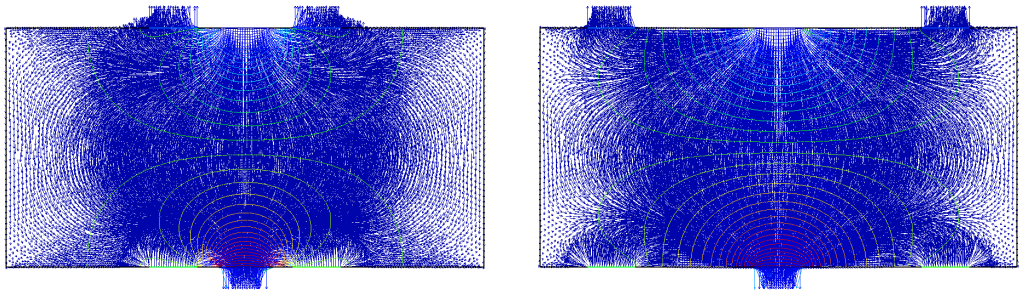

(a) $L_d = 0.3$. (b) $L_d = 0.7$.

FIGURE 2.12: The current streamlines and equipotential lines in the domain for $L_e = 0.2$ and $L_d = 0.3, 0.7$, the guarding electrodes are grounded (at zero potential).

Figure 2.11 shows the results where the guarding electrodes are excited by the same voltages as the main plane electrodes, while Figure 2.12 shows that with grounded guarding electrodes (zero potential is exerted). As we can see, despite the local changes taking place nearby the electrodes, the axial extend of the high concentration region of the current streamlines is not constrained by the guarding electrodes for both cases, on the contrary, the extend is even enlarged in cases with $L_d = 0.7$. Besides, comparing the current streamlines between the main plane in Figure 2.9(b) and 2.11(b), it is interesting that the excited guarding electrodes may flatten the current streamlines comparing to the case without guarding electrodes, which may bring some benefits diminishing the inhomogeneous of EIT sensitivity distribution.

Although some researches argued that the guarding electrodes does not fulfill the expectation that it reduces the geometrical spreading effect (Plonsey and Collin, 1977), they may bring some advantages, such as a more homogeneous sensitivity distribution and a stronger measurement signals. Furthermore, the use of multiple planes of electrodes may favor 3D image reconstructions: exploiting the excitations on the electrodes of different planes, the sensitivity in the center of the sensing domain may be improved. Several cross-plane excitation patterns have been studied in Wagenaar and Adler (2016), proving the advantages of multiple electrode planes in 3D image reconstructions.

Chapter 3

EIT system design for two-phase flow imaging

The aim of two-phase flow measurement is to estimate (online or offline) various parameters of the flow, including the phase distribution, the cross-sectional or volumetric phase fraction, the flow pattern, among others. These information are vital to assess the flow instability and heat transfer coefficient. To fulfill the expectations, the EIT systems dedicated to two phase flow measurements should be designed to have adequate spatial and temporal resolutions, and be robust to measurement noise.

In this chapter, the EIT systems used in the present thesis study, namely the ProME-T and ONE-SHOT systems, are briefly introduced. Then, the four excitation strategies presented in Section 2.2.2 are compared regarding several practical implementation criteria. Afterwards, the influences of electrode size on the system performance are studied applying two sets of electrodes with different sizes into the ProME-T system, with respect to the impedance response, noise level, and residual error induced by multiplexing. The results are considered in the design of a dual-plane test section for the PKL facility.

3.1 EIT systems developed in LTHC

A practical EIT system consists of hardwares and software. Typically the hardwares include: i) a data acquisition system to generate the excitation signals and measure the boundary voltages/currents; ii) a multiplexer routing the excitation signals to the selected electrodes, possibly through Time Division Multiplexing (TDM) or Frequency Division Multiplexing (FDM); iii) a Printed Circuit Board (PCB) handling the operating mode explained in Figure 2.7, commonly the multiplexer is also mounted on the PCB for optimal performance, sometimes with the signal filter and amplifier; iv) a test section with certain number of electrodes; v) auxiliary devices for input/output and proper wires to connect all components together. In terms of the software, a data acquisition code is required to manage the multiplexing, data logging and possible online display; also, proper data post-processing codes should be developed to handle the measurement data, for further image reconstruction and flow features extraction. Here, we focus on the hardwares, the software would be investigated in the latter chapters.

Two EIT systems have been developed in LTHC based on the TDM and FDM separately, *i.e.* the ProME-T system developed in Dupré (2017), and the ONE-SHOT system developed in Darnajou et al. (2020). Both of them implement the full-scan excitation strategy using voltage sources, their system specifications, realization procedures and data processing methods are described as follows.

3.1.1 ProME-T system

Hardwares

The ProME-T system was developed in Dupré (2017) for the purposes of two-phase flow measurement and phase fraction estimation, while only static experiments were accomplished for system validation. The main components of the system are shown in Figure 3.1. It has 16 electrodes on the internal boundary of a PMMA test section, with an angular separation of 22.5°. The signal excitation and acquisition are both realized by the National Instrument PXI-6368e card (PXIe, 2016), which has four Analogue Output (AO) channels at a sampling rate up to 3.33 MHz, and 16 differential Analogue Input (AI) channels up to 2 MHz. The operating mode in Figure 2.7(b) is implemented in ProME-T, the excitation signals are alternating voltages with an amplitude of ±1 V to avoid the electrolysis reaction of water. For each excitation pattern, the difference voltages between all neighboring electrodes are measured simultaneously. The excitation current is calculated from the voltage measurement across the constant resistor R_0 connecting to the excitation source, with $R_0 = 200\Omega$ in the present system.

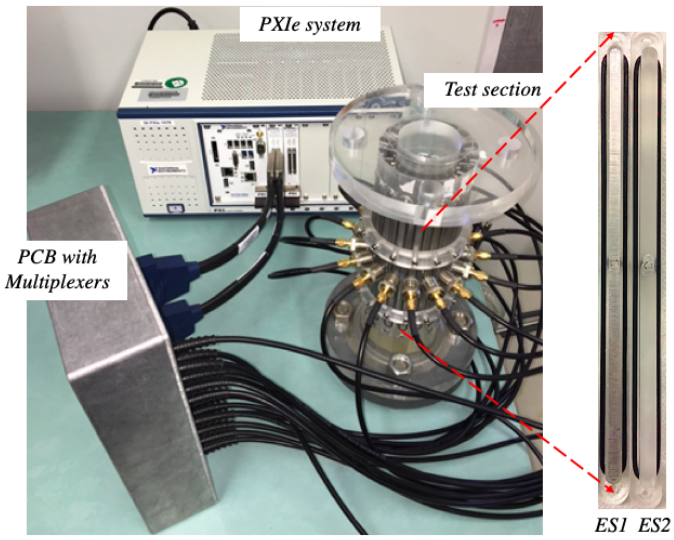

FIGURE 3.1: *Left*: the ProME-T system in LTHC applying TDM with 16 electrodes. *Right*: the two sets of electrodes with different lengths available for ProME-T.

The full-scan strategy is implemented in the ProME-T, giving 120 different excitation patterns. A 16 ports multiplexer is mounted on the PCB to perform TDM, routing the excitation signals to the selected pair of electrodes for each excitation pattern. The addresses of the source and drain electrodes are assigned to the multiplexer by the eight Digital Output (DO) channels of the PXIe card, four channels for each.

The test section is a cylinder pipe with diameter of 51 mm and height of 270 mm, the electrodes are designed to be removable. Two sets of electrodes with different sizes are available: the Electrode Set 1 (ES1) of size 154 mm×4 mm and the Electrode Set 2 (ES2) of size 5 mm×4 mm, as shown in Figure 3.1. The connections between the electrodes and the PCB are realized by the co-axial wires and Bayonet Neill-Concelman (BNC) connectors, to reduce the electro-magnetic distortion.

The speed of two-phase flows can be up to 10 m/s during the measurement, a high acquisition rate is always advantageous, however, high frequency electronic operations may induce extra electrical noise to the measured signal. The typical frame rate of the ProME-T implementing the full-scan strategy is 208 fps, which is a compromise between the acquisition rate and measurement accuracy.

Equivalent circuit model

Considering the operating mode of the ProME-T system, the measurement system at each excitation pattern can be assumed as a closed circuit shown in Figure 3.2, where V_0 represents the excitation voltage, the combination of the charge transfer resistance R_e and the double layer capacitance C_e contributes to the electrode-electrolyte contact impedance, here it represents the summation of the contact impedances at the source and drain electrodes, Z is the *bulk impedance* of the medium. They are connected in a cascade way with the constant resistor R_0. The current I_Z passing through the circuit can be calculated from $I_Z = V_R / R_0$, with V_R the voltage measurement across R_0.

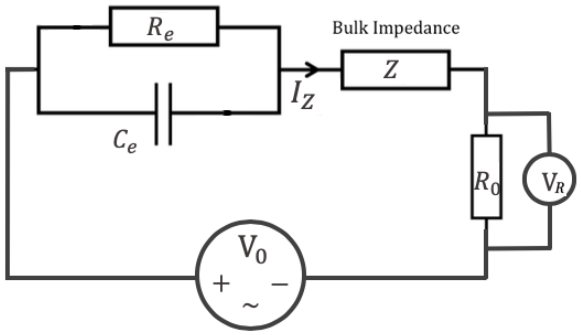

FIGURE 3.2: Closed circuit between the source and drain electrodes for each excitation pattern.

The total impedance Z^{tot} of the system is

$$Z^{tot} = Z^{source} + Z^{drain} + Z + R_0 = V_0 / I_Z, \tag{3.1}$$

with Z^{source} and Z^{drain} the contact impedances at the source and drain electrodes, they are electrode-specific and invariant with the phase distributions inside the domain, thus can be calculated and excluded from the closed circuit, giving the bulk impedance Z.

Clearly, Z evolves with the phase distribution and the excitation electrodes, while it is also affected by the frequency of the excitation signals, so do the Z^{source} and Z^{drain}. Dupré studied the frequency response of the total impedance Z^{tot} between two point-like electrodes located on the opposite of a pipe, using a homogeneous electrolyte of different concentrations as the conductive medium, the results are presented in Dupré (2017, Figure 2.29 and 2.30). It is shown that at medium excitation frequencies (typically from 1 kHz up to 100 kHz), the total impedance is mainly real: the bulk impedance dominates the global impedance while the electrode contact impedance is not significant. In current study, the frequency responses of the total impedances using the two sets of electrodes have been investigated, the results are shown in Section 3.3.

Measurement data processing

As mentioned, the excitation signal used in the ProME-T is sinusoidal wave of specific frequency, which is sampled N_{sp} times for each period. In each excitation pattern, N_p periods of excitation signal are held on the selected electrodes, meanwhile, boundary measurements are taken simultaneously on all the $\ell = 16$ AI channels. A frame of acquisition is composed by N_e excitation patterns of one excitation strategy, giving $(N_{sp} \times N_p \times N_e) \times \ell$ measurements. Typically in ProME-T, $N_p = 2$ and $N_{sp} = 20$ are taken, yielding ~ 600 kB of measurement data with double precision for one frame.

During data post-processing, Fast Fourier Transform (FFT) is performed on every $N_p \times N_{sp}$ data points for each channel, the amplitude at excitation frequency corresponds to the measurement of an excitation pattern. In the present thesis study, the image part of the amplitude is not considered, the real part is taken as the fundamental signal. The data size after FFT is reduced to $N_e \times \ell$, it will be further used in the eigenvalue-based approach presented in Chapter 4, and in the image reconstructions discussed in Chapter 5.

3.1.2 ONE-SHOT system

Hardwares

The logic of EIT hardware design has been mature for decades now and recent advances have focused on greater accuracy, faster acquisitions and the ability to apply parallel multi-frequency excitations (Aguiar Santos et al., 2016). Recently, an innovative concept ONE-SHOT has been proposed in Dupré and Mylvaganam (2018), in which the FDM is used to discriminate some superimposed signals at multiple frequencies, giving access to boundary measurements of multiple excitation patterns simultaneously. It is applicable to both pair drive and multiple drive systems avoiding the need of multiplexing.

The principle of ONE-SHOT method is to assign a specific frequency to the excitation signal of each excitation pattern. The superimposed excitation signals are injected to the corresponding electrodes simultaneously, with the resulting boundary voltages measured at the same time. The boundary measurements are discriminated through FFT, to obtain the measurement amplitude for each excitation pattern. That is, in FDM the multiplexing is not accomplished physically, but mathematically through FFT. According to the Nyquist criterion, the measurement sampling frequency should be at least double of the highest excitation frequency to correctly reconstruct the amplitudes of all excitation frequencies. Thus, the number of sampling points acquired for one frame is $N_d = \text{nextpowerof2}(2N_e)$ at the minimum to discriminate the signals, which is the next number over $2N_e$ that is the power of 2, to ease the FFT computation. Considering the sampling rate S_m of the data acquisition module, the maximum frame rate can be up to S_m / N_d fps.

The ONE-SHOT method has been implemented in Darnajou et al. (2019, 2020) with $\ell = 16$ electrodes, the developed system is shown in Figure 3.3. The system employs the CRIO-9039 module (cRIO, 2018) as the controller, it has eight ports for AI/AO modules with a sampling rate up to 1 MHz, with which the excitation signals generation and data acquisition are realized. The full-scan strategy implemented requires a $N_d > 240$, supporting an ultra-high frame rate up to 3906 fps.

The operating mode shown in Figure 2.7(c) is implemented, a PCB board is designed to connect each electrode with a constant resistor $R_0 = 100\,\Omega$. Again, the co-axial wires and BNC connectors are used to connect the electrodes to the PCB. The test section is

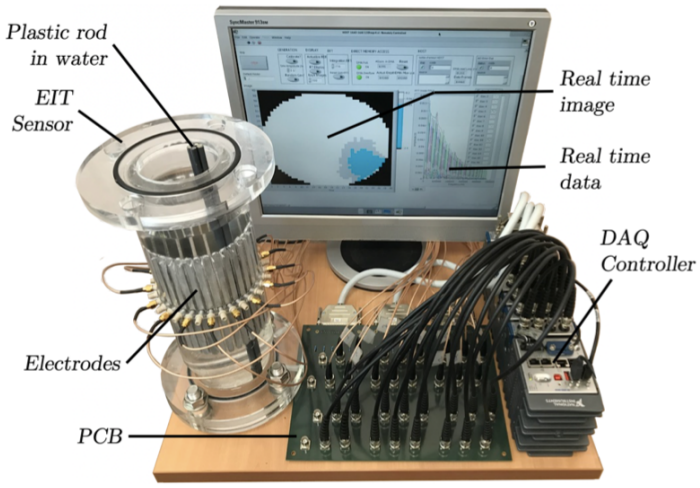

FIGURE 3.3: The ONE-SHOT system developed in LTHC using FDM with 16 electrodes, adapted from Darnajou et al. (2020).

a PMMA pipe with diameter of 80 mm and height of 336 mm, it has 32 electrodes of size 150 mm×6 mm on the boundary, allowing possible upgrade of the present system.

Equivalent circuit model

The equivalent closed circuit model of the ONE-SHOT system for each excitation pattern is shown in Figure 3.4, which is similar to that of the ProME-T system but with an extra R_0. Considering the current measurements at all electrodes meet the zero summation (see Eqn. (2.4)), the current I_Z flowing through the closed circuit can be calculated by $I_Z = -(\sum_{e=1}^{N_s} V_s)/R_0$, where $\sum_{e=1}^{N_s} V_s$ represents the summation of the voltage measurements at the electrodes other than the exciting ones. Moreover, Darnajou et al. (2020) showed that the effect of contact impedance is eliminated in the ONE-SHOT system due to the continuous excitation signal, *i.e.* $Z^{source} = Z^{drain} = 0$. Finally, the total impedance is calculated directly by $Z^{tot} = Z + 2R_0 = V_0/I_Z$.

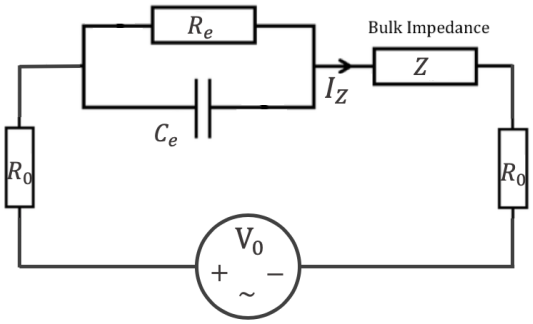

FIGURE 3.4: Equivalent closed circuit of the ONE-SHOT EIT system.

Measurement data processing

As explained, N_d data points are acquired at each measurement channel for one frame of acquisition, giving $N_d \times \ell$ data points in total. The measured data contains the information

at N_e excitation frequencies to be retrieved through FFT. Benefiting from the Field Programmable Gate Array (FPGA) incorporated in the controller, the FFT of the acquired data can be computed almost simultaneously with data acquisition, giving the corresponding amplitude for each excitation pattern in frequency domain, so that the raw measurement signals can be discarded, only the fundamental amplitude at each excitation frequency are saved, giving a data size of $N_e \times \ell$ for one frame. Finally, the data saved to the local host in the ONE-SHOT system is $N_p \times N_{sp}$ times less than in ProME-T, facilitating the data logging for ultra-high speed EIT (several thousands of fps).

3.2 Practical comparison of excitation strategies

The excitation strategy is one of the key aspects one have to choose prior to EIT system design. On one hand, it determines the number of AO channels required and the multiplexing sequence in the data acquisition code. On the other hand, it has strong effects on the boundary measurement responses and sensitivity distribution in the probed domain, hence on the reconstructed images.

There has been an intensive search for *optimal* current patterns (or excitation strategies in a general sense), starting in the field of medical imaging in the 1990s. Gisser et al. (1987) introduced the concept of *distinguishability* as a quantitative criterion to evaluate the *quality* of a current pattern. It is defined as the quantity $\delta_d = \|\boldsymbol{V}_s - \boldsymbol{V}_0\|^2_{L^2} / \|I_e\|^2_{L^2}$, where $\boldsymbol{V}_s$ and $\boldsymbol{V}_0$ are the boundary voltage measurements associated with the studied and reference configurations, given the current excitation I_e. Cheney and Isaacson (1992) proved analytically that the trigonometric pattern maximizes δ_d. However, the use of an alternative criterion may lead to a different optimal current pattern. For example, if the total injected current is constrained, then it has been shown in Lionheart et al. (2001) that the optimal current pattern turns out to be the pair drive pattern. Furthermore, Demidenko et al. (2005) deployed a criterion that quantifies the *accuracy* of the reconstructed tomographic images, based on the total variance of the estimated resistance (or conductance) matrix, and developed an adaptive approach with real-time updating of the current pattern.

The *optimal* current patterns described above have been investigated in depth mathematically. Yet, there is a lack of a systematic comparison of these physical and numerical models using actual experimental data and indicators of the quality of reconstructed images, which is the ultimate goal of tomography. Clearly, there is not a consensus on the *optimal* current pattern to be used, but most of the practical systems in use employ the adjacent pattern (Dickin and Wang, 1996; Sun and Yang, 2015; Jia et al., 2017) with the advantage of easy implementation, although it is considered to be harmful to distinguish changes in internal conductivity distributions (Adler et al., 2011).

The four excitation strategies presented in Section 2.2.2 have their own pros and cons but lack exhaustive comparisons in practical set-ups. Up to the author's knowledge, only the adjacent and opposite strategies were compared in terms of reconstruction performances in Stephenson et al. (2008). In the present thesis study, the adjacent, opposite, full-scan and trigonometric strategies have been compared comprehensively in terms of (i) feasibility of the hardware implementation, (ii) amplitude of the measurement responses, (iii) sensitivity distribution, and (iv) quality of the reconstructed images. The results of the first three aspects are presented in this section, as of the last aspect will be described in Section 5.3.

3.2.1 Representative frame rates

To begin with, typical EIT architectures and some estimations of the representative acquisition frame rates for each strategy (a frame being composed of the acquisitions associated with all of its excitation patterns) are presented with $\ell = 16$ electrodes.

TDM systems

For pair drive excitations, the TDM systems generally use a multiplexer to switch the signals to the selected pair of source and drain electrodes. For such systems, the transient phases during multiplexing have been shown to be harmful to the measurements, in particular due to the contact impedance, see Wang (2005). Therefore, the measurements performed at the excitation carrying electrodes are generally discarded. However, it has been evidenced in Dupré (2017) that the residual error induced by multiplexing could be neglected when employing an appropriate switching approach and large electrode area. In the present study, all measurements are taken into account when considering pair drive excitations.

For the multiple drive trigonometric strategy, the multiplexing is not needed since each electrode is directly connected to an individual electrical source whose amplitude varies with the excitation pattern. Nonetheless, with the requirement to control all of these individual sources, the system becomes more complex.

Here, the ProME-T system is taken as a prototypical example, to estimate the associated frame rates for the various excitation strategies, see Table 3.1. Using ProME-T, the typical frame rate for the full-scan strategy is 208 fps. Recalling the number N_e of excitation patterns of various strategies in Section 2.2.2, the typical frame rates for the adjacent and opposite strategies would be 1560 fps and 3120 fps, respectively. Lastly, for the trigonometric strategy, three more PXIe cards are required to drive excitation signal at each electrode, which therefore bear an extra cost. The resulting frame rate is estimated at 1664 fps.

FDM systems

In FDM systems, the excitation signals of all excitation patterns in one strategy are superimposed and exerted to corresponding electrodes simultaneously, with the boundary measurements taken at the same time. The frame rate is only relevant to the number N_d of sampling points acquired at each measurement channel in one frame, as explained in Section 3.1.2. Taking the ONE-SHOT system as a prototypical example, the maximum frame rate is $10^6/N_d$ fps for all excitation strategies. Considering the N_e of various strategies, the estimated frame rates are provided in Table 3.1. It is underlined that even for pair drive excitation strategies, the FDM systems require 14 extra electrical sources than conventional systems.

TABLE 3.1: Estimated acquisition frame rates (fps) for the excitation strategies considered and using EIT systems with 16 electrodes.

Strategies	**Adjacent**	**Opposite**	**Full-scan**	**Trigonometric**
ProME-T	1560	3120	208	1664
ONE-SHOT	31250	62500	3906	31250

3.2.2 Statistics of measurement amplitudes

Due to the *ill-posedness* of the EIT inverse problem, even a small measurement noise can lead to large discrepancies in the reconstructed images. Thus, in practice, additionally to the number N_m^i of independent measurement discussed previously, it is also insightful to evaluate the statistical distributions of the measurement amplitudes at different electrodes for various excitation strategies. Specifically, the mean and standard deviation of synthetic boundary measurements are computed, which give a hint on the robustness of various excitation strategies to measurement noise.

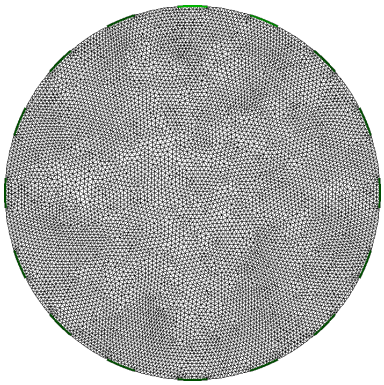

FIGURE 3.5: 2D forward simulation model with 16 evenly spaced electrodes.

These are investigated based on numerical simulations using EIDORS. An EIT model is built with the homogeneous background conductivity and compute a set $\boldsymbol{V}$ of boundary measurements for each excitation strategy, as shown in Figure 3.5. The domain is set to be a 2D disk with unit radius and 16 evenly spaced electrodes with peripheral width equal to 0.16, which coincides with the experimental test section of ProME-T system introduced in Section 3.1.1. A triangle mesh with 8791 nodes is used in the FEM model. For each strategy one considers a current source of unit amplitude. The mean (average amplitude) and the standard deviation (spatial variability) computed for each measurement set $\boldsymbol{V}$ are reported in Table 3.2.

TABLE 3.2: Mean and standard deviation of the boundary measurements for the various excitation strategies and a 16 electrodes EIT system.

Strategies	**Adjacent**	**Opposite**	**Full-scan**	**Trigonometric**
Mean (V)	0.1931	0.3220	0.2817	0.8067
Standard deviation (V)	0.3915	0.2668	0.3130	0.3352

For pair drive systems, the adjacent strategy is characterized by the lowest mean and the highest standard deviation, and conversely for the opposite strategy. The full-scan is associated with intermediate values. Indeed, the adjacent strategy has much lower measurement amplitudes at electrodes away from the source electrodes, which are more distant on average compared to the opposite strategy. The full-scan strategy contains the excitation patterns of the two previous strategies among others. For multiple drive systems, considering the trigonometric strategy yields measurements of a much larger amplitude in average compared to pair drive systems, since it inputs more power into the system with all electrodes being active in each pattern. Moreover, the measurements standard deviation is comparable to the full-scan strategy.

3.2.3 Sensitivity distributions

The effectiveness of each internal region contribution to the overall measurement signal is assessed numerically through the sensitivity maps for each strategy. Kauppinen et al. (2006) visualized such sensitivity distributions for the adjacent and opposite strategies, and also the so-called cross and adaptive ones, but it was for single excitation patterns rather than for the global excitation strategies that we consider here.

Given an EIT system, a localized conductivity perturbation $\delta\sigma$ within the probed medium can induce a perturbation δu of the electric potential, which can in turn be measured on the boundary. For a certain excitation strategy, the greater the perturbation δu, the more sensitive the system under consideration is. Considering a finite-element discretization of the background domain, with piecewise-constant conductivity, and a perturbation $\sigma_j \to (\sigma_j + \delta\sigma_j)$ in the j-th element, then excitation is driven at electrode pair i and the potential perturbation $V_{ik} \to (V_{ik} + \delta V_{ik})$ is measured at electrode pair k. Note that the labelling (i,k) of excitation and measurement electrode pairs is a numbering specific to each excitation strategy that is kept implicit here to avoid technicalities. In order to characterize the imaging capabilities of the EIT system, one considers the ratio

$$s_{(i,k)j} = \frac{\delta V_{ik}}{\delta \sigma_j} = \int_j \nabla u_i(\boldsymbol{x}) \cdot \nabla u_k(\boldsymbol{x}) \, \mathrm{d}\boldsymbol{x}, \tag{3.2}$$

which quantifies the *sensitivity* of the k-th measurement in the i-th excitation pattern to a local conductivity perturbation in the j-th element. Renumbering the double index (i,k) using a single *row* index for all possible excitation/measurement pairs, then the complete set of sensitivities $s_{(i,k)j}$ can be concatenated in the form of a Jacobian, or sensitivity, matrix $\boldsymbol{J}$. The second equality uses the adjoint method (Adler et al., 2017), with the integral being carried over the j-th element, u_i is the voltage field associated with i-th current pattern while u_k is the voltage field computed using the k-th voltage measurement as an excitation current.

An overall (discrete) sensitivity map $S_j = \sum_i \sum_k s_{(i,k)j}$ is defined as the element-wise summation of the sensitivities of all patterns in one given excitation strategy. Using the same finite element EIT model as in Section 3.2.2, the overall sensitivity map S_j has been computed for all excitation strategies considered. Figure 3.6(a) shows the computed sensitivity distributions along a diameter, which are radially symmetric (local averaging have been performed to smooth out discretization effects), and these values are normalized in Figure 3.6(b) relatively to the associated maximal sensitivity, which is naturally attained on the boundary. Some relevant statistics are reported in Table 3.3.

From Figure 3.6 and Table 3.3, the adjacent strategy is characterized by the lowest overall sensitivity among the four strategies considered, with a 80% drop in sensitivity at the centre of the domain. The opposite strategy has a more homogeneous sensitivity distribution (small standard deviation) compared to the adjacent one. The full-scan strategy is characterized by the highest overall sensitivity values. Finally, the trigonometric strategy has relatively large sensitivity values but they significantly drop (by about 66%) at the center of the probed domain.

3.2.4 Practical implementation criteria

To conclude the section on the practical aspects of the implementation of the four excitation strategies considered, Figure 3.7 concatenates all of the quantitative criteria of the

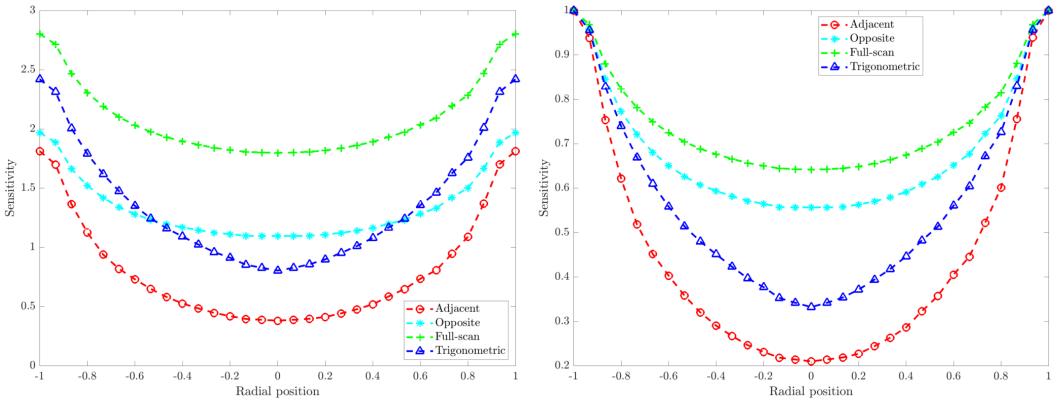

(a) Sensitivity distribution.

(b) Normalized distribution.

FIGURE 3.6: Locally averaged sensitivity distributions along one diameter for the excitation strategies considered.

TABLE 3.3: Mean and standard deviation of the sensitivity distributions for the various excitation strategies and a 16 electrodes EIT system, see also Figure 3.6(a).

Strategies	**Adjacent**	**Opposite**	**Full-scan**	**Trigonometric**
Mean	0.8090	1.3406	2.0921	1.3810
Standard deviation	0.4636	0.2816	0.3234	0.5166

Tables 2.1, and 3.1 to 3.3. With the exception of standard deviation criteria, which one generally intends to minimize, all of these criteria are increasing functions of performance. For a synthetic representation, these criteria are plotted after being each normalized by the largest value among the excitation strategies. Note that, according to the previous comment, reversed ranking is used for the standard deviation criteria. Such a representation highlights that defining what is an *optimal* strategies depends on which criteria are important in a practical implementation. For example, the trigonometric strategy satisfies well most criteria on average. As for the full-scan, on the one hand it bears substantial acquisition costs but, on the other hand, it is characterized by high responses signals and sensitivity. In this context, we turn in the Section 5.3 to a comparison of reconstructed images with some quantitative evaluations of their quality.

3.3 Influences of electrode size on EIT system performance

Recall the numerical simulations concerning the 3D effect of EIT in Section 2.2.3, the length of the electrodes defines the potential field inside the studied domain, hence the sensitivity distribution. Besides, it was proved that the contact impedance and measurement amplitude are dependent on the electrode surface area (Boyle and Adler, 2011). In the present study, the two sets of electrodes with different lengths, namely the ES1 and ES2, have been applied in the ProME-T system, to study their influences on the performances of the system regarding the total impedance spectrum, bulk impedance response, noise analysis, and residual error induced by multiplexing.

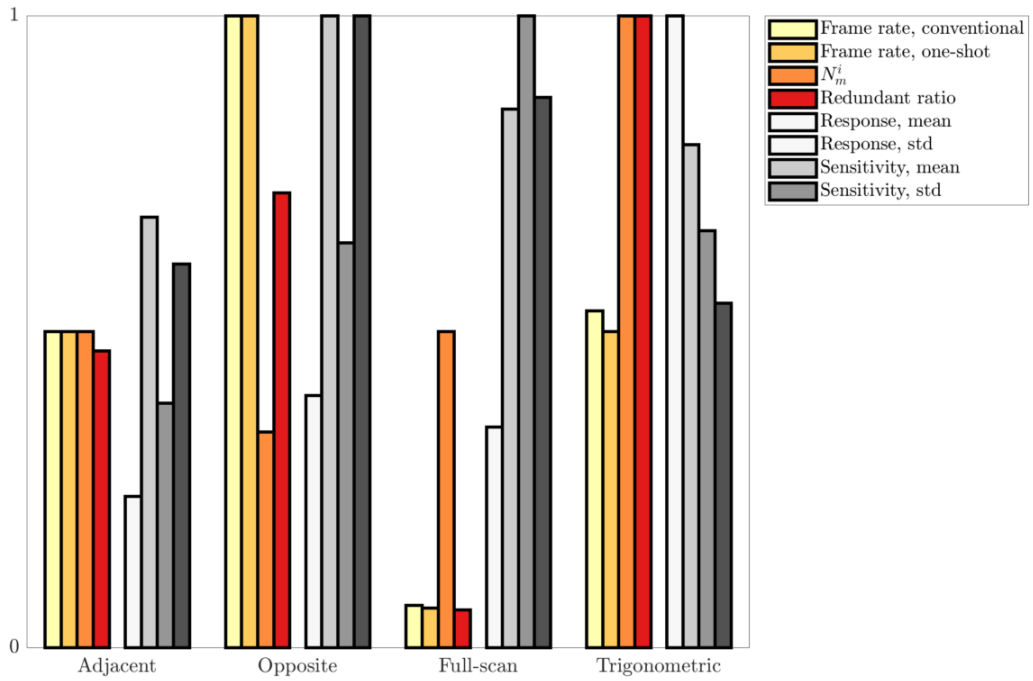

FIGURE 3.7: Practical implementation criteria, each normalized by the largest value among the four excitation strategies. The value 1 is associated with the best practical *performance* and low values indicate relatively lower-performing strategies.

3.3.1 Total impedance spectrum

Here, the total impedance Z^{tot} between an opposite pair of electrodes is evaluated. Experiments have been carried out fixing the source and drain on the opposite electrodes, with homogenous electrolyte of various conductivities filling the test section. A set of 27 different excitation frequencies f_{exc} are investigated, in the range of 1 Hz to 200 kHz. According to the equivalent closed circuit model shown in Eqn. 3.1 for ProME-T system, the Z^{tot} for ES1 and ES2 at various excitation frequencies are calculated, giving the total impedance spectrum as shown in Figure 3.8. In the figure, the module (left axis) and the phase (right axis) of the complex total impedance are plotted against f_{exc}, with three different electrolyte conductivities: 350, 550, 1200 μS/cm. The curves in blue represent the module, in brown represent the phase.

From Figure 3.8 we can see that the modules and phases of the total impedances associated with the two electrode sets evolve with f_{exc} in similar patterns. At low frequency, the phase is tending to the resistive regime, representing a high contact impedance contributes significantly to the total impedance; at middle frequency, the phase is nearly 0, which means the total impedance is mainly real and the contact impedance is negligible, indicating the preferable operation range for EIT; at high frequency, dielectric effect arises, the phase drops quickly to negative, the contact impedance increases sharply. Furthermore, the modules of the total impedances with ES2 are generally higher than ES1, because a large surface area decreases the contact impedance significantly.

For a practical EIT system, a lower total impedance is favorable, as it gives stronger voltage measurements at the boundary, hence more robust to measurement noise. This is proved in the following section through noise analysis. Moreover, comparing to the total impedance spectrum shown in Dupré (2017) using point-like electrodes, it is found that

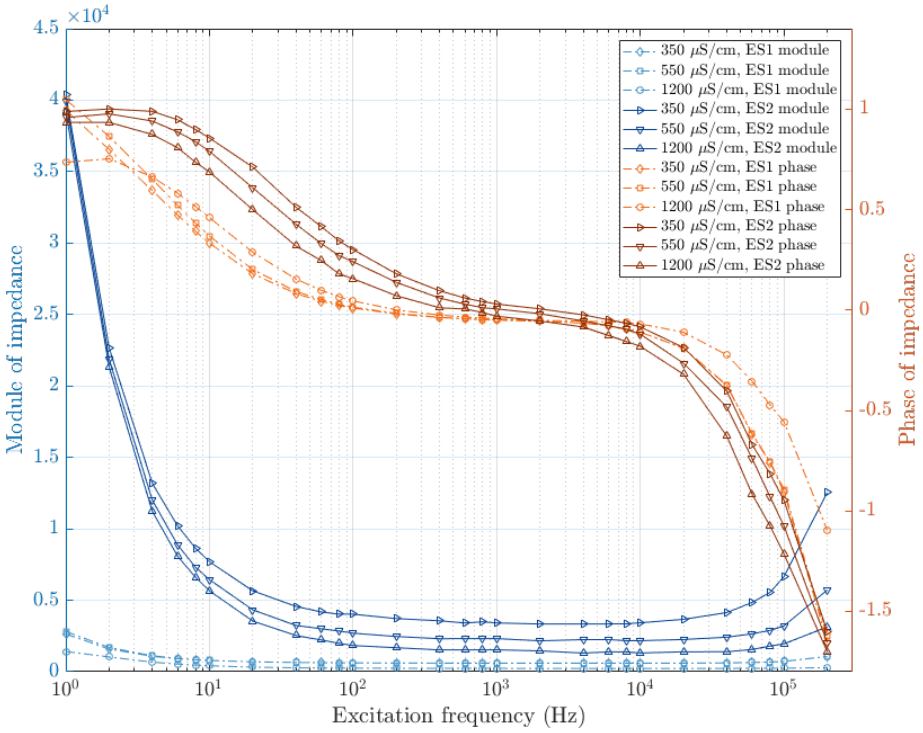

FIGURE 3.8: The module and phase of the total impedance changing with excitation frequencies, three different electrolyte conductivities are used for each electrode set.

the middle frequency range extends further to the left (low frequency region) as the electrode size increases. In the current thesis study, the excitation frequencies used in ProME-T for measurements of static and dynamic experiments range from 5 kHz to 80 kHz.

3.3.2 Bulk impedance

Calibration is a procedure to compute the bulk impedance by subtracting the corresponding electrode-specific contact impedances from the total impedance. Considering Eqn. 3.1 and a homogeneous medium in the test section, when the source and drain switch among the 16 electrodes, there will be 16 contact impedances Z^{source} or Z^{drain} at the electrodes, and 8 different bulk impedances associated with the angular distances between the source and drain. Implementing the full-scan strategy, each excitation pattern gives a linear equation as Eqn. 3.1, forming an array of 120 equations with 24 unknowns, which can be solved in the least squares sense, the contact impedance at each electrode is obtained, hence the bulk impedance Z. Figure 3.9 shows the bulk impedance of each excitation pattern for both ES1 and ES2 electrodes, applying an excitation frequency of $f_{exc} = 50$ kHz. The impedances before and after calibration are the total impedance and bulk impedance, respectively. The abscissa represents the index of excitation pattern.

As we can see, the ES1 gives comparable total and bulk impedances, indicating the low contact impedance associated with large electrode size. Besides, for both ES1 and ES2 the bulk impedances after calibration depend only on the angular separations between source and drain, verifying the reliability of the measurements from the present system: the systematic errors can be diminished taking the difference measurements between two frames, which is a common strategy used in difference image reconstructions.

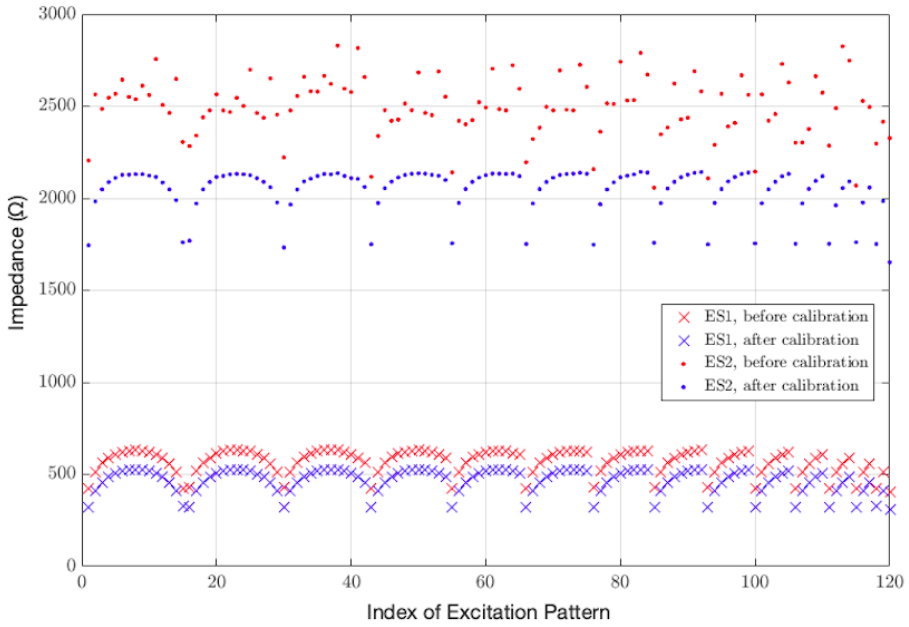

FIGURE 3.9: Total and bulk impedances of each excitation pattern in the full-scan strategy, for two sets of electrodes.

3.3.3 Noise analysis

In a practical EIT system, measurement noise may originate from the system or background environment, including: 1) the higher harmonics of the signal; 2) cross-talks among channels; 3) transients induced by multiplexing operation; 4) external noise, such as background noise. During data post-processing, the time domain measurements are transformed into frequency domain by FFT, only the amplitudes at excitation frequency are considered as the fundamental signals, all the others are discarded as noise. The Signal to Noise Ratio (SNR) is computed as a representation of the noise level:

$$\mathrm{SNR} = 10 \cdot \log_{10}\left(\frac{P_{\text{fundamental freq}}}{\sum P_{\text{all other freq}}}\right) = 10 \cdot \log_{10}\left(\frac{(x^{\mathrm{FFT}}_{i=f_{exc}})^2}{\sum_{i \neq f_{exc}} (x^{\mathrm{FFT}}_i)^2}\right), \tag{3.3}$$

in which x^{FFT}_i represents the FFT amplitude at frequency i.

The SNR considers the level of noise relative to the fundamental signal, it is expressed in decibel (dB). To get a reliable estimation of SNR, a high number of samples should be acquired achieving a fine resolution of the FFT spectrum. Excitation voltages at frequency $f_{exc} = 5\,\mathrm{kHz}$ has been applied to a pair of neighboring electrodes $(1,2)$ with homogeneous water of conductivity $750\,\mu\mathrm{S/cm}$ filling the test section, 10^6 samples were acquired at 500 kHz acquisition rate in 2 second, the frequency resolution of the FFT spectrum is thus 0.5 Hz. The voltage measurement across the constant resistor R_0 features a high amplitude signal, while across electrode pair $(9,10)$ it is extremely low. Their spectrums associated with ES2 electrodes are plotted as in Figure 3.10. In the plots, the peaks at 5 kHz are the fundamental amplitudes, the rest are noises. The peaks at frequencies of multiple of f_{exc} scaling with the fundamental amplitudes are higher-order harmonics induced by non-linearities in the electronics of the data acquisition system. The baseline noises, or background noises, are homogeneously distributed at all frequencies, invariant with fundamental amplitudes.

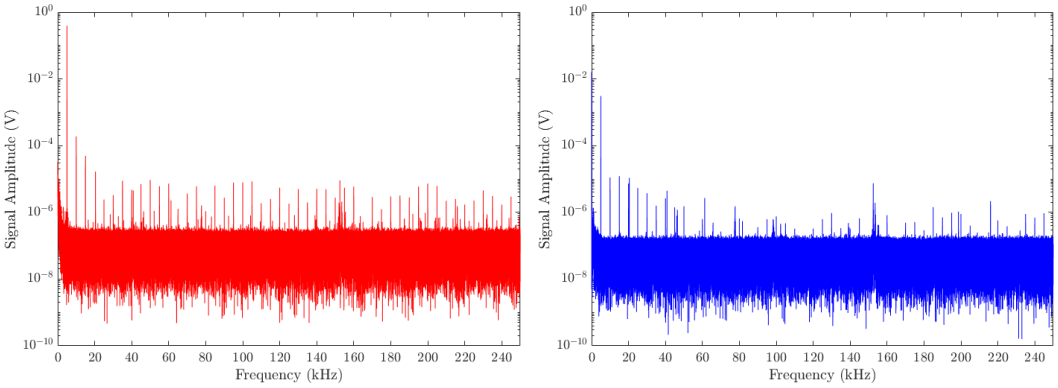

(a) High amplitude measurements, ES2.

(b) Low amplitude measurements, ES2.

FIGURE 3.10: Spectrums of the high and low amplitude measurements using ES2 electrodes, with homogeneous water of conductivity 750 μS/cm in the test section.

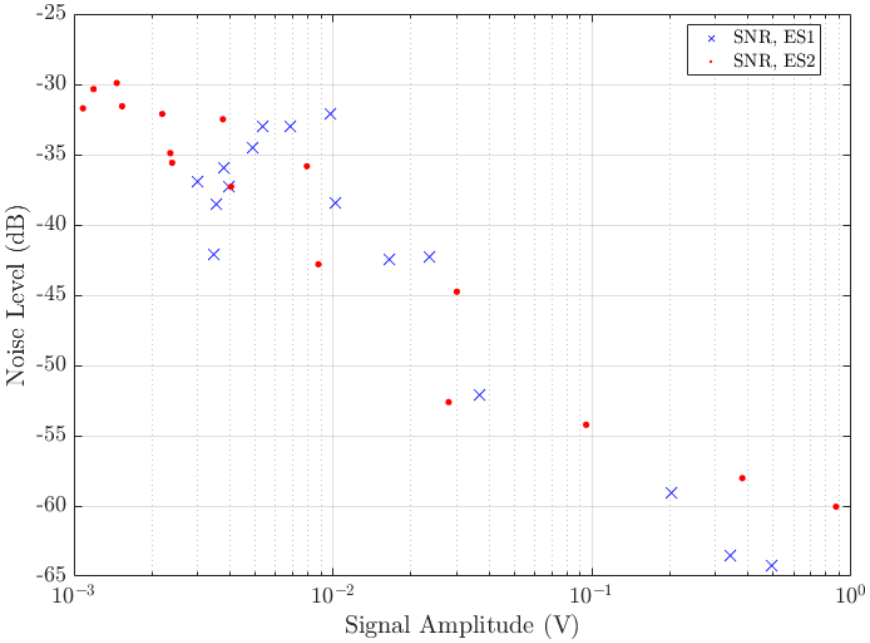

FIGURE 3.11: The Signal to Noise Ratio (SNR) of two sets of electrodes.

The corresponding SNR of each measurement channel are computed by Eqn. (3.3) for both sets of electrodes and plotted in Figure 3.11, the abscissa represents the signal amplitude of each channel. As we can see, the SNR are low for both ES1 and ES2, characterizing a low noise level under laboratory environment. Generally, the SNR decreases with signal amplitude, such that the ES2 gives some higher SNR associated with its lower amplitude signals (on the left). Besides, both ES1 and ES2 give low amplitude measurements in mV, which can be easily distorted by the noise under complex environment.

The SNR and spectrum analysis in frequency domain highlight the origin and level of the noise, however, they are insufficient to evaluate the noise resistance of the system, as only the fundamental signal of FFT is kept in post-processing. The repeatability of the measurements is conventionally used to assess the noise robustness of an EIT system. That is, a number of consecutive frames are taken repeatedly under a certain configuration, the

Relative Error (RE) of each measurement is assessed by

$$\mathrm{RE} = -10 \cdot \log_{10}\left(\frac{\sum_{i=1}^{n_c} V_i^2}{\sum_{i=1}^{n_c}(V_i - \overline{V_i})^2}\right) \tag{3.4}$$

with V_i the measurement at i^{th} frame, n_c the number of repeating frames, $\overline{V_i}$ the mean value of V_i of all frames. Finally, the RE for all the 1920 measurements ($\ell = 16$ channels with $N_e = 120$ excitation patterns) in full-scan strategy could be obtained, their mean value $\overline{\mathrm{RE}}$ is taken as the indicator to the repeatability of the measurements, a higher $\overline{\mathrm{RE}}$ means a better consistency among the repeated frames, hence a higher resistance to noise.

Here, $n_c = 50$ consecutive frames has been acquired at $f_{exc} = 50$ kHz, the RE of each measurement is plotted versus the corresponding signal amplitude for ES1 and ES2 in Figure 3.12. Their mean values $\overline{\mathrm{RE}}$ are 68 dB and 48 dB for ES1 and ES2, respectively. As we can see, the RE decreases with signal amplitude for both ES1 and ES2, and generally it is lower for ES1 than ES2 at the same signal amplitude, possibly because of the low contact impedance associated with ES1. Besides, the RE tends to cluster into a line for each electrode set, which may be caused by the propagation of the discretization error of the excitation signal during FFT.

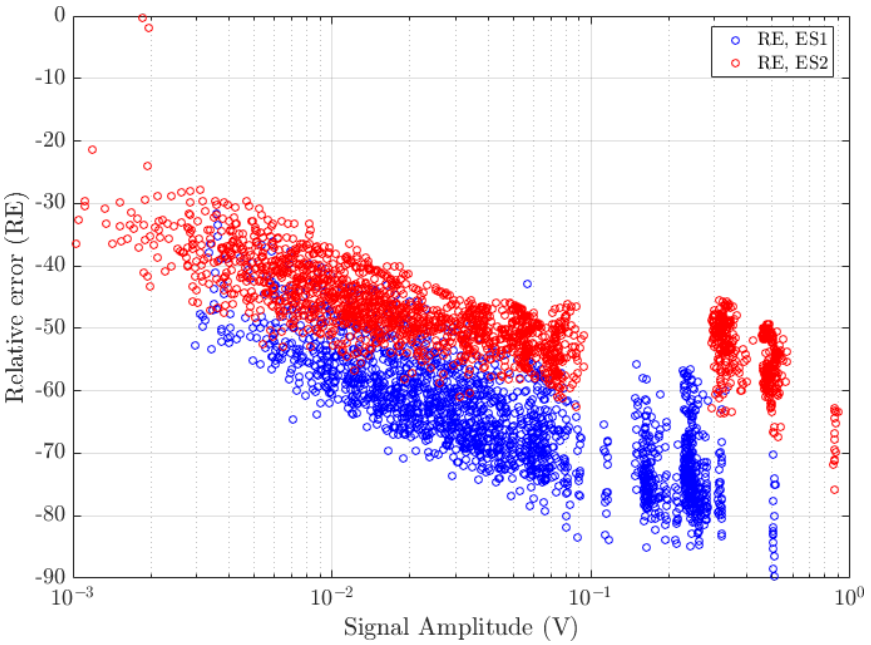

FIGURE 3.12: Relative errors of all measurements at 50kHz excitation frequency for ES1 and ES2.

3.3.4 Residual error analysis

Considering the switch operation performed in multiplexing, it introduces a transient noise to the measurements associated with the former excitation electrodes, where a certain residual voltage might remain for a short time after switching. Although filtering is applied to the signal by discarding the out-of-frequency components in the FFT spectrum, significant error may sustain if insufficient data is discarded.

To investigate the residual error induced by multiplexing, the measurements are classified into four categories: i) measurements over the constant resistor R_0; ii) measurements over

the excitation electrodes; iii) measurements at previous excitation electrodes; iv) measurements at the other electrodes. The type 3 measurement is of special interest because it just experienced a switch operation.

Experiments have been done with $f_{exc} = 50$ kHz and homogeneous water of conductivity 750 μS/cm filling the test section. The number N_p of periods per excitation pattern is fixed as $N_p = 10$ with $N_{sp} = 20$ samples per period, giving 200 data points per excitation pattern at each channel. The measured data are then sliced into 10 blocks, one period for each block, to which the FFT is performed respectively. Using the fundamental amplitude from the 10-th period as reference, the relative error of each period is computed and plotted in Figure 3.13 for both sets of electrodes, for the sake of clarity, one measurement channel is selected to represent each of the four measurement types.

Overall, the measurement errors for the four types of measurements are small (lower than 1%), especially for type 1 and 2, the relative errors are well below 0.1%. The type 4 measurements have relative large errors due to their low signal amplitudes. Regarding the size of the electrodes, mostly ES2 gives lower errors than ES1, as a result of its higher measurement amplitudes, also, the electrons in a larger electrode could be emitted more easily. Considering the errors in type 3 measurements, the influence of switch operation can be clearly seen: the relative error of the first period is much higher than the others. While this residual error can be diminished simply by discarding the measurement data from the first excitation period. Therefore, it is claimed that discarding the measurements over the excitation electrodes, which is commonly done in many practical EIT systems, is unnecessary with current hardware design and electrode configurations. In the present thesis study, the measurement data from all measurement channels are taken into account.

To sum up, the superiority of the electrodes with large surface area is evidenced, through investigating the total and bulk impedance responses, the measurement amplitudes, the robustness to noise, and the residual error caused by multiplexing. However, increasing the length of the electrodes means a larger sensing domain, being less sensitive to small local conductivity changes.

3.4 Dual-plane test section design for the PKL facility

This section concerns the design of a dual-plane test section for the PKL facility. For a dual-plane test section, the individual plane can either work independently, by which the bubble velocity can be estimated through cross-correlation of the measurements from the two plans (Deng et al., 2001), or work collectively, where cross-plane excitations and measurements are performed, the sensitivity in the center of the studied domain may be increased. Here, the former strategy is the primary concern, the optimal distance between the two planes should be carefully selected (Yan et al., 2006). Additionally, some practical issues have to be considered for the applications in industrial cases, for example, the current leakages from the electrodes to the nearby grounded pipe, the limitation of working space, the extend of sensing domain, and so on.

To start with, the working space of the EIT sensor in the PKL is introduced. The number of electrodes is decided considering the compromise between frame rate and quality of image reconstructions. After that, the parameters of the electrodes are determined through relative error analysis and/or literature reviews, giving the final design of the dual-plane test section.

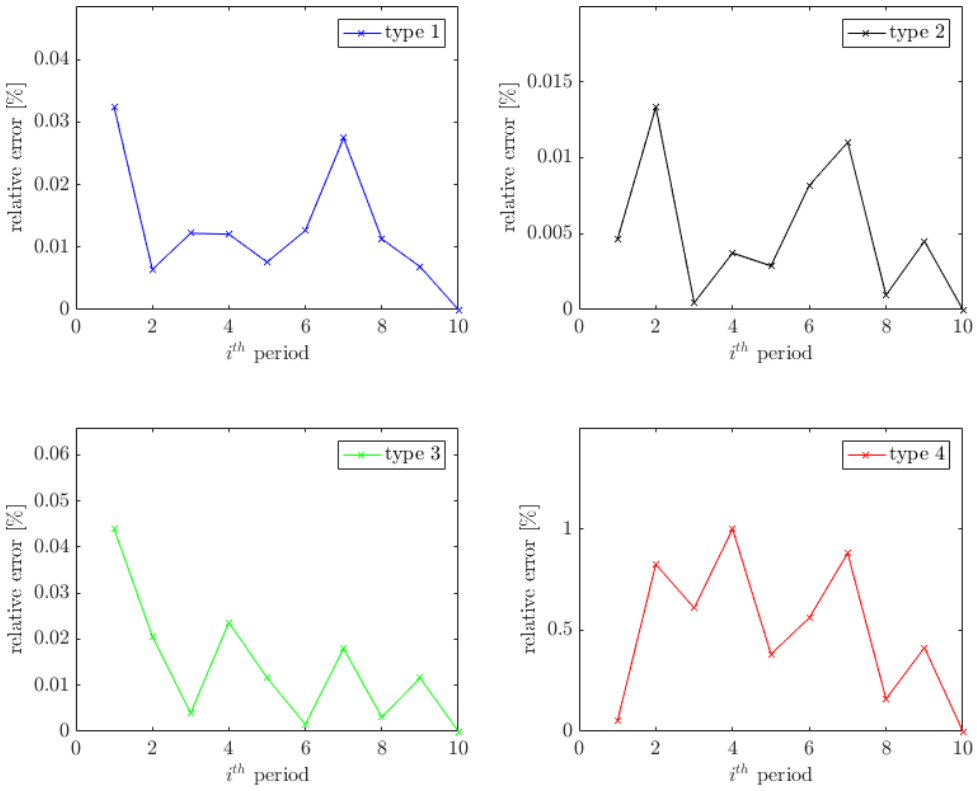

(a) Using ES1 electrodes.

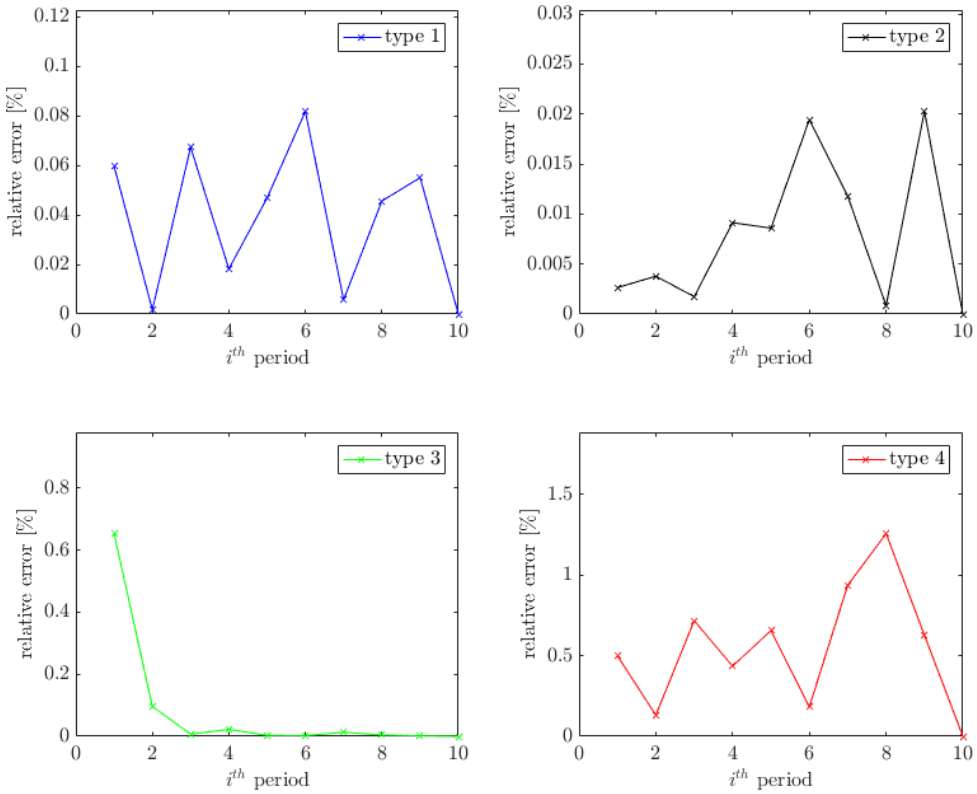

(b) Using ES2 electrodes.

FIGURE 3.13: Relative errors of the four types of measurements induced by multiplexing, for both sets of electrodes.

The hot leg of the PKL facility works under a high temperature high pressure environment, steel pipelines are used to withstand the harsh thermal load, such that the hot leg is conductive and grounded. A short section of length $L_{EIT} = 170$ mm would be cut and replaced by the test section, the simplified 2D scheme of the configuration is shown in Figure 3.14, the inner diameter of the pipe is $D = 128.2$ mm. Comparing to L_{EIT}, the grounded pipe can be considered as infinitely long. The parameters of the dual-plane test section to be decided include: the number of electrodes ℓ, the length of the electrodes L_e, the distance between two planes L_{dis}, the isolation distance from the electrodes to the grounded pipe L_{iso}, as well as the electrode circumferential width that is not shown in the figure.

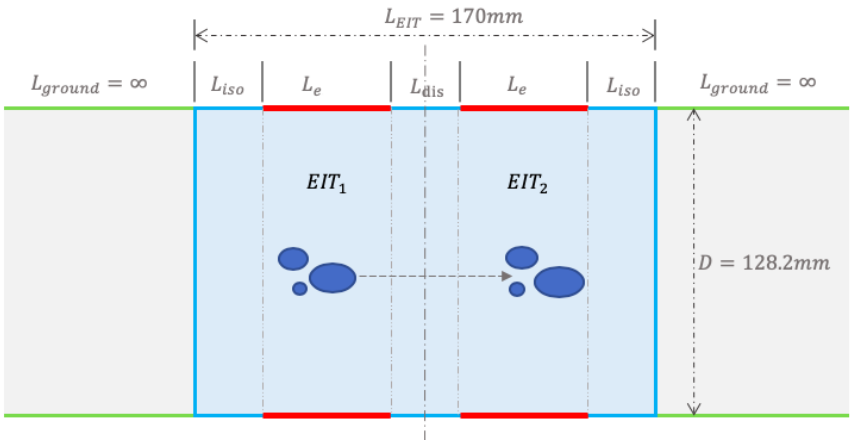

FIGURE 3.14: Configuration of the working space for the dual-plane test section.

The number of electrodes

A larger number ℓ of electrodes allows a higher spatial resolution in image reconstruction, meanwhile, it requires a longer time for data acquisition and much higher computation power for data processing. As explained in Section 2.2.2, the number N_m^i of independent measurements for various excitation strategies are proportional to ℓ^2, the computation power required by FFT is relative to $N_e \times \ell$, which is proportional to ℓ^2 for adjacent and opposite strategies, and to ℓ^3 for full-scan and trigonometric strategies.

Numerical simulations have been carried out using the EIDORS to compare the image reconstructions with $\ell = 16, 32, 64$. The EIT model considered is a 2D unit disk with ℓ point electrodes on the boundary. Full-scan strategy with current sources of unit amplitude is applied. The reference measurements are taken with a homogeneous conductivity, then, a small object with a significant different conductivity is put in the disk, giving the image measurements. As shown in Figure 3.15, the figures from left to right are the pixel representation of the real conductivity profile and the image reconstructions with $\ell = 16$, 32 and 64 electrodes, separately. It can be seen that the image reconstruction with $\ell = 32$ is comparative to that with $\ell = 64$, while with $\ell = 16$ some artifacts present around the reconstructed object.

Additionally, Gisser et al. (1990) proved that a theoretical limit ℓ_{max} exists on the number of electrodes of a practical EIT system, due to its finite measurement precision, utilizing more electrodes than ℓ_{max} would not improve the image reconstruction. A correlation

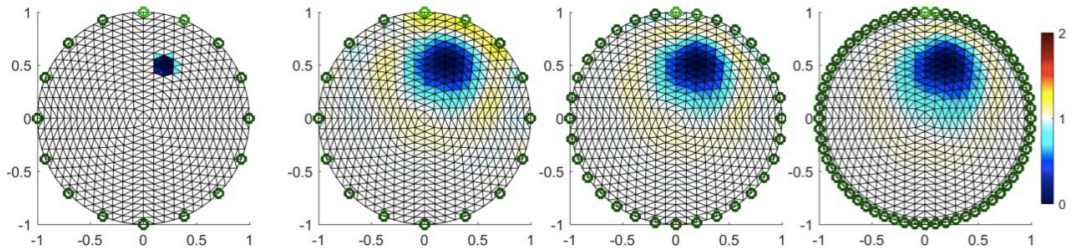

FIGURE 3.15: From left to right: the real object, and the image reconstructions with $\ell = 16,\ 32,\ 64$.

was proposed to decide ℓ_{max} by:

$$\ell_{max} \approx 2(2|\mu|/\varepsilon_p)^{1/2} + 1, \tag{3.5}$$

with ε_p the measurement precision, μ a non-dimensional value representing the conductivity contrast between the background and object, for gas-water two-phase flows $\mu = 1$. The PXIe system has a measurement precision of ε_p =314 μV for a signal amplitude below 1 V (PXIe, 2016), giving $\ell_{max} \approx 51$, that is, the maximum number of electrodes supportive by ProME-T system is 51.

Considering the number of excitation patterns $N_e = \ell(\ell-1)/2$ for full-scan strategy, the typical frame rates of the ProME-T system with $\ell = 16$, 32 and 64 are 208, 50 and 12 fps, respectively, the corresponding data size for one frame would be around 600 kB, 4960 kB, and 40 MB. While using the ONE-SHOT system, the typical frame rates for $\ell = 16,\ 32,\ 64$ would be 3906, 976, and 244 fps, separately, the saved data matrix would be of size 120×16, 496×32, and 2016×64. Considering the frame rates, measurement data sizes, computation powers required and quality of reconstructed images for various ℓ, the number of electrodes is decided to be $\ell = 32$ for each plane of the designed test section.

Distance between two planes L_{dis}

Regarding the cross-correlation method for velocity estimation, a prior assumption is that the bubble distribution holds similar structure when passing through the two measurement planes, see the bubble group shown in Figure 3.14. On one hand, the L_e and L_{dis} should be small to ensure this similarity, because the bubble distribution evolves along the flow. Further, the bubble structure is less distinguishable as L_e increases due to the averaging effect in the 3D sensing domain. On the other hand, the L_{dis} should be large to reduce the estimation error induced by acquisition time. Assuming an ideal EIT system with infinite frame rate and infinitely small electrodes, the time delay of the bubble group passing through the two planes is τ_{ideal}, giving the estimated velocity $v_{ideal} = L_{dis}/\tau_{ideal}$. While for a practical system, the time delay has an error t_{frame}, that is, $\tau_{real} = \tau_{ideal} \pm t_{frame}$, with t_{frame} the acquisition time for one frame, it is essentially the reciprocal of the frame rate. The relative error of the estimated velocity is

$$\varsigma = \left|\frac{v_{real} - v_{ideal}}{v_{ideal}}\right| = \left|\frac{L_{dis}/\tau_{ideal}}{L_{dis}/(\tau_{ideal} \pm t_{frame})} - 1\right| = \frac{t_{frame}}{\tau_{ideal}}, \tag{3.6}$$

therefore, a larger L_{dis} and a higher frame rate are favorable to decrease the relative error of velocity estimation .

Compromise should be made ensuring the similarity of bubble distribution and reducing the estimation error induced by acquisition time. For now, there is no mathematical model on this, the L_e and L_{dis} are commonly decided empirically. Dong et al. (2006) used a pipe of diameter 12.5 cm to study the cross-correlation method for bubble velocity estimation, with $L_{dis} = 10$ cm and $L_e = 1.5$ cm, good results were obtained with satisfying accuracy. Hao et al. (2017) investigated various distances between two planes of electrodes with a pipe diameter of 16 cm and electrode length $L_e = 2$ cm, giving an optimal distance $L_{dis} = 3.5$ cm for 3D image reconstruction. Graham and Adler (2007) used $L_{dis} = 11$ cm in a tank of 28 cm diameter and $L_e = 1$ cm, to investigate the influence of electrode placement on 3D image reconstructions. Above all, $L_e = 15$ mm and $L_{dis} = 65$ mm are chosen in the current test section design.

Circumferential width of the electrodes

Intensive researches have been done on the influences of electrode size on the performance of an EIT system. In the topic review of Cheney et al. (1999), it is suggested that to improve the spatial resolution of EIT, more electrodes should be involved, as well as larger electrodes that fill as much of the internal circumference as possible. Boyle and Adler (2011) showed that electrodes with larger surface area would provide higher signal amplitude and better image reconstruction. Wtorek et al. (2004) proved that increasing the electrode size is equivalent to reducing the maximal value of the potential gradient and to introducing the averaging effect of the measurement electrodes. As a result, the variance of Jacobian's element value is reduced, which may reduce the *ill-posedness* of the EIT inverse problem. The numerical simulations concerning the 3D effect and the performance assessment using the two electrode sets presented in the former sections also verify these results. Therefore, the total circumferential width of the electrodes is decided to occupy as much of the internal circumference as the manufacture process allows. Finally, the circumferential width of each electrode is 11.5 mm, with a gap between neighboring electrodes of ~ 2.5 mm.

The isolation length L_{iso} is restricted by the total length of the test section, considering $L_e + 2L_{iso} + L_{dis} \leq 170$ mm, it is determined to be $L_{iso} = 45$ mm given L_e and L_{dis}. Moreover, Darnajou et al. (2018) performed a series of numerical simulations on the current leakages from the electrodes to the ground pipe with different L_e and L_{iso}. The presented design parameters grant a low current leakage concerning the ratio of the leaking power to the total input power.

The test section design parameters have been further modified before production in cooperation with the mechanical engineer from Framatome GmbH, to meet the practical manufacture restrictions. The final design of the dual-plane test section for the PKL facility is presented in Appendix A, see Figure A.1. The electrode design is shown in Figure A.2, the size of the electrodes is 15 mm × 11.5 mm × 1 mm for both planes of electrodes, with the distance between two planes $L_{dis} = 65$ mm and the isolation length $L_{iso} = 40.5$ mm.

Chapter 4

Eigenvalue-based approach using EIT raw data

In general, EIT image reconstructions produce smoothing images with low spatial resolution compared to the hard-field tomography techniques, like X-ray tomography. This makes it difficult to distinguish the phase interface from the reconstructed images. Iterative methods yield images of higher resolutions but they usually require high computation power and are sensitive to measurement noise. In this chapter, an alternative methodology based on the eigenvalues of the impedance matrix is proposed to estimate the phase fraction inside the studied domain. It circumvents the need to reconstruct images in the extreme non-linear case of two-phase flows, which are characterized by a high resistivity contrast between phases, while allows to consider a wide range of void fraction.

4.1 Methodology

The proposed methodology is originated from the NtD model introduced in Section 2.2.1, an *impedance matrix* can be derived as a discrete representation of the NtD map. Considering the closed circuit models of the EIT systems shown in Section 3.1, each excitation pattern has a representative *bulk impedance*. Implementing the full-scan excitation strategy, the impedance array of each frame (with $\ell(\ell-1)/2$ excitation patterns) can be conveniently arranged into a $\ell \times \ell$ *impedance matrix*, which is a symmetric matrix with diagonal entries related to the mutual impedances. In the work of Fang and Cumberbatch (2005), the relation between the void fraction and the eigenvalues of the capacitance matrix obtained from ECT data is investigated, it is shown that the multiplicity of the eigenvalues is correlated to the degree of symmetry of the flow. Dupré et al. applied the eigenvalue analysis to ECT data for the purpose of flow regime identification as well as the estimation of two-phase flow void fraction, the result is promising (Dupré et al., 2017b). In this context, the literature dealing with void fraction estimation from EIT data and through eigenvalue analysis is scarce. Here, the *impedance matrix* of EIT is investigated, its eigenvalues are used to devise some metrics of the void fraction.

4.1.1 Mathematical basis

Recall the EIT forward model introduced in Section 2.2.1, the electrostatic potential inside the domain satisfies the Laplace equation (since $\sigma = 1$ in $\Omega \setminus \Omega_i$),

$$\Delta u = 0, \quad \text{in } \Omega \setminus \Omega_i. \tag{4.1}$$

Applying the shunt model Eqn. (4.1) has a unique solution and allows to define a matrix $\boldsymbol{Z}$, which is the discrete mapping from the boundary current excitations to the boundary voltage measurements. The matrix $\boldsymbol{Z}$ is referred to as the *impedance matrix* and it takes over the role of the NtD operator Λ_σ as its discrete representation. Defining the discrete version of $L^2_\diamond(\partial\Omega)$ as the ℓ-dimensional vector space $\mathbb{R}^\ell_\diamond = \{y = [y_1 \ \cdots \ y_\ell] \in \mathbb{R}^\ell, \sum_{i=1}^\ell y_i = 0\}$, one gets

$$\begin{aligned} \boldsymbol{Z}: \quad & \mathbb{R}^\ell_\diamond \to \mathbb{R}^\ell_\diamond \\ & [I_0 \ I_1 \ \cdots \ I_\ell] \longmapsto [V_0 \ V_1 \ \cdots \ V_\ell] \end{aligned} \tag{4.2}$$

where $V_k = u|_{e_k}$ for $k = 1, \ldots, \ell$ are the boundary measurements of the electric potential solution u corresponding to the set of imposed currents I_k considered.

Each element in $\boldsymbol{Z}$ is a *bulk impedance* corresponding to a certain imposed current and boundary measurement. When the continuous liquid phase is the only conducting phase, given the mixture conductivity σ_m, the liquid conductivity σ_l and the liquid volume fraction η_l, the Maxwell-Hewitt relation (Ceccio and George, 1996) reads:

$$\eta_l = 1 - \frac{1-\sigma_m/\sigma_l}{1+\sigma_m/\sigma_l}, \text{ in 2D}, \quad \eta_l = 1 - \frac{1-\sigma_m/\sigma_l}{1+0.5\cdot\sigma_m/\sigma_l}, \text{ in 3D}. \tag{4.3}$$

This relation yields an approximation of the volume fraction of each phase, as shown in George et al. (2000). The water-gas two-phase flow system conforms this relation, so that the measured impedance can be correlated to the void fraction. In the present study, the impedance matrix contains the impedance of all the possible electrode separations. In this framework, the impedance matrix is assumed to be directly correlated to the void fraction and our objective is to investigate this correlation based on an eigenvalue analysis of numerical and experimental standardized tests.

4.1.2 Impedance matrix and normalization

For each excitation pattern, denoting the source and drain electrodes pair as (i, j), there is a corresponding bulk impedance $Z_{i,j}$, which is governed by the conductivity distribution $\sigma(x)$ in Ω, as well as the selected source and drain electrodes. The impedance between source electrode j and drain electrode i is the mutual impedance of $Z_{i,j}$, so that they satisfy the reciprocity relation $Z_{i,j} = Z_{j,i}$. According to the definition of $\mathbb{R}^\ell_\diamond$, the diagonal term $Z_{i,i}$ is not measured but computed by summing up the corresponding mutual impedances as $Z_{i,i} = -\sum_{j\neq i} Z_{i,j}$, which finally yields the $\ell \times \ell$ square impedance matrix $\boldsymbol{Z} = (Z_{i,j})_{1\leq i,j\leq \ell}$.

The relative NtD map $\Pi = \Lambda_\sigma - \Lambda_0$ is commonly used in EIT to retrieve information of the probed domain. This amounts to consider the matrix $\Delta\boldsymbol{Z} = \boldsymbol{Z} - \boldsymbol{Z^0}$, where $\boldsymbol{Z^0}$ is the impedance matrix of a homogeneous conductivity distribution for which $\Omega_\mathrm{i} = \emptyset$. The matrix $\Delta\boldsymbol{Z}$ is referred to as the Differential Impedance Matrix (DIM).

To perform a non-dimensional analysis, a normalization method of the matrix entries $Z_{i,j}$ is needed to reduce the dependencies on the geometric parameters of the sensor and on the background conductivity, as well as to enhance the presence of inhomogeneities. In this study, the normalization method has been proposed as:

$$\hat{Z}_{i,j} = \frac{Z_{i,j} - Z^0_{i,j}}{Z^0_{i,j}} \quad \text{for } i, j \in \{1, \ldots, \ell\}. \tag{4.4}$$

The associated matrix $\hat{\boldsymbol{Z}} = (\hat{Z}_{i,j})_{1\leq i,j\leq \ell}$ is referred to as the Normalized Impedance Matrix (NIM). Note that $\hat{Z}_{i,j}$ is equal to zero for all i, j when $\Omega_\mathrm{i} = \emptyset$ and is infinite when $\Omega_\mathrm{i} = \Omega$.

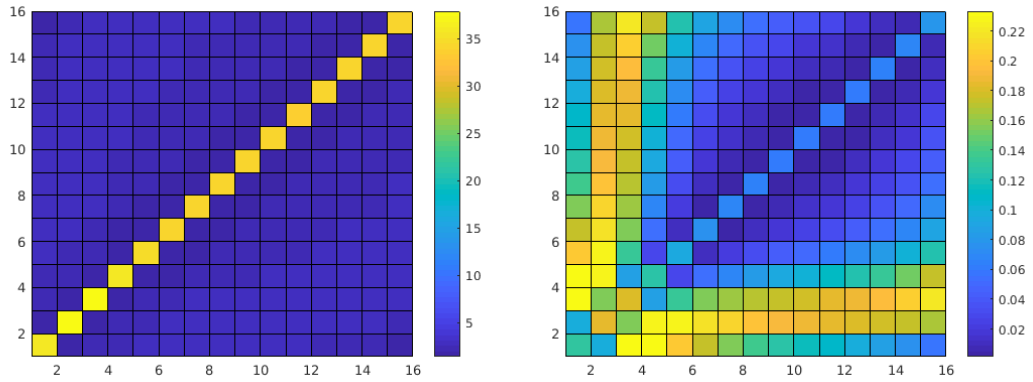

(a) Differential impedance matrix $\Delta\boldsymbol{Z}$.

(b) Normalized impedance matrix $\hat{\boldsymbol{Z}}$.

FIGURE 4.1: Effect of the normalization on the entries of the impedance matrices in the case of a single bubble.

Considering the case shown in Figure 2.5 with a single non-conductive inclusion of radius 0.3 and an EIT system with 16 electrodes, the corresponding DIM and NIM are visualized with the two axes as the matrix entry indices and the assigned color for the associated entry value, as in Figure 4.1. The effect of normalization is highlighted: The DIM has significant values on the diagonal, which is consistent with the computation of its diagonal terms $Z_{i,i}$. The normalization diminishes this effect and enhances the impedance discrepancies between electrodes, see for example the entries associated with the electrodes 2 and 3 that are the closest to the inclusion.

As, by definition, the normalized impedance matrix $\hat{\boldsymbol{Z}}$ is a real-valued symmetric matrix, it is diagonalizable and its eigenvalues $\lambda^{(i)}$ are real. Therefore, it has a set of ℓ pairs of eigenvectors $\boldsymbol{v}^{(i)} \in \mathbb{R}^\ell_\diamond$ and eigenvalues $\lambda^{(i)} \in \mathbb{R}$ satisfying

$$\hat{\boldsymbol{Z}} \cdot \boldsymbol{v}^{(i)} = \lambda^{(i)} \boldsymbol{v}^{(i)}, \quad i \in \{1, \ldots, \ell\}. \tag{4.5}$$

Sorting the eigenvalues in an increasing order, the resulting eigenvalue array is defined as

$$\lambda = [\lambda^{(1)}\ \lambda^{(2)}\ \cdots\ \lambda^{(\ell)}] \text{ with } \lambda^{(1)} < \lambda^{(2)} < \cdots < \lambda^{(\ell)}, \tag{4.6}$$

where $\lambda^{(\ell)}$ is the so-called leading eigenvalue. Moreover, considering the rotational symmetry of the electrodes placement, the eigenvalues of $\hat{\boldsymbol{Z}}$ are invariant under similarity transformations of the electrodes, such as rotation or renumbering.

The largest eigenvalues contain the most information about the matrix $\hat{\boldsymbol{Z}}$ and represent its main features, while $\hat{\boldsymbol{Z}}$ is decided by the conductivity distribution within the probed domain, the other smallest eigenvalues are also affected by it but contain qualitatively less information. Hereafter, the characteristics of these eigenvalues are investigated numerically and validated experimentally. Note that in the configurations where different numbers of electrodes are used to impose the current and to measure the potential on the domain boundary, then the associated impedance matrices are not square. In such cases, their singular value decompositions can be considered alternatively.

4.2 Estimation of cross-sectional phase fraction

In the previous section, the mathematical basis of the proposed approach and the normalized impedance matrix $\hat{\boldsymbol{Z}}$ are introduced. In this section, numerical simulations are considered to investigate the characteristics of the eigenvalues and their correlations to the conductivity distribution within the probed medium, the attained results are further validated by static experimental data. The ProME-T system has been applied for the static experiments concerned with an excitation frequency $f_{exc} = 50\,\text{kHz}$.

4.2.1 Numerical simulations

In the present study, the typical two-phase flow regimes are classified into three different canonical cases, a series of numerical simulations have been carried out, in which the bulk impedances are computed numerically and arranged into a square impedance matrix, the eigenvalues of which are used to devise some metrics of the void fraction.

Canonical cases considered

The typical regimes of two-phase flows (horizontal, inclined or vertical) include bubbly flow, stratified flow, slug flow, plug flow, churn flow and annular flow, see Taitel and Dukler (1976); Rossi et al. (2018). The phase distributions can be classified into three classes, regardless of pipe placement and flow directions, that is, (i) single bubble case, representing the water slug in slug, plug and churn flows and the annular flow as well; (ii) stratified case; (iii) multiple bubbles case, relevant to the bubbly flow and the bubble cloud that follows the slug/plug in slug and churn flows.

Consider a 2D circular pipeline Ω with a radius $r_0 = 1$, *i.e.* $\Omega = \{(x, y) : x^2 + y^2 < 1\}$. Given the rotational symmetry of the impedance matrix, three classes of bubble distribution patterns are defined as follows:

- Case 1 (single bubble): $\Omega_\text{i} = \{(x, y) : (x - d\cos\theta_0)^2 + (y - d\sin\theta_0)^2 \leq r^2\}$ with $0 \leq \theta_0 \leq 2\pi$ and such that $0 \leq r + d \leq 1.0$.
- Case 2 (stratified): $\Omega_\text{i} = \{(x, y) : y \geq r_0 \cdot \cos\theta\}$, with $r_0 = 1$ and $0 \leq \theta \leq \pi$.
- Case 3 (multiple bubbles): a number $n_{bub} \in \{1,\ 3,\ 11,\ 36,\ 62,\ 84\}$ of uniformly distributed bubbles of radius r_{dis} is considered. To fix the void fraction relatively to an equivalent concentric bubble of radius r_e then r_{dis} is defined as $r_{dis} = r_e/\sqrt{n_{bub}}$.

The conductivity distributions of the three cases are depicted in Figure 4.2, the area in light blue represents the water phase and the one in white is the gas phase. The electrical conductivity of gas is set to be eight magnitudes lower than that of water, which is in accordance with the physical conductivity values of water and gas. Each case corresponds to specific regimes of two phase flow: in Case 1, one single bubble with various diameter is varied spatially along one specific diameter inside the domain; Case 2 represents stratified flow with various water level, in which $h = 1 - d = 1 - \cos\theta$; Case 3 is characterized by multiple bubbles uniformly distributed inside the domain, Figure 4.2 shows the case with 11 bubbles.

To investigate the eigenvalues of the impedance matrix for these three canonical cases, the EIDORS code has been used to compute the boundary measurements. The numerical model is a 2D unit disk with 16 evenly distributed electrodes, the peripheral width of the

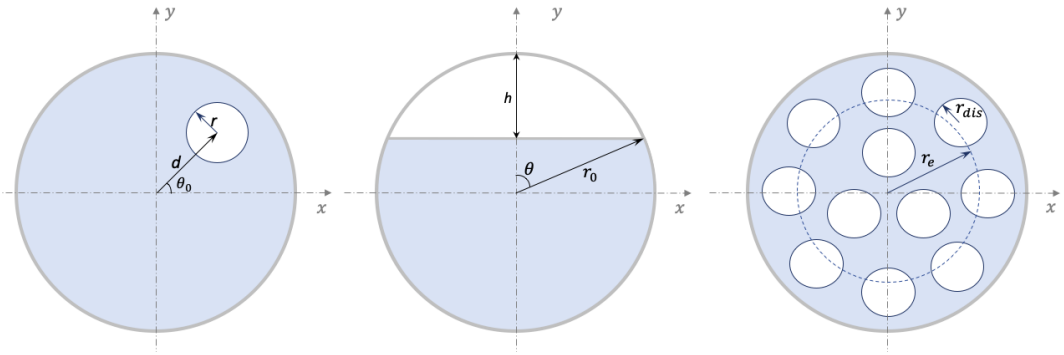

FIGURE 4.2: Conductivity distribution patterns for the three canonical cases considered.

electrodes have the ratio between the area occupied by the electrodes and the total area the same than the test section shown in Figure 3.3. A triangle mesh with 15725 nodes is used for forward computation.

The full-scan excitation strategy with a current amplitude of $I_0 = 1\,\mathrm{A}$ at source and drain electrodes is employed. For each excitation pattern, the difference voltage between adjacent electrodes are computed. The voltage difference $V_{i,j}$ between source i and drain j could be obtained by summing up the voltage differences at all adjacent electrodes between the source and drain. Since the injected current is a constant, the corresponding bulk impedance $Z_{i,j}$ can be obtained by Ohm's law:

$$Z_{i,j} = V_{i,j}/I_0. \tag{4.7}$$

With $\ell = 16$ electrodes ($i, j = 1, \cdots, 16$), there are 120 different bulk impedances for one frame of acquisition. After normalization, the square matrix $\hat{\boldsymbol{Z}}$ of size 16×16 is obtained, along with the $\ell = 16$ pairs of eigenvalues and eigenvectors, see Eqn. (4.6).

The NIM of the three simulated cases considered are visualized to highlight their correlation with the phase pattern. Case 1 is shown in Figure 4.1(b) with $r = 0.3$ and the cases 2 and 3 are shown in Figure 4.3, in which Case 2 is computed with $h = 0.8$ and Case 3 is computed with 3 bubbles and $r_e = 0.3$. These parameters are chosen to obtain the same phase fraction for all three cases. As it can be seen, the main features of the NIM vary significantly with the phase pattern (noting the extremely high values presented in Figure 4.3(a) for Case 2), even at the same phase fraction. This characteristic is at the foundation of the present study.

In the following sections, the eigenvalues of various simulation cases are investigated and compared to study their dependence on the bubble distribution. In particular, the void fraction is plotted with the leading eigenvalue and the sum of the absolute value of the first 15 eigenvalues, to assess their correlations. For convenience, we denote the leading eigenvalue as $\lambda^{(16)}$ and the sum of the absolute value of the first 15 eigenvalues as $\sum_{|\lambda|}^{15} = |\lambda^{(1)}| + \cdots + |\lambda^{(15)}|$. Moreover, the void fraction η is defined in 2D by the area ratio occupied by the bubble inclusion over the total area, *i.e.* $\eta = |\Omega_\mathrm{i}|/|\Omega| = |\Omega_\mathrm{i}|/\pi$.

Result analysis

Case 1 Due to the fact that the properties of the impedance matrix are invariant with the rotation of the electrodes, we only need to simulate the bubble inclusion moving along

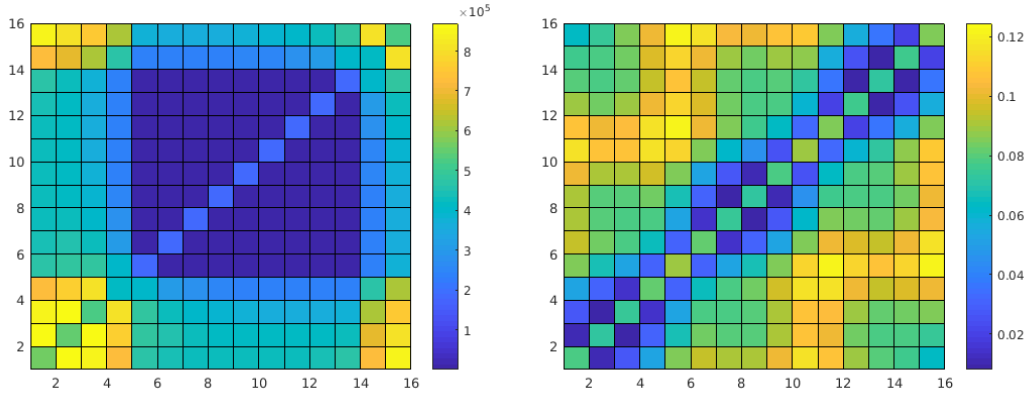

(a) $\hat{\boldsymbol{Z}}$ of case 2 (stratified). (b) $\hat{\boldsymbol{Z}}$ of case 3 (three bubbles).

FIGURE 4.3: Entries of the normalized impedance matrix of the cases 2 and 3.

one radius of the domain. We set $\theta_0 = 0$, which is representative of all cases of a single bubble moving within the domain. Applying the restriction condition $r + d \leq 0.95$ and an increment step of 0.05, we get 19 different bubble radius r and placements d, separately, which will give 190 different simulation cases $\big(190$ pairs of $(r,d)\big)$ in total. Here, $r+d \leq 0.95$ is chosen because of the extremely high sensitivity near the boundary, which could cause an abnormal deviation, besides, in practical applications it is also rare to have a bubble occupying 95% of the pipe diameter.

The eigenvalues are computed for each case and plotted. Figure 4.4(a) shows the 16 eigenvalues of concentric bubble inclusions with $d = 0$ and $0.05 \leq r \leq 0.95$, while Figure 4.4(b) shows the 16 eigenvalues of eccentric bubble inclusions with $d = 0.35$ and $0.05 \leq r \leq 0.6$. In both figures, each curve represents an eigenvalue $\lambda^{(i)}$, and they are evolving with the bubble radius. As we can see, the leading eigenvalue is much larger than the others, and its amplitude is correlated to the bubble size, especially when the bubble edge is close to the domain boundary. Besides, for concentric bubble configurations, the first 15 eigenvalues are symmetrical around zero due to the symmetry of the conductivity distribution.

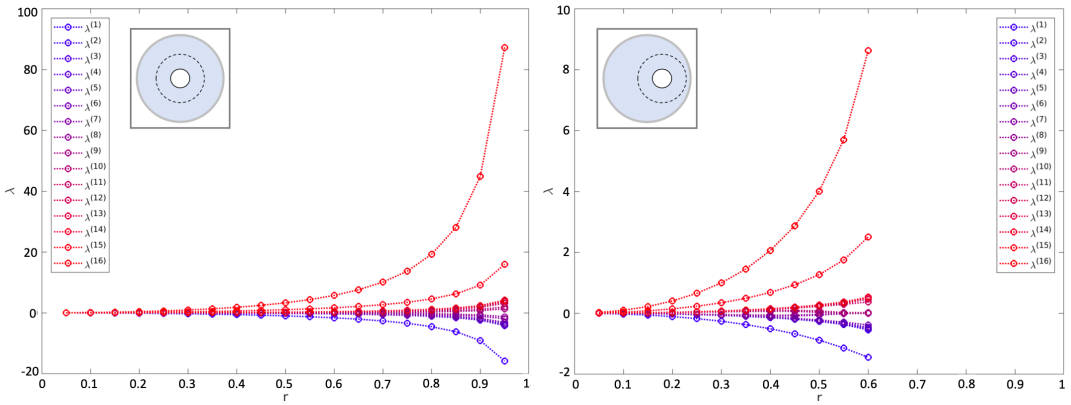

(a) Concentric bubble, $d = 0$. (b) Eccentric bubble, $d = 0.35$.

FIGURE 4.4: Eigenvalue array for some configurations corresponding to Case 1.

Figure 4.5 shows the 16 eigenvalues of a bubble inclusion with $r = 0.35$ moving from $d =$

0 to $d = 0.6$. As it can be seen, as the bubble moves toward the boundary, the leading eigenvalue increases rapidly, while the other eigenvalues vary little with d.

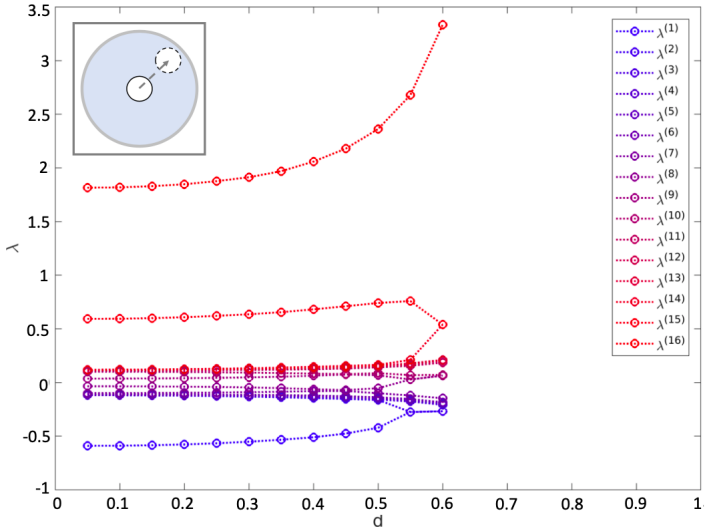

FIGURE 4.5: Eigenvalue array of one bubble inclusion ($r = 0.35$) moving from $d = 0$ to $d = 0.6$.

As we know, adding bubble inclusions increases the overall bulk impedance, hence the normalized impedance $\hat{Z}_{i,j}$, which in turn affects the eigenvalues. That is why the eigenvalues are changing with bubble size. To study the influence of bubble location, the sensitivity map of EIT has to be considered. As explained in Section 3.2.3, the high sensitivity areas of EIT concentrate near the boundary and the vicinity of the active electrodes while the domain interior contains low sensitivity regions. The sensitivity $s_{(i,k)j}$ (see Eqn. (3.2)) for an element $j \in \Omega$ describes how effectively a local conductivity perturbation is contributing to the measurement. The overall sensitivity maps S_j for one single measurement and for the full-scan strategy are shown in Figure 4.6. The color map in the left panel shows the sensitivity distribution of one excitation at electrodes 1 and 7, and one single measurement at electrodes 12 and 13 (refer to Figure 2.5 for electrode numbering). The sensitivity map of the full-scan strategy is shown in the right panel. Considering the same bubble inclusion placed either in the center or near the boundary, the boundary voltage turns out to be more affected on average in the latter configuration, and so are the impedance matrix and its eigenvalues. Thus, the eigenvalues are affected by both the size and position of the bubble inclusion.

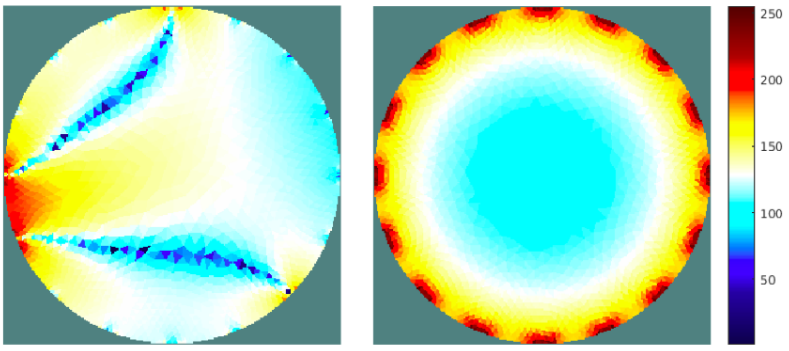

FIGURE 4.6: Map of the logarithm of the sensitivity distribution, *left:* source/drain at electrodes (1,7) and measurement at electrodes (12,13), refer to Figure 2.5 for electrode numbering; *right:* full-scan strategy.

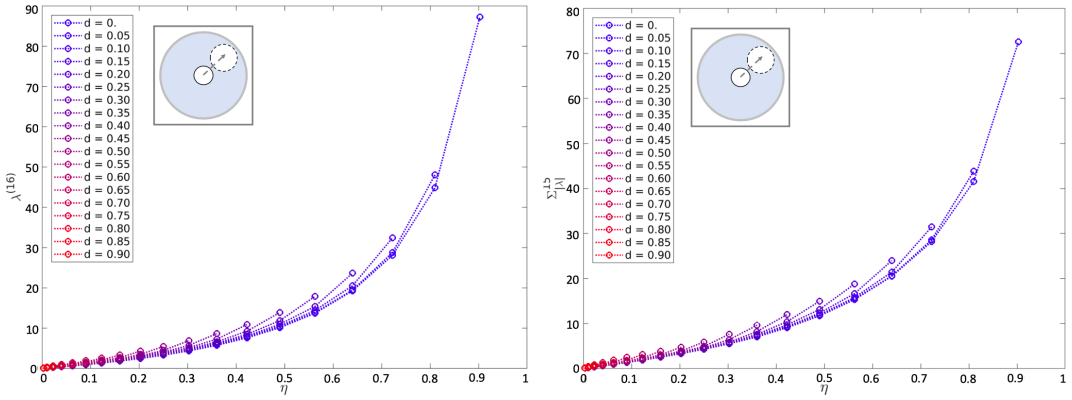

(a) $\lambda^{(16)}$ vs. η. (b) $\sum_{|\lambda|}^{15}$ vs. η.

FIGURE 4.7: Eigenvalues vs. void fraction for Case 1.

Figure 4.7 shows the relation between the void fraction and the leading eigenvalue $\lambda^{(16)}$ and the sum of the absolute value of the first 15 eigenvalues $\sum_{|\lambda|}^{15}$. For Case 1, the void fraction satisfies $\eta = \pi r^2/\pi r_0^2 = r^2$, which is invariant with d. In both figures, each curve corresponds to a specific value d with varying r, for example, the curve at the right most represents a bubble in the center ($d = 0$), its radius r increases from 0.05 to 0.95, hence the void fraction ranges from 0 to 0.9025. The figures show that both $\lambda^{(16)}$ and $\sum_{|\lambda|}^{15}$ increase with the void fraction and vary with the distance to the center. The void fraction can be estimated by $\lambda^{(16)}$ or $\sum_{|\lambda|}^{15}$, from Figure 4.7 we can estimate the void fraction with an error less than 10%. Furthermore, the error can be reduced drastically when the position of the bubble is known a priori (distance to the center d).

Case 2 In the stratified configuration, a horizontal liquid-gas interface is considered since the impedance matrix is invariant with electrodes rotation. Note that the void fraction η in Case 2 satisfies the relation

$$\eta = (\theta - \sin\theta \cdot \cos\theta)/\pi \quad \text{with} \quad \theta = \arccos(1-h), \tag{4.8}$$

where h is the *height* of the gas segment as in Figure 4.2.

The eigenvalue array of Case 2 is plotted in Figure 4.8(a). A linear approximation can be found for the relation between h and the leading eigenvalue, while the data points at high void fraction ($h > 1.99$) are considered to be abnormal and discarded. The other eigenvalues are not strongly correlated to h. In Figure 4.8(b), $\lambda^{(16)}$ is plotted with h, and the curve is fitted linearly with a fitting measure R^2 of 0.9905. The deviation between the fitting line and the data points may originate from the finite number and size of the electrodes and from their limited geometrical extent too.

Case 3 In Case 3, a number $n_{bub} \in \{1, 3, 11, 36, 62, 84\}$ of bubble inclusions are considered with a radius adjusted to get the same water fraction as an equivalent single concentric bubble of radius r_e. The void fraction of Case 3 is calculated by $\eta = r_e^2$, it is restricted by n_{bub} to avoid contact among bubbles. With $n_{bub} = 3$ the top limit of void fraction is 0.5, for $n_{bub} = 11$ it is 0.6, while for other cases it ranges from 0.65 to 0.7. For practical two-phase flows, the intensive bubbly flow rarely reaches a void fraction over 0.5, otherwise the bubbles would collapse and form bigger bubbles and the flow regime would change.

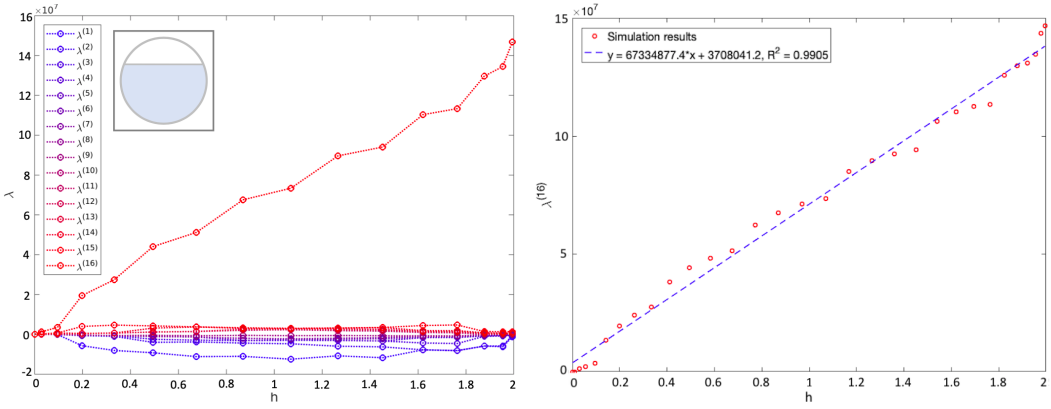

(a) Eigenvalue array vs. h.

(b) $\lambda^{(16)}$ vs. h and its linear fit.

FIGURE 4.8: Eigenvalue arrays and $\lambda^{(16)}$ as a function of h for Case 2.

The eigenvalue $\lambda^{(16)}$ is plotted with the void fraction and the bubbles radius in Figure 4.9 respectively. In Figure 4.9(a) the right most curve represents the single concentric bubble case, from right to left the curves correspond to an increasing value of n_{bub}. As we can see, at the same void fraction the leading eigenvalue $\lambda^{(16)}$ is increasing with n_{bub}. The same behaviour is also observed in Figure 4.9(b): at the same void fraction, $\lambda^{(16)}$ is decreasing with the bubbles radius. Besides, the smaller the bubbles, the stronger the effect on $\lambda^{(16)}$, which is shown by the drop of $\lambda^{(16)}$ when r_{dis} is close to zero. After that point $\lambda^{(16)}$ decreases smoothly as r_{dis} increases.

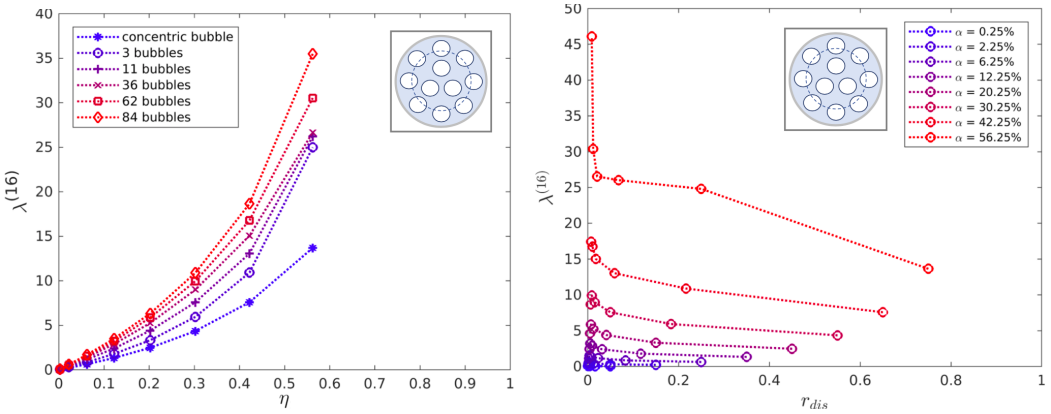

(a) $\lambda^{(16)}$ vs. η.

(b) $\lambda^{(16)}$ vs. $r_e/\sqrt{n_{bub}}$.

FIGURE 4.9: Eigenvalues vs. void fraction for Case 3.

For the multiple bubbles case, two parameters have to be known to predict the void fraction: the eigenvalues and the number of bubbles within the sensor area. However, it is not practical to observe the bubble distribution inside a pipe. As mentioned, the eigenvalues of $\Lambda_\sigma - \Lambda_0$ can be used to locate the inhomogeneities non-iteratively (Brühl, 2001; Hanke and Brühl, 2003), which will be further discussed in Section 5.1.3. It is a promising method to be combined with the eigenvalue based approach proposed here, to obtain a reliable and accurate void fraction estimation for two-phase flows.

4.2.2 Robustness of the proposed approach

The properties of the eigenvalue distribution of the normalized impedance matrix $\hat{\boldsymbol{Z}}$ are analyzed in the previous section based on 2D simulations. In the present section, the robustness of this methodology is investigated by studying the case where the data is noisy and when the inclusions are conductive.

Noisy data

In practical EIT systems, the boundary measurements are always polluted by some noise, including background white noise or the cross-talk of electrical devices. Thus, the robustness of the eigenvalue analysis to noisy data has to be assessed. The averaging relative error $\overline{\text{RE}}$ of the measurements in ProME-T system has been evaluated to be above 48 dB at an excitation frequency of 50 kHz and amplitude of 1 V. Given this $\overline{\text{RE}}$ value then adding a noise of 10 dB to the measurement data from numerical simulations is conservative.

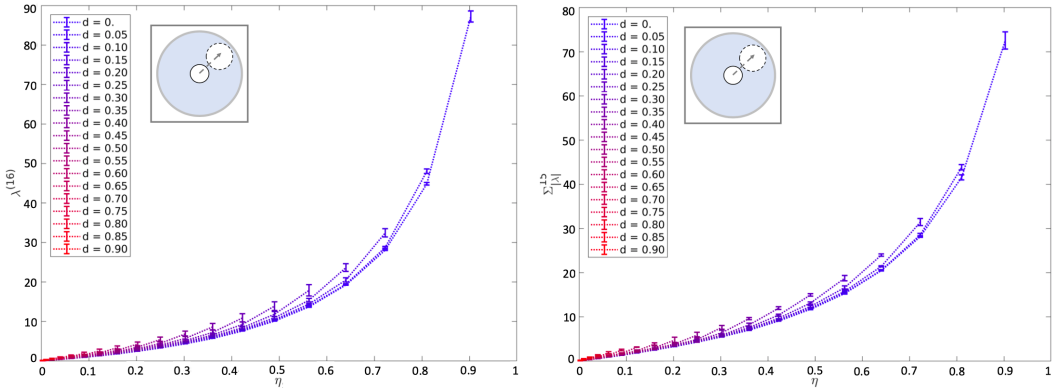

(a) $\lambda^{(16)}$ vs. η with error bars.

(b) $\sum_{|\lambda|}^{15}$ vs. η with error bars.

FIGURE 4.10: Eigenvalue trends obtained with noisy data in Case 1.

The noise is added to the measurement data from both the homogenous and inhomogeneous configurations. The eigenvalues of Case 1 are computed and compared to the results without noise. Again, $\lambda^{(16)}$ and $\sum_{|\lambda|}^{15}$ are the metrics this study is focusing on, so they are plotted with error bars as in Figure 4.10. The error ξ on $\lambda^{(16)}$ is computed as $\xi = |\lambda^{(16)}_{noisy} - \lambda^{(16)}|/\lambda^{(16)}$ where $\lambda^{(16)}$ is computed without noise and $\lambda^{(16)}_{noisy}$ is computed with a 10dB noise. The error on $\sum_{|\lambda|}^{15}$ is computed in the same fashion. As we can see, the relative error for both $\lambda^{(16)}$ and $\sum_{|\lambda|}^{15}$ are very small, the maximum values being 4.3% and 2.0% respectively.

Extension to conductive inclusions

Apart from the application in two-phase flow measurements, EIT sensors can also be used in various industrial processes, which may concern conductive inclusions rather than non-conductive bubbles. Here, the definition of the conductivity contrast $\mathscr{R} = \sigma_{high}/\sigma_{low}$ from Seagar et al. (1987) is used to represent the conductivity difference between two

phases. For water-gas two-phase flows, $\mathscr{R}$ tends to infinity. In the section, some configurations with $\mathscr{R} \in \{100,\ 10,\ 5,\ 2.5,\ 1.25\}$ are simulated and compared to the results associated with $\mathscr{R} \approx \infty$ (*i.e.* water-gas two-phase flows), to assess the general applicability of the proposed methodology.

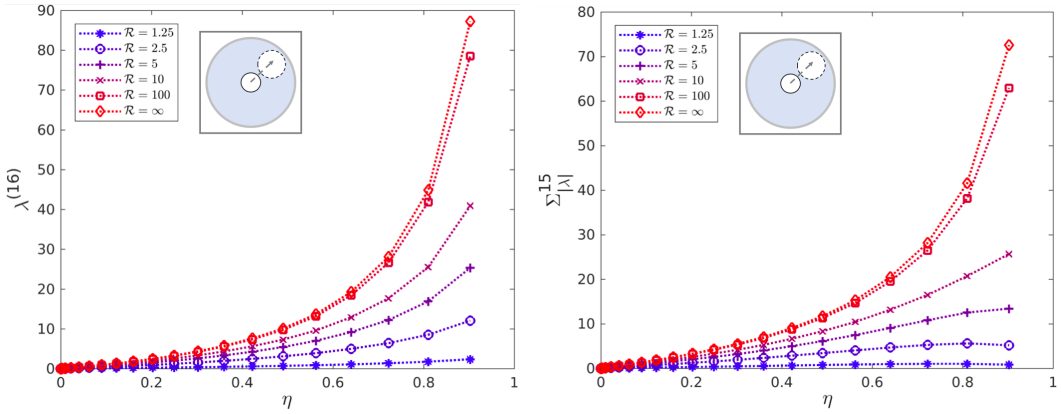

(a) $\lambda^{(16)}$ vs. η. (b) $\sum_{|\lambda|}^{15}$ vs. η.

FIGURE 4.11: $\lambda^{(16)}$ and $\sum_{|\lambda|}^{15}$ vs. η for various values of $\mathscr{R}$ in Case 1.

All three cases are simulated in 2D when varying $\mathscr{R}$ and the results for the cases 1 and 2 are plotted in Figures 4.11 to 4.12. In Figure 4.11(a), the eigenvalue $\lambda^{(16)}$ for the single concentric bubble case is plotted with η and each curve represents different values of $\mathscr{R}$. As we can see, the trends of $\lambda^{(16)}$ changing with η are similar for different values of $\mathscr{R}$, while the amplitude are increasing globally with $\mathscr{R}$. Also, as $\mathscr{R}$ increases to large values, $\lambda^{(16)}$ increases less and less, especially after $\mathscr{R} = 100$, *i.e.* there exists a threshold effect. The same conclusions are obtained for $\sum_{|\lambda|}^{15}$, see Figure 4.11(b).

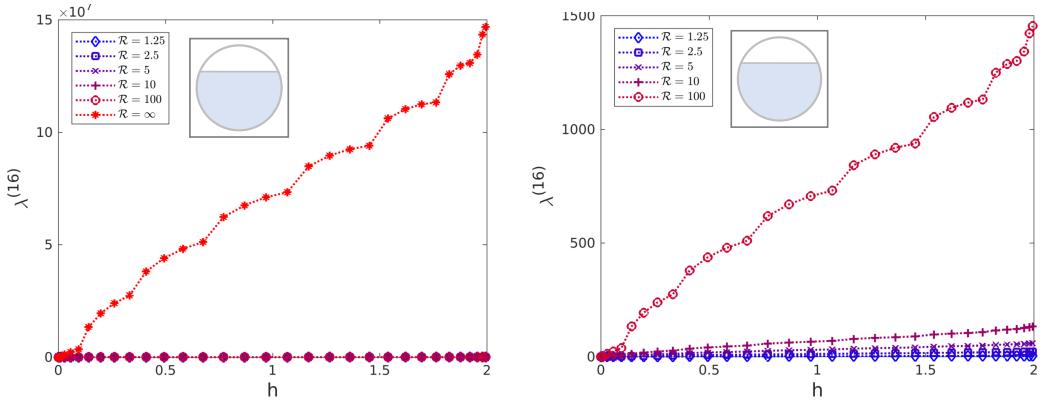

(a) $\lambda^{(16)}$ vs. h, all cases. (b) $\lambda^{(16)}$ vs. h, excluding $\mathscr{R} = \infty$.

FIGURE 4.12: $\lambda^{(16)}$ vs. h in Case 2.

For the stratified case, the same results can be obtained, while the contrast $\mathscr{R}$ has a much stronger effect on the eigenvalues, especially for large values. As shown in Figure 4.12, $\lambda^{(16)}$ is 5 to 6 magnitudes higher for $\mathscr{R} = \infty$ than for the other cases, so that $\lambda^{(16)}$ vs. h is plotted in Figure 4.12(b) excluding the case $\mathscr{R} = \infty$. Nevertheless, a linear correlation can be found between $\lambda^{(16)}$ and h for varying $\mathscr{R}$.

Lastly, the results for the multiple bubbles case have been found to be similar to the single bubble case. The applicability of the eigenvalue analysis to conductive inclusions is

therefore emphasized but the conductivity contrast $\mathscr{R}$ between phases is an important information to be known beforehand.

4.2.3 Validation by static experiments

In this section, the proposed methodology, which has been devised based on numerical simulations, is validated experimentally. Static experiments were performed in LTHC with a pipe containing still water, for a number of configurations corresponding to the three inclusion patterns considered previously. The motivations for performing such static experiments are as follows: (i) they are easily implementable using standard laboratory equipment and allow to control the phase distribution accurately, which is crucial to validate the proposed approach, (ii) EIT measurements can be performed at a high frame rate (of the order of 800 fps for the system considered), which allows to treat a dynamic flow as if it were quasi-static on each frame.

These static experiments were carried out with the ProME-T system using the test section shown in Figure 3.3. The system uses voltages of ± 1 V as excitation signals, which is different from the current excitation considered in the numerical simulations but we consider the two settings as being equivalent. For the single bubble and multiple bubbles cases, different diameters and numbers of rods were placed into the water to emulate bubbles, giving various void fractions. Considering the complete model, the bulk impedance for both homogeneous and inhomogeneous configurations can be obtained excluding the electrode specific contact impedance from the total impedance, as shown in Section 3.3.2, giving the corresponding normalized impedance matrix $\hat{\boldsymbol{Z}}$.

Result comparison

Numerical simulations in 2D can be considered as being equivalent to configurations with infinite long electrodes and inclusions, while in practical 3D implementations, the electrodes and the inclusions have finite extents. Therefore, it is more relevant to compare the results from a practical EIT system with 3D simulations. As a consequence, we consider here a 3D cylindrical model implemented in EIDORS, as shown in Figure 4.13. The radius of the numerical model is 1 while all other parameters are normalized from the prototype EIT system so that the length of the model is 7.5, the electrodes have a width of 0.125 and a length of 4.25. A fine tetrahedral mesh with 54308 nodes is generated on the 3D simulation model. The bubble inclusion is emulated by a non-conductive rod of the height of the model.

As of the static experiments, a series of configurations were investigated to obtain data for all of the three patterns considered. For Case 1, a single non-conductive rod with different diameters was placed in the test section at different distances to the center: the diameter of the rod ranges from 10 mm to 70 mm, the distance to the center being $d \in \{0,\ 12,\ 24\}$ mm, corresponding to $d \in \{0,\ 0.3r_0,\ 0.6r_0\}$ in the 3D simulations. For Case 2, the test section was placed horizontally with different water levels. In Case 3, different experiments with three rods placed symmetrically were carried out, the diameter of the rods ranges from 10 mm to 40 mm. The normalized impedance matrix and its eigenvalues were computed for each case. The evolutions of the eigenvalue $\lambda^{(16)}$ with the void fraction are shown along with 3D simulation results in Figure 4.14 for the cases 1 and 3, and in Figure 4.15 for Case 2.

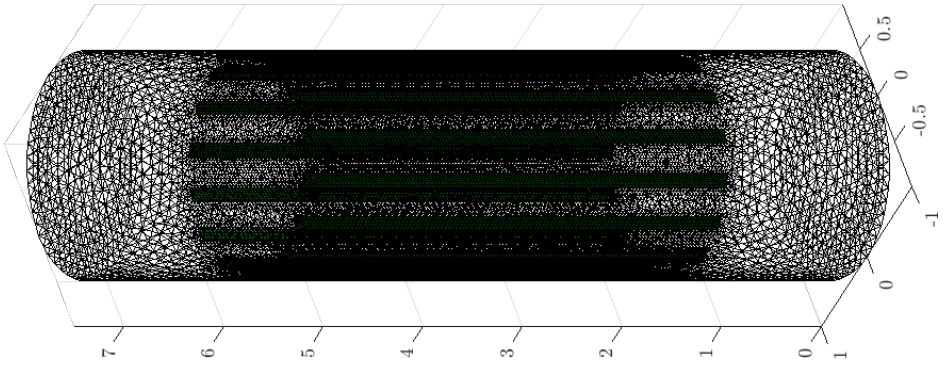

FIGURE 4.13: 3D simulation model to compare with the static experiments, non-conductive rods with the same height of the model would be used to emulate the bubble inclusion.

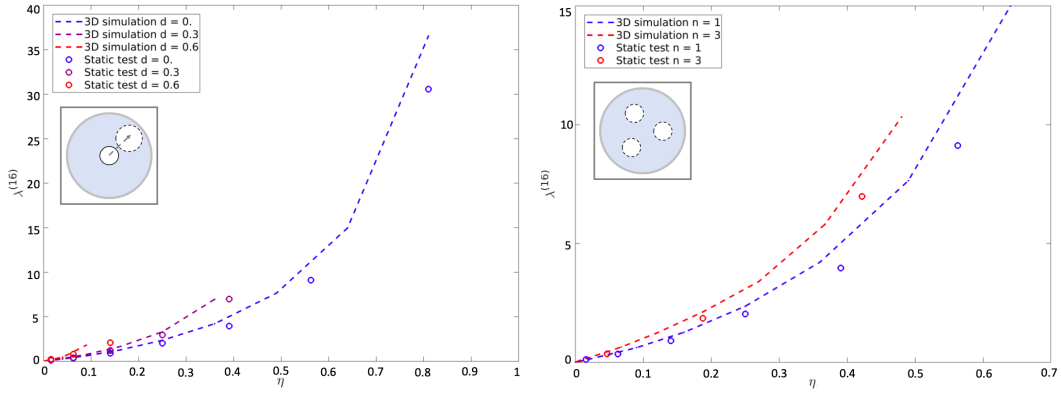

(a) Case 1. (b) Case 3.

FIGURE 4.14: Comparison between 3D simulations and experimental static experiments for the cases 1 and 3: eigenvalue $\lambda^{(16)}$ as a function of the void fraction η.

For the cases 1 and 3, the trends of the eigenvalue $\lambda^{(16)}$ for the static experiments agree well with the 3D simulations, which validates the proposed methodology. Deviations of low relative amplitude can be observed, which may be due to the following facts: (i) the simulation model is non-dimensional with normalized size and conductivity; (ii) the stimulation signal is a constant current in the simulations while it is a constant voltage in the experiments.

For Case 2, the trends of the eigenvalue $\lambda^{(16)}$ with the thickness h of the gas layer, see (4.8), for the experiments and the 3D numerical simulations are very different, as seen in Figure 4.15(a), especially at small h. The magnitudes in the experiments are also significantly lower than in the simulations. These discrepancies may come from: (i) the surface tension of water causes a rise at the interface between the plastic pipe and the water, especially at low h; (ii) a conductive water film may be present on the uncovered part of the pipe surface, while in the simulation there is no such film. Moreover, the magnitude of the eigenvalue $\lambda^{(16)}$ is remarkably high for all values of h compared to the other phase distribution patterns (at the same void fraction), as shown in Figure 4.15(b). Lastly, the electrodes that are immersed in water can be directly revealed by the distribution of the entries of the normalized impedance matrix, as seen in Figure 4.3(a), which could therefore be used as an indicator of the water level.

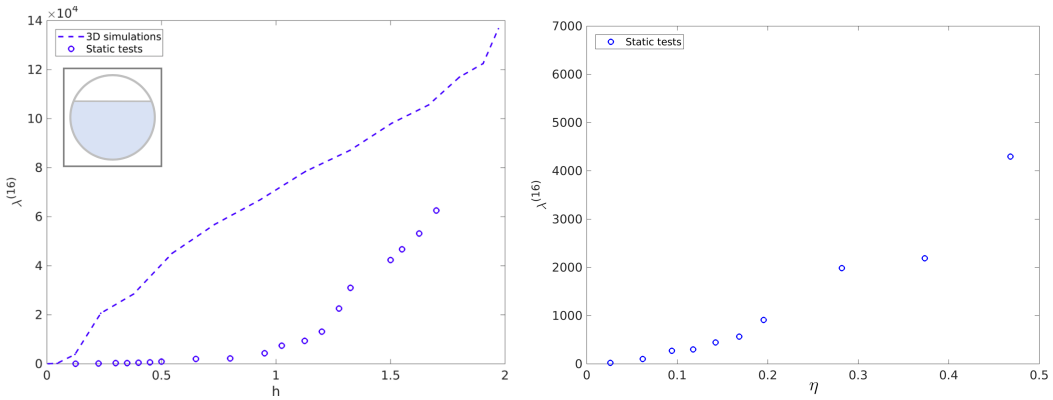

(a) $\lambda^{(16)}$ vs. h. (b) $\lambda^{(16)}$ vs. η for low values of h.

FIGURE 4.15: Comparison between 3D simulations and experimental static experiments for Case 2.

To sum up, the impedance data from EIT sensor and its relation to the void fraction of two-phase flows is investigated numerically and experimentally for a cylindrical pipe configuration. The boundary measurements at discrete electrodes lead to one bulk impedance matrix for each excitation pattern. A normalization of the impedance matrix is considered to extract information from the data and reduce the influences of factors other than the bubble inclusion distribution, such as the diameter of the sensor, the background medium conductivity or the stimulation signal.

Numerical simulations are carried out for three different canonical cases that cover a diversity of bubble distribution patterns for two-phase flows. Synthetic boundary measurements are computed to obtain normalized impedance matrices, the eigenvalues of which are investigated in the different configurations considered. The robustness of the proposed approach to noisy data is assessed by adding 10 dB of noise to the measurement data and the presented results highlight some satisfying performances. Moreover, this methodology can be extended to case of conductive inclusions.

From the numerical simulations, it is found that the leading eigenvalue $\lambda^{(16)}$ and the sum of eigenvalues $\sum_{|\lambda|}^{15} = |\lambda^{(1)}| + \cdots + |\lambda^{(15)}|$ are strongly correlated to the void fraction for all of the cases considered: (i) in the single bubble case (Case 1), the simulation results are encapsulated by the curves of $\lambda^{(16)}$ and $\sum_{|\lambda|}^{15}$ vs. η excluding the data point at $\eta > 0.9025$. The void fraction can be estimated by $\sum_{|\lambda|}^{15}$ with an error of 10% regardless of the bubble position; (ii) in the stratified case (Case 2), a linear correlation is found between $\lambda^{(16)}$ and h with a fitting measure $R^2 = 0.9905$; (iii) in the multiple bubbles case (Case 3), the relation between the void fraction and the eigenvalues are strongly dependent on the number n_{bub} of inclusions and an accurate estimation of the void fraction requires the knowledge of both $\lambda^{(16)}$, or $\sum_{|\lambda|}^{15}$, and n_{bub}.

Static experiments corresponding to the three cases considered are carried out and the eigenvalues of the NIM from experimental data are compared with 3D simulations. The trends for the eigenvalue $\lambda^{(16)}$ with η agree well for the cases 1 and 3, although there are small deviations in terms of the magnitudes; for Case 2 there is a large discrepancy between the static experiments and the simulations, while $\lambda^{(16)}$ is remarkably high at all h compared to other phase distribution patterns at the same phase fraction.

Chapter 5

Image reconstruction of highly contrasted profiles

The EIT inverse problem can be described as seeking the unknown admittivity distribution from the knowledge of boundary excitation and measurement. Theoretically, all possible boundary measurements determine the internal model parameters uniquely (Somersalo et al., 1992), while in practice the number of boundary measurements is limited by the finite number of electrodes and excitation patterns, yet the measurements are degraded by measurement error and noise. Therefore, the solution to the EIT inverse problem is usually a discretized conductivity profile with *piece-wise* constant values.

The EIT inverse problem is challenging because: i) it is a non-linear problem, the electrical current spreads out in the sensing domain in all directions, even out of the sensor plan; ii) it is severely *ill-posed*, the boundary measurement is much more sensitive to conductivity change near the boundary than in the center. Intensive researches have been carried out on the EIT image reconstruction algorithms. In this chapter, the conventional and non-conventional reconstruction algorithms or methods for the EIT are reviewed, some of them are implemented using numerical simulation data. The reconstruction methods feasible for two-phase flow imaging are decided, with which benchmark reconstructions are made for several static experiments. In addition, the quality of the reconstructed images associated with various excitation strategies are compared quantitively using both simulation and static experimental data.

5.1 Review of image reconstruction methods

The approaches to the EIT inverse problem is straightforward: linearize the non-linear problem, reduce the *ill-posedness* through regularization, and solve a sequence of linearized problem iteratively to reconstruct large conductivity contrasts or complex geometries. Various iterative and non-iterative algorithms have been thoroughly investigated and compared in the context of high contrast imaging in chemical engineering or process tomography, see *e.g.* Kim et al. (2001); Kotze et al. (2019), and comprehensive reviews presented in Lionheart (2004), Polydorides (2002) and Borcea (2002).

Non-iterative algorithms are commonly based on the linear assumption: the conductivity profile is close to a constant. Typical approaches include the sensitivity back-projection (Santosa and Vogelius, 1990; Kotre, 1994; Barber and Brown, 1984), one-step Newton method (Cheney et al., 1990; Fuks et al., 1991), and so on. Iterative methods solve the reconstruction problem minimizing the cost functions in the least-squares sense, such as the modified Newtom-Raphson method (Yorkey et al., 1987) and variational method (Kohn and

McKenney, 1990), the essence is solving a sequence of regularized linear problem and updating the conductivity approximation iteratively.

The iteration method may stop at a local minimum without noticing, Breckon (1990) proved that the minimum of the cost function is not unique, it lies in a *deep-sided narrow valley with a very flat floor where the lowest value is hard to find*. Also, it is computationally expensive solving the direct problem in every iteration. Therefore, non-iterative methods solving the nonlinear inverse problem directly have been proposed, *e.g.* factorization method (Hanke and Brühl, 2003), topological sensitivity analysis (Bonnet, 2009; Bonnet and Cakoni, 2019), level set method (Chung et al., 2005), and D-bar method (Isaacson et al., 2004). These methods either only retrieve partial information of the conductivity profile, for example the position or shape of the inclusion, or require to choose the hyperparameter subjectively or empirically, since there is rare mathematical model available on this aspect. Until now, they are mainly investigated theoretically, further studies are needed implementing with practical EIT data. A comprehensive and in-depth introduction to nonlinear inverse problems with practical applications in Sparse X-ray and EIT imaging can be found in Mueller and Siltanen (2012).

5.1.1 Back-projection

Back-projection is a fast reconstruction method widely used in hard-field imaging, such as the FBP method for X-ray imaging. The idea is to back-project the measured data onto the probed domain, that is, assigning the measured data to the elements on the trajectory line connecting the emitter and receiver, an image is formed summating the measurement data of all projections. For EIT inverse problem, modifications should be made to the conventional back-projection, since the trajectory line of electrical current is not straight. Barber and Brown (1984) considered the equipotential line as the current 'trajectory' to apply back-projection. Kotre (1994) proposed a sensitivity weighted back-projection approach, the normalized transpose of the Jacobian matrix is applied to the voltage difference data. Typically, a smooth image is obtained from back-projection method. It was widely used in the process tomography, while shows few advantage than the Tikhonov regularization formula with one-step Newton method, which will be introduced in the following sections.

5.1.2 Least-squares methods

The least-squares methods estimate the conductivity profile by minimizing a cost function, or objective function as:

$$\boldsymbol{\sigma}_{\mathrm{id}} = \arg\min_{\boldsymbol{\sigma}} \Phi(\boldsymbol{\sigma}), \qquad \text{with } \Phi(\boldsymbol{\sigma}) = \frac{1}{2}\|\boldsymbol{U}(\boldsymbol{\sigma}) - \boldsymbol{V}\|^2, \tag{5.1}$$

where $\boldsymbol{V}$ is a vector of discrete boundary measurements associated with an objective (discrete) conductivity distribution to be reconstructed, while $\boldsymbol{U}(\boldsymbol{\sigma})$ is a vector of simulated boundary measurements associated with a trial conductivity field $\boldsymbol{\sigma}$, $\|\cdot\|^2$ is the standard 2-norm on vectors. The minimizer $\boldsymbol{\sigma}_{\mathrm{id}}$ gives the reconstructed profile.

Differentiating Φ with respect to $\boldsymbol{\sigma}$, we have:

$$\Phi' = \boldsymbol{U}'(\boldsymbol{\sigma})^T(\boldsymbol{U}(\boldsymbol{\sigma}) - \boldsymbol{V}), \tag{5.2}$$

in which the term $\boldsymbol{U}'(\boldsymbol{\sigma})$ is essentially the Jacobian matrix $\boldsymbol{J}$.

Eqn. (5.2) is still nonlinear with $\boldsymbol{\sigma}$, thus, a Taylor series expansion at an arbitrary point $\boldsymbol{\sigma}^{\mathrm{k}}$ is taken neglecting the high order terms, giving:

$$\Phi'(\boldsymbol{\sigma}^{\mathrm{k}}+\delta\boldsymbol{\sigma}^{\mathrm{k}}) \approx \Phi'(\boldsymbol{\sigma}^{\mathrm{k}}) + \Phi''(\boldsymbol{\sigma}^{\mathrm{k}})\delta\boldsymbol{\sigma}^{\mathrm{k}}, \tag{5.3}$$

where Φ'' is the so-called Hessian matrix, it is given by:

$$\Phi'' = \boldsymbol{J}^T\boldsymbol{J} + \boldsymbol{U}''(\boldsymbol{\sigma})^T\big[\boldsymbol{I}\otimes[\boldsymbol{U}(\boldsymbol{\sigma})-\boldsymbol{V}]\big], \tag{5.4}$$

with $\otimes$ the Kronecker matrix product (Brewer, 1978), $\boldsymbol{I}$ the identity matrix. The term $\boldsymbol{U}''$ is the second order derivative of $\boldsymbol{U}$, it is difficult to calculate explicitly, while $[\boldsymbol{U}(\boldsymbol{\sigma})-\boldsymbol{V}]$ becomes negligible as the minimum is approached, giving the approximate Hessian matrix as:

$$\Phi'' \approx \boldsymbol{J}^T\boldsymbol{J}. \tag{5.5}$$

Minimizing the function in Eqn. (5.1) means seeking a step $\delta\boldsymbol{\sigma}^{\mathrm{k}}$ for which $\Phi'(\boldsymbol{\sigma}^{\mathrm{k}}+\delta\boldsymbol{\sigma}^{\mathrm{k}}) \approx 0$, by substituting Eqn. (5.2) and (5.5) into Eqn. (5.3), we have:

$$\delta\boldsymbol{\sigma}^{\mathrm{k}} = -(\boldsymbol{J}^T\boldsymbol{J})^{-1}\boldsymbol{J}^T[\boldsymbol{V}-\boldsymbol{U}(\boldsymbol{\sigma}^{\mathrm{k}})], \tag{5.6}$$

which is an iteration step to find $\boldsymbol{\sigma}_{\mathrm{id}}$ for the nonlinear inverse problem through the well-known Gauss-Newton iteration. From an initial point, usually a homogeneous conductivity profile is taken, the conductivity approximation is updated by $\delta\boldsymbol{\sigma}^{\mathrm{k}}$ at each step, that is, $\boldsymbol{\sigma}^{\mathrm{k+1}} = \boldsymbol{\sigma}^{\mathrm{k}}+\delta\boldsymbol{\sigma}^{\mathrm{k}}$, with $\boldsymbol{\sigma}^{\mathrm{k}}$ and $\boldsymbol{\sigma}^{\mathrm{k+1}}$ the conductivity estimation at step k and k+1, separately. The procedure continues until the convergence criteria is reached, the approximation at the final step corresponds to $\boldsymbol{\sigma}_{\mathrm{id}}$. Nevertheless, this procedure can be stopped at the first step, giving the so called one-step Gauss-Newton method.

Unfortunately, in the presence of measurement error the Gauss-Newton iteration does not work well: the term $[\boldsymbol{V}-\boldsymbol{U}(\boldsymbol{\sigma}^{\mathrm{k}})]$ may be below the measurement error, leading to an undesired conductivity approximation. Also, the Hessian matrix $\boldsymbol{J}^T\boldsymbol{J}$ is highly ill-conditioned, which makes its inverse very inaccurate and sensitive to measurement errors.

Thus, regularization techniques are applied to improve the conditioning of the objective function, that is, a penalty regularization term $Q(\boldsymbol{\sigma})$ is introduced into Φ, the least-squares problem is now to seek $\boldsymbol{\sigma}_{\mathrm{id}}$ minimizing:

$$\Phi = \frac{1}{2}\|\boldsymbol{U}(\boldsymbol{\sigma})-\boldsymbol{V}\|^2 + \alpha Q(\boldsymbol{\sigma}), \tag{5.7}$$

where $\alpha \in \mathbb{R}$ is the non-negative regularization hyperparameter to be chosen from case to case, while $Q(\boldsymbol{\sigma})$ can have various forms, corresponding to different types of regularizations. In Eqn. (5.7), the first term represents the fidelity to the measurement data, the second term incorporates certain *a priori* information into the cost function, α acts as a weighting coefficient to control the tradeoff between the two terms. The regularization term improves the stability of the reconstruction algorithm, while it incorporates *a priori* information which may be unrepresentative of the real conductivity profile.

The hyperparameter α is a critical parameter to choose in regularized image reconstructions, it controls the weighting of the penalty term in the objective function. A large α smoothens the reconstructed image, a small α gives more weight to data misfit and offers increased resolution. However, if it is set too small, the data lying below the noise threshold dominates the inverse matrix, the resulting image represents measurement noise instead of conductivity distribution.

There are several ways to decide the *optimal* hyperparameter depending on whether the noise covariance of the measurement is known or not (Vauhkonen, 1997), *e.g.* discrete Picard condition method, Moore-Penrose method, and L-curve method. Amongst, the L-curve method is the most widely applied approach, although it gives case specific *optimal* values associated with the conductivity profiles concerned. It is noted that Graham and Adler (2006) used the so-called 'blur ratio' as a representation to image resolution and proposed the *BestRes* method to obtain the optimal hyperparameter that gives the minimum blur ratio. The advantage is that the optimal α is universal to all conductivity profiles and noise levels.

Tikhonov type regularization

A typical choice of $Q(\boldsymbol{\sigma})$ is a quadratic function, substituting into Eqn. (5.7), we have the generalized Tikhonov type regularization for EIT inverse problem:

$$\boldsymbol{\sigma}_{\text{id}} = \arg\min_{\boldsymbol{\sigma}} \Phi(\boldsymbol{\sigma}), \qquad \text{with } \Phi(\boldsymbol{\sigma}) = \frac{1}{2}\|\boldsymbol{U}(\boldsymbol{\sigma}) - \boldsymbol{V}\|^2 + \alpha\|\boldsymbol{L}(\boldsymbol{\sigma} - \boldsymbol{\sigma}_{\text{ref}})\|^2, \tag{5.8}$$

with $\boldsymbol{\sigma}_{\text{ref}}$ a reference conductivity profile, $\boldsymbol{L}$ the regularization matrix which is the approximation to some partial differential operators.

The L2-norm of Tikhonov type regularization guarantees its non-negativity, so that the resulting functional is differentiable, leading to a well-posed minimization problem (the inversion is stabilized). An approximate solution for Eqn. (5.8) is:

$$\delta\boldsymbol{\sigma}^{\text{k}} = -(\boldsymbol{J}^T\boldsymbol{J} + \alpha\boldsymbol{L}^T\boldsymbol{L})^{-1}\big(\boldsymbol{J}^T\delta\boldsymbol{V}^{\text{k}} + \alpha\boldsymbol{L}^T\boldsymbol{L}(\boldsymbol{\sigma}_{\text{ref}} - \boldsymbol{\sigma}^{\text{k}})\big), \tag{5.9}$$

with $\delta\boldsymbol{V}^{\text{k}} = \boldsymbol{V} - \boldsymbol{U}(\boldsymbol{\sigma}^{\text{k}})$. Applying the Gauss-Newton iteration, the regularized inverse problem is solved using the same procedure as the non-regularized one.

To understand how regularization ameliorates the *ill-posed* problem, the condition numbers κ of the inverse terms in Eqn. (5.6) and (5.9), that is, $\boldsymbol{J}^T\boldsymbol{J}$ and $(\boldsymbol{J}^T\boldsymbol{J} + \alpha\boldsymbol{L}^T\boldsymbol{L})$, are compared. The condition number κ can be used as an indicator of the *ill-posedness* of a problem, the larger the condition number, the more *ill-posed* the inverse problem. Here, κ is defined as $\kappa(\boldsymbol{A}) = \lambda_n(\boldsymbol{A})/\lambda_1(\boldsymbol{A})$, with $\lambda_n(\boldsymbol{A})$ and $\lambda_1(\boldsymbol{A})$ the maximum and minimum eigenvalues of a matrix $\boldsymbol{A}$, a larger κ means a higher ill-conditioning. Taking a simple case with $\boldsymbol{L} = \boldsymbol{I}$, the condition numbers with and without regularization are:

$$\begin{aligned} \kappa &= \frac{\lambda_n(\boldsymbol{J}^T\boldsymbol{J})}{\lambda_1(\boldsymbol{J}^T\boldsymbol{J})}, \qquad \text{without regularization,} \\ \kappa &= \frac{\lambda_n(\boldsymbol{J}^T\boldsymbol{J}) + \alpha}{\lambda_1(\boldsymbol{J}^T\boldsymbol{J}) + \alpha}, \qquad \text{with regularization.} \end{aligned} \tag{5.10}$$

The ill-conditioned matrix $\boldsymbol{J}^T\boldsymbol{J}$ has a sufficiently small eigenvalue $\lambda_1(\boldsymbol{J}^T\boldsymbol{J})$, the κ in regularized case is approximated as $\kappa \approx \frac{\lambda_n(\boldsymbol{J}^T\boldsymbol{J})}{\alpha} + 1$, implying a well-conditioned problem with a large α.

Various regularization matrices $\boldsymbol{L}$ incorporating different *a priori* information can be used, *e.g.* the identity matrix $\boldsymbol{I}$, or the matrices corresponding to the first and second order difference operators. For example, using the penalty form $\|\boldsymbol{\sigma}\|^2$ gives good result if the conductivity distribution is known to be bounded and fluctuating, $\|\boldsymbol{\sigma}'\|^2$ fits a continuous conductivity profile, while $\|\boldsymbol{\sigma}''\|^2$ gives a smooth solution (Hua et al., 1988). Also, there are

regularizations exploiting the information from the sensitivity matrix $\boldsymbol{J}$, *i.e.* the standard Tikhonov regularization.

In standard Tikhonov regularization, the regularization matrix is scaled with the sensitivity of each element, giving $\boldsymbol{L} = \text{diag}(\boldsymbol{J}^T\boldsymbol{J})^p$, with $0 \leqslant p \leqslant 1$ an exponent coefficient. The value of p can be chosen arbitrarily, it is a compromise between pushing noise to the boundary (for $p = 0$) or to the centre (for $p = 1$). It becomes the Zeroth-order regularization with $\boldsymbol{L} = \boldsymbol{I}$ when $p = 0$, and gives the Newton's One-Step Error Reconstructor (NOSER) algorithm (Cheney et al., 1990) with $p = 1$.

The NOSER method is widely used in practical EIT image reconstructions for flow monitoring and clinical imaging, benefiting from its low computation cost and robustness to noise. It performs only one step of iteration with an updating step:

$$\Delta\boldsymbol{\sigma} = -\left(\boldsymbol{J}^T\boldsymbol{J} + \alpha \cdot \text{diag}(\boldsymbol{J}^T\boldsymbol{J})\right)^{-1}\boldsymbol{J}^T\Delta\boldsymbol{V}, \tag{5.11}$$

where $\Delta\boldsymbol{V} = \boldsymbol{V}_i - \boldsymbol{V}_h$ is the differences between the image measurements $\boldsymbol{V}_i$ associated with the conductivity distribution to be reconstructed and the reference measurements $\boldsymbol{V}_h$ associated with the reference conductivity distribution, which is usually taken as a homogeneous conductivity. The inverse matrix, being $(\boldsymbol{J}^T\boldsymbol{J} + \alpha \cdot \text{diag}(\boldsymbol{J}^T\boldsymbol{J}))^{-1}\boldsymbol{J}^T$, can be pre-calculated and saved, allowing a fast image reconstruction for online display.

Total variation regularization

Another type of regularization term $Q(\boldsymbol{\sigma})$, *i.e.* the Total Variation (TV) regularization, takes the L1-norm formula. The resulting TV regularized least-squares problem has the form:

$$\boldsymbol{\sigma}_{\text{id}} = \arg\min_{\boldsymbol{\sigma}} \Phi(\boldsymbol{\sigma}), \qquad \text{with } \Phi(\boldsymbol{\sigma}) = \frac{1}{2}\|\boldsymbol{U}(\boldsymbol{\sigma}) - \boldsymbol{V}\|^2 + \alpha\|\boldsymbol{L}\boldsymbol{\sigma}\|^1. \tag{5.12}$$

In continuum form, the TV of a conductivity profile is defined as:

$$TV = \int_\Omega |\nabla\sigma| \text{d}\Omega, \tag{5.13}$$

with Ω the sensing domain. Considering the discretization with pixel-wise constant conductivity, $\nabla\sigma$ is non-null only on the edges between elements, where the conductivity presents a step change from one element to the other, giving the discretized TV matrices as:

$$TV = \sum_i \|\boldsymbol{L}_i\boldsymbol{\sigma}\|^1, \tag{5.14}$$

where $\boldsymbol{L}$ is a sparse matrix with one row per each edge in the mesh, and every row $\boldsymbol{L}_i$ has two nonzero elements in column m and n, which are the indices of the two elements sharing the same edge, for example,

$$\boldsymbol{L}_i = [0, \cdots, 0, 1, \cdots, 0, -1, \cdots, 0]. \tag{5.15}$$

The L1-norm guarantees a positive penalty term, however, it leads to the minimization of a non-differentiable function $|\nabla\sigma|$, which cannot be solved efficiently with conventional Gauss-Newton method. In the research of Borsic et al. (2009), the Primal Dual-Interior Point Methods (PDIPM) is proposed to solve the TV regularized functional numerically.

The TV regularization rules out wild fluctuations in conductivity while preserving discontinuities in the reconstructed profile, its ability in reconstructing sharp conductivity contrasts gives clear benefits to two-phase flow imaging: it may yield a better phase segmentation. It is noting that the TV regularization is normally applied in iterative reconstructions, because it converges much slower than quadratic regularizations, stopping at the first iteration step would not give valuable information about the conductivity profile.

Some other regularization forms are available incorporating various *a priori* information, *e.g.* the information from magnetic resonance imaging, the noise level of the measurement system. A good review can be found in Vauhkonen (1997).

Probabilistic regularization

The Tikhonov and TV regularizations are essentially deterministic regularizations that incorporate *a priori* knowledge or assumption on the conductivity profile to be reconstructed, which may be unrealistic in many cases. On the contrary, the probabilistic regularization treats the conductivity distribution as random variables with probability distributions. Considering the Bayes' theorem relating conditional probabilities of random variables:

$$P(x|b) = \frac{P(b|x)P(x)}{P(b)}, \tag{5.16}$$

the most likely x is obtained through maximizing $P(x|b)$, giving the so-called Maximum *A Posteriori* (MAP) approach (Holder, 2004). The Gaussian high pass filter regularization proposed in Adler and Guardo (1996) is a good example of the MAP approach using knowledge of the noise variance of the measurement and the covariance of the conductivity distribution.

The GREIT method

A specialized reconstruction method, namely the Graz consensus Reconstruction algorithm for EIT (GREIT), has been proposed based on the consensus of a large and representative group of experts in EIT algorithm design and clinical applications for pulmonary monitoring (Adler et al., 2009). It is a linear reconstruction method producing conductivity difference images in 2D or 3D (Grychtol et al., 2016). The reconstructed difference image $\Delta\boldsymbol{\sigma}$ is calculated from an inverse matrix $\boldsymbol{R}$ and the difference data $\Delta\boldsymbol{V} = \boldsymbol{V}_i - \boldsymbol{V}_h$ by:

$$\Delta\boldsymbol{\sigma} = \boldsymbol{R}\,\Delta\boldsymbol{V}. \tag{5.17}$$

Conventionally, $\boldsymbol{R}$ is computed from the ill-conditioned EIT inverse problem with linearization and regularization, while in GREIT the *best* inverse matrix $\boldsymbol{R}$ is obtained through optimizing several performance metrics, namely the amplitude response, position error, ringing artifacts, shape deformation, resolution, and noise figure, associated with a number of small 'training' targets following some specific distribution patterns inside the forward model.

Similar to the NOSER algorithm, the *best* inverse matrix $\boldsymbol{R}$ of GREIT can be pre-calculated and saved for online image reconstruction. Also, the GREIT is designed favoring the clinical applications, which is analog to two-phase flows in terms of high conductivity contrasts and sharp interfaces between the objects and the background. Therefore, it is of interest to test the GREIT method in two-phase flow imaging.

5.1.3 Factorization method

Unlike the conventional image reconstruction methods giving the conductivity approximations within the studied domain, the Factorization Method (FM) only allows a binary test to the points inside the domain, checking whether they are inside the object(s) or not. The method is originated from a far-field inverse scattering theory proposed in the fundamental research by Kirsch (1998), the main idea is to construct a test function, the value of which shows a singularity peak at a test point inside the object, while a low value outside. The schematic is as shown in Figure 5.1 with four electrodes on the boundary, a virtual testing grid is put overlaying the studied domain Ω, the value of the test function at each test point z is calculated, which would be extremely high for $z \in \Omega_i$ and low for $z \in \Omega \setminus \Omega_i$. A binary image can be reconstructed from the FM.

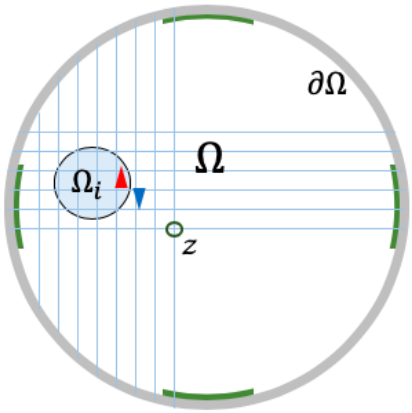

FIGURE 5.1: Schematic of the factorization method with four electrodes on the boundary. The test function gives significant value for a test point z inside the object Ω_i.

Defining the test function

The Green's function is used to construct the test function in Bellis et al. (2012). For a linear differential operator $\mathscr{H}$ defined on a domain with specified initial or boundary conditions, its Green's function $G(x,s)$ is defined as the solution of $\mathscr{H}G(x,s) = \delta(s-x)$, where δ is Dirac's delta function, it equals to zero everywhere except for $s = x$.

Considering the Green's function for EIT forward problem in the infinite two-dimensional real coordinate space $\mathbb{R}^2$:

$$\sigma \Delta_x G(x,z) = \delta(z-x), \quad \text{in } \mathbb{R}^2, \tag{5.18}$$

while in a closed and connected domain Ω with Neumann boundary conditions, we have:

$$\sigma \Delta_x G_\Omega(x,z) = \delta(z-x), \quad \text{in } \Omega, \tag{5.19}$$

$$\sigma \nabla_x G_\Omega(x,z) \cdot \boldsymbol{n} = 0 \ \text{ on } \partial\Omega, \quad \text{and} \quad \int_{\partial\Omega} G_\Omega(x,z) \mathrm{d}S = 0. \tag{5.20}$$

Then, a function $N(\cdot,z) = G_\Omega(\cdot,z) - G(\cdot,z)$ is introduced, so that

$$\sigma \Delta_x N(x,z) = 0, \quad \text{in } \Omega, \tag{5.21}$$

$$\sigma \nabla_x N(x,z)\cdot \boldsymbol{n} = -\sigma \nabla_x G(x,z)\cdot \boldsymbol{n}, \quad \text{on } \partial\Omega. \tag{5.22}$$

The function $G(\cdot,z)$ can be obtained analytically and explicitly, while $N(\cdot,z)$ can be solved numerically. Specifically for the unit disc case considered in the present study, $N(\cdot,z)$ can also be solved analytically. Therefore, we have the function $G_\Omega(\cdot,z) = N(\cdot,z)+G(\cdot,z)$, which is harmonic in $\Omega\setminus\Omega_i$. The test function is defined as $T_z = \boldsymbol{d}\cdot\nabla G_\Omega(\cdot,z)$, with $\boldsymbol{d}$ a given arbitrary unit vector.

Some other researchers (Brühl and Hanke, 2000; Brühl, 2001) defined the test function by introducing the dipole function:

$$D_z(x) = \frac{1}{\omega_n}\frac{(z-x)\cdot\boldsymbol{d}}{|z-x|^n}, \quad x\neq z, \tag{5.23}$$

located in z with an arbitrary unit vector $\boldsymbol{d}\in\mathbb{S}^{d-1} = \{\boldsymbol{x}\in\mathbb{R}^d, |\boldsymbol{x}|=1\}$, and ω_n the surface measure of the unit sphere in $\mathbb{R}^n$. D_z corresponds to the electrostatic potential created by a dipole source at position z pointing to the direction $\boldsymbol{d}$. It is then augmented by a harmonic function v_z in Ω with Neumann data as:

$$\frac{\partial v_z}{\partial \boldsymbol{n}} = -\frac{\partial D_z}{\partial \boldsymbol{n}}, \quad \text{on } \partial\Omega, \tag{5.24}$$

with $\boldsymbol{n}$ the unit outward normal vector on the boundary $\partial\Omega$. The test function is defined as:

$$T_z = D_z + v_z, \tag{5.25}$$

which is harmonic in $\Omega\setminus\Omega_i$ with vanishing flux $\partial T_z/\partial\boldsymbol{n}$ on $\partial\Omega$. Essentially, the test functions defined from the dipole function and from the Green's function are equivalent.

Hanke and Brühl (2003) proved that,

$$z\in\Omega_i \quad \text{if and only if} \quad t_z = T_z|_{\partial\Omega} \in \mathscr{R}_f(\Lambda_\sigma-\Lambda_0)^{1/2}, \tag{5.26}$$

with t_z the trace of the test function T_z, $\mathscr{R}_f$ representing the range, and $(\Lambda_\sigma-\Lambda_0)$ the relative NtD map defined in Section 2.2.1.

For the unit disc case, t_z can be computed analytically by the explicit expression:

$$t_z = \frac{1}{\pi}\frac{(z-x)\cdot\boldsymbol{d}}{|z-x|^2}, \tag{5.27}$$

with x the measurement points on $\partial\Omega$.

Numerical implementation

Picard criterion. In numerical implementation, the range $\mathscr{R}_f(\Lambda_\sigma-\Lambda_0)^{1/2}$ in the criterion (5.26) is difficult to compute explicitly, the Picard criterion is applied considering the eigenvalues λ_k and eigenvectors v_k of $(\Lambda_\sigma-\Lambda_0)$. For the cavity problem, the eigenvalues λ_k (sorting in descending order) of $(\Lambda_\sigma-\Lambda_0)$ exhibit exponential decay, so do the squared norms of the eigen-components $\langle t_z, v_k\rangle^2$. Their average decay parameters are determined separately through:

$$\begin{aligned} \log\lambda_k &\approx c + k\log q, \quad k=1,\cdots,m_0,\\ \log\langle t_z, v_k\rangle^2 &\approx \gamma_z + k\log\rho_z, \quad k=1,\cdots,m_0, \end{aligned} \tag{5.28}$$

with c and γ_z some constant numbers, m_0 the number of eigenvalues and eigenvectors considered in the implementation, it is usually small due to the error in approximating $\mathscr{R}_f(\Lambda_\sigma - \Lambda_0)^{1/2}$ and the presence of noise in measurement data. The criterion (5.26) then becomes:

$$z \in \Omega_i \quad \text{if and only if} \quad \rho_z < q. \tag{5.29}$$

Computing λ_k and v_k. In continuum form, considering the boundary excitation as a trigonometric function f and the difference measurement as $\Delta V = V_i - V_h$, with V_i the boundary measurement from the case with objects and V_h that of the homogeneous case, we have $\Delta V = (\Lambda_\sigma - \Lambda_0) \cdot f$.

In discrete form, the boundary excitation $\boldsymbol{f}_i$ is exerted on ℓ discrete electrodes, they form an orthogonal basis as $\boldsymbol{f} = \{\boldsymbol{f}_i\}$, with $i = 1, \cdots, \ell$. The discrete boundary measurement $\boldsymbol{V}_i$ and $\boldsymbol{V}_h$ are directly measurable at the electrodes, their difference $\Delta \boldsymbol{V} = \boldsymbol{V}_i - \boldsymbol{V}_h$ can be projected onto the span of $\boldsymbol{f}_i$, the corresponding expansion coefficients compose a matrix $\boldsymbol{A} \in \mathbb{R}^{\ell \times \ell}$, *i.e.* $\Delta \boldsymbol{V} = \boldsymbol{A}\boldsymbol{f}$. That is, $\boldsymbol{A}$ is the matrix representation of the Galerkin projection $\boldsymbol{P}(\Lambda_\sigma - \Lambda_0)\boldsymbol{P}^*$, with $\boldsymbol{P}$ the orthonormal projector onto the span of trigonometric functions and $\boldsymbol{P}^*$ the conjugation of $\boldsymbol{P}$, here we have $\boldsymbol{P}^* = \boldsymbol{P}$ and $\boldsymbol{P}^2 = \boldsymbol{P}$. In numerical analysis, Galerkin projection converts a continuous operator into a discrete matrix. Noticing that the equation has remained unchanged applying the Galerkin projection, only the spaces have changed. The problem is then reduced to a finite-dimensional vector subspace, allowing to compute numerically the terms λ_k and v_k associated with $(\Lambda_\sigma - \Lambda_0)$.

Knowing that $\boldsymbol{P}$ is the orthonormal projector onto the span of trigonometric functions $\boldsymbol{f}_i$, with $\boldsymbol{f}_i$ a vector of length ℓ containing the currents imposed at the electrodes in one excitation pattern, we have $\boldsymbol{P} = \boldsymbol{f} \cdot (\boldsymbol{f}^T \cdot \boldsymbol{f})^{-1} \cdot \boldsymbol{f}^T$ of size $\ell \times \ell$, with:

$$\begin{aligned} \boldsymbol{A} &= \boldsymbol{P} \cdot (\Lambda_\sigma - \Lambda_0) \cdot \boldsymbol{f} \cdot (\boldsymbol{f}^T \cdot \boldsymbol{f})^{-1} \cdot \boldsymbol{f}^T \\ &= \boldsymbol{P} \cdot \Delta \boldsymbol{V} \cdot (\boldsymbol{f}^T \cdot \boldsymbol{f})^{-1} \cdot \boldsymbol{f}^T. \end{aligned} \tag{5.30}$$

The eigenvalues and eigenvectors of the matrix $\boldsymbol{A}$ are approximations to that of $(\Lambda_\sigma - \Lambda_0)$. Considering the correlation in Eqn. (5.28) and the criterion in Eqn. (5.29), the q and ρ_z are computed and compared at each test point, giving the reconstructed image of the FM.

Reconstructions using the factorization method

Numerical simulations have been carried out in 2D applying the trigonometric excitation strategy. The forward model is a unit disk with $\ell = 64$ point electrodes, a mesh with 8965 nodes is generated to compute the boundary measurements $\boldsymbol{V}_h$ and $\boldsymbol{V}_i$ associated with the reference and image cases separately. Two different image cases with one and three objects inside the domain were investigated, the schematics of the real conductivity profiles are shown in Figure 5.2.

The criterion (5.29) is to compare the slope q of $\log \lambda_k$ and the slop ρ_z of $\log \langle t_z, v_k \rangle^2$ from $k = 1$ to $k = m_0$ for each test point z. Figure 5.3 plots $\log \lambda_k$ and $\log \langle t_z, v_k \rangle^2$ versus the index k of two points $z \in \Omega_i$ and $z \in \Omega \setminus \Omega_i$, for the two cases. As we can see, for both cases the slop ρ_z for the test point $z \in \Omega \setminus \Omega_i$ is significantly different to that of $z \in \Omega_i$, and to q as well. While for the test point $z \in \Omega_i$, the choice of m_0 is critical to compare ρ_z and q, for example in one object case, $m_0 = 18$ and $m_0 = 22$ would give totally different results. This is because the eigenvalues of matrix $\boldsymbol{A}$ only *approximate the dominant eigenvalues*

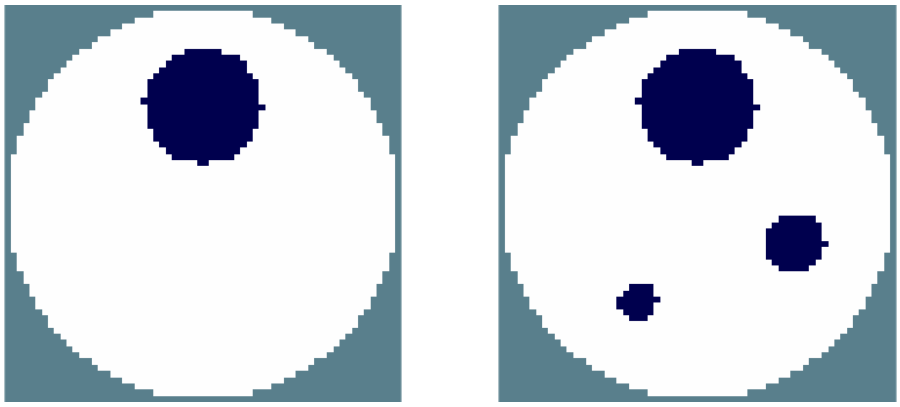

(a) One object case. (b) Three objects case.

FIGURE 5.2: Schematics of the real conductivity profiles with one and three objects inside the domain.

of $(\Lambda_\sigma - \Lambda_0)$ (Hanke and Brühl, 2003), so that only the first m_0 eigenvalues follow an exponential decay. The other eigenvalues have large approximation error, hence decaying super-linearly. An objective estimation of m_0 remains a problem for the FM.

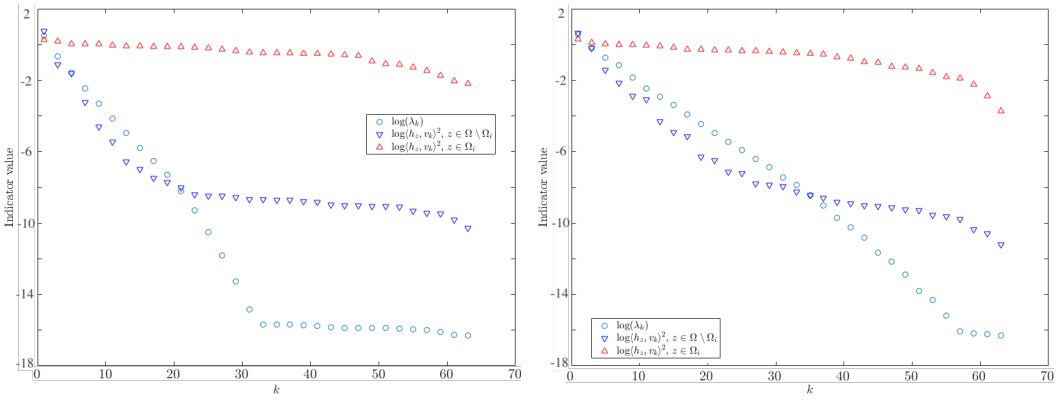

(a) One object case. (b) Three objects case.

FIGURE 5.3: $\log \lambda_k$ and $\log\langle t_z, v_k\rangle^2$ changing with k for one and three objects cases. One out of two points are plotted for the sake of clarity.

The final reconstructed images are plotted in Figure 5.4 for the two cases, with $m_0 = 16$ and $m_0 = 24$ separately. It is shown that the one object case gives a very good reconstruction, the position and area of the object agree well with that in the real case. While for the three objects case, the separated objects are reconstructed as one connected object, although the extremes of the connected object seem agree with the positions of the real objects. Varying m_0 may change the size of the reconstructed object, but the distribution pattern would be consistent.

To sum up, the factorization method allows a binary test on a testing grid, checking whether they are inside the object(s) or not, the result is strongly affected by the choice of m_0. The method gives good reconstruction for single object case, but seems not working well for multiple objects case. Moreover, the singularity feature of the test function is commonly poorly represented in the computation scheme, making the method susceptible to data error and noise.

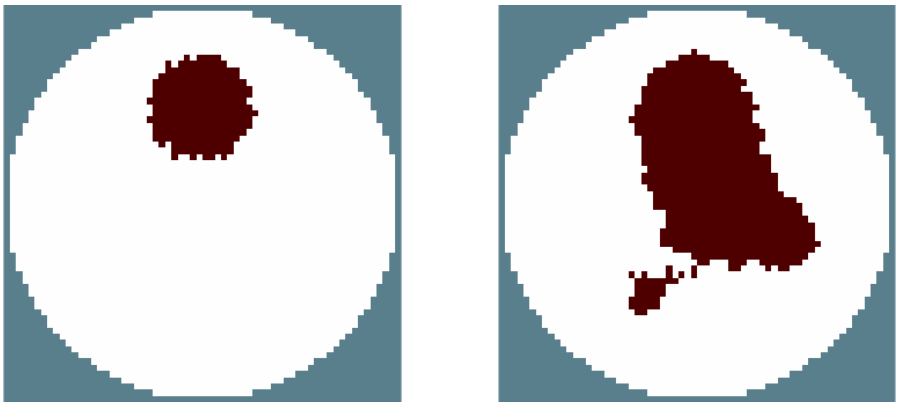

(a) One object case, $m_0 = 16$. (b) Three objects case, $m_0 = 24$.

FIGURE 5.4: Image reconstructions using the FM for one and three objects cases.

MUSIC algorithm

The MUltiple-SIgnal-Classification (MUSIC) algorithm is based on the same mathematical basis with the factorization method, while it only gives possible locations of inhomogeneities inside the domain. In MUSIC algorithm, the inhomogeneities are considered having the form $\Omega_i = z_i + \varepsilon_0 r_i \Omega$ with $z_i \in \Omega, i = 1, \cdots, p$ the centers of small disc-shaped inhomogeneities Ω_i, $\varepsilon_0 r_i$ the radius of Ω_i, where $\varepsilon_0 > 0$ is a common coefficient for all Ω_i and $r_i > 0$ can be different for each inhomogeneity (Hanke and Brühl, 2003). With these assumption, the MUSIC algorithm emphasizes the center z_i of inhomogeneity.

In this context, the criteria in Eqn. (5.26) is modified as computing the angle θ_z between t_z and $\mathscr{R}_f(\Lambda_\sigma - \Lambda_0)^{1/2}$ by:

$$\cot\theta_z \approx \|P^{\delta_n} t_z\|^2 / \|(I - P^{\delta_n}) t_z\|^2, \tag{5.31}$$

where

$$\|P^{\delta_n} t_z\|^2 = \sum_{k=1}^{n_0} \langle t_z, v_k \rangle^2 \quad \text{and} \quad \|(I - P^{\delta_n}) t_z\|^2 = \sum_{k=n_0+1}^{\ell} \langle t_z, v_k \rangle^2, \tag{5.32}$$

with n_0 the index of the minimum eigenvalue corresponding to the noise level δ_n. The $\cot\theta_z$ at each grid point z can be calculated, its value indicates the possibility of the presence of inhomogeneity, which should not be mistaken as the conductivity value.

Image reconstructions of the MUSIC algorithm for the two cases concerned are plotted in Figure 5.5, the noise level considered is $\delta_n = 4 \times 10^{-4}$ and $\delta_n = 5 \times 10^{-6}$, separately. As we can see, the positions of the objects (represented by the discrete peaks) are well reconstructed for both cases. Noting that the size information in the reconstructed images is not relevant to the physical sizes of the objects, only the discrete peak values represent the presence of objects.

Additionally, the influences of measurement noise on the reconstructions of the FM and MUSIC methods have been studied. The noisy data is obtained by adding 40 dB of random noise to the image data $\boldsymbol{V}_i$. The values of $\log\lambda_k$ and $\log\langle t_z, v_k \rangle^2$ are plotted versus the index k for two selected points $z \in \Omega_i$ and $z \in \Omega \setminus \Omega_i$, as in Figure 5.6. Comparing to the plots in Figure 5.3, it is found that much less number of eigenvalues can be used for reconstruction, which is $m_0 = 6$ and $m_0 = 10$ separately for the two cases.

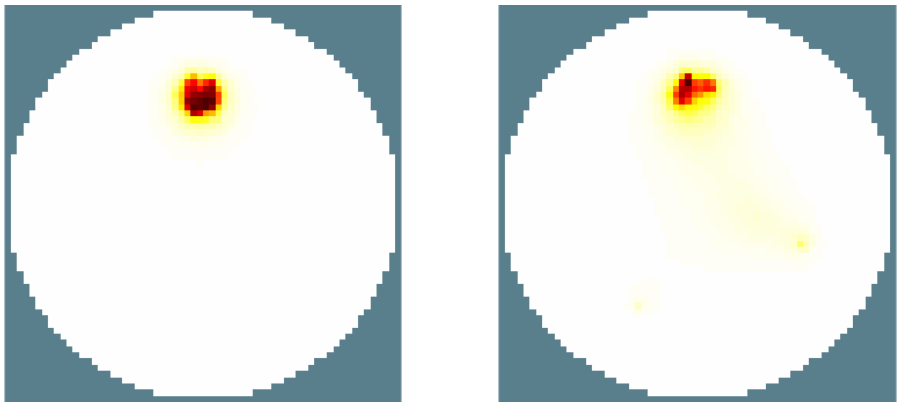

(a) One object case. (b) Three objects case.

FIGURE 5.5: Reconstructions using the MUSIC algorithm for one and three objects cases.

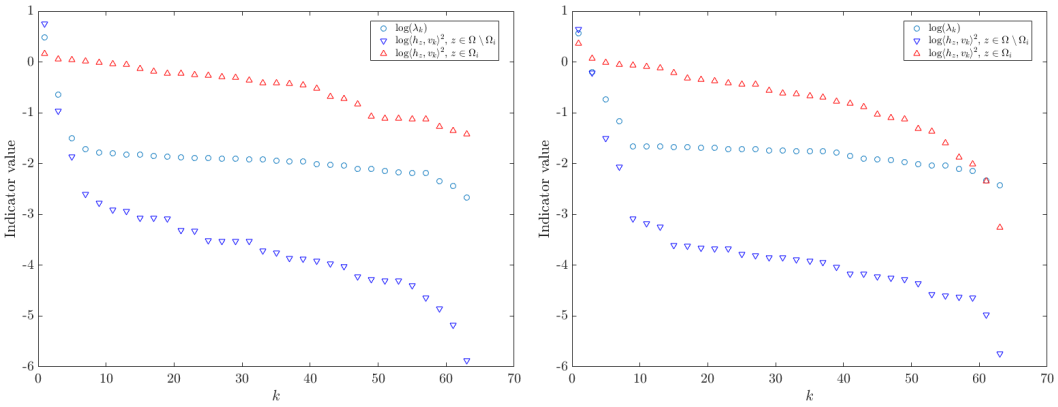

(a) One object case. (b) Three objects case.

FIGURE 5.6: $\log \lambda_k$ and $\log\langle t_z, v_k\rangle^2$ associated with noisy data for one and three objects cases. One out of two points are plotted for the sake of clarity.

The associated image reconstructions are shown in Figure 5.7 using the FM and MUSIC methods, $m_0 = 6$ and $m_0 = 8$ are taken separately for the two cases in the FM, while $\delta_n = 10^{-2}$ and $\delta_n = 5 \times 10^{-3}$ for MUSIC algorithm. It is shown that the reconstructions from the FM are severely distorted by the noisy data, the area estimation of the objects has a great error for both cases. The MUSIC algorithm gives a good position estimation for one object case, while for three objects case only the position of the largest object is identifiable. Overall, the FM and MUSIC methods are both sensitive to measurement noise, 40 dB of noise can depreciate the resulting images.

5.1.4 Topological sensitivity

The concept of topological sensitivity firstly appeared in the context of topological optimization of mechanical structure (Eschenauer et al., 1994). The aim is to quantify the perturbation of an objective function with respect to a small object $\Omega_\varepsilon(a)$ at location a associated with a characteristic radius ε. The object $\Omega_\varepsilon(a)$ has Neumann or transmission conditions on the boundary $\partial\Omega_\varepsilon(a)$, and it is the only perturbation to a known reference background.

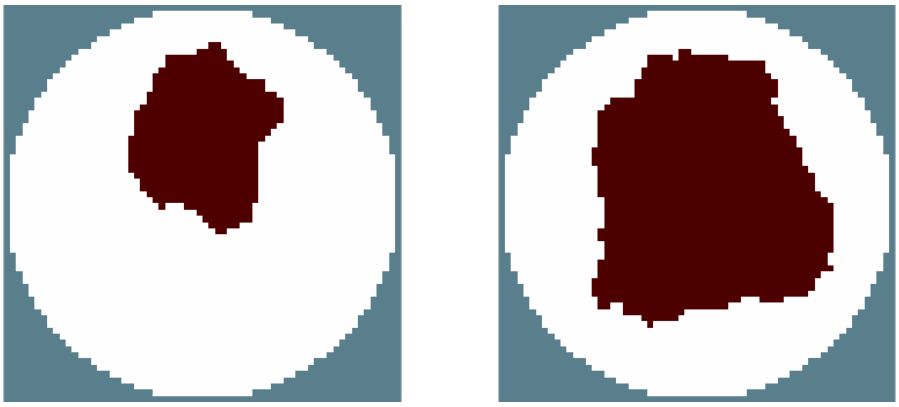

(a) One object case, FM.

(b) Three objects case, FM.

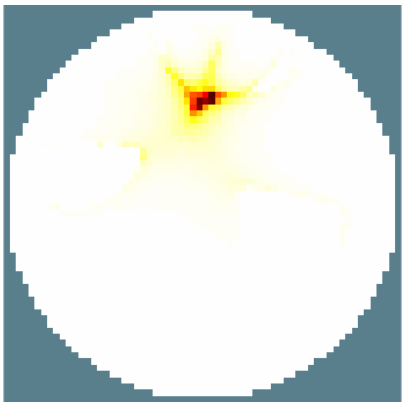

(c) One object case, MUSIC.

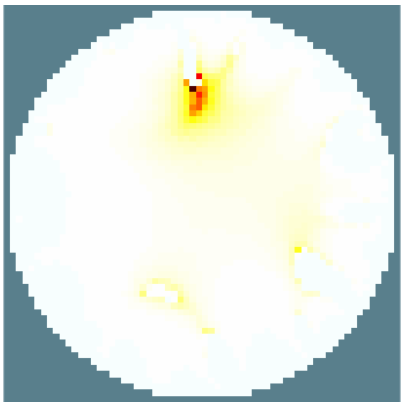

(d) Three objects case, MUSIC.

FIGURE 5.7: Reconstructions from the FM and MUSIC methods with noisy data for one and three objects cases.

The shape and topology is optimized by minimizing the objective function $J(\varepsilon;a)$. The topological derivative $\mathscr{J}_2(a)$ appears in the $o(\varepsilon^2)$ expansion of the objective function:

$$J(\varepsilon;a) = J(0) + \varepsilon^2 \mathscr{J}_2(a) + o(\varepsilon^2). \tag{5.33}$$

In the researches of Guzina and Bonnet (2006) and Dominguez and Gibiat (2010), the topological derivative is used to locate complex defects in a structure by ultrasonic technique, it is named as 'topological energy' in their paper. Two ultrasonic fields are computed to obtain the topological energy efficiently, namely the forward field and the adjoint field. The forward filed plays as a 'photographic developer', while the adjoint field carries the information of the defects. The topological energy is the product of the gradients of the forward and adjoint fields, it gives the shape and location of the defects.

The objective function $J(\boldsymbol{\sigma})$ for EIT problem is commonly defined as:

$$J(\boldsymbol{\sigma}) = \int_{\partial\Omega} \|\boldsymbol{U}(\boldsymbol{\sigma}) - \boldsymbol{V}\|^2, \tag{5.34}$$

its topological derivative is given by:

$$\mathscr{J}_2(\boldsymbol{\sigma}_{\varepsilon;a}) = \lim_{\varepsilon\to 0} \frac{J(\boldsymbol{\sigma}_{\varepsilon;a}) - J(\boldsymbol{\sigma}_0)}{\varepsilon}, \tag{5.35}$$

with $\boldsymbol{\sigma}_{\varepsilon;a}$ and $\boldsymbol{\sigma}_0$ the conductivity profile with and without the object $\Omega_\varepsilon(a)$. $J(\boldsymbol{\sigma})$ is minimized through searching for $\mathscr{J}_2(\boldsymbol{\sigma}_{\varepsilon;a}) < 0$, *i.e.* in a gradient descend approach.

The adjoint method is also applicable to EIT to compute the topological derivative $\mathscr{J}_2(\boldsymbol{\sigma}_{\varepsilon;a})$. Considering an EIT system with four electrodes and unit disc domain, three cases are simulated to obtain the topological derivative, as shown in Figure 5.8. The simulation model has two electrodes for current excitations, and the other two for absolute voltage measurements, the background has a uniform conductivity, while the object has a nearly zero conductivity.

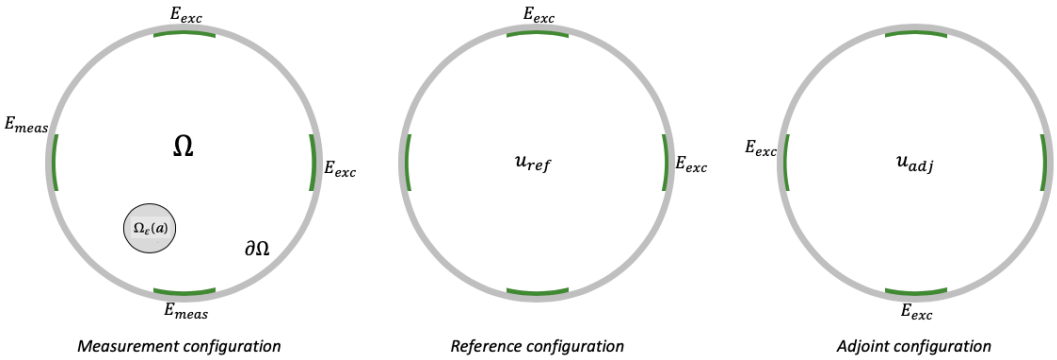

FIGURE 5.8: Schematic of measurment, reference and adjoint configurations simulated, E_{exc} represents the excitation electrode.

The reference configuration has a homogeneous domain, current excitations are exerted on two adjacent electrodes E_{exc}, voltages are measured on the others, giving the boundary measurements $\boldsymbol{V}_{ref}$ and the potential field u_0. The measurement configuration has one object inside Ω, the same excitation and measurement patterns are applied as in the reference configuration, giving the boundary measurements $\boldsymbol{V}_{img}$. Finally, the adjoint configuration uses the homogeneous medium as in the reference, while the current sources are exerted on the measurement electrodes in the former cases, the amplitudes are taken as $(\boldsymbol{V}_{ref} - \boldsymbol{V}_{img})$, giving the associated potential field u_{adj}, *i.e.*

$$\begin{aligned} \nabla \cdot (\boldsymbol{\sigma}_0 \nabla u_{adj}) &= 0, && \text{in } \Omega, \\ \boldsymbol{\sigma}_0 \nabla u_{adj} \cdot \boldsymbol{n} &= \boldsymbol{V}_{ref} - \boldsymbol{V}_{meas}, && \text{on excitation electrodes.} \end{aligned} \tag{5.36}$$

The topological derivative $\mathscr{J}_2(\boldsymbol{\sigma}_{\varepsilon;a})$ is computed by:

$$\mathscr{J}_2(\boldsymbol{\sigma}_{\varepsilon;a}) = \nabla u_0 \cdot \nabla u_{adj}, \qquad \text{in } \Omega. \tag{5.37}$$

A simple case with a single object of radius 0.1 inside the domain has been studied, the conductivity profile is shown in Figure 5.9(a). The associated reference, measurement and adjoint configurations are computed, giving the topological derivative shown in Figure 5.9(b). As we can see, the topological derivative distribution is hard to interpret, it cannot give meaningful information about the object.

Recent researches in Bonnet (2009); Bonnet and Cakoni (2019) prove mathematically that the $o(\varepsilon^2)$ expansion of the objective function is not sufficient to retrieve the shape and topology of an object in EIT problem, because it is not unique regarding $\Omega_\varepsilon(a)$. They established the $o(\varepsilon^4)$ approximation of $J(\varepsilon; a)$ as in Eqn. (5.38), to achieve the uniqueness. Numerical tests were performed to identify small objects at given locations, shapes and

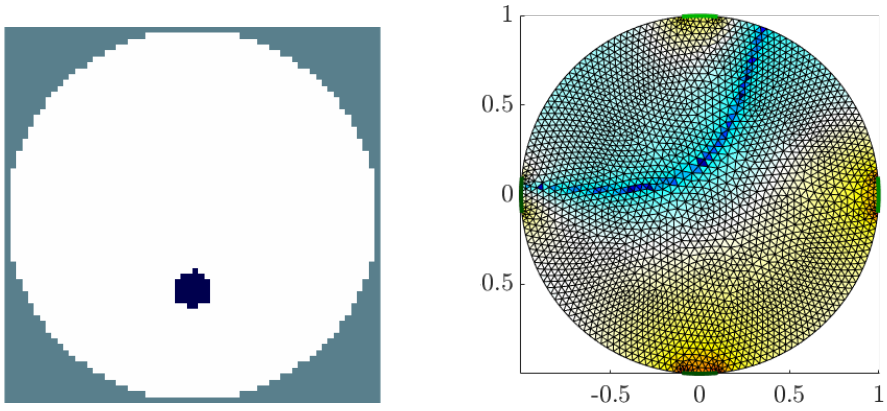

(a) Real conductivity profile, $r = 0.1$.

(b) Topological derivative.

FIGURE 5.9: The image case studied and the resulting adjoint sensitivity map using four electrodes.

conductivities in a 2D domain, showing promising results.

$$J(\varepsilon;a) = J(0) + \varepsilon^2 \mathscr{J}_2(a) + \varepsilon^3 \mathscr{J}_3(a) + \varepsilon^4 \mathscr{J}_4(a) + o(\varepsilon^4) = J(0) + J_4(\varepsilon;a) + o(\varepsilon^4). \tag{5.38}$$

Here, we argue that the topological sensitivity method is not worthwhile to apply in the current thesis work, the reasons are: 1) the $o(\varepsilon^4)$ expansion requires to compute the second order adjoint field and update the terms with the power of ε iteratively, which are computationally expensive; 2) in the case with multiple objects inside the domain, the objects have to be identified one by one iteratively, each time the effects of known objects have to be excluded from the $o(\varepsilon^4)$ approximation, which drastically increases the complexity of the method.

5.2 Imaging of two-phase flows

For dynamic two-phase flow imaging, the feasible reconstruction methods should on one hand work well with the high conductivity contrast between the two phases, on the other hand consume low computational power, allowing real-time image reconstruction. Also, the methods should be robust to measurement noise, giving reasonable reconstructions even at high noise level. Finally, they should be able to operate on an image matrix that is larger than the number of independent measurements, as the achievable spatial resolution of EIT varies with the location in the image, it is necessary to operate on a fine image representing the maximum spatial resolution expected.

Considering the various methods discussed in the former sections, the factorization and MUSIC methods are fast in computation, however, they are applicable only to trigonometric excitations, also they are either very sensitive to measurement noise or only give partial information about the flow. The regularized least-squares methods with Gauss-Newton iteration seem to meet all the requirements, proper regularization matrices $\boldsymbol{L}$ and hyperparameters α should be chosen carefully. In this section, least-squares methods with various regularization matrices $\boldsymbol{L}$ are implemented iteratively or non-iteratively, benchmark reconstructions are made using measurement data from several static experiments.

Noting that two types of reconstructions are available for EIT, *i.e.* absolute imaging and difference imaging. By their names, absolute imaging approximates the real conductivity

distribution in the imaging domain, while difference imaging reconstructs changes in the conductivity between the measurements at two time instants, using the difference data between them. Difference imaging is favorable to two-phase flow measurement, where the conductivity changes between the present instant and the reference instant with homogeneous distribution is of interest, in addition, the reference measurements are feasible in this context. It could circumvent modeling errors arise from the mismatch of geometrical configurations and the presence of contact impedance, which may degrade the image accuracy, or even lead to incorrect results. In the following sections difference imaging is applied, the conductivity difference $\Delta\boldsymbol{\sigma}$ is plotted in the reconstructed images.

5.2.1 2D or 3D reconstruction

The regularized least-squares methods are applicable to both 2D and 3D reconstructions, leading to three different reconstruction strategies, namely, 3D reconstruction, 2.5D reconstruction, and 2D reconstruction. A number of EIDORS built-in functions are used to realize these strategies, mainly including the *calc_jacobian* function to compute the Jacobian matrix $\boldsymbol{J}$ of 2D or 3D finite element model, and several functions to generate various regularization matrices $\boldsymbol{L}$, such as *prior_noser*, *prior_tikhonov* and *prior_laplace*. The associated inverse solvers *inv_solve_diff_GN_one_step* and *inv_solve_GN* are employed to carry out one-step or iterative Gauss-Newton methods separately.

3D reconstruction

It is intuitive to implement 3D image reconstruction in EIT because of its 3D sensing domain, the conductivity changes in the voxels are reconstructed. Usually the 3D reconstruction model is with the same geometry as the test section used for experiments, a coarse mesh is generated on the model to reduce the computation effort, on which the Jacobian matrix $\boldsymbol{J}$ and various regularization matrices $\boldsymbol{L}$ are calculated. The images can be reconstructed iteratively or non-iteratively. Numerical simulations have been carried to demonstrate this strategy.

To begin with, a forward model is built, as shown in Figure 5.10(a), to compute the boundary measurements of image and reference cases. The model has the same geometry parameters than in the test section of ProME-T system with ES2 electrodes, the diameter is 51 mm with a height of 270 mm, the electrode size is 5 mm in height and 4 mm in circumferential width. The simulations in Section 2.2.3 concerning the 3D effect prove that the longitude extend of the sensing domain is within a diameter for a small electrode size, therefore the 3D model takes a height of 100 mm to reduce the computation power. A tetrahedral mesh is generated with 36103 nodes for accurate computations of the boundary measurements, the mesh is refined near the electrodes. Full-scan strategy is exerted with unit excitation amplitude, the reference measurements $\boldsymbol{V}_h$ are computed with a unit conductivity in the geometry. An object with a radius of 10 mm and conductivity nearly 0 is added to the electrode plane, giving the image measurements $\boldsymbol{V}_i$. A slice is taken across the electrode plane to better display the configuration, as shown in Figure 5.10(b), the electrodes are in green, the object in blue has significantly low conductivity, its boundary is stressed in red.

The inverse model is built with a coarse mesh of 2499 nodes generated on the same geometry as of the forward model, on which the $\boldsymbol{J}$ and $\boldsymbol{L}$ are computed for 3D image reconstruction. Applying the NOSER method, the conductivity difference is given by Eqn. (5.11)

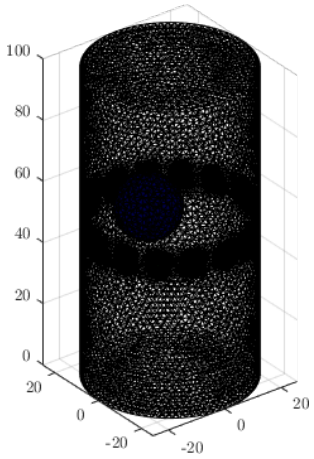

(a) 3D model for forward solution.

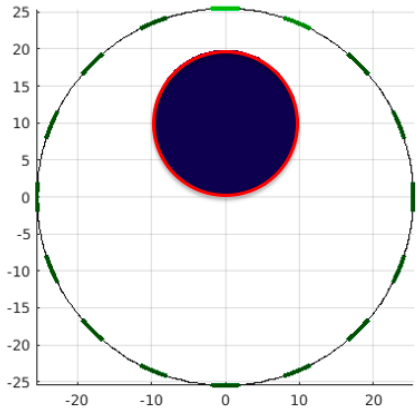

(b) A slice across the electrode plane.

FIGURE 5.10: The 3D forward model with a ball-shaped object locating at the middle of electrode plane.

with $\Delta \boldsymbol{V} = \boldsymbol{V}_i - \boldsymbol{V}_h$ and $\alpha = 0.05$, the reconstructed image is plotted in Figure 5.11(a). As we can see, the reconstructed object spreads out of the electrode plane until the ends of the test section. Taking a slice across the electrode plane gives the cross-sectional image as in Figre 5.11(b), it is shown that the position of the reconstructed object is comparable to the real case, while the area estimation has a large error due to the extremely low spatial resolution across the electrode plane in the 3D inverse model.

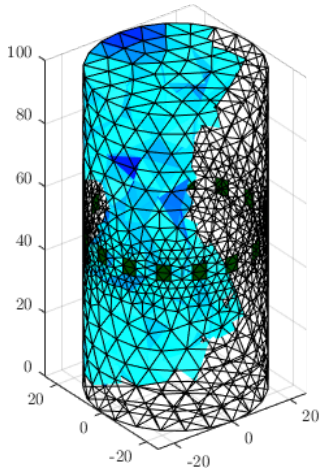

(a) Reconstructed 3D image.

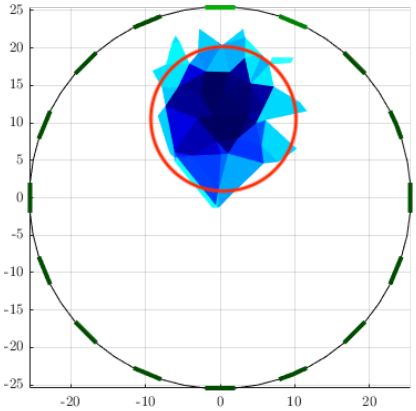

(b) A slice across the electrode plane.

FIGURE 5.11: The 3D image reconstruction for the case with a ball located at electrode plane.

The 3D image reconstruction can be implemented iteratively with $\boldsymbol{J}$ updated at each iteration step, which is computationally expensive, however, it cannot constrain the reconstructed object in z direction neither. Consequently, the 3D reconstruction seems not favorable to single plane EIT, multi-plane EIT with cross-plane excitations may improve the quality of reconstructed images.

2.5D reconstruction

Results of the 3D reconstruction show that only the slice across the electrode plane gives meaningful information about the conductivity profile (see Figre 5.11), stimulating the idea of 2.5D reconstruction. Similar to the 3D reconstruction, the 2.5D reconstruction starts from a 3D inverse model, while it projects the 3D model onto a 2D model before performing image reconstruction. A key step is to construct a fine to coarse mapping from 3D model to 2D model, assuming that the profile is invariant in z direction.

A possible way to construct this mapping is directly projecting the 3D inverse matrix onto a pseudo-2D inverse matrix, as presented in the Algorithme de Tomographie en 3D NOSER et Aplanissement (AT3NA) (Dupré, 2017). The pseudo-2D plane is subdivided into a Cartesian grid of certain size, considering one pixel in the grid, its extrusion along the z direction generates a parallelepiped. The inverse matrices of the voxels in the 3D inverse model located inside the parallelepiped contribute to the inverse matrix of this pixel, their summation defines the pseudo-2D inverse matrix. To achieve a reliable projection, the 3D inverse model should be sufficiently fine (unlike in 3D reconstruction), requiring a high computation power to obtain $\boldsymbol{J}$ and $\boldsymbol{L}$. Here, a fine mesh with 36103 nodes is used, as shown in Figure 5.12(a). The inverse matrix is computed using the NOSER method, then projected onto a coarse 2D grid of size 39×39. The reconstructed image is shown in Figure 5.12(b), it presents a highly smoothing image, the position of the reconstructed object is pushed toward the pipe boundary comparing to the real case, due to the projection of 3D sensing domain into 2D.

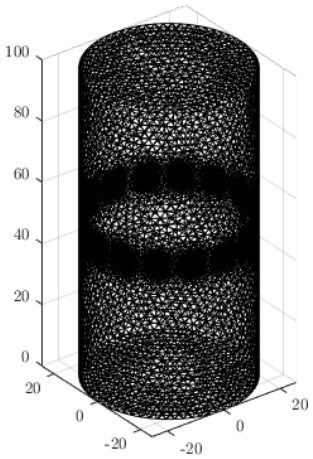

(a) 3D inverse model with fine mesh.

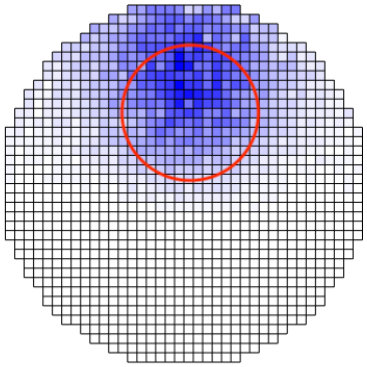

(b) 2.5D image reconstruction.

FIGURE 5.12: The 3D fine inverse model used for 2.5D reconstruction and the final reconstructed image.

Both the 3D and 2.5D reconstructions require to compute $\boldsymbol{J}$ and $\boldsymbol{L}$ based on 3D models with large number of meshing elements, especially the 2.5D reconstruction requires a fine 3D mesh, making it difficult to be implemented iteratively. Typically, they are applied in one-step Gauss-Newton methods with Tikhonov type regularizations. The advantage is that the inverse matrix can be computed and saved in prior, enabling real-time image reconstruction.

2D reconstruction

Unlike the 3D and 2.5D reconstructions, the 2D reconstruction operates on a 2D inverse model, the difference data from 3D simulations or experiments are used directly for reconstructions: the 3D effect of the sensitivity field is not considered. Benefiting from the low number of meshing elements, 2D image reconstruction can be performed iteratively at acceptable computational cost. A triangle mesh with 719 meshing nodes is used in 2D inverse model, as shown in Figure 5.13, the mesh is refined near the boundary (especially the electrodes) to support the high sensitivity nearby.

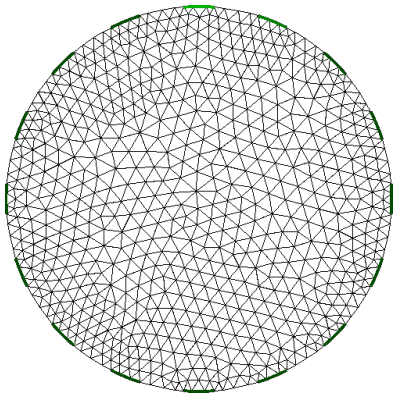

FIGURE 5.13: 2D inverse model with coarse mesh used for image reconstruction.

The reconstructed images associated with $\boldsymbol{V}_h$ and $\boldsymbol{V}_i$ are shown in Figure 5.14, applying iterative methods with Tikhonov and TV regularizations, respectively. The maximum iteration step is set to 10 for both regularizations. In the figures, the real object is represented by the red circle, it seems that the center of the reconstructed object is pushed toward the boundary in both methods. Additionally, Tikhonov regularization gives smoothed reconstruction, while TV regularization gives sharp contrast and an over constrained area estimation.

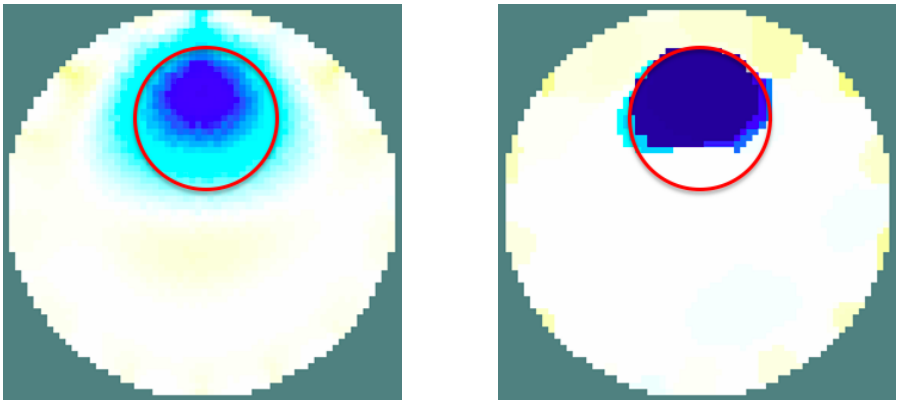

(a) Iterative Tikhonov method. (b) Iterative TV method.

FIGURE 5.14: 2D reconstructions using iterative Tikhonov and TV regularized methods and 3D measurement data.

For comparison, the 2D reconstructions using the same inverse model, but 2D boundary measurements have been carried out. The 2D boundary measurements are computed

using the 2D forward model same as in Section 3.2.2. The object has the same position and radius as in Figure 5.10(b). The final 2D reconstructions are shown in Figure 5.15 using iterative methods with Tikhonov and TV regularizations, respectively. Comparing to the results in Figure 5.14, it is found that 2D reconstructions with 2D measurement data give more accurate estimations of the position and area of the reconstructed object.

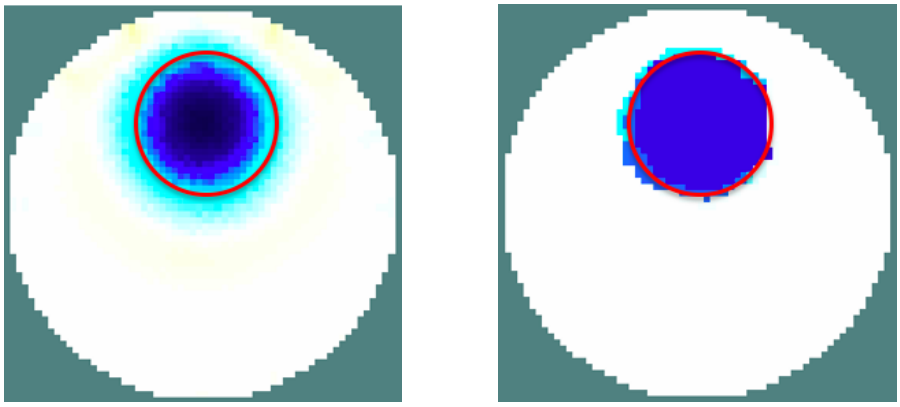

(a) Iterative Tikhonov method. (b) Iterative TV method.

FIGURE 5.15: 2D reconstructions using iterative Tikhonov and TV regularized methods and 2D measurement data.

As a conclusion, the 3D reconstruction seems not suitable considering the single electrode plane used in the present EIT systems. The 2.5D reconstruction gives smoothed reconstruction, while the position and area of the reconstructed object are identifiable, also it has the advantage to perform online image reconstruction by pre-computing the 2D inverse matrix. The 2D reconstruction makes it possible for iterative reconstructions with various regularizations, while it may be more sensitive to measurement noise.

GREIT reconstruction

Except for the conventional regularization methods, it is of interest to investigate the GREIT method for two-phase flow imaging. Here, the GREIT method is applied to reconstruct the two cases considered. A 3D GREIT model is established using the same geometry as in Figure 5.12(a) with 17604 meshing nodes. A small target with a diameter of $0.1D$ (D is the domain diameter) is placed randomly inside the domain, giving the associated inverse matrix and various performance metrics (see Section 5.1.2). The *best* inverse matrix $\boldsymbol{R}$ is estimated on a 2D structured mesh, through optimizing the performance metrics of n_t such targets, typically n_t is chosen between 1000 to 10000. The reconstructed image is obtained multiplying the *best* $\boldsymbol{R}$ with the measurement differences $\Delta\boldsymbol{V} = \boldsymbol{V}_i - \boldsymbol{V}_h$, as shown in Figure 5.10(a) for $n_t = 1000$ and 3000, separately. As we can see, GREIT method gives very good estimations of the position and area of the object, although smoothing effect presents. Besides, the reconstruction with $n_t = 3000$ gives a better area estimation closer to the real case.

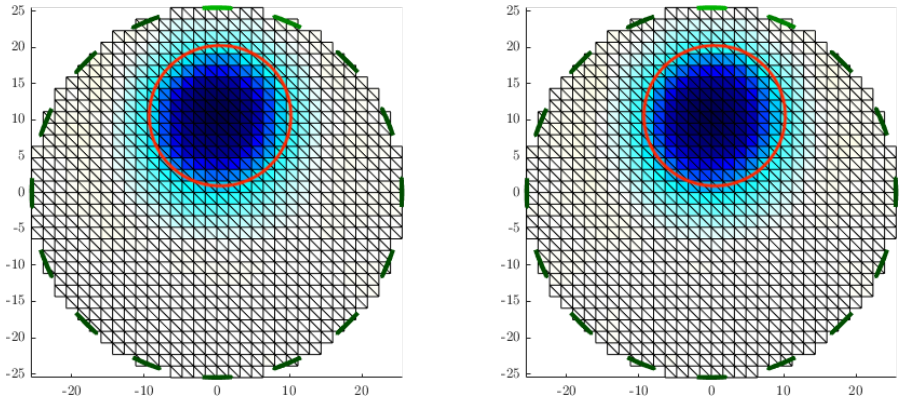

(a) $n_t = 1000$. (b) $n_t = 3000$.

FIGURE 5.16: 2D GREIT reconstructions using the *best* inverse matrix $\boldsymbol{R}$ estimated from $n_t = 1000$ and $n_t = 3000$ small targets.

5.2.2 Benchmark reconstruction of static experiments

Here, the selected image reconstruction methods, namely the 2.5D NOSER method, 2D iterative methods with Tikhonov and TV regularizations, and 2D GREIT method, are applied to the image reconstructions of several static experiments. The experimental data were acquired by the ProME-T system implementing full-scan strategy. Both the two sets of electrodes ES1 and ES2 have been used, with plastic rod(s) placed in the test section simulating the insulating bubbles. The conductivity distributions studied include: i) a single rod in the center of the test section; ii) a single rod near the boundary; iii) two rods placed oppositely.

The reconstructed images with ES1 electrodes are shown in Figure 5.17 to 5.19 for the three cases concerned, with ES2 electrodes are shown in Figure 5.20 and 5.21, only the first two cases are studied. In the figures the difference conductivity $\Delta\boldsymbol{\sigma}$ is plotted, the positions and radius of the rods used in the corresponding experiments are presented by the red circles.

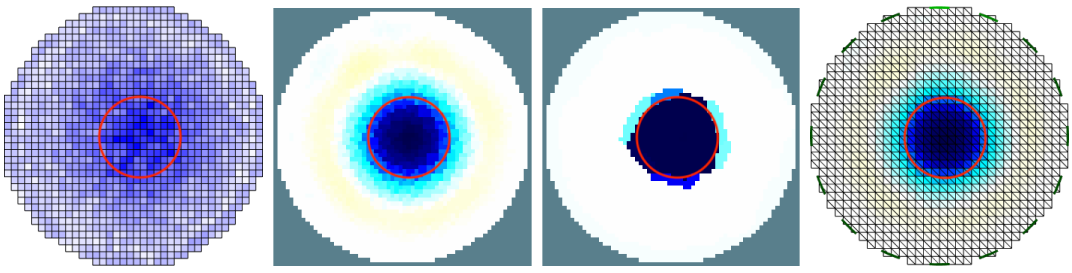

(a) 2.5D NOSER method. (b) 2D iterative Tikhonov methods. (c) 2D iterative TV methods. (d) 2D GREIT method.

FIGURE 5.17: Image reconstructions using selected methods for static experiments with ES1 electrodes, center rod case.

Generally, the image reconstructions with ES1 electrodes agree well with the real cases for all the four methods, the positions and areas are well estimated, except that the 2.5D reconstruction gives highly smoothed images. Specifically, the GREIT has a very good performance for all the three cases, while the 2D iterative reconstructions give considerable

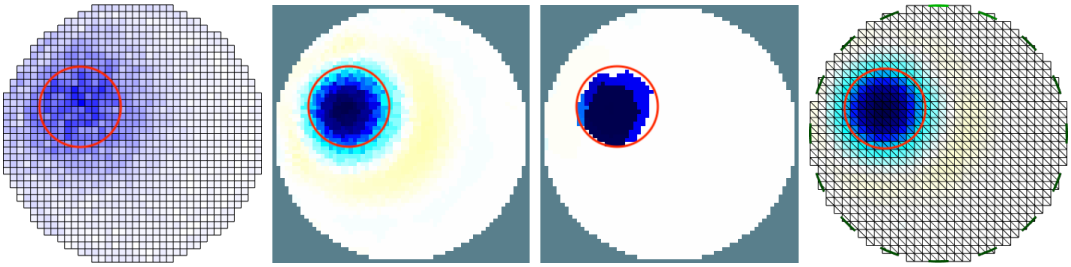

(a) 2.5D NOSER method. (b) 2D iterative Tikhonov methods. (c) 2D iterative TV methods. (d) 2D GREIT method.

FIGURE 5.18: Image reconstructions using selected methods for static experiments with ES1 electrodes, boundary rod case.

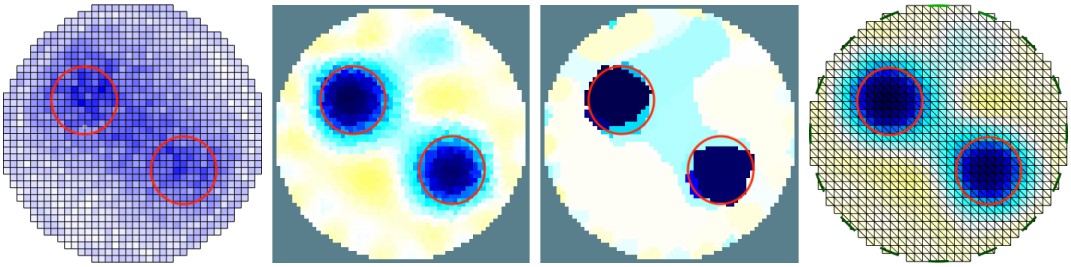

(a) 2.5D NOSER method. (b) 2D iterative Tikhonov methods. (c) 2D iterative TV methods. (d) 2D GREIT method.

FIGURE 5.19: Image reconstructions using selected methods for static experiments with ES1 electrodes, two rods case.

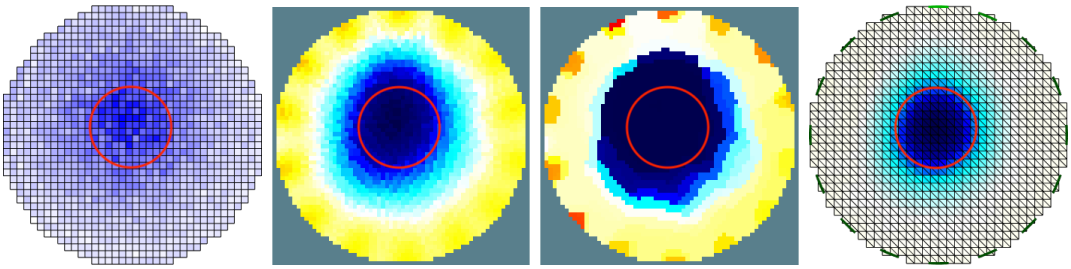

(a) 2.5D NOSER method. (b) 2D iterative Tikhonov methods. (c) 2D iterative TV methods. (d) 2D GREIT method.

FIGURE 5.20: Image reconstructions using selected methods for static experiments with ES2 electrodes, center rod case.

artifacts for the two rods case. As to the ES2 electrodes, the 2.5D and GREIT methods seem promising, while the 2D iterative methods give large errors in both position and area estimations. Possible reasons include: i) the high noise level associated with the ES2 electrodes due to the low measurement amplitude; ii) the pseudo-2D experimental configurations with long rods inserted in the test section favor the long electrodes in ES1.

5.3 Quantitive comparisons of various excitation strategies

In this section, we focus specifically on the role of the excitation strategy itself on the reconstructed images. The images obtained for the excitation strategies considered are

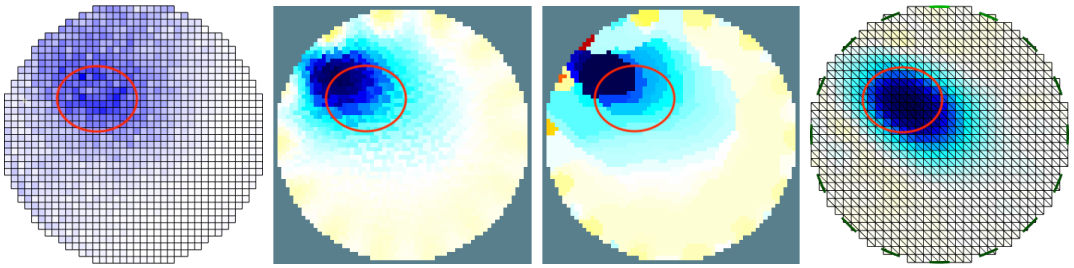

(a) 2.5D NOSER method. (b) 2D iterative Tikhonov methods. (c) 2D iterative TV methods. (d) 2D GREIT method.

FIGURE 5.21: Image reconstructions using selected methods for static experiments with ES2 electrodes, boundary rod case.

compared numerically for different reference conductivity profiles. Different criteria are proposed for quantitive comparisons, including the global error in the identification of the conductivity field and geometrical errors in the reconstruction of the sought object(s) (area and position). Moreover, two types of regularizations are applied in the reconstruction process, namely the Tikhonov regularization and the TV regularization. A set of tomographic images are compared, corresponding to static experiments carried out with still water and plastic rod(s) as the object(s) to be reconstructed.

The two reconstruction methods considered here are: (i) the NOSER method, which constrains the image amplitude and for which regularization is performed through penalization by the diagonal elements of the Jacobian matrix $\boldsymbol{J}$; (ii) an iterative method with TV regularization, which tends to preserve discontinuities in the reconstructed conductivity distribution thus leading to reconstructions with sharp contrasts (Borsic et al., 2009). The GREIT method is not used in the current section since we consider the effects of the excitation strategy itself on the reconstructions, so that it is more reasonable to employ conventional reconstruction methods.

For various excitation strategies, a value of α is decided for each reconstruction method through the L-curve method in a preliminary analysis with a reference object, then used in corresponding image reconstructions. In regularization methods, we have the fidelity term and the penalty term, the L-curve method plots the values of the penalty term against that of the fidelity term for a series of α values. In current research, an object with a radius of 0.05 and a nearly zero conductivity located at the halfway along the radius of the unit disc domain is used to obtain the optimal α. The L-curves for full-scan strategy with NOSER regularization is plotted in Figure 5.22, 40 values of α ranging from 10^{-6} to 0.5 are applied. As we can see, we have the 'L' shape in which the optimal α is located at the point of maximum curvature, which corresponds to $\alpha \approx 0.1$ in this case.

5.3.1 From synthetic data

Five different objective conductivity distributions $\boldsymbol{\sigma}_{\text{true}}$ are considered in a finite element setting. The background medium is a disk with unit diameter endowed with conductivity of 1.0, which contains one or two low conductivity *objects* with conductivity 0.1. These objects are circular, with radius r and distance d to the origin, and the case defining values are reported in Table 5.1. For such configurations, both the forward and inverse problems are solved using EIDORS, with the two reconstruction methods described previously.

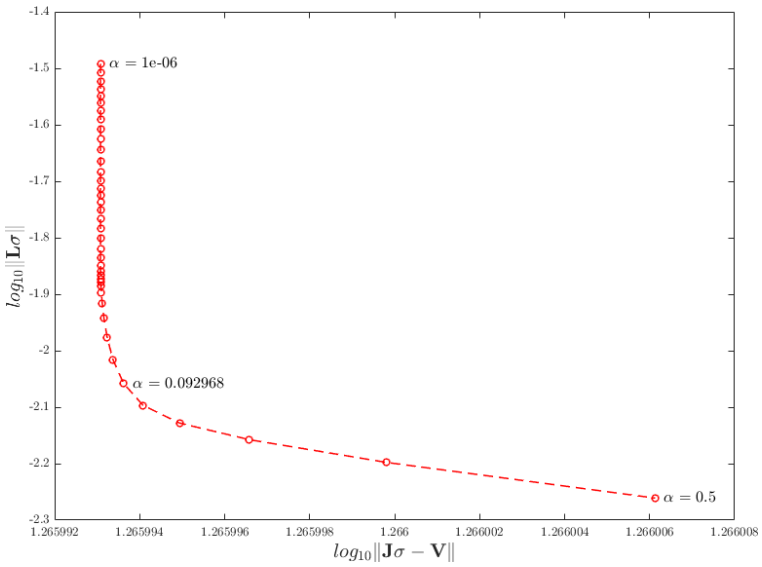

FIGURE 5.22: The L-curve for full-scan strategy with NOSER method. The point at maximum curvature corresponds to the optimal hyperparameter.

TABLE 5.1: Geometric parameters defining the cases considered with the circular object(s) to be reconstructed.

Case	1	2	3	4	5
r	0.2	0.7	0.2	[0.25 0.15]	[0.25 0.15]
d	0	0	0.7	[0 0.7]	[0.5 0.7]

Reconstructed images

The obtained images, *i.e.* the reconstructed conductivity contrasts $\Delta\boldsymbol{\sigma}_{\text{id}} = (\boldsymbol{\sigma}_{\text{id}} - 1)$, for the various excitation strategies considered are shown in Table 5.2 for both the NOSER method and TV regularization. In each case, the object(s) are correctly identified qualitatively, but their sizes is not systematically constrained quantitatively, see the cases 1, 2 and 4. In terms of excitation strategy, the full-scan and trigonometric strategies seem to constrain the object(s) size(s) more than the others, but they may lead to artifacts in the reconstructions, see the cases 4 and 5.

The profiles of the reconstructed conductivity distributions are extracted along one diameter and plotted in the Figures 5.23 and 5.24 for the cases 1 and 4 respectively. The true objects to be reconstructed are indicated by the grey regions. These results highlight that the full-scan and trigonometric strategies lead systematically to images with higher conductivity contrasts compared to the others approaches. For Case 1, the opposite strategy leads to the least accurate reconstructions, in terms of object size and conductivity contrast, which agrees with the earlier statement that its resolution is limited by its relatively low number of independent measurements. It gives also unsatisfactory reconstructions in Case 4, with the concentric object being smooth out in the obtained image, thus making it difficult to discriminate the two objects. In comparison, the full-scan and trigonometric strategies give better reconstructions in Case 1, in terms of conductivity contrast and object size, as well as in Case 4, with the two objects being clearly distinguished.

TABLE 5.2: Reconstructions $\Delta\boldsymbol{\sigma}^{h}_{\mathrm{id}}$ of the conductivity contrast from synthetic measurements and using the NOSER method and TV regularization.

Methods	**NOSER one step**				**TV regularization**			
Strategies	Adjacent	Opposite	Full-scan	Trigonometric	Adjacent	Opposite	Full-scan	Trigonometric
Case 1	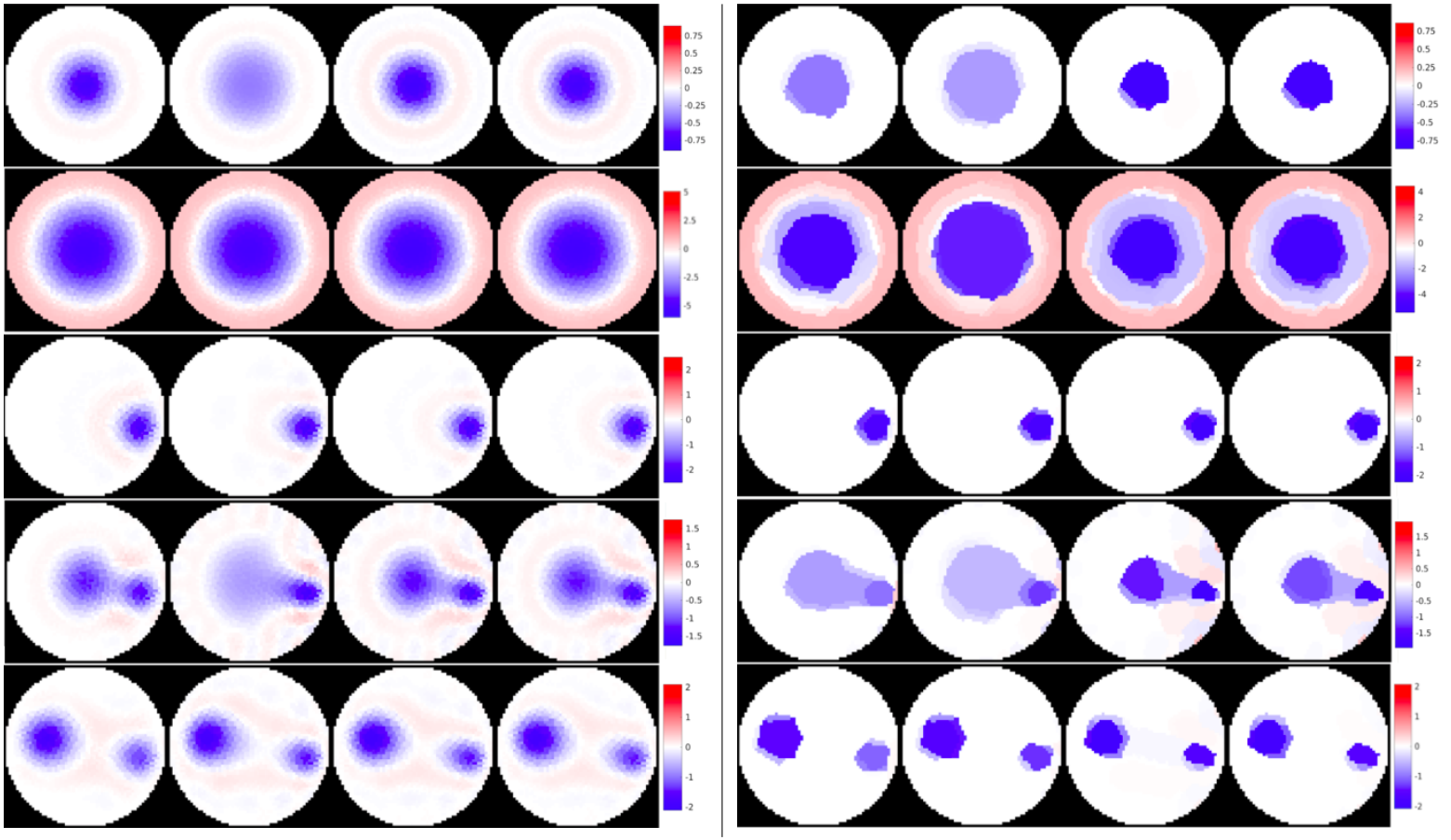							
Case 2								
Case 3								
Case 4								
Case 5								

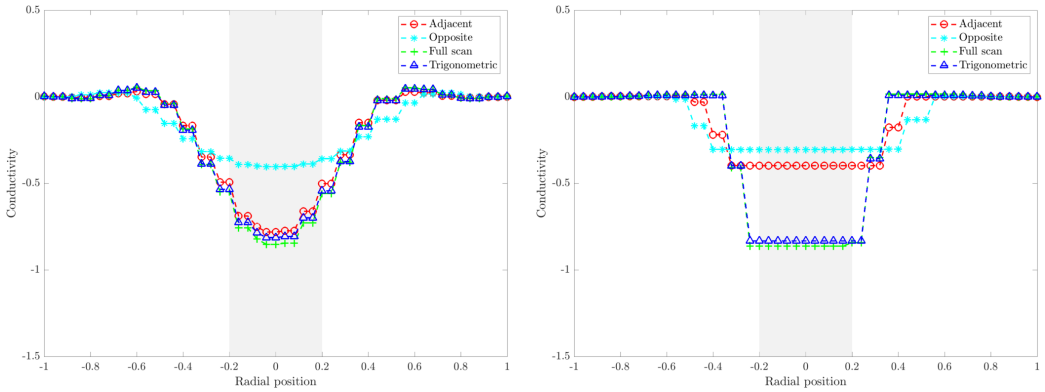

(a) NOSER method. (b) TV regularization.

FIGURE 5.23: [Case 1] Profiles of the reconstructed conductivity contrasts $\Delta\boldsymbol{\sigma}^h_{\text{id}}$ along one diameter for the different excitation strategies and reconstruction methods considered.

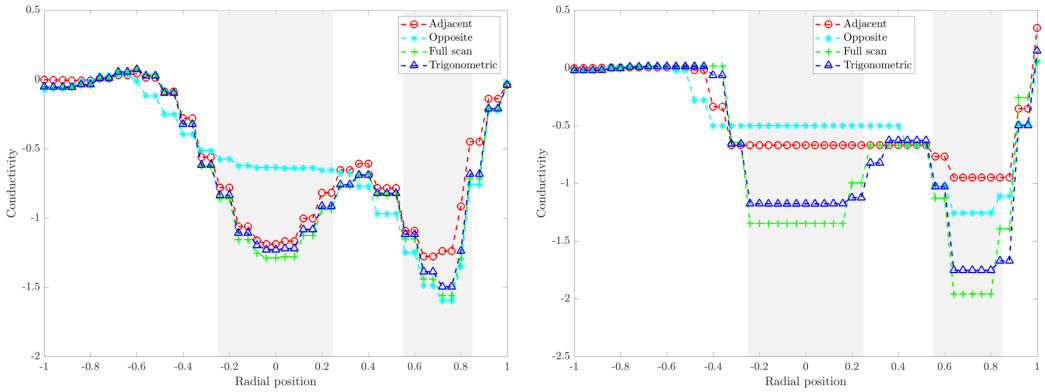

(a) NOSER method. (b) TV regularization.

FIGURE 5.24: [Case 4] Profiles of the reconstructed conductivity contrasts $\Delta\boldsymbol{\sigma}^h_{\text{id}}$ along one diameter for the different excitation strategies and reconstruction methods considered.

Quantitative indicators

This section focuses on a quantitative evaluation of the quality of the reconstructed images of Section 5.3.1. To do so, three criteria are introduced and evaluated on the obtained images.

Global identification error. An error indicator ϵ_{id} is defined as the overall relative reconstruction error on the conductivity field. In the discrete setting considered, it is defined as:

$$\epsilon_{\text{id}} = \frac{1}{A}\sum_{n_e=1}^{N_{\text{el}}} \frac{|\boldsymbol{\sigma}_{\text{id}}(n_e) - \boldsymbol{\sigma}_{\text{true}}(n_e)|}{\boldsymbol{\sigma}_{\text{true}}(n_e)} \boldsymbol{A}_{\text{el}}(n_e), \qquad \text{with} \qquad A = \sum_{n_e=1}^{N_{\text{el}}} \boldsymbol{A}_{\text{el}}(n_e), \tag{5.39}$$

where the summation is performed over elements, whose total number is N_{el} and given their individual area $\boldsymbol{A}_{\text{el}}(n_e)$. The indicator ϵ_{id} is computed for all of the reconstructed images of Table 5.2. For each case and each reconstruction method, the values ϵ_{id} are normalized by the largest error among the four excitation strategies and their logarithm

is then plotted in Figure 5.25. In such a figure, low values indicate good relative performances.

The opposite strategy is almost systematically associated with the largest identification errors (with the normalized value 1 giving a zero logarithmic value). The adjacent method performs quite well on average while the full-scan and trigonometric strategies lead to comparable but lightly less accurate reconstructions overall. Yet, it should be noted that a low value ϵ_{id} does not necessarily implies that the object(s) are correctly identified geometrically, see *e.g.* the reconstructions of Figure 5.24(b). Therefore, one considers next two additional indicators of the geometrical errors on the reconstructed objects.

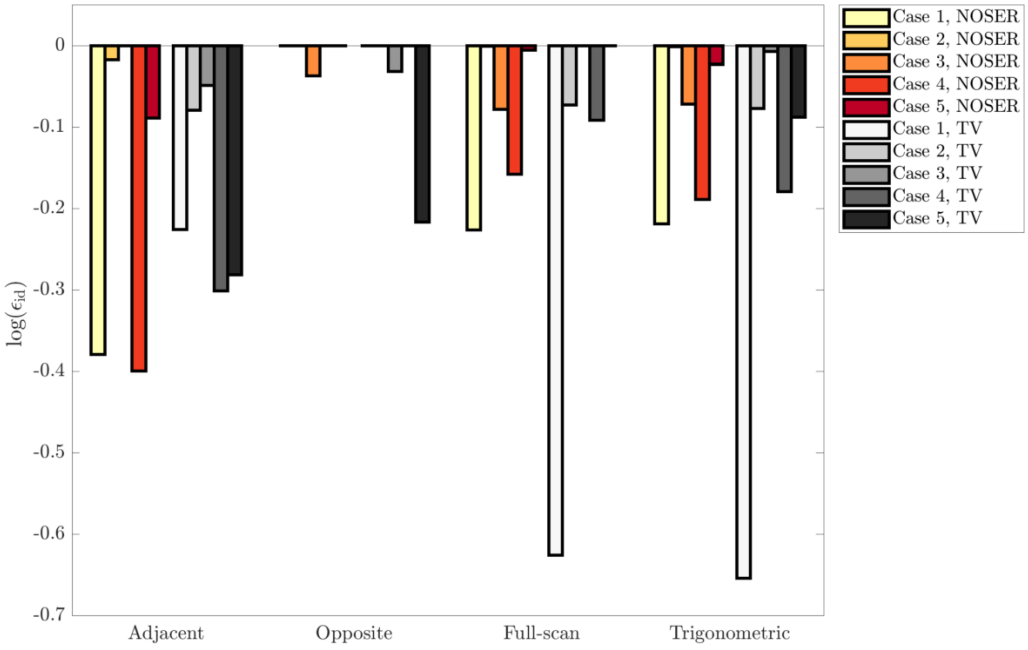

FIGURE 5.25: Logarithm of the global identification errors ϵ_{id}, normalized by the largest error among the four excitation strategies for each case and each reconstruction method. The value 0 is associated with the lowest-performing strategy and low values indicate relatively better performances.

Geometrical area error. In EIT, the boundaries of highly contrasted objects are notoriously smooth out in reconstructed images. While total variation regularization can remedy to that, in certain applications, such as two-phase flow imaging, the phase fraction is a critical parameter to estimate. In such situations, the reconstructed conductivity $\boldsymbol{\sigma}_{\text{id}}$ can be further segmented into $\tilde{\boldsymbol{\sigma}}_{\text{id}}$ as:

$$\tilde{\boldsymbol{\sigma}}_{\text{id}} = \begin{cases} -1 & \text{if } \Delta\boldsymbol{\sigma}_{\text{id}} \leq \dfrac{1}{4}\min \Delta\boldsymbol{\sigma}_{\text{id}} \\ 0 & \text{otherwise,} \end{cases} \tag{5.40}$$

where $1/4$ is actually a user-chosen value. Doing so, a geometrical area error ϵ_{A} is defined as:

$$\epsilon_{\text{A}} = \frac{|A_{\text{id}} - A_{\text{true}}|}{A_{\text{true}}}, \tag{5.41}$$

where A_{id} and A_{true} are respectively the area of the object(s), *i.e.* the region(s) of lowest conductivity, in the segmented reconstruction and in the true image, respectively. The error indicator ϵ_{A} is computed for all of the reconstructed images of Table 5.2. As done for

the global identification error, normalization by the largest error among the four excitation strategies is employed for each case and each reconstruction method. Logarithmic values are then plotted in Figure 5.26.

According to this indicator, both the adjacent and opposite strategies perform poorly, on average, in identifying the phase fraction in the cases considered. In contrast, the performances of the full-scan and trigonometric strategies are relatively comparable to each other and significantly better than the former ones. This sheds a new light on the results of Figure 5.25, as a low global identification error value is not necessarily associated with an inaccurate geometric reconstruction of the targeted object(s).

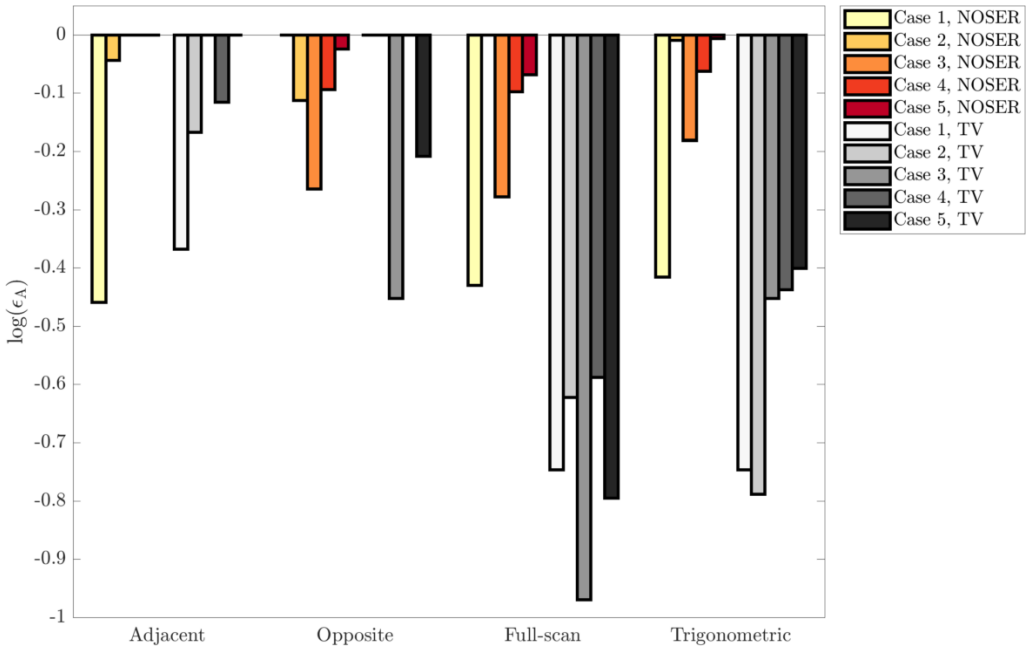

FIGURE 5.26: Logarithm of the geometrical area errors ϵ_A, normalized by the largest error among the four excitation strategies for each case and each reconstruction method. The value 0 is associated with the lowest-performing strategy and low values indicate relatively better performances.

Positioning error. A third criterion is finally introduced to evaluate the accuracy of the object(s) position(s) in the reconstructed $\boldsymbol{\sigma}_{\text{id}}$ distribution. As in some cases the objects connectedness can be difficult to assess in the reconstructed images, one focuses only on the objects barycenter. Doing so, one introduces the positioning error ϵ_p as:

$$\epsilon_p = \frac{|d_{\text{id}} - d_{\text{true}}|}{D}, \tag{5.42}$$

with d_{id} and d_{true} being the distance of the objects barycenter to the origin in the reconstructed and true image, respectively, while D is the diameter of the domain. As done with the two error indicators considered previously, normalization by the largest error among the four excitation strategies is employed for each case and each reconstruction method. Logarithmic values are then computed and the results are plotted in Figure 5.27.

According to this third geometrical criterion, the adjacent strategy is associated with large systematic errors. The performances of the opposite, full-scan and trigonometric strategies are relatively comparable to each other. In some cases, the full-scan and trigonometric strategies seem to yield reconstructions that are slightly more accurate than the opposite strategy.

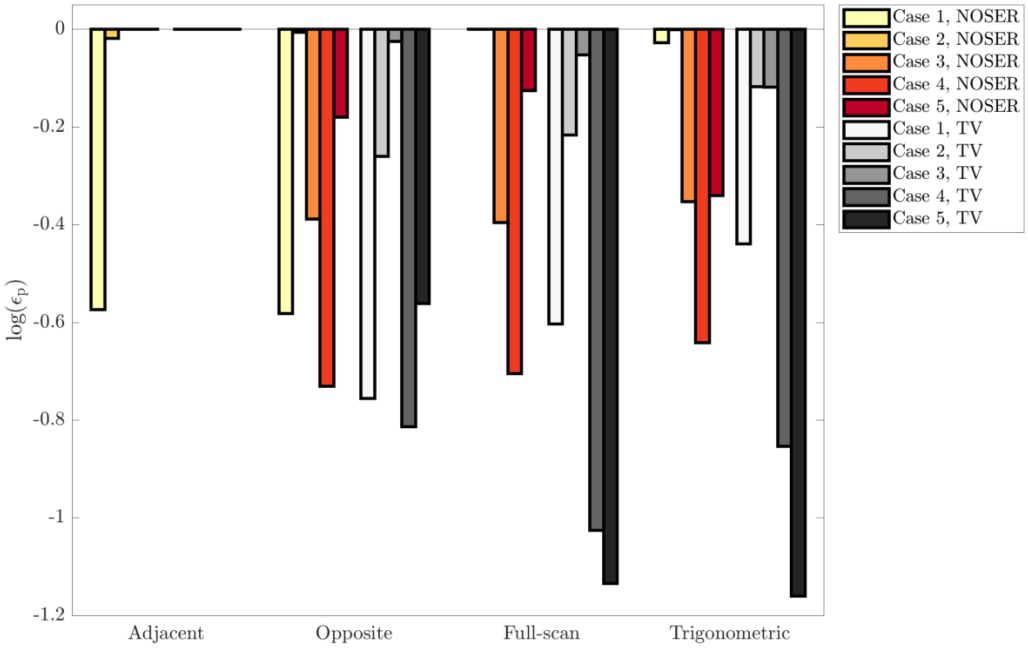

FIGURE 5.27: Logarithm of the positioning errors ϵ_p, normalized by the largest error among the four excitation strategies for each case and each reconstruction method. The value 0 is associated with the lowest-performing strategy and low values indicate relatively better performances.

5.3.2 From experimental data

In this last section, a number of image reconstructions from experimental data are provided. The experiments are static tests conducted using the ProME-T system with ES1 electrodes. The system has 16 electrodes and a $\overline{\text{RE}}$ of 50-60 dB, from which the numerical results are evaluated with the noisy experimental data. Low conductive plastic rods were placed in a test section filled with water to create the objective conductivity maps to be reconstructed. The system operates using the full-scan excitation strategy, which allows us to extract the measurement data for the adjacent and opposite strategies. Note that the implementation of the trigonometric strategy is currently beyond the technical capabilities of this system as it would require an upgrade with additional acquisition cards. Therefore, the latter strategy is not considered in this section, but the reader can refer to, *e.g.* Cook et al. (1994, Figure 11) and Newell et al. (1993, Figure 5.3), for typical reconstructed images from experimental data using the trigonometric strategy for configurations that are comparable to these considered here.

In the experimental setting, the test section has height of 270 mm and diameter of 51 mm, the static experiments can therefore be considered as pseudo-2D, which allows us to use the same reconstruction methods as the Section 5.3.1. The reconstructed images are provided in Table 5.3 for experimental configurations that correspond to the cases 1, 3 and 5

of Section 5.3.1. In combination with the quantitative results of Section 5.3.1, the image reconstructions from experimental data tend to confirm qualitatively the preeminence of the full-scan strategy over the two other modes.

To conclude, the adjacent, opposite, full-scan and trigonometric excitation strategies for EIT have been compared in a number of criteria, namely, complexity of a practical implementation, number of independent measurements, amplitude of the measured responses, sensitivity distribution and quality of the final reconstructed images, see Section 3.2 and 5.3. Both numerical simulations and static experiments are employed for such a comparison. All of these excitation protocols are well within the reach of standard up-to-date hardware.

Considering first the practical implementation criteria synthesized in Section 3.2.4, it appears that the choice of a particular excitation strategy has to be closely related to specific practical constraints. For example, one might favor the quick response of the system rather than its amplitude or sensitivity distribution. Moreover, it should be noted that the practical criteria considered do not necessarily predict the imaging capabilities of a given excitation strategy. Therefore, this analysis is complemented by an evaluation of the quality of reconstructed images for the different excitation strategies, both from synthetic and experimental data in Section 5.3. Five objective conductivity maps are considered and two different reconstruction methods are employed. For the studied configurations, the full-scan and trigonometric strategies lead to the best results on average, both qualitatively and quantitatively. They allow a better geometrical reconstruction of the object(s) geometry and yield images with sharper contrasts compared to the adjacent and opposite strategies.

The preeminence of the full-scan and trigonometric protocols is confirmed with respect to the quality of the reconstructed images. Yet, they are associated with larger acquisition times or a system more complex compared to the adjacent and opposite strategies. Alme and Mylvaganam (2007) reached similar conclusions for ECT through comparing several measurement protocols numerically. While these drawbacks can generally be circumvented using modern hardware and softwares implementations (*e.g.* FPGA and FDM), and sufficient computational power.

TABLE 5.3: Reconstructions of the conductivity contrast $\Delta\boldsymbol{\sigma}^h_{\text{id}}$ from experimental data and using the NOSER method or TV regularization.

Methods	**NOSER one step**			**TV regularization**		
Strategies	Adjacent	Opposite	Full-scan	Adjacent	Opposite	Full-scan
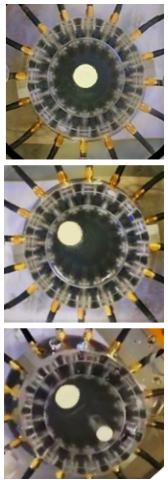	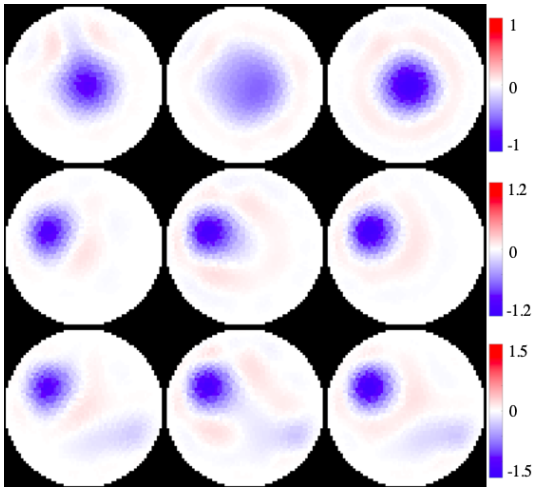			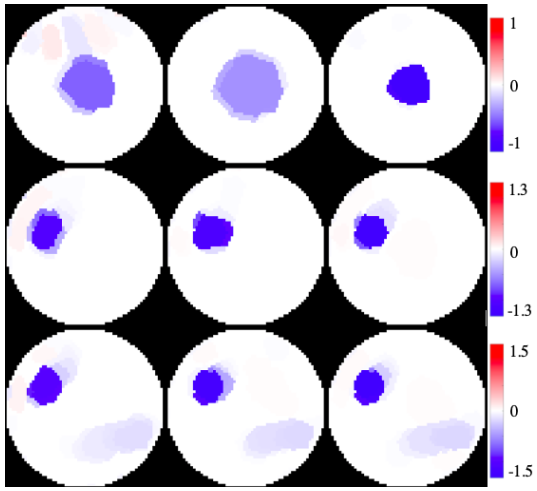		

Chapter 6

Dynamic two-phase flow experiments

Despite the numerous EIT systems used in two-phase flow measurements, the full-scan strategy gives a new insight into this research field, its advantages regarding the robustness to measurement noise and quality of reconstructed images are evidenced (Dang et al., Submitted). Additionally, taking advantage of the redundant measurements from the full-scan strategy, the eigenvalue-based approach has been proposed in the current thesis study, allowing to estimate the phase fraction from the EIT raw data without image reconstruction. In this chapter, the comprehensive EIT measurement mode consists of the EIT system exploiting full-scan strategy and the associated data post-processing approaches, is applied to measure the horizontal two-phase flows in both research and industrial loops, to perform online and offline flow imaging and extract information of flow related features, namely, the void fraction and flow regime.

Two sets of dynamic tests have been performed in different horizontal flow loops. The first one was performed in the multiphase flow loop in the processing lab of USN by Mathieu Darnajou during his visit, it took two days to run all the experimental series. The ONE-SHOT system was applied for flow measurements. A total of 80 experimental series have been conducted with various air/water mass flow rates, covering slug, plug, stratified smooth, stratified wavy and annular flows. The EIT measurement data are processed and compared with the reference measurements from other meters in the loop, the results are presented here. The second test was performed in the BENSON loop in cooperation with the PKL research group of Framatome GmbH. I've stayed there for 2 weeks to perform the experiments, it took one week to mount and calibrate the EIT system and another week for experiments under various configurations. The BENSON loop is an industrial experiment loop with metal pipelines for high temperature high pressure two-phase flows. A total of 33 experimental series have been carried out at various temperatures and void fractions. The ProME-T system with an extra acquisition card was used for dual-plane EIT measurements with the two plans working independently, its performance under complex environment is assessed. The EIT data analysis provides insights on the merits and deficiencies of the proposed measurement mode, its applicability is evaluated under laboratory and industrial environments.

6.1 Horizontal two-phase flow regimes

Different flow regimes may appear in a flow pipe depending on the governing mechanisms of gas-liquid two phase flow: gravity, gas momentum, and surface tension. It is complex to decide the flow regime by numerical simulation, the mass, momentum and energy transfer among phases are very sensitive to phase distribution. Experimentally, well-developed flow regimes can be parametrized by a limited set of parameters (*e.g.*

mass flow rate of each phase) for a given experimental setup, referring as the multiphase flow regimes. A number of experimental (Mandhane et al., 1974) and analytical (Taitel and Dukler, 1976; Taitel et al., 1980) studies have assessed the flow regimes for various flow conditions in horizontal, vertical and inclined configurations, leading to various flow regime maps. Specifically for horizontal gas-water two-phase flow, which is concerned in current thesis study, the well-developed flow regimes typically include: bubble, stratified smooth, stratified wavy, plug, slug, annular and mist flows (Chen et al., 1999; Perera et al., 2017), the typology is shown in Figure 6.1. An example of flow regime map is shown in Figure 6.2.

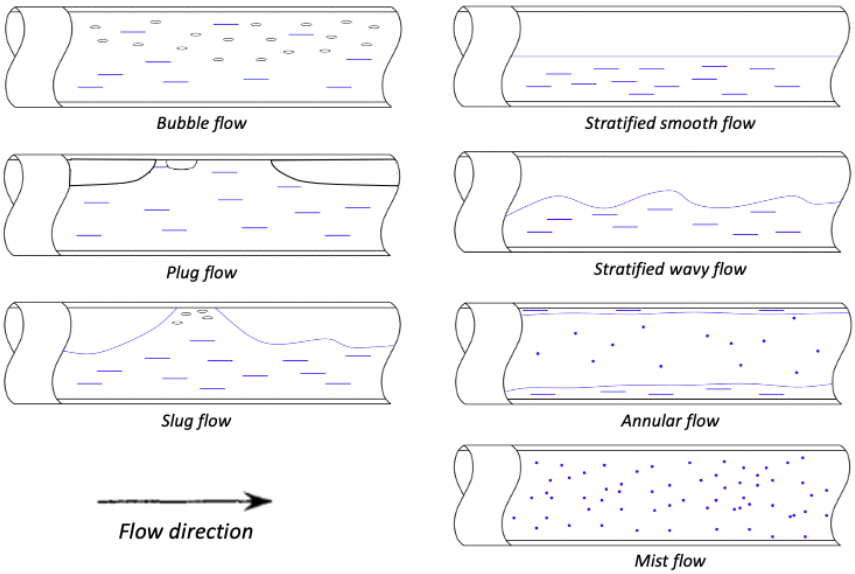

FIGURE 6.1: Sketches of various horizontal gas-water flow regimes.

The flow regimes distinguish from each other in terms of radial and/or axial distribution of liquid and gas. In bubble flow, the gas phase is distributed as discrete bubbles in continuous liquid phase, mainly gathering near the top in horizontal flow. For slug flow, most of the gas is located in the large bullet shaped bubbles on the top, they move uniformly along with the continuous liquid which bridges the pipe and contains small gas bubbles between the slugs. Plug flow is somewhat similar to slug flow, but with large bubbles existing between the plugs, instead of small gas bubbles between slugs. Stratified flow is completely separated with gas in the upper part and liquid in the lower part of the pipe, the interface can be smooth or wavy, giving stratified smooth and wavy flows, respectively. In annular flow, liquid forms a coat all around the pipe walls, with gas flowing in the middle possibly with liquid droplets inside, usually the coat is thicker at the bottom than at the top because of gravity effects. Mist flow is characterized by the continuous gas phase in the core of the pipe, with liquid drops dispersed in the gas core.

Flow regime identification can be realized using the signals from single or multiple sensors, *e.g.* radiation-based densitometers, impedance probe (Ahmed and Ismail, 2008), wire-mesh sensor (Schleicher et al., 2016) and electrical tomography sensors (Wang and Zhang, 2009; Tan et al., 2007). The signal need to be representative to the cross-sectional averaging void fraction, the time series of consecutive signals contain information about the flow regime. Conventionally, mathematical or statistical tools such as probability density function, principal component analysis and power spectral density are used to analyze the time series signal (Ahmed and Ismail, 2008; Paranjape et al., 2012). While the recent trend in flow regime identification is to use machine learning algorithms, such as

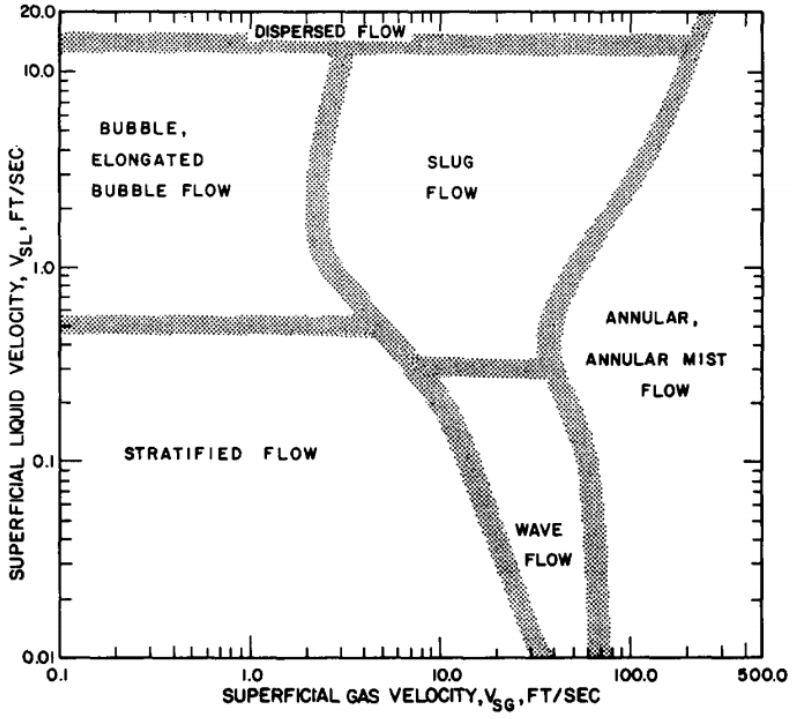

FIGURE 6.2: Flow regime map of the horizontal air-water flow in a pipe with 50 mm diameter, adapted from Mandhane et al. (1974). Hatched regions are regime boundaries by observation.

the artificial neural network (Johansen et al., 2018) and support vector machines (Wang and Zhang, 2009). The major arguments remain in generalizing the methods beyond the training data for various geometries or temperatures.

For electrical tomography techniques, the flow regime can be identified either through image reconstruction or from raw measurement data. The former strategy extracts synthetic information directly from flow imaging to understand the specific phenomena (Ru and Mylvaganam, 2014). The latter strategy analyzes the time series measurement data using simple methods widely applied in signal processing (Dupré, 2017), bypassing the complicated image reconstructions of *soft-field* electrical tomography.

6.2 Preliminary validation in LTHC

Before digging into the experiments in horizontal flow loops, it is of interest to present some preliminary results from experiments conducted in a vertical flow loop. At the beginning of my thesis work, I performed several experiments in the MERCURE-200 flow loop of LTHC using the ProME-T system with both the ES1 and ES2 electrodes, the goal was to assess the ability of the developed EIT sensor in dynamic two-phase flow imaging. Although the experimental data is not fully exploitable due to the malfunction of the air flow meter, there are still some interesting results leveraging the videos taken by a high speed camera.

The MERCURE-200 flow loop has a vertical test section made by PMMA, the diameter is 51 mm. The volume flow rate of water can be up to 15 m^3/h, of air up to 10.5 m^3/h, their flow rates are monitored and measured separately. A high speed camera was used to take the videos of dynamic flows, it has a speed up to 2000 fps with full resolution (1024×1024),

and up to 120000 fps with reduced resolution. A total of 11 experimental series were carried out at a fixed water flow rate of 0.08 m/s, while the air flow rate ranges from 0.08 m/s to 5 m/s, covering bubble and churn flows. During each experiment, the ProME-T system took 100 consecutive frames at 208 fps, while high speed videos were taken at 500 fps.

Image reconstructions have been performed using the 2.5D reconstruction with the NOSER method. The pixels on the horizontal central strip of the reconstructed images are extracted and stacked along time to form an axial tomogram for each experiment. Figure 6.3 and 6.4 shows the tomograms of two example experimental series with the ES1 and ES2 electrodes, separately. The actual bubble distributions are shown in the frames taken from the corresponding high speed videos. It is noted that the frames taken from the high speed videos are not synchronized with the EIT measurements, as the two systems observe different altitudes of the test section. Besides, the transverse cross-section taken by the EIT tomograms may not align with that of the high speed camera, so that the high speed videos are not exact references to EIT tomograms, they only indicate the topology of bubble distributions. As shown in Figure 6.3 and 6.4, the ProME-T system with both sets of electrodes give good estimations of bubble topologies. Besides, the ES1 electrodes are more sensitive to the small bubbles passing through the EIT sensor, while the ES2 electrodes measure the averaging distribution of a large sensing domain, hence less sensitive to small bubbles.

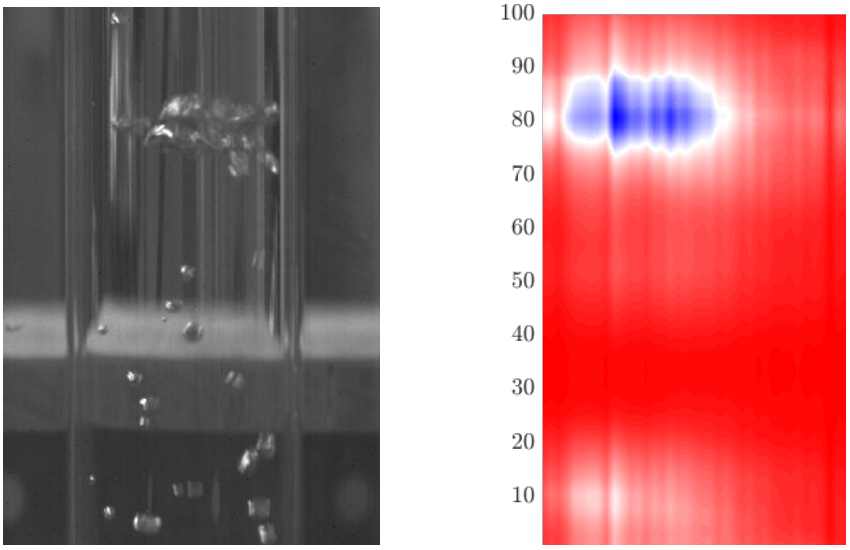

(a) High speed photo.

(b) Tomogram with ES1 electrodes.

FIGURE 6.3: The EIT tomogram with ES1 electrodes comparing to a frame taken from the high speed video.

6.3 Dynamic experiments in laboratory loop

Two-phase flow experiments involving multi-modal sensors including the EIT, ECT and Gamma-Ray Meter (GRM) have been done in the processing lab of USN supervised by Professor Saba Mylvaganam, with the help of senior engineer Fredrik Hansen and master student Aleksander Tokle Poevrud. Various flow regimes are realized monitoring the water and air flow rates, covering plug, slug, stratified smooth, stratified wavy and annular flows. I did not participate in performing the experiments because I had decided to

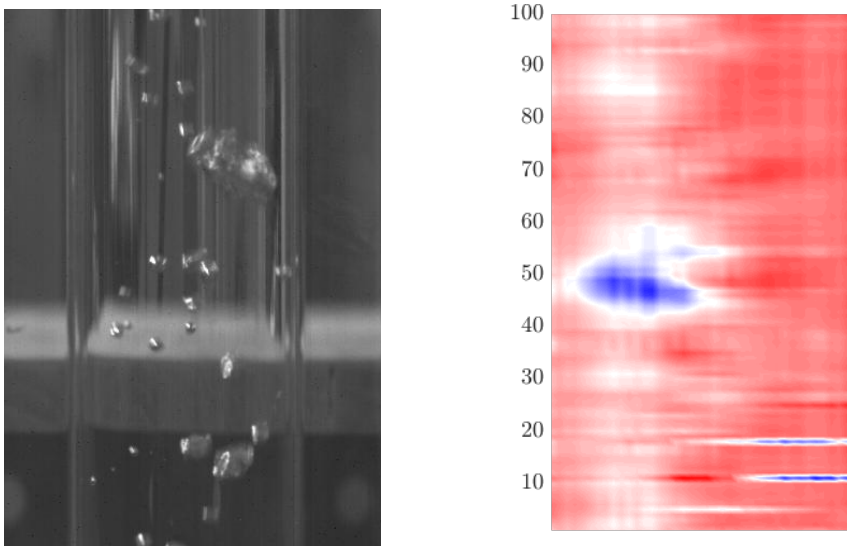

(a) High speed photo.

(b) Tomogram with ES2 electrodes.

FIGURE 6.4: The EIT tomogram with ES2 electrodes comparing to a frame taken from the high speed video.

attend the SWINTH-2019 workshop before scheduling the experiments, while I designed the test matrix and post-processed the experiment data for image reconstruction and flow features extraction.

In this section, EIT image reconstruction is performed using 2.5D reconstruction with the NOSER method, through which the transverse cross-sectional images are obtained. Then, the conductivity profiles along the longitudinal section are extracted and axially stacked along acquisition time, giving a stacked EIT tomogram for each experimental series. Then, the eigenvalue-based approach proposed in Chapter 4 is applied to identify the flow regime using the eigenvalues of the normalized impedance matrix, the correlation between the leading eigenvalue and the reference volume averaged void fractions (AVF) is analyzed, a calibration diagram is obtained for further application. Furthermore, the estimated AVF is integrated into the EIT tomogram for a better visualization of phase distribution. The experimental procedures, data processing methodology and main results are presented as follows.

6.3.1 Experiment procedures

Multiphase flow rig

The multiphase flow rig used for experiments is shown in Figure 6.5, it enables the injection of oil, water and air in a horizontal or inclined pipe at room temperature. The injection of each medium is monitored independently using the dedicated meter. The inner diameter of the pipe is 51 mm, its thickness is 2.5 mm with a length of 15 m, the mediums are mixed at the inlet of the pipe so that the flow is well developed at the observation and measurement sections. The transparent PMMA section enables to determine the flow regime by visual observation or take high speed video. The ECT/EIT sensor and GRM are installed along the flow direction at the downstream, the data from the ECT sensor is not used in the present study. The ONE-SHOT system was used for experiments.

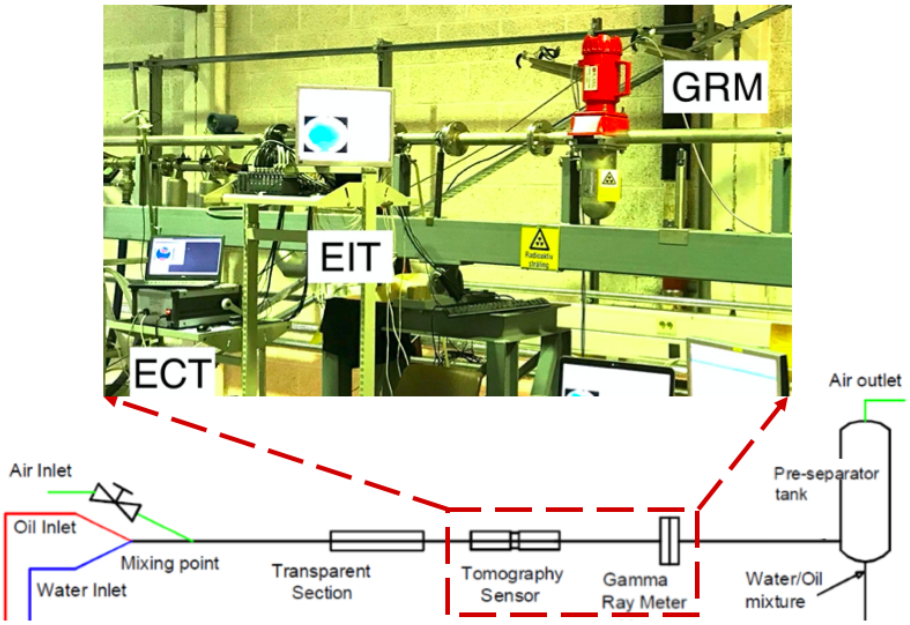

FIGURE 6.5: Horizontal multiphase flow rig of USN.

During the experiments, only the water and air phases were injected under the horizontal pipe configuration, with the mass flow rate of water ranging from 1.58 to 79.43 kg/min, of air from 0.1 to 5.0 kg/min. The conductivity of air is negligible compared to that of water.

The goal of GRM is to determine the density of a certain substance through the attenuation of the radiation beam, the mechanism is presented in Figure 6.6. The measurment error mainly comes from the non-parallel beams generated by the low energy γ-ray emitter. For air-water two-phase flow, the attenuation in the air phase is negligible, the GRM measured signal is only related to the fraction of water along the trajectory. The GRM used in the current experiments is operating with a single beam projection, yielding the equivalent density measurement in the transversal cross-section of the pipe. Careful calibration should be carried out with two measurements with the full and empty pipe, giving the minimum and maximum measured density, respectively.

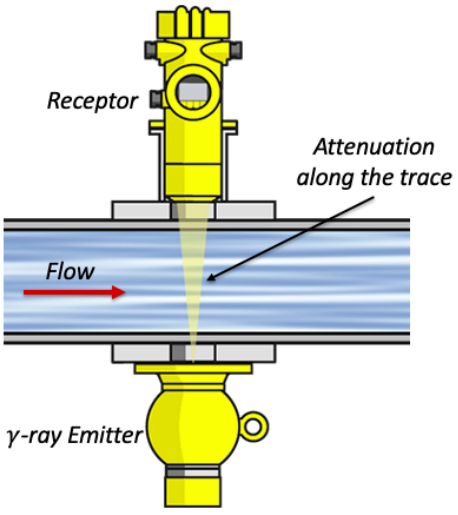

FIGURE 6.6: Schematic of a gamma ray Meter.

Given a measured density ρ_m from the GRM, the cross-sectional water phase fraction η_l, also called water-cut, can be calculated by $\eta_l = (\rho_m - \rho_g)/(\rho_w - \rho_g)$ with ρ_w and ρ_g the density of water and air, separately. In current study, the GRM provides valuable information of the real-time cross-sectional equivalent phase fraction, which is used as the reference value to the EIT measurement.

Test matrix

The flow regime map of Mandhane et al. (1974) for a horizontal pipe with 50 mm diameter is used to select the water and air flow rates. A total of 80 experimental sets are considered, consisting of approximately 2/5 of intermittent flows (plug and slug), 2/5 of stratified flows and 1/5 of annular flow. The selected flow conditions (pairs of water and air mass flow rates) are plotted in the flow regime map as in Figure 6.7, with the index and flow regime of each experiment indicated. The flow regimes were assessed by visual inspection during experiments combining with the GRM signals. Here, only the stratified smooth, stratified wavy, plug, slug and annular flows are considered because of the limitation to the input mass flow rate, their sketches are shown in Figure 6.1.

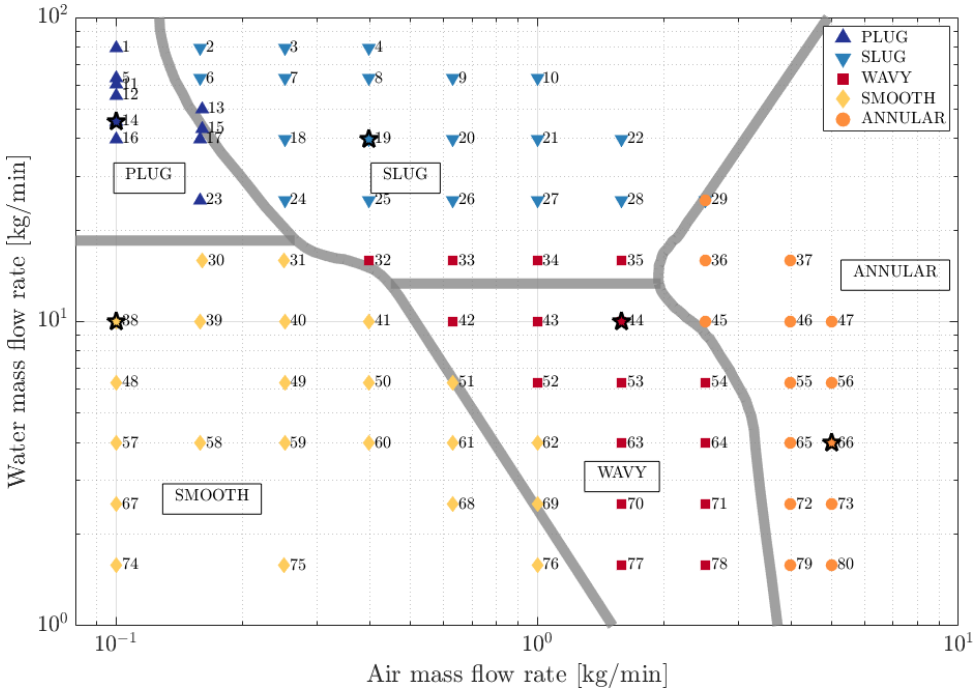

FIGURE 6.7: The test matrix composed of 80 experimental data points, the indicated flow regimes are identified from visual observation and GRM measurement.

During each experiment, EIT measurements are acquired at a rate of 100 fps over 30 seconds in order to capture the characteristics of the flows for the various phase injection conditions. The GRM operates during 60 seconds at an acquisition rate of 20 Hz, i.e. at a rate 5 times slower than the EIT measurements.

6.3.2 Eigenvalue-based approach

In this section, we expose our approach combining EIT-based image reconstructions and the eigenvalue correlation method. The proposed flow visualization procedure is as follows:

A. For the configuration considered and the EIT system employed, the correlation between the mean NIM leading eigenvalue and the AVF is investigated for different flow regimes, from which a calibration diagram is constituted.

B. For a given experiment, the temporal evolution of the NIM leading eigenvalue $\lambda^{\max}$ (i.e. $\lambda^{(16)}$ in Chapter 4) is analyzed and associated with a raw image guess, from which the flow regime is identified.

C. Cross-sectional EIT-based raw image reconstructions are stacked axially to form a time-dependent tomogram.

D. Knowing the flow regime from B, the calibration diagram of A is used to estimate the AVF, thus leading to a threshold value that is used to binarize the EIT tomogram of C.

Remark 1 *In the present study, the raw image reconstructions are computed using the NOSER method. Yet, the procedure above does not rely on it specifically and alternative image reconstruction methods can be used as well.*

Remark 2 *The threshold value determined in step D is here applied to all the images along the time sequence, i.e. the AVF is estimated only once for a given experimental sequence. Yet, the proposed approach can be applied to each cross-sectional image, i.e. at each time step, if necessary, with the knowledge of the current state of the flow regime.*

Each of the steps of the procedure above is now detailed and illustrated on the experimental data set obtained on the USN loop.

6.3.3 System calibration from NIM leading eigenvalue and AVF correlation

The Maxwell-Hewitt relation can be used to approximate the phase fraction from EIT data, see e.g. George et al. (2000). However, this relation is only applicable when the background medium is continuous and the non-conductive phase is mono-dispersed, which is not the case for the horizontal two-phase flows considered here. Up to the Authors' knowledge, there are only few methods reported on void fraction estimation in such configurations based on EIT data only. Note however that a dual-modality ECT/EIT measurement based approach has been used in Wang et al. (2017) for image segmentation. Here, the correlation between the NIM leading eigenvalue and the AVF is investigated from EIT raw data, with the reference AVF being calculated by averaging the GRM void fraction for each experimental set. This leads to a system calibration diagram applicable to subsequent (i.e. unknown) flow conditions.

Given a flow regime calibration condition, a number N_F of EIT measurement frames are acquired, each being associated with a normalized impedance matrix $\hat{\boldsymbol{Z}}_f$. A mean NIM $\hat{\boldsymbol{Z}}_{\text{mean}}$ is then computed as:

$$\hat{\boldsymbol{Z}}_{\text{mean}} = \frac{1}{N_F} \sum_{f=1}^{N_F} \hat{\boldsymbol{Z}}_f,$$

whose leading eigenvalue is denoted as $\lambda_{\text{mean}}^{\max}$. The matrix $\hat{\boldsymbol{Z}}_{\text{mean}}$ then contains information on the measured flow, which is extracted by a principal component analysis, see Dang et al. (2019a).

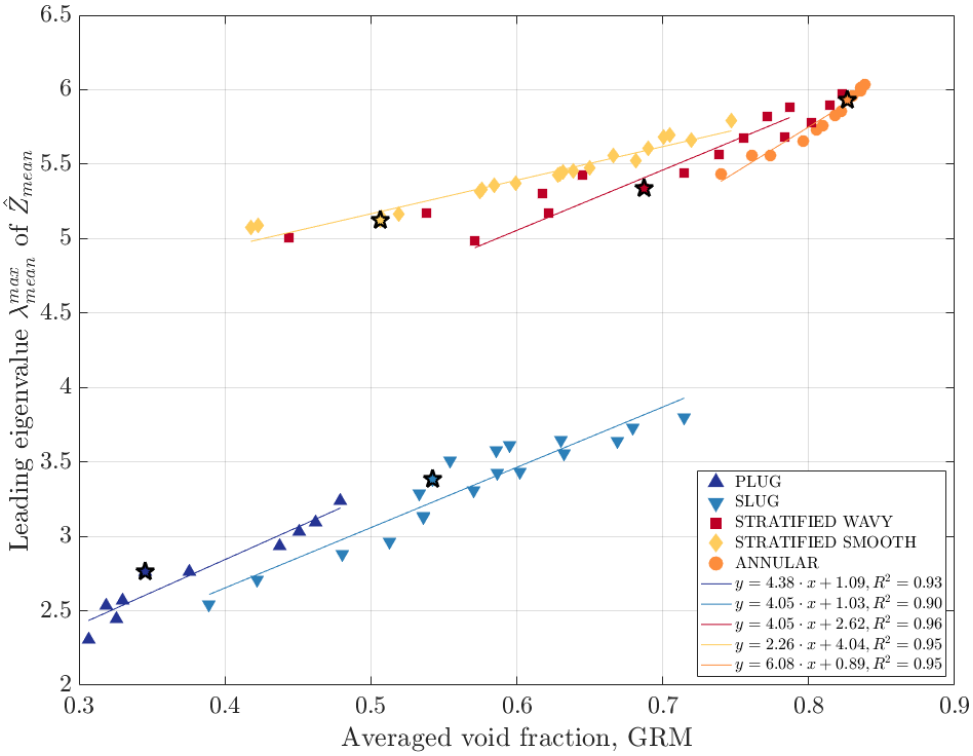

FIGURE 6.8: System calibration diagram: eigenvalue $\lambda_{\text{mean}}^{\max}$ vs. reference AVF from GRM, with indication of the flow regimes. Stars indicate the experiments selected in Fig. 6.9.

This is applied to the system investigated at USN and Figure 6.8 represents the calibration diagram thus obtained. The eigenvalue $\lambda_{\text{mean}}^{\max}$ is plotted against the reference GRM void fraction for the 80 of calibration experiments represented in Figure 6.7, along with the determined flow regimes.

Remark 3 *Here, each calibration experiment is monitored with the same number* N_F = 3000 *of EIT frames. Yet, different numbers of frames can be considered in practice from one experiment to another.*

For each flow regime a linear correlation is found between $\lambda_{\text{mean}}^{\max}$ and the AVF with a high confidence, which agrees with the conclusions of Dang et al. (2019a), which were based on numerical and experimental benchmarking. It should be noted that estimating this correlation for stratified wavy flows is more involved as the transitions between smooth, wavy and annular flows are continuous, which makes them difficult to discriminate from one another, even through visual inspection. Therefore, the experiments associated with such transition zones (see Fig. 6.7) are excluded from the assessment of the leading eigenvalue correlation.

For a given EIT system configuration, due to the normalization of the impedance matrix, the correlation between the eigenvalue $\lambda_{\text{mean}}^{\max}$ and the AVF is a robust characteristic relatively to the property of the conductive (liquid) phase. Lastly, while we only make use of the behavior of the leading eigenvalue as a simple and robust criterion in the present study, it has been underlined in Dang et al. (2019a) that alternative NIM-based metrics can be employed to investigate the phase fraction.

6.3.4 Temporal evolution of the leading eigenvalue

With the calibration diagram at hand, we investigate now a given experiment. In this second step, the leading eigenvalue $\lambda^{\max}$ of the normalized impedance matrix $\hat{\boldsymbol{Z}}_f$ is computed for each frame $f = 1, \ldots, N_F$ of the experiment considered. Figure 6.9 then shows the temporal evolution of $\lambda^{\max}$ along time (or, equivalently, frame f) for the five selected experiments identified in the figures 6.7 and 6.8, and which correspond to different flow regimes. The eigenvalue $\lambda^{\max}$ for the stratified and annular flows are plotted together to emphasize the differences in their behaviors. In the figures 6.9(a) and 6.9(b), the intermittent flows present characteristic features: $\lambda^{\max}$ varies significantly between 0 and 4, while the slug and plug flows are distinguished from one another by the value of $\lambda^{\max}$ in between the plateaus. Moreover, the plug flow is associated with more abrupt variations of $\lambda^{\max}$. This can be related to the different behaviors of the plug and slug flows, with the small plugs encountered between long plugs compared to the intensive bubbles entrained in the water bulk between the slugs (see Fig. 6.1). As to the stratified and annular flows, Figure 6.9(c) shows large and chaotic variations of $\lambda^{\max}$ for wavy flow, and similarly for the annular flow but at higher values, the smooth flow being associated with a steady level.

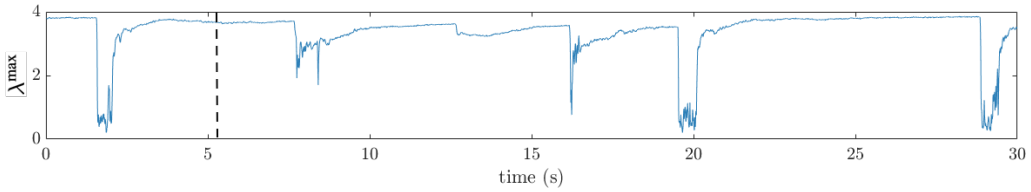

(a) Slug flow.

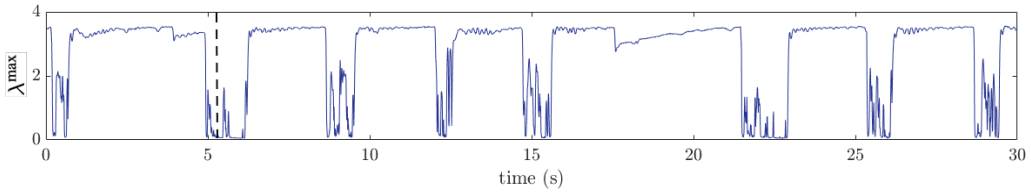

(b) Plug flow.

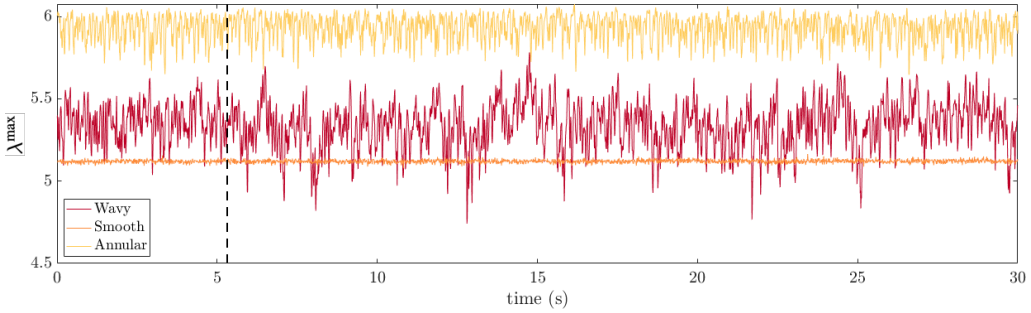

(c) Stratified and annular flows.

FIGURE 6.9: Temporal evolution of the leading eigenvalue $\lambda^{\max}$ of $\hat{\boldsymbol{Z}}_f$ along time (or frame f) for the five selected experiments identified in Fig. 6.7 and 6.8. The cross-sectional images at time $t = 5.3$ s (vertical dashed line) are shown in Fig. 6.10.

In addition, Figure 6.10 plots the raw cross-sectional image reconstructions $\Delta\boldsymbol{\sigma} = (\boldsymbol{\sigma} - \boldsymbol{\sigma}_{\text{ref}})$ obtained with the NOSER method (or "image guesses") for the experiments considered, and computed at the time $t = 5.3$ s (indicated by black dashed line in Fig. 6.9). We recall that $\boldsymbol{\sigma}_{\text{ref}}$ is chosen as the conductivity of water. Comparison of the figures 6.10(a)

and 6.10(b) illustrates how a high value of $\lambda^{\max}$ correlates with a high void fraction. Note that for the stratified and annular flows the voltage measurements over the top electrodes are noisy, as these are only partially covered by the conductive water, thus leading to inaccurate reconstructions in this region, see Fig. 6.10(e). Lastly, the time being fixed, the reconstructions of the figures 6.10(c), 6.10(d) and 6.10(e) are very similar, while the associated flows can be clearly discriminated from the temporal evolution of $\lambda^{\max}$, as discussed previously.

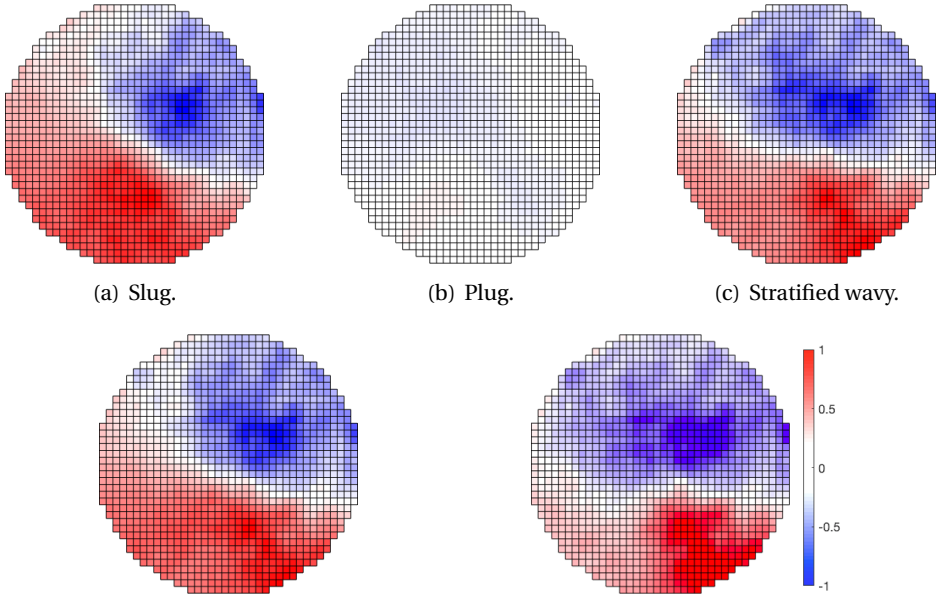

(a) Slug. (b) Plug. (c) Stratified wavy.

(d) Stratified smooth. (e) Annular.

FIGURE 6.10: Cross-sectional image reconstructions $\Delta\boldsymbol{\sigma} = (\boldsymbol{\sigma} - \boldsymbol{\sigma}_{\text{ref}})$ for the selected cases and at the time $t = 5.3\,\text{s}$, indicated by the black dashed lines in Fig. 6.9.

These results highlight that it is the combination of *both* the temporal evolution of $\lambda^{\max}$, as in Fig. 6.9, and raw image guesses, as in Fig. 6.10, that allows to determine the flow pattern with certainty for a given experiment.

6.3.5 Stacked EIT tomogram

Considering a time sequence of EIT measurements, the instantaneous reconstructed cross-sectional images are fragmented and not representative of the whole flow, as seen previously in Figure 6.10. Instead, the axially stacked tomogram are more suitable to flow visualization. Therefore, the pixels on the central vertical line of the cross-sectional images are extracted and stacked along time (or frame f), forming a tomogram for the experiment considered.

Here, comparison is made with the reference GRM information and its measurement β of the water phase fraction, see Section 6.3.1. As for horizontal flows it is reasonable to assume that in most cases the air gathers at the top of the pipe, except that the front of the slug contains intensive bubbles entrained in the water bulk, then the water phase forms a segment at the bottom with area A. With this assumption, we get $\beta = A/\pi r_0^2$ where r_0 is the radius of the pipeline, from which the time-dependent height h of the water phase is obtained. This results in a reference GRM tomogram for each experimental set.

Both the raw EIT tomogram and the reference GRM one are shown in Figure 6.11 (top and bottom panels respectively) for three distinctive flow regimes (slug, stratified wavy and annular) among these considered previously. The time resolution of the EIT and GRM tomograms are 10 ms and 50 ms, respectively. In the following section, we finally show how these EIT tomograms can be binarized using the AVF estimated by the eigenvalue correlation method.

6.3.6 Tomogram binarization and flow visualization

Classically in EIT, the reconstructed images do not give a precise indication of the phase distribution because of their over-smoothness. Yet, a threshold value σ_{th} can be computed using the eigenvalue correlation method: the mean leading eigenvalue $\lambda^{\max}_{\text{mean}}$ is computed for the experiment considered and, having determined the flow regime at step B, the calibration diagram of step A (Fig. 6.8) is then used to estimate the AVF. The threshold σ_{th} is then defined so that the phase fraction in the binarized tomogram matches the estimated phase distribution (see also Remark 2). This procedure is exemplified on the experiment considered with the binarized tomograms shown in the middle panels of Figure 6.11.

Overall, there is an excellent agreement between the air-water interface in the binarized EIT tomograms and in the reference GRM ones. In addition, the temporal resolution of EIT is five times higher than that of GRM. In Figure 6.11(a), the characteristic intermittent behavior of the slug flow can be clearly identified from both the EIT and GRM tomograms. Note also the strong correlation between the temporal evolution of $\lambda^{\max}$ in Figure 6.9(a) and the phase distribution variations in Figure 6.11(a). Similarly, the fluctuations at the air-water interface in the stratified wavy flow are well captured in the binarized EIT tomogram of Figure 6.11(b). For the annular flow, the assumption that the air phase gathers at the top of pipe does not hold anymore. Paras and Karabelas (1991) made some observation-based predictions of the film circumferential thickness distribution for a horizontal pipe. The predicted ratio of the top and bottom film thicknesses is used here to form the reference GRM tomogram of Figure 6.11(c). However, the thin top water film is not well reconstructed using EIT. Generally speaking, to explain the small observed discrepancies between the EIT and GRM tomograms, certain phenomena should be taken into account. First, EIT measurements have a 3D nature that tends to induce a local (volume) averaging in images. Second, noisy voltage measurements at the top electrodes induce high conductivity artifacts in the vicinity of the latter in EIT images and tomograms, as previously discussed. We have observed that discarding the top measurements tends to reduce this effect.

As a conclusion, the eigenvalue correlation method of Dang et al. (2019a) is applied to dynamic experimental data for horizontal two-phase flows, with the aims of identifying the flow regime and estimating the volume averaged void fraction. The presented results consider a number of experimental sets under various air-water flow conditions. Redundant EIT measurements are acquired using the full-scan excitation strategy, which enables to directly estimate the void fraction without performing image reconstruction. Yet, the extracted flow features are further integrated into EIT tomograms to improve flow visualizations.

The proposed eigenvalue correlation method yields excellent results, with the correlation between the leading eigenvalue of the normalized impedance matrix and the void fraction being consistent given the EIT system configuration. It can be pre-calibrated as a chart then usable for void fraction estimation by direct lookup. The estimation error is low, with linear correlation fits for the different flow regimes. Moreover, the temporal evolution of

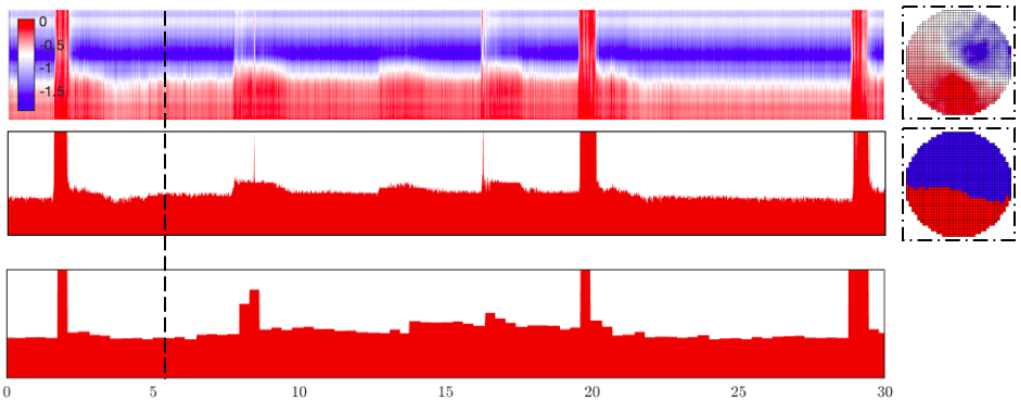

(a) Slug flow.

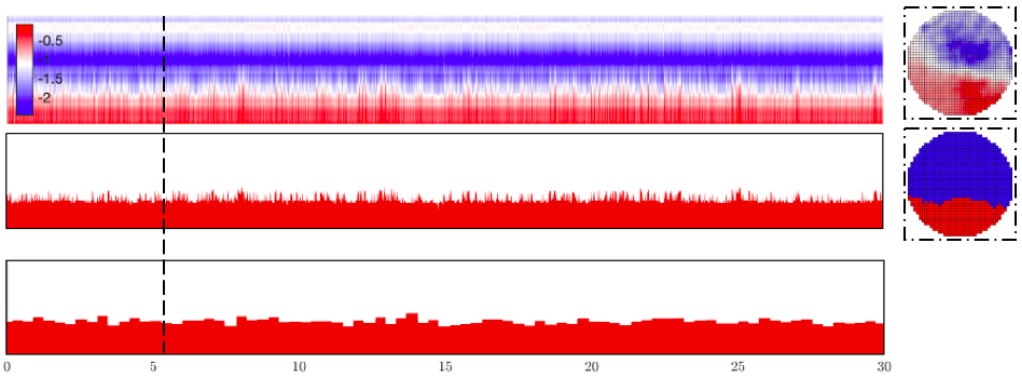

(b) Stratified wavy flow.

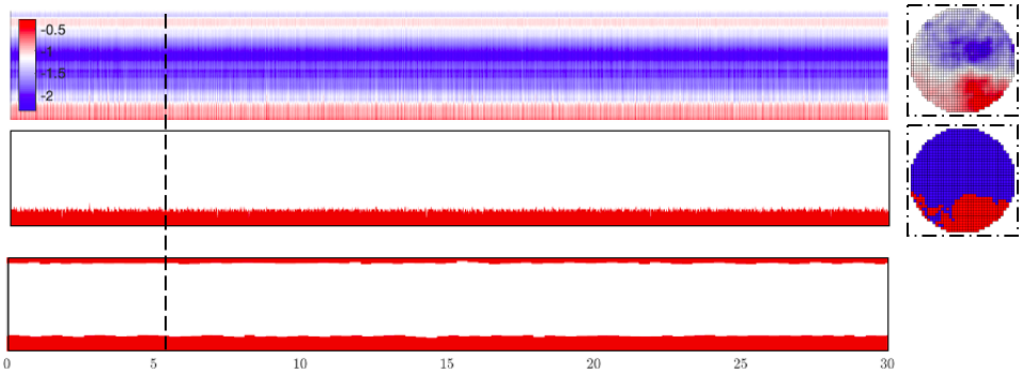

(c) Annular flow.

FIGURE 6.11: (*top*) Raw EIT tomograms, i.e. $\Delta\boldsymbol{\sigma}$, (*middle*) binarized EIT tomograms, and (*bottom*) reference GRM tomograms, for the experimental sets considered of slug, stratified wavy and annular flows. The abscissae represents the measurement time in second (or frame f). The vertical dashed lines corresponds to $t = 5.3$ s with the corresponding cross-sectional images shown in the right panels.

the leading eigenvalue coupled with a raw image guess gives a clear indication of the flow regime, which can be used as a prior information for the eigenvalue correlation method to estimate the volume averaged void fraction. The estimated AVF can then be applied to adjust the phase interface in the EIT tomogram, leading to a more reliable indication of the phase distribution.

For future studies, applying the proposed method to vertical air-water two-phase flows

would be interesting, as most of the peripheral electrodes will be in contact with the conductive phase, thus preventing from the issues related to uncovered electrode. Furthermore, considering the substantially large amount of data generated by EIT, i.e. the NIM for each frame, it is appealing to apply a statistical learning approach to estimate the void fraction using the proposed method.

6.4 Dynamic experiments in industrial loop

Another set of experiments was performed in the BENSON loop managed by Dr. Holger Schmidt in Framatome, Germany. I stayed in the Erlangen technical center for two weeks in June 2019 to perform the experiments, with the help from senior engineer Peter Burwitz. A total of 33 experimental series were accomplished at various water mass flow rates and steam qualities, under a system pressure of 20 bar. The dual-plane EIT test section designed in Section 3.4 was mounted in a horizontal pipeline in the loop to measure the steam-water flows under complex industry environments. The experimental procedures and results analysis are presented in this section.

6.4.1 Experiment procedures

Setups

The BENSON loop is a thermal-hydraulic separate effects test loop, Figure 6.12 shows the scheme of the loop, it can withstand a system pressure up to 330 bar, and a temperature up to 600 °C. The water in the loop can circulate in a mass flow rate up to 28 kg/s, the heating electrical coils has a heating capacity of 2000 kW. During the experiments, the water is heated up by the main heater, steam is generated from water evaporation, the resulting steam-water mixture passes through the test section for measurement. Various steam qualities can be obtained through monitoring the heating power and water mass flow rate, the system pressure is stabilized by a pressurizer.

The dual-plane test section was installed in a horizontal test pipe on the top of the platform, having a distance of 1 m to the pipe inlet. The internal surface of the test section is covered by electrically insulating coating except for the electrodes, while the test pipe is electrically conductive and grounded. The manufactured test section is shown in Figure 6.13(a), the connectors of the electrodes are specifically designed to avoid water leakages. During the experiments, only half of the electrodes at each plane were used due to the limited number of measurment channels, therefore, the EIT measurements were taken from 2×16 electrodes.

The two electrode planes work independently with the same excitation and measurement strategies. An extra data acquisition card and PCB are added to the ProME-T system to handle the second electrode plan, the system is shown in Figure 6.13(b). The interferences between the two planes are neglected. They can be considered as two individual EIT systems with exactly the same configurations. During the experiments, the excitation frequency for both planes is 80 kHz, with 20 samples per excitation period and 2 periods per excitation pattern, giving a frame rate of ~333 fps.

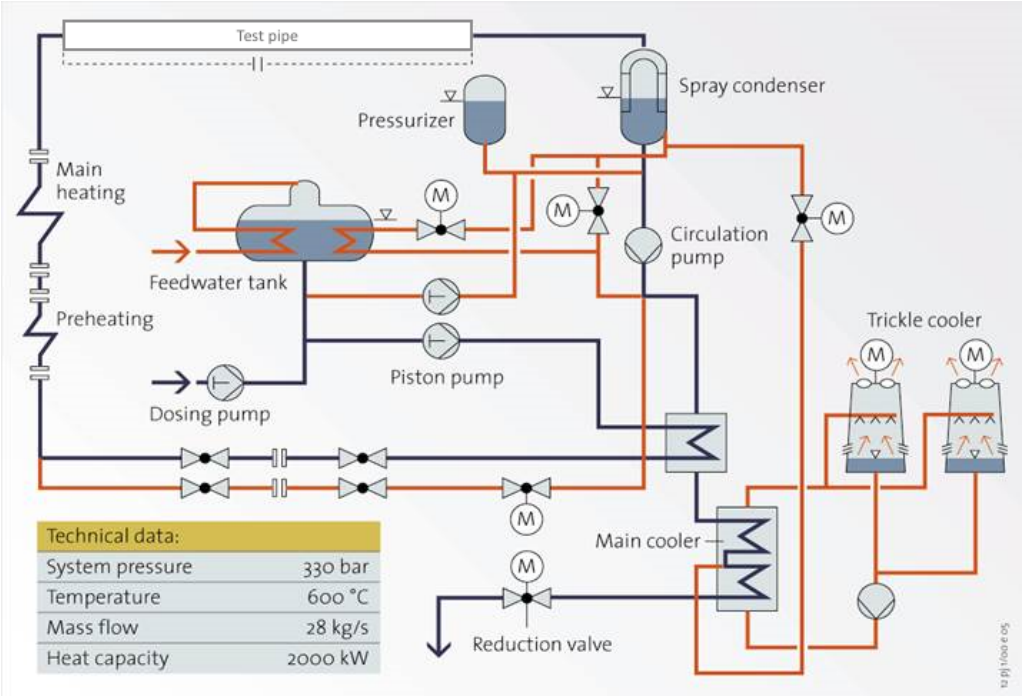

FIGURE 6.12: Schematic of the BENSON loop. The dual-plane EIT test section was installed in the horizontal test pipe.

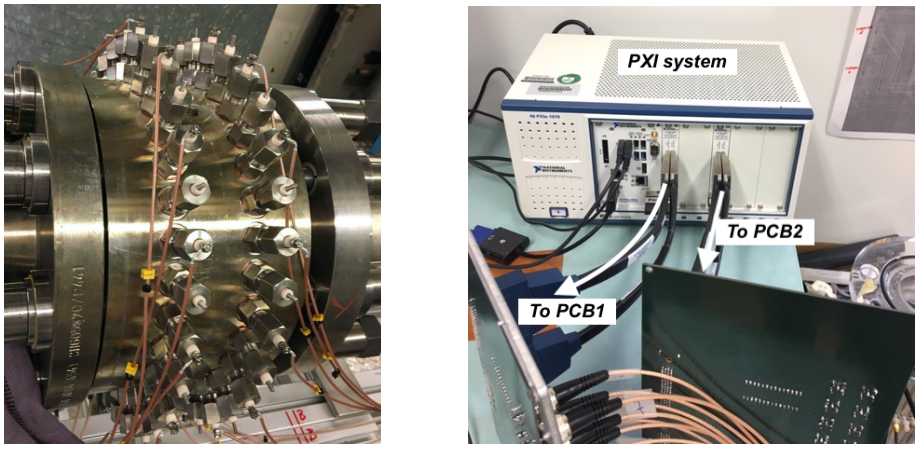

(a) Dual-plane test section. (b) Data acquisition system.

FIGURE 6.13: Dual-plane EIT system used for the BENSON experiments.

Test matrix

For the saturated steam-water flow concerned in the BENSON loop, the void fraction η is correlated to the steam quality χ following the curves shown in Figure 6.14 for different water mass flow rates $\dot{m}$. Since χ is imposed by the heating power, various volumetric void fractions could be obtained through adjusting $\dot{m}$ and the heating power. The experimental procedure is as follows: the system pressure is fixed to 20 bar with a certain water mass flow rate $\dot{m}$, the heating power is increased step by step to reach 11 different χ values selected in prior. For each χ, the heating power is maintained until a quasi-static state is achieved, then the EIT system is applied to measure the steam-water flows. Finally, three different water mass flow rates $\dot{m}$ = 0.15, 0.4, 1.0 kg/s were applied, giving the test matrix

as in Table 6.1, a total of 33 experimental series were conducted, with 3000 frames of image taken for each experiment.

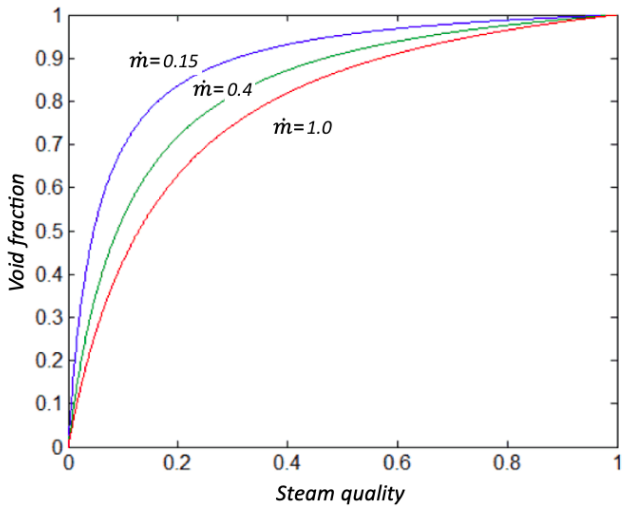

FIGURE 6.14: Correlation between the void fraction and the steam quality at different water mass flow rates.

TABLE 6.1: Test matrix of the experiments in the BENSON loop.

Pressure (bar)	20
Mass flow rate (kg/s) $\dot{m}$	0.15, 0.4, 1.0
Steam quality (%) χ	3, 6, 10, 15, 20, 25, 30, 40, 50, 60, 70

6.4.2 Result analysis

During the experiments, the online display of the EIT system gave very poor image reconstructions, the phase distribution could hardly be identified. Possible reasons are discussed in this section, through analyzing the measurement data and assessing the performance of the EIT system under complex environment, also some perspectives for further experiments are given. In the following analysis, only the data from the second electrode plane is considered, the analyzed results are compared to that of the ProME-T system under laboratory environment with ES2 electrodes (of size 5 mm×4 mm), as they have similar ratios between the circumferential width occupied by the electrodes and the internal circumference of the test section.

Noise analysis

In the noise analysis presented in Section 3.3.3, the spectrums of the high and low amplitude measurements are analyzed in frequency domain, indicating possible origins of noises. The SNR and $\overline{\text{RE}}$ are proposed to represent the noise resistance of the system. The same analysis has been carried out for the experiments in the BENSON loop.

Figure 6.15 shows the spectrums of the measurement signals at high and low amplitudes, respectively. In the figures, the first peak value at 5 kHz is the fundamental signal, the rest are noise. Comparing to the spectrums in laboratory environment shown in Figure 3.10,

it is found that the background noises are almost one order higher for both signals, moreover, there are noises at all frequencies varying with the fundamental amplitudes, while in Figure 3.10 only the higher-order harmonics vary in such way. From these analysis, the possible origins of the noises include: 1) the electro-magnetic field caused by the heating coils with high power capacity; 2) the vibration of the data acquisition system along with the platform induced by the circulating pump; 3) other experimental facilities in the same building with the BENSON loop.

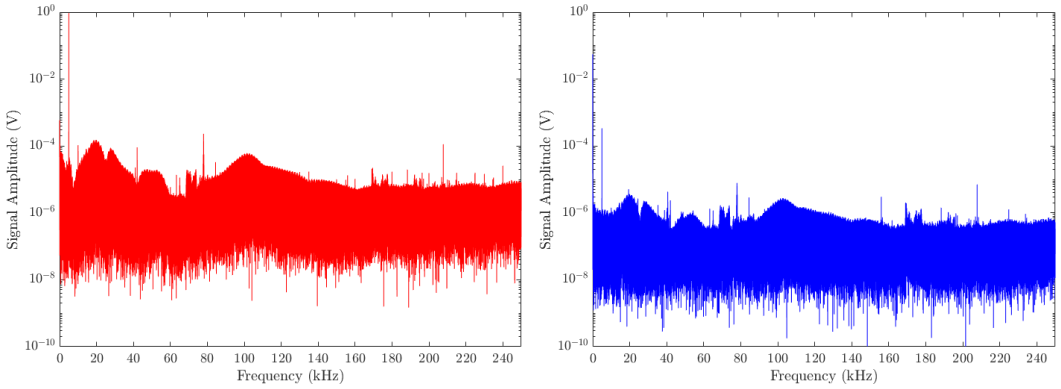

(a) High amplitude measurement. (b) Low amplitude measurement.

FIGURE 6.15: Spectrum analysis of the high and low amplitude measurements during the BENSON experiments.

The SNR is computed taking the energy of the fundamental signal over the total energy. Figure 6.16 plots the SNR versus the signal amplitude at each measurement channel during the BENSON experiments, comparing to that of the ProME-T system with ES2 electrodes under laboratory environment. As we can see, for the signals with comparative amplitudes, the SNR in BENSON is significantly higher than in LTHC, yet there are signals with extremely low amplitudes.

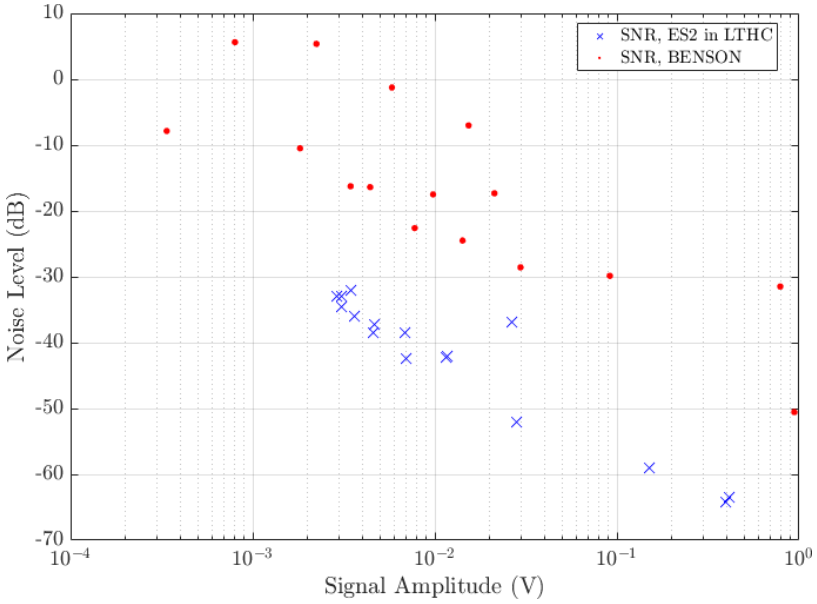

FIGURE 6.16: The Signal to Noise Ratio (SNR) of the system in the BENSON loop comparing to that in laboratory environment.

The relative errors RE of repeating measurements have been assessed with $n_c = 100$ consecutive frames measured at the reference case with homogeneous water filling the pipeline. Five different cases are studied with different configurations listed in Table 6.2, *e.g.* the number of period per excitation pattern N_p, the conductivity of water σ_0, the excitation amplitudes V_0, and whether the heating system is working or not. The RE of case no.2 is plotted versus the signal measurment as in Figure 6.17, in comparison with that of ES2 in LTHC. As we can see, for the measurements at comparable amplitudes, the RE for the BENSON loop are considerably lower than that in LTHC in most cases.

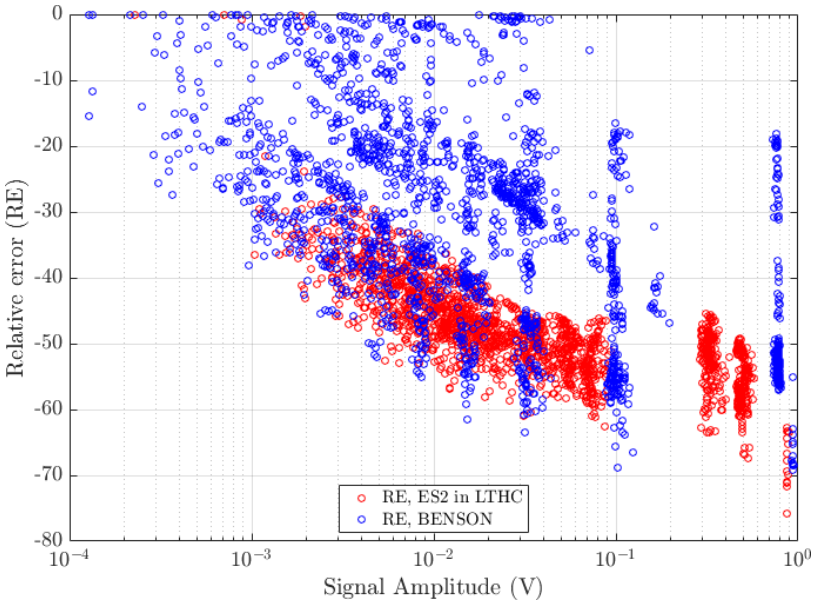

FIGURE 6.17: Relative errors of repeating measurements at 50 kHz excitation frequency for the BENSON and ES2 in LTHC.

TABLE 6.2: Mean relative error $\overline{\text{RE}}$ for various EIT configurations.

Case no.	N_p	σ_0 (μS/cm)	V_0 (V)	Heat	$\overline{\text{RE}}$ (dB)
1	1	70	1	heating	18.9
2	2	70	1	heating	19.5
3	1	220	1	heating	29.3
4	1	220	1	no heating	34.9
5	1	220	3	heating	38.9

The mean relative errors $\overline{\text{RE}}$ of various cases are listed in Table 6.2. It seems that $\overline{\text{RE}}$ increases with σ_0 and V_0, due to the higher measurement amplitudes associated. While the influences of transient multiplexing are negligible as the $\overline{\text{RE}}$ with $N_p = 1$ and $N_p = 2$ are comparable. Furthermore, the $\overline{\text{RE}}$ increases when the heating system is stoped, indicating the effects of the electro-magnetic field caused by the heating system. As a conclusion, the mean relative error $\overline{\text{RE}}$ of the EIT system during the BENSON experiments is low for all cases, which explains the poor image reconstructions.

Nevertheless, the eigenvalue based methodology proposed in current thesis study allows to estimate the phase fraction from boundary measurement without performing image reconstruction. Specifically for stratified configuration, the phase interface may be identified directly by the indices of the normalized impedance matrix NIM, see Figure 4.3(a)

for the NIM of a simulated stratified configuration with a void fraction of 0.09. The measurements over the electrodes uncovered by water would be nearly zero, giving high bulk impedances. The entries of the low amplitudes in the center of the NIM indicate the indices of electrodes uncovered by water, see Figure 6.18 for the NIM of a measured frame under the conditions $\dot{m} = 0.4$ and $\chi = 15\%$, the corresponding void fraction is $\eta = 0.52$.

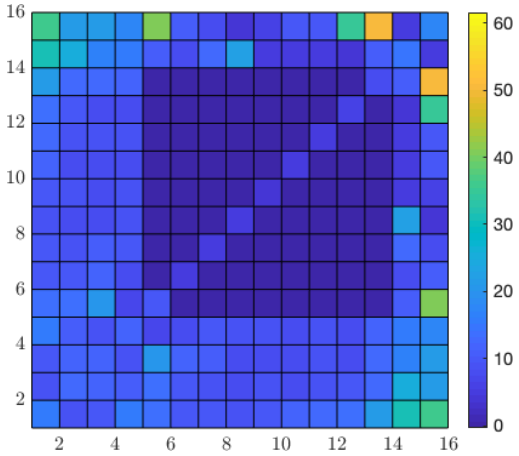

FIGURE 6.18: Identifying the water level from the indices of the normalized impedance matrix, void fraction $\eta = 0.52$.

Error analysis and perspectives

In this section, the dual-plane EIT system is assessed by the experiments in the BENSON loop, in terms of noise analysis and features extraction. Overall, the EIT measurements are too noisy to give meaningful image reconstruction. The possible reasons are: i) the low measurement signals caused by a low water conductivity and a large pipe diameter; ii) a significantly high noise level comparing to the laboratory environment. Nevertheless, the indices of the normalized impedance matrix may give an indication of the water level.

The perspectives are as follows:

- Reducing the noise level, possible ways include: i) using a Faraday cage to enclose the data acquisition system; ii) keeping a large distance between the system and the heating coils; iii) increasing the excitation amplitude to have stronger measurement signals; iv) reducing the vibration of the data acquisition system, insuring a robust contact of the BNC connector on the board.
- Image reconstruction with EIT measurements from a subset of electrodes.
- Analyzing the effects of the grounded pipe on the measurements. The measurement amplitudes may be reduced because of the current leakages from the excitation electrodes to the grounded pipe.

Chapter 7

Conclusion

Conclusion and discussion

The present Ph.D thesis work demonstrates a comprehensive EIT-based measurement mode for dynamic two-phase flow measurements, with emphasis on the image reconstruction methods and a novel eigenvalue-based approach for flow features extraction, i.e. flow imaging, void fraction estimation, and flow regime identification.

The full-scan excitation strategy considered in the present work sheds new light in the researches of EIT, where the adjacent strategy is commonly applied. Traversing all independent pairs of electrodes possible for boundary excitations, full-scan strategy produces highly redundant measurement data containing that of the adjacent and opposite strategies, among others. On one hand, the large number of excitation patterns requires a heavy effort for multiplexing hence reducing the frame rate. On the other hand, the redundant measurements improve the robustness of the system to noise and the overall sensitivity in the sensing domain, also the sensitivity distribution is more homogeneous comparing to that of the adjacent strategy. The preeminence of the full-scan and trigonometric strategies are evidenced through image reconstructions of several simulation cases and static experiments, they give a better geometrical reconstruction of the object(s) and a sharper conductivity contrast compared to the adjacent and opposite strategies. Moreover, the redundant measurements allow alternative approaches for void fraction estimation of two-phase flow other than the image reconstruction, namely the eigenvalue-based approach.

The NtD map defined on EIT forward problem and the Neumann boundary conditions stimulate the idea of impedance matrix, which can be considered as a discrete representation of the NtD map from certain current excitations to corresponding boundary measurements. The impedance matrix contains the complete information of phase distribution, its eigenvalues are directly correlated to the phase fraction, allowing an eigenvalue-based methodology for phase fraction estimation. Different correlations are established for three phase distribution patterns through numerical simulations, the reliability of the proposed approach is highlighted by static experiments. A higher estimation accuracy is expected by incorporating a priori knowledge on phase distribution pattern, e.g. the number and location of the bubbles. Additionally, it underlines the need for an in-depth mathematical analysis of the relation between the phase distribution and the eigenvalues of the impedance matrix, such an analysis would allow to determine which information can be retrieved from such a matrix and which metrics are suitable to do so. Lastly and as in Bellis et al. (2012), this methodology can be used to devise an initial guess for iterative image reconstruction algorithms thereby improving their convergence.

Two-phase flows feature a quickly evolving phase distribution and a high conductivity contrast between the phases, raising additional requirements for image reconstructions. Various reconstruction methods, e.g. the least-squares methods with different regularizations, GREIT, factorization method, MUSIC algorithm, and topological sensitivity method, are reviewed and discussed in terms of two-phase flow imaging. Their implementation procedures are demonstrated by numerical simulations, finally the one-step 2.5D reconstruction, 2D iterative methods with Tikhonov and TV regularizations, and GREIT are selected for further studies with experimental data. Although the MUSIC algorithm seems appealing considering the high efficiency in locating inhomogeneities, some improvements should be made to enhance its performance with noisy data. Benchmark reconstructions are made applying the four selected methods to several static experiments with the ES1 and ES2 electrodes. Results show that the quality of the reconstructed images are significantly affected by the length of the electrodes, generally, the 2.5D and GREIT methods give satisfactory image reconstructions for both the ES1 and ES2 electrodes, while the 2D iterative methods are not promising for ES2 electrodes. Considering the performance analysis of the ProME-T system with two sets of electrodes and the numerical simulations of 3D effect, longer electrodes (with a larger surface area) are envisaged to give a higher overall measurement amplitude and a more homogeneous sensitivity distribution in the sensing domain, hence a better image reconstruction. On the contrary, the axial sensing domain associated with longer electrodes would extend further, being less sensitive to small local changes in dynamic flows. A compromise should be made between the two aspects.

Dynamic two-phase flow experiments have been conducted in the processing lab of University College of South-East Norway in collaboration with Professor Mylvaganam. Developed horizontal air-water flows at ambient temperature and pressure were measured using the ultra-high speed ONE-SHOT system developed in LTHC. The transverse cross-sectional images are reconstructed from the EIT measurements using 2.5D method, the axially stacked EIT tomograms provide valuable information about the flows: the flow pattern could be identified by visual inspection, the volume averaged void fraction could be estimated from the eigenvalues correlation method and conductivity threshold method separately. The high frame rate of EIT allows a higher time resolution than GRM, revealing the different characters at the front of a plug/slug. The reliability of the eigenvalue-based approach is again highlighted by dynamic experimental results, the volume averaged void fraction is well correlated to the leading eigenvalue of the averaged normalized impedance matrix, except for some cases where transition between stratified smooth and wavy flows occurs. Applying correlation techniques with the eigenvalues of the EIT impedance matrix in vertical two-phase flows would lead to interesting results with respect to annular and stratified flows, as most of the peripheral electrodes will be in contact with the conducting water medium. Additionally, efforts have been made to apply GREIT method to the measurement data, the result is not promising because of the relatively high noise level in dynamic experiments and the measurement errors induced by the multiple excitation frequencies used for FDM in the ONE-SHOT system.

Another set of dynamic experiments were performed in the BENSON loop during my visit at Framatome GmbH, Germany, horizontal steam-water flows at high temperature high pressure were measured at various steam qualities. The designed dual-plane test section is proved to sustain the harsh flows successfully, however, the image reconstructions are too noisy to retrieve meaningful information. The measured signals are analyzed in frequency domain, giving possible origins of the measurment noises, including: i) the

electro-magnetic field generated by the high capacity electrical heating coils; ii) the malfunction of the BNC connectors induced by the vibration of the system. Future experiments with proper electro-magnetic shielding and anti-vibration practice are expected to give better results.

Perspective

Insensitive researches on electrical tomography are ongoing for the development of innovative instrumentations, there are several aspects to be studied in-depth which brings prospects toward the long-term goal of applying EIT for flow measurements under harsh environments.

Considering that the number of independent measurements of an EIT system is restricted by the number of electrodes, a straightforward way to improve the spatial resolution is employing more electrodes, especially, the current hardwares for data acquisition and manipulation are sufficient to handle 32 even 64 electrodes. Currently two test sections are available in LTHC, one with a single plane of 32 electrodes, another one with three planes of 16 electrodes. It is feasible and promising to upgrade the ProME-T system to a 32 channels EIT system, allowing different excitation and measurement strategies. Specifically for the multi-plane test section, two different strategies can be applied with proper updates of the acquisition codes and PCB, i.e. i) independent working strategy where two electrode planes work independently at different excitation frequencies, cross-plane measurements can be obtained discriminating the measured signals through FFT, making frequency difference reconstruction possible, which can circumvent the need of a reference measurement (Malone et al., 2013); ii) adjoint working strategy where cross-plane excitations are applied to improve the sensitivity in the center of the domain, several researches have proved the superiority of cross-plane excitations and measurements for 3D image reconstructions (Wagenaar and Adler, 2016; Grychtol et al., 2019).

In the light of present thesis work, the preeminence of the full-scan excitation strategy is evidenced comparing to the adjacent one, however, it is somehow time assuming to traverse all independent pairs of electrodes for full-scan excitations, especially when there are large number of electrodes on multiple planes for cross-plane excitations. Other strategies, for example the over-2 or -3 strategies with a separation of 2 or 3 electrodes between the source and drain (Alme and Mylvaganam, 2007), may have comparably good performances as the full-scan while requiring less redundant excitations, hence a higher frame rate. Moreover, the weighting of adjacent excitation is reduced in over-2 or -3 strategies comparing to the full-scan, which may grant a more homogeneous sensitivity distribution and reduce the *ill-posedness* of EIT inverse problem.

Multi-modality sensors are attracting more attentions and of interest for continuation of the present work, they can discriminate different materials with similar conductivity or permittivity, or improve the system performance. For example, the dual-modality EIT/ECT sensor can discriminate three phases through conductivity and permittivity reconstructions, allowing wide applications in oil extraction (Wang et al., 2017). The EIT and ultrasonic sensors can perform image reconstructions on the same mesh model, since a change in conductivity is usually accompanied by a change in acoustic impedance, dual-modality EIT and ultrasonic sensors may have a better performance in terms of image quality and robustness to noise (Liang et al., 2019).

In terms of image reconstruction, the present work puts a lot efforts on the feasible reconstruction methods for two-phase flow imaging. The GREIT method seems very promising considering the computation efficiency and image quality for both sets of electrodes. Further investigations should be performed with measurment data from dynamic experiments, also the method itself maybe modified specifically for the applications in two-phase flow imaging. The MUSIC algorithm has been studied preliminarily in the present work, considering point electrodes on the boundary with gap electrode model and numerical simulation data. For practical implementation, electrodes with physical size and complete electrode model should be considered, by which its performance with noisy data may be improved. Further, the position and number of the inclusions provided by the MUSIC algorithm may be incorporated in iterative image reconstruction methods as an initial guess to improve their convergences.

Considering the applications in industrial flow measurements, the background noise and current leakage from the electrodes to the conductive pipelines are challenging. Increasing the electrode length may strengthen the measurement signals, while it also enlarges the sensing volume and reduces the sensitivity to local flow changes, a compromise should be made between the two aspects. Besides, in some cases a reference measurement with homogeneous medium filling the pipeline may be not feasible, the temperature changes during the experiments may induce conductivity variations and distort the reconstructed images. It is difficult and expensive to acquire the real-time conductivity, a *temperature coefficient* can be considered to bypass this problem (Jia et al., 2015). That is, the medium in the loop can be sampled before the experiments, the conductivity is measured at a set of temperatures to estimate the temperature coefficient. The reference boundary measurements at various temperatures can be obtained given the real-time temperature and the temperature coefficient. The influences of changing temperature on the reconstructed images are excluded, only the phase change is considered.

Appendix A

Dual-plane test section design for PKL

Figure A.1 shows the final design of the dual-plane test section for the PKL facility, it has an inner diameter of 128.2 mm and a length of 170 mm. To withstand the high temperature high pressure flows inside the pipe, the test section is made of stainless steel, but its inner surface is coated to be electrically insulating except for the surfaces of electrodes. The test section has 32 plate-like electrodes on each plane, the connectors of the electrodes are designed specifically to avoid water leakage under harsh environment. The design of the electrodes is shown in Figure A.2, the electrode surface is a rectangular of size 15 mm×11.5 mm, the long bar passes through the pipe wall and carries the signals between the electrode surface and the PCB.

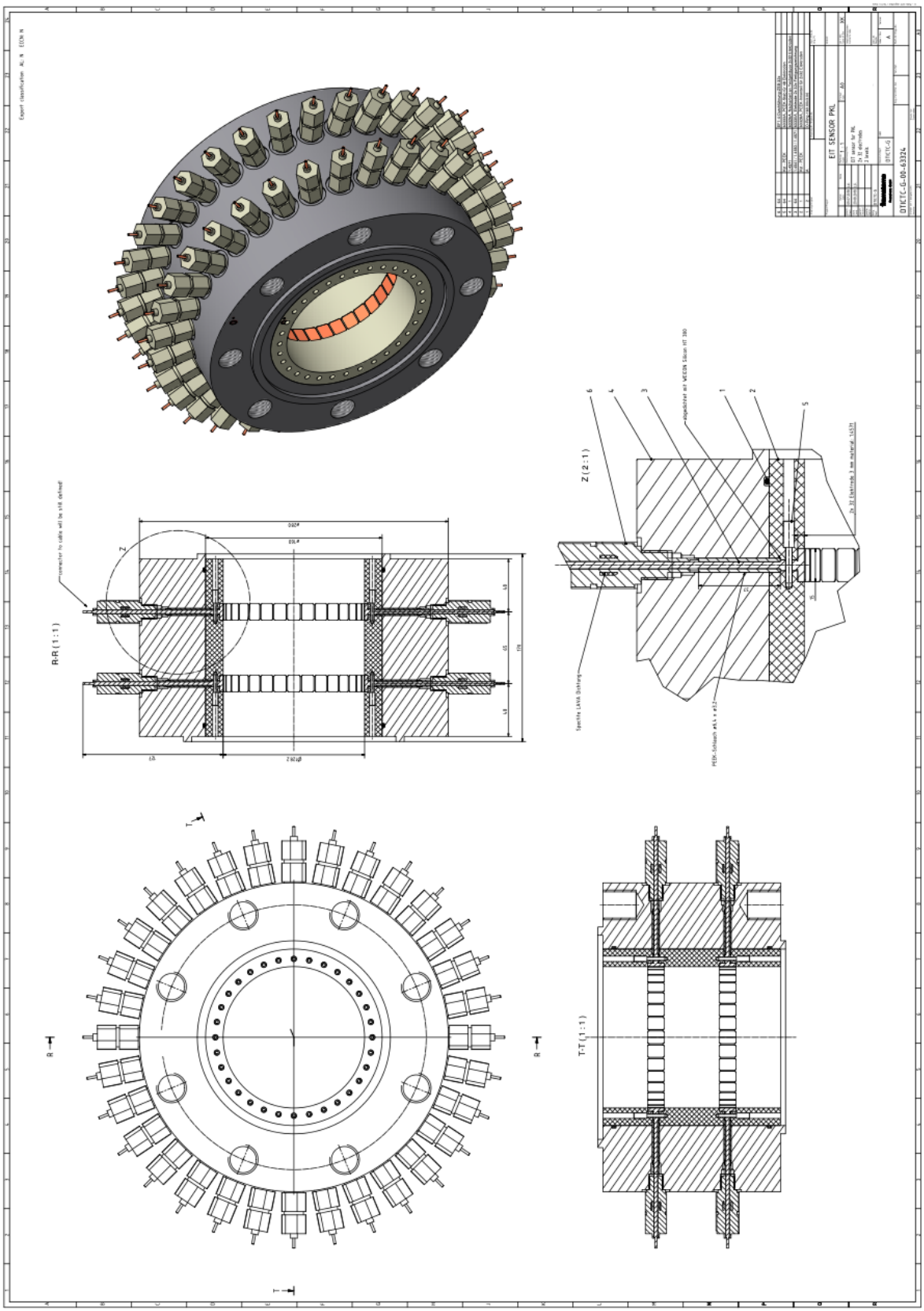

FIGURE A.1: Schematic of the EIT test section design for PKL facility.

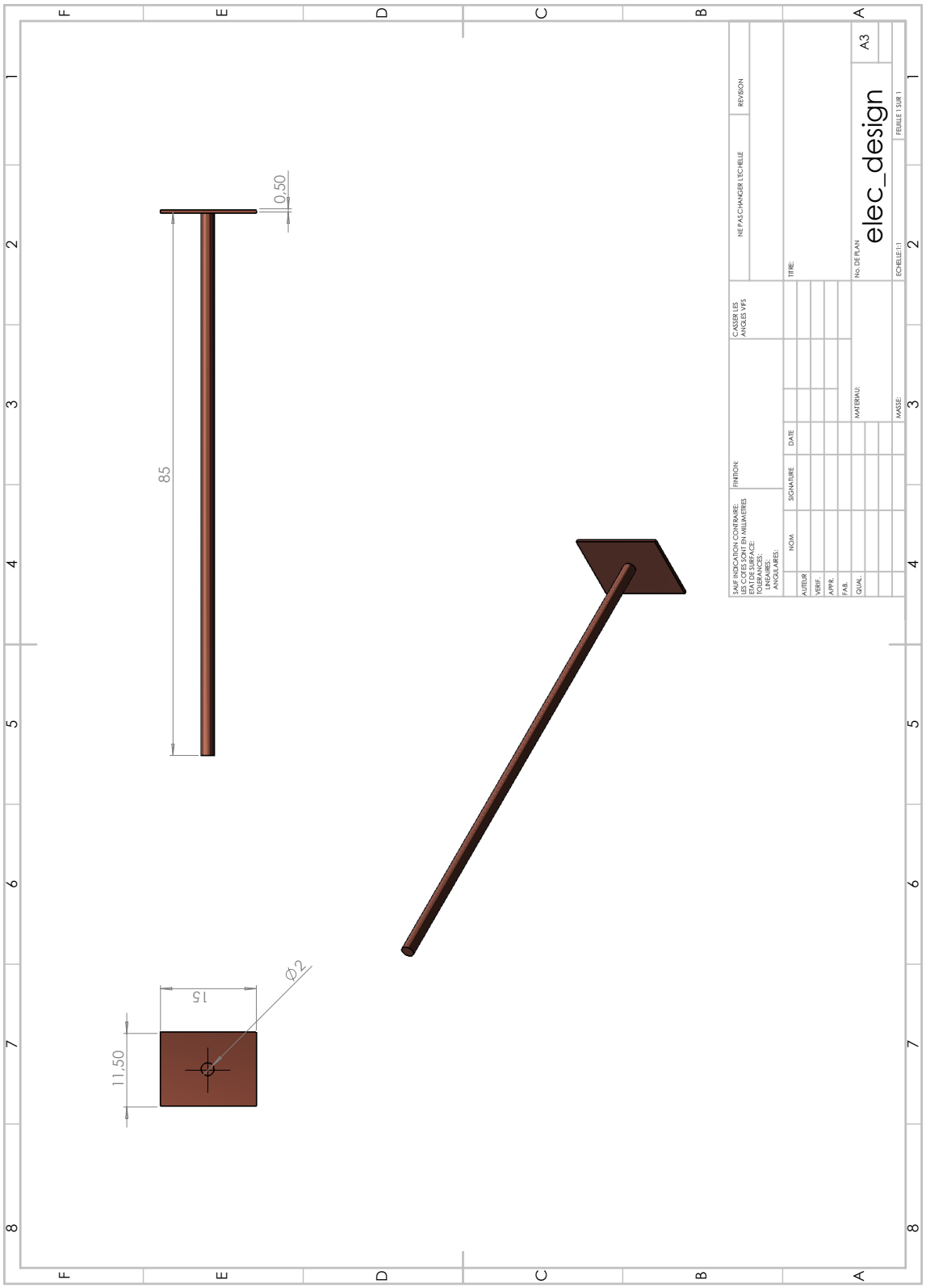

FIGURE A.2: Schematic of the electrodes used in the EIT test section for PKL facility.

Appendix B

EIT and GRM tomograms for experiments in USN

This Appendix shows the EIT and GRM tomograms for some selected experimental series conducted in the horizontal flow loop of USN. Each experimental series corresponds to a pair of water and air flow rates, the experiment numbering and associated flow regime are shown in Figure 6.7. A total of 10 experimental series are chosen, two for each flow regime, including: test 03 and 09 for slug flow, test 01 and 13 for plug flow, test 39 and 74 for stratified smooth flow, test 44 and 71 for stratified wavy flow, test 66 and 73 for annular flow.

In both EIT and GRM tomograms, the abscissa represents the measurement time, 30 seconds of measurements are taken for both tomograms. The EIT tomograms plot the difference conductivity $\Delta\boldsymbol{\sigma}$ between water and air, therefore, the red color indicates the water, the blue for air. Similar in the GRM tomograms, the red color represents the water.

EIT tomograms on the top, GRM tomograms on the bottom

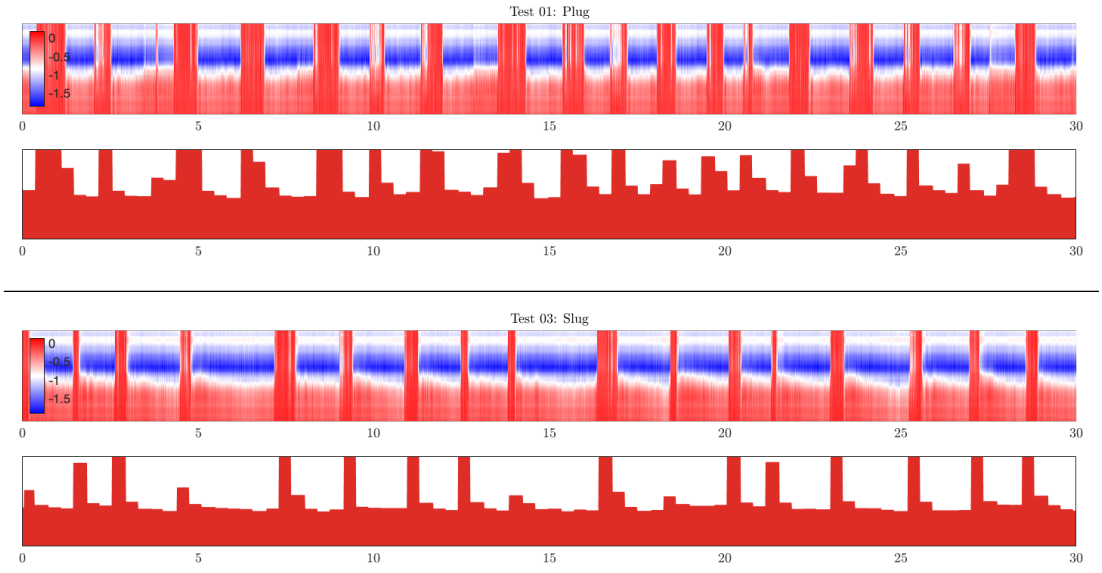

Continued on next page

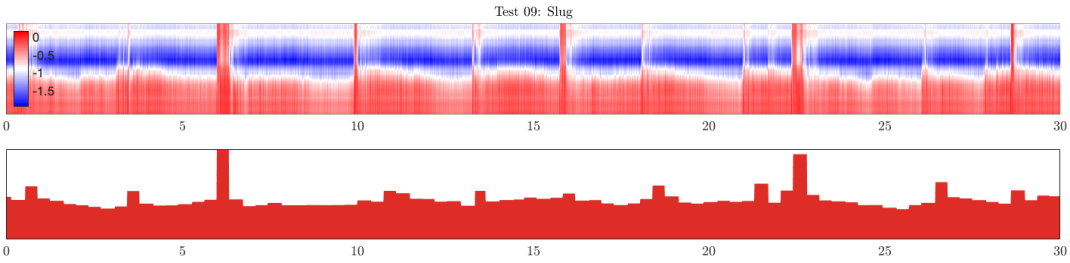

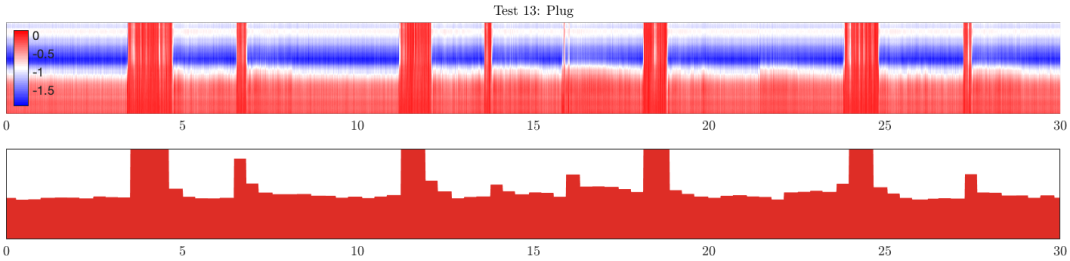

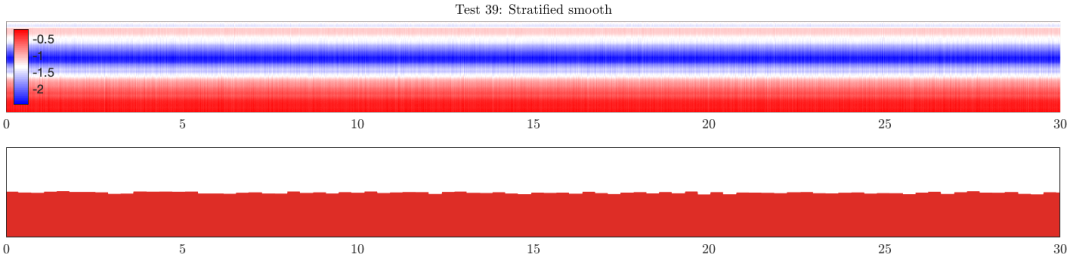

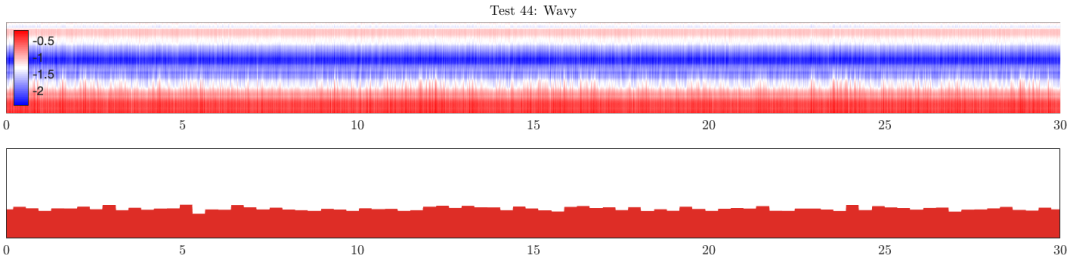

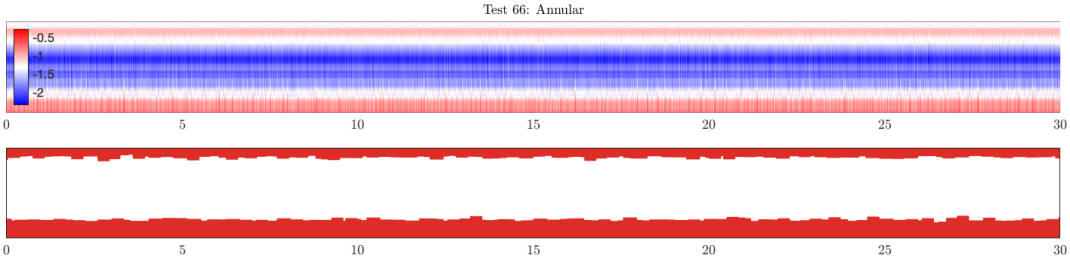

Continued on next page

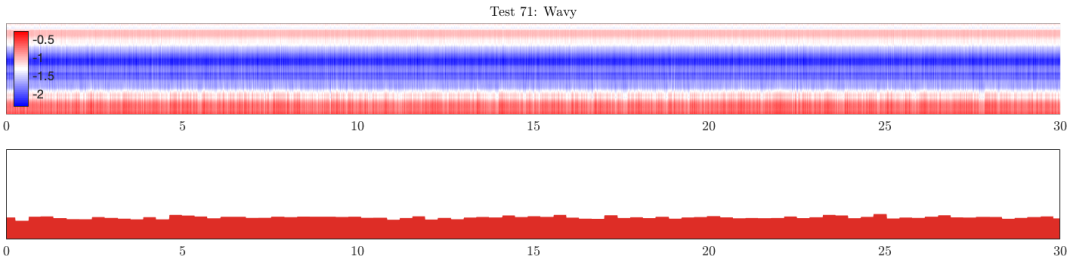
Test 71: Wavy
-0.5
-1
-1.5
-2
0
5
10
15
20
25
30

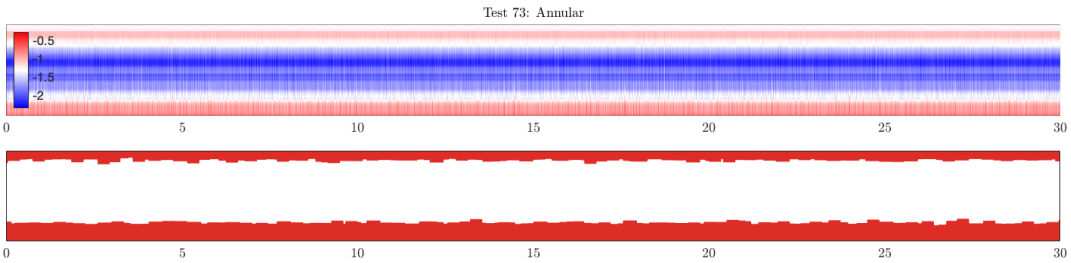
Test 73: Annular
-0.5
-1
-1.5
-2
0
5
10
15
20
25
30

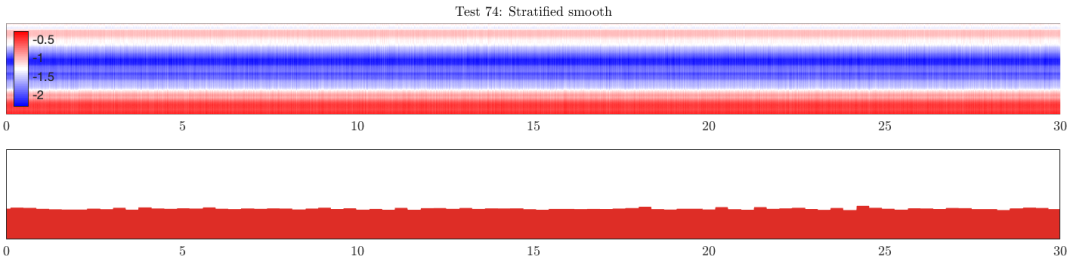
Test 74: Stratified smooth
-0.5
-1
-1.5
-2
0
5
10
15
20
25
30

Bibliography

A. Adler and R. Guardo. Electrical impedance tomography: regularized imaging and contrast detection. *IEEE transactions on medical imaging*, 15(2):170–179, 1996.

A. Adler and W. R. Lionheart. Uses and abuses of EIDORS: an extensible software base for EIT. *Physiological measurement*, 27(5):S25, 2006.

A. Adler, J. H. Arnold, R. Bayford, A. Borsic, B. Brown, P. Dixon, T. J. Faes, I. Frerichs, H. Gagnon, Y. Gärber, et al. GREIT: a unified approach to 2D linear EIT reconstruction of lung images. *Physiological measurement*, 30(6):S35, 2009.

A. Adler, P. O. Gaggero, and Y. Maimaitijiang. Adjacent stimulation and measurement patterns considered harmful. *Physiological measurement*, 32(7):731, 2011.

A. Adler, A. Boyle, and W. R. Lionheart. Efficient computations of the Jacobian matrix using different approaches are equivalent. *ELECTRICAL IMPEDANCE TOMOGRAPHY!*, 21:75, 2017.

S. Aguiar Santos, A. Robens, A. Boehm, S. Leonhardt, and D. Teichmann. System description and first application of an FPGA-based simultaneous multi-frequency electrical impedance tomography. *Sensors*, 16(8):1158, 2016.

W. H. Ahmed and B. I. Ismail. Innovative techniques for two-phase flow measurements. *Recent Patents on Electrical & Electronic Engineering (Formerly Recent Patents on Electrical Engineering)*, 1(1):1–13, 2008.

K. J. Alme and S. Mylvaganam. Comparison of different measurement protocols in electrical capacitance tomography using simulations. *IEEE Transactions on Instrumentation and Measurement*, 56(6):2119–2130, 2007.

G. Bal and K. Ren. On multi-spectral quantitative photo-acoustic tomography in diffusive regime. *Inverse Problems*, 28(2):025010, 2012.

G. Bal and G. Uhlmann. Inverse diffusion theory of photoacoustics. *Inverse Problems*, 26 (8):085010, 2010.

D. C. Barber and B. H. Brown. Applied potential tomography. *Journal of Physics E: Scientific Instruments*, 17(9):723, 1984.

C. Bellis, A. Constantinescu, T. Coquet, T. Jaravel, and A. Lechleiter. A non-iterative sampling approach using noise subspace projection for EIT. *Inverse Problems*, 28(7):075015, 2012.

M. Bonnet. Higher-order topological sensitivity for 2-D potential problems. Application to fast identification of inclusions. *International Journal of Solids and Structures*, 46 (11-12):2275–2292, 2009.

M. Bonnet and F. Cakoni. Analysis of topological derivative as a tool for qualitative identification. *Inverse Problems*, 2019.

L. Borcea. Electrical impedance tomography. *Inverse problems*, 18(6):R99, 2002.

A. Borsic, B. M. Graham, A. Adler, and W. R. Lionheart. In vivo impedance imaging with total variation regularization. *IEEE transactions on medical imaging*, 29(1):44–54, 2009.

A. Boyle and A. Adler. The impact of electrode area, contact impedance and boundary shape on EIT images. *Physiological measurement*, 32(7):745, 2011.

W. Breckon and M. Pidcock. Some mathematical aspects of electrical impedance tomography. In *Mathematics and computer science in medical imaging*, pages 351–362. Springer, 1988.

W. R. Breckon. *Image reconstruction in electrical impedance tomography*. PhD thesis, Oxford Polytechnic, 1990.

J. Brewer. Kronecker products and matrix calculus in system theory. *IEEE Transactions on circuits and systems*, 25(9):772–781, 1978.

M. Brühl. Explicit Characterization of Inclusions in Electrical Impedance Tomography. *Siam Journal on Mathematical Analysis - SIAM J MATH ANAL*, 32, 02 2001. doi: 10.1137/S003614100036656X.

M. Brühl and M. Hanke. Numerical implementation of two noniterative methods for locating inclusions by impedance tomography. *Inverse Problems*, 16(4):1029, 2000.

A. P. Calderón. On an inverse boundary value problem. *Computational & Applied Mathematics*, 25(2-3):133–138, 2006.

S. Ceccio and D. George. A review of electrical impedance techniques for the measurement of multiphase flows. *Journal of fluids engineering*, 118(2):391–399, 1996.

Y. Chen, W. P. Jepson, and H. J. Chen. Effects of multiphase flow on corrosion inhibitor. *CORROSION 99*, 1999.

M. Cheney and D. Isaacson. Distinguishability in impedance imaging. *IEEE Transactions on Biomedical Engineering*, 39(8):852–860, 1992.

M. Cheney, D. Isaacson, J. C. Newell, S. Simske, and J. Goble. NOSER: An algorithm for solving the inverse conductivity problem. *International Journal of Imaging systems and technology*, 2(2):66–75, 1990.

M. Cheney, D. Isaacson, and J. C. Newell. Electrical impedance tomography. *SIAM review*, 41(1):85–101, 1999.

K.-S. Cheng, D. Isaacson, J. Newell, and D. G. Gisser. Electrode models for electric current computed tomography. *IEEE Transactions on Biomedical Engineering*, 36(9):918–924, 1989.

E. T. Chung, T. F. Chan, and X.-C. Tai. Electrical impedance tomography using level set representation and total variational regularization. *Journal of Computational Physics*, 205(1):357–372, 2005.

R. D. Cook, G. J. Saulnier, D. G. Gisser, J. C. Goble, J. Newell, and D. Isaacson. ACT3: A high-speed, high-precision electrical impedance tomograph. *IEEE Transactions on Biomedical Engineering*, 41(8):713–722, 1994.

N. cRIO. *DEVICE SPECIFICATIONS NI cRIO-9039: Embedded CompactRIO Controller with Real-Time Processor and Reconfigurable FPGA*. National Instrument, 2018.

C. Dang, M. Darnajou, G. Ricciardi, A. Beisiegel, S. Bourennane, and C. Bellis. Performance analysis of an electrical impedance tomography sensor with two sets of electrodes of different sizes. *Proc. WCIPT-9 (Bath, UK)*, 2018a.

C. Dang, M. Darnajou, G. Ricciardi, L. Rossi, S. Bourennane, C. Bellis, and H. Schmidt. Two-phase flow void fraction estimation from the raw data of electrical impedance tomography sensor. *Proc. ICAPP (Juan-les-Pins, France)*, 2018b.

C. Dang, M. Darnajou, C. Bellis, G. Ricciardi, H. Schmidt, and S. Bourennane. Numerical and experimental analysis of the correlation between EIT data eigenvalues and two-phase flow phase fraction. *Measurement Science and Technology*, 31(1):015302, 2019a.

C. Dang, M. Darnajou, G. Ricciardi, L. Rossi, S. Bourennane, C. Bellis, and H. Schmidt. Spectral And Eigenvalues Analysis of Electrical Impedance Tomography Data For Flow Regime Identification. *Proc. SWINTH (Livorno, Italy)*, 2019b.

C. Dang, C. Bellis, M. Darnajou, G. Ricciardi, S. Mylvaganam, and S. Bourennane. Practical Comparisons of EIT Excitation Protocols with Applications in High Contrast Imaging. *Instrumentation Science and Technology*, Submitted.

C. Dang, M. Darnajou, C. Bellis, G. Ricciardi, S. Mylvaganam, and S. Bourennane. Improving EIT-based visualizations of two-phase flows using an eigenvalue correlation method. *IEEE Transactions on Instrumentation and Measurement*, Submitted.

M. Darnajou, C. Dang, G. Ricciardi, S. Bourennane, C. Bellis, and H. Schmidt. The Design of Electrical Impedance Tomography Detectors in Nuclear Industry. *Proc. WCIPT-9 (Bath, UK)*, 2018.

M. Darnajou, A. Dupré, C. Dang, G. Ricciardi, S. Bourennane, and C. Bellis. On the Implementation of Simultaneous Multi-Frequency Excitations and Measurements for Electrical Impedance Tomography. *Sensors*, 19(17):3679, 2019.

M. Darnajou, A. Dupré, C. Dang, G. Ricciardi, S. Bourennane, C. Bellis, and S. Mylvaganam. High Speed EIT with Multifrequency Excitation using FPGA and Response Analysis using FDM. *IEEE Sensors Journal*, 2020.

E. Demidenko, A. Hartov, N. Soni, and K. D. Paulsen. On optimal current patterns for electrical impedance tomography. *IEEE Transactions on Biomedical Engineering*, 52(2): 238–248, 2005.

X. Deng, F. Dong, L. Xu, X. Liu, and L. Xu. The design of a dual-plane ert system for cross correlation measurement of bubbly gas/liquid pipe flow. *Measurement Science and Technology*, 12(8):1024, 2001.

F. Dickin and M. Wang. Electrical resistance tomography for process applications. *Measurement Science and Technology*, 7(3):247, 1996.

N. Dominguez and V. Gibiat. Non-destructive imaging using the time domain topological energy method. *Ultrasonics*, 50(3):367–372, 2010.

F. Dong, Y. Xu, L. Hua, and H. Wang. Two methods for measurement of gas-liquid flows in vertical upward pipe using dual-plane ERT system. *IEEE Transactions on Instrumentation and Measurement*, 55(5):1576–1586, 2006.

A. Dupré. *Electrical impedance tomography for void fraction measurements of harsh two-phase flows: prototype development and reconstruction techniques*. PhD thesis, Ecole Centrale Marseille, 2017.

A. Dupré and S. Mylvaganam. A Simultaneous and Continuous Excitation Method for High-Speed Electrical Impedance Tomography with Reduced Transients and Noise Sensitivity. *Sensors*, 18(4):1013, 2018.

A. Dupré, G. Ricciardi, and S. Bourennane. Novel Approach for Analysis and Design of High-Speed Electrical Impedance Tomographic System for Void Fraction Measurements in Fast Two-Phase Flows. *IEEE Sensors Journal*, 17(14):4472–4482, 2017a.

A. Dupré, G. Ricciardi, S. Bourennane, and S. Mylvaganam. Electrical Capacitance-Based Flow Regimes Identification - Multiphase Experiments and Sensor Modeling. *IEEE Sensors Journal*, 17(24):8117–8128, 2017b.

J. Enrique Julia, W. K. Harteveld, R. F. Mudde, and H. E. Van den Akker. On the accuracy of the void fraction measurements using optical probes in bubbly flows. *Review of scientific instruments*, 76(3):035103, 2005.

H. A. Eschenauer, V. V. Kobelev, and A. Schumacher. Bubble method for topology and shape optimization of structures. *Structural optimization*, 8(1):42–51, 1994.

W. Fang and E. Cumberbatch. Matrix properties of data from electrical capacitance tomography. *Journal of engineering mathematics*, 51(2):127–146, 2005.

L. F. Fuks, M. Cheney, D. Isaacson, D. G. Gisser, and J. Newell. Detection and imaging of electric conductivity and permittivity at low frequency. *IEEE Transactions on Biomedical Engineering*, 38(11):1106–1110, 1991.

J. Gamio, J. Castro, L. Rivera, J. Alamilla, F. Garcia-Nocetti, and L. Aguilar. Visualisation of gas–oil two-phase flows in pressurised pipes using electrical capacitance tomography. *Flow Measurement and Instrumentation*, 16(2-3):129–134, 2005.

D. George, J. Torczynski, K. Shollenberger, T. O'Hern, and S. Ceccio. Validation of electrical-impedance tomography for measurements of material distribution in two-phase flows. *International Journal of Multiphase Flow*, 26(4):549–581, 2000.

D. Gisser, D. Isaacson, and J. Newell. Current topics in impedance imaging. *Clinical Physics and Physiological Measurement*, 8(4A):39, 1987.

D. Gisser, D. Isaacson, and J. Newell. Electric current computed tomography and eigenvalues. *SIAM Journal on Applied Mathematics*, 50(6):1623–1634, 1990.

C. Goh, A. Ruzairi, F. Hafiz, and Z. Tee. Ultrasonic tomography system for flow monitoring: A review. *IEEE Sensors Journal*, 17(17):5382–5390, 2017.

B. Graham and A. Adler. Objective selection of hyperparameter for EIT. *Physiological measurement*, 27(5):S65, 2006.

B. Graham and A. Adler. Electrode placement configurations for 3D EIT. *Physiological measurement*, 28(7):S29, 2007.

B. Grychtol, B. Müller, and A. Adler. 3D EIT image reconstruction with GREIT. *Physiological measurement*, 37(6):785, 2016.

B. Grychtol, J. P. Schramel, F. Braun, T. Riedel, U. Auer, M. Mosing, C. Braun, A. D. Waldmann, S. H. Böhm, and A. Adler. Thoracic EIT in 3D: experiences and recommendations. *Physiological measurement*, 40(7):074006, 2019.

B. B. Guzina and M. Bonnet. Small-inclusion asymptotic of misfit functionals for inverse problems in acoustics. *Inverse Problems*, 22(5):1761, 2006.

M. Hanke and M. Brühl. Recent progress in electrical impedance tomography. *Inverse Problems*, 19(6):S65, 2003.

Z. Hao, S. Yue, B. Sun, and H. Wang. Optimal distance of multi-plane sensor in three-dimensional electrical impedance tomography. *Computer Assisted Surgery*, 22(sup1): 326–338, 2017.

F. Hecht. New development in FreeFem++. *J. Numer. Math.*, 20(3-4):251–265, 2012. ISSN 1570-2820. URL https://freefem.org/.

T. J. Heindel. A review of X-ray flow visualization with applications to multiphase flows. *Journal of Fluids Engineering*, 133(7):074001, 2011.

D. Holder. *Electrical impedance tomography: methods, history and applications*. CRC Press, 2004.

P. Hua, J. Webster, and W. Tompkins. A regularised electrical impedance tomography reconstruction algorithm. *Clinical Physics and Physiological Measurement*, 9(4A):137, 1988.

Z. Huang, B. Wang, and H. Li. Application of electrical capacitance tomography to the void fraction measurement of two-phase flow. *IEEE Transactions on Instrumentation and Measurement*, 52(1):7–12, 2003.

D. Isaacson, J. L. Mueller, J. C. Newell, and S. Siltanen. Reconstructions of chest phantoms by the D-bar method for electrical impedance tomography. *IEEE Transactions on Medical Imaging*, 23(7):821–828, 2004.

J. Jia, M. Wang, Y. Faraj, and Q. Wang. Online conductivity calibration methods for EIT gas/oil in water flow measurement. *Flow Measurement and Instrumentation*, 46:213–217, 2015.

J. Jia, H. Wang, and D. Millington. Electrical resistance tomography sensor for highly conductive oil-water two-phase flow measurement. *IEEE Sensors Journal*, 17(24):8224–8233, 2017.

R. Johansen, T. Østby, A. Dupre, and S. Mylvaganam. LONG SHORT-TERM MEMORY NEURAL NETWORKS FOR FLOW REGIME IDENTIFICATION USING ECT. 09 2018.

O. C. Jones Jr and J.-M. Delhaye. Transient and statistical measurement techniques for two-phase flows: a critical review. *International Journal of Multiphase Flow*, 3(2):89–116, 1976.

P. Kauppinen, J. Hyttinen, and J. Malmivuo. Sensitivity distribution visualizations of impedance tomography measurement strategies. *International Journal of Bioelectromagnetism*, 8(1):1–9, 2006.

M. T. M. Khairi, S. Ibrahim, M. A. M. Yunus, M. Faramarzi, G. P. Sean, J. Pusppanathan, and A. Abid. Ultrasound computed tomography for material inspection: Principles, design and applications. *Measurement*, 146:490–523, 2019.

M. C. Kim, S. Kim, K. Y. Kim, and Y. J. Lee. Regularization methods in electrical impedance tomography technique for the two-phase flow visualization. *International communications in heat and mass transfer*, 28(6):773–782, 2001.

A. Kirsch. Characterization of the shape of a scattering obstacle using the spectral data of the far field operator. *Inverse problems*, 14(6):1489, 1998.

R. V. Kohn and A. McKenney. Numerical implementation of a variational method for electrical impedance tomography. *Inverse Problems*, 6(3):389, 1990.

V. Kolehmainen, S. Siltanen, S. Järvenpää, J. P. Kaipio, P. Koistinen, M. Lassas, J. Pirttilä, and E. Somersalo. Statistical inversion for medical x-ray tomography with few radiographs: II. Application to dental radiology. *Physics in Medicine & Biology*, 48(10):1465, 2003.

C. Kotre. EIT image reconstruction using sensitivity weighted filtered backprojection. *Physiological measurement*, 15(2A):A125, 1994.

R. Kotze, A. Adler, A. Sutherland, and C. Deba. Evaluation of Electrical Resistance Tomography imaging algorithms to monitor settling slurry pipe flow. *Flow Measurement and Instrumentation*, page 101572, 2019.

G. Liang, S. Ren, S. Zhao, and F. Dong. A Lagrange-Newton method for EIT/UT dual-modality image reconstruction. *Sensors*, 19(9):1966, 2019.

W. R. Lionheart. EIT reconstruction algorithms: pitfalls, challenges and recent developments. *Physiological measurement*, 25(1):125, 2004.

W. R. Lionheart, J. Kaipio, and C. N. McLeod. Generalized optimal current patterns and electrical safety in EIT. *Physiological measurement*, 22(1):85, 2001.

Y. Ma, H. Wang, L.-A. Xu, and C. Jiang. Simulation study of the electrode array used in an ERT system. *Chemical engineering science*, 52(13):2197–2203, 1997.

E. Malone, G. S. dos Santos, D. Holder, and S. Arridge. Multifrequency electrical impedance tomography using spectral constraints. *IEEE transactions on medical imaging*, 33(2):340–350, 2013.

J. Mandhane, G. Gregory, and K. Aziz. A flow pattern map for gas-liquid flow in horizontal pipes. *International Journal of Multiphase Flow*, 1(4):537–553, 1974.

R. Mudde. Bubbles in a fluidized bed: A fast X-ray scanner. *AIChE journal*, 57(10):2684–2690, 2011.

J. L. Mueller and S. Siltanen. *Linear and nonlinear inverse problems with practical applications*, volume 10. Siam, 2012.

S. Nedeltchev, U. Hampel, and M. Schubert. Investigation of the radial effect on the transition velocities in a bubble column based on the modified Shannon entropy. *Chemical Engineering Research and Design*, 115:303–309, 2016.

J. Newell, D. Isaacson, M. Cheney, G. Saulnier, D. Gisser, J. Goble, R. Cook, P. Edic, C. Newton, and D. Holder. In Vivo impedance images using sinusoidal current patterns. *Clinical and Physiological Applications of Electrical Impedance Tomography*, pages 277–98, 1993.

S. Paranjape, S. N. Ritchey, and S. V. Garimella. Electrical impedance-based void fraction measurement and flow regime identification in micro-channel flows under adiabatic conditions. *International Journal of Multiphase Flow*, 42:175–183, 2012.

S. Paras and A. Karabelas. Properties of the liquid layer in horizontal annular flow. *International journal of multiphase flow*, 17(4):439–454, 1991.

H. V. Peña and O. Rodriguez. Applications of wire-mesh sensors in multiphase flows. *Flow measurement and instrumentation*, 45:255–273, 2015.

K. Perera, C. Pradeep, S. Mylvaganam, and R. W. Time. Imaging of oil-water flow patterns by electrical capacitance tomography. *Flow Measurement and Instrumentation*, 56:23–34, 2017.

R. Plonsey and R. Collin. Electrode guarding in electrical impedance measurements of physiological systems—a critique. *Medical and Biological Engineering and Computing*, 15(5):519–527, 1977.

N. Polydorides. Image reconstruction algorithms for soft-field tomography. *PhD Thesis, UMIST*, 2002.

N. Polydorides and W. R. Lionheart. A Matlab toolkit for three-dimensional electrical impedance tomography: a contribution to the Electrical Impedance and Diffuse Optical Reconstruction Software project. *Measurement science and technology*, 13(12):1871, 2002.

H.-M. Prasser, A. Böttger, and J. Zschau. A new electrode-mesh tomograph for gas–liquid flows. *Flow measurement and instrumentation*, 9(2):111–119, 1998.

J. Pusppanathan, R. A. Rahim, F. A. Phang, E. J. Mohamad, N. M. N. Ayob, M. H. F. Rahiman, and C. K. Seong. Single-plane dual-modality tomography for multiphase flow imaging by integrating electrical capacitance and ultrasonic sensors. *IEEE Sensors Journal*, 17 (19):6368–6377, 2017.

N. PXIe. *DEVICE SPECIFICATIONS NI 6368 X Series Data Acquisition*. National Intrusment, 2016.

G. Ricciardi, M. Pettigrew, and N. Mureithi. Fluidelastic Instability in a Normal Triangular Tube Bundle Subjected to Air-Water Cross-Flow. *Journal of Pressure Vessel Technology*, 133:9, 10 2011. doi: 10.1115/1.4004562.

L. Rossi, R. De Fayard, and S. Kassab. Measurements using X-ray attenuation vertical distribution of the void fraction for different flow regimes in a horizontal pipe. *Nuclear Engineering and Design*, 336:129–140, 2018.

Y. Ru and S. Mylvaganam. Enhanced flow regime identification with SVM using electrical capacitance tomography (ECT) in fluidized beds. *7th World Congress in Industrial Process Tomography*, pages 809–817, 01 2014.

C. M. Salgado, C. M. Pereira, R. Schirru, and L. E. Brandão. Flow regime identification and volume fraction prediction in multiphase flows by means of gamma-ray attenuation and artificial neural networks. *Progress in Nuclear Energy*, 52(6):555–562, 2010.

F. Santosa and M. Vogelius. A backprojection algorithm for electrical impedance imaging. *SIAM Journal on Applied Mathematics*, 50(1):216–243, 1990.

E. Schleicher, M. Tschofen, R. Kipping, and U. Hampel. Wire-mesh Sensors: Recent Developments and Applications. *Proc. SWINTH (Livorno, Italy)*, 2016.

A. Seagar, D. Barber, and B. Brown. Theoretical limits to sensitivity and resolution in impedance imaging. *Clinical Physics and Physiological Measurement*, 8(4A):13, 1987.

M. Sharifi and B. Young. Electrical resistance tomography (ERT) applications to chemical engineering. *Chemical Engineering Research and Design*, 91(9):1625–1645, 2013.

E. Somersalo, M. Cheney, and D. Isaacson. Existence and uniqueness for electrode models for electric current computed tomography. *SIAM Journal on Applied Mathematics*, 52 (4):1023–1040, 1992.

D. Stephenson, R. Mann, and T. York. The sensitivity of reconstructed images and process engineering metrics to key choices in practical electrical impedance tomography. *Measurement Science and Technology*, 19(9):094013, 2008.

J. Sun and W. Yang. Evaluation of fringe effect of electrical resistance tomography sensor. *Measurement*, 53:145–160, 2014.

J. Sun and W. Yang. A dual-modality electrical tomography sensor for measurement of gas–oil–water stratified flows. *Measurement*, 66:150–160, 2015.

Y. Taitel and A. E. Dukler. A model for predicting flow regime transitions in horizontal and near horizontal gas-liquid flow. *AIChE journal*, 22(1):47–55, 1976.

Y. Taitel, D. Bornea, and A. Dukler. Modelling flow pattern transitions for steady upward gas-liquid flow in vertical tubes. *AIChE Journal*, 26(3):345–354, 1980.

C. Tan, F. Dong, and M. Wu. Identification of gas/liquid two-phase flow regime through ERT-based measurement and feature extraction. *Flow Measurement and Instrumentation*, 18(5-6):255–261, 2007.

M. Vauhkonen. Electrical impedance tomography and prior information. *PhD thesis, Kuopio University, Kuopio*, 1997.

J. Wagenaar and A. Adler. Electrical impedance tomography in 3D using two electrode planes: characterization and evaluation. *Physiological measurement*, 37(6):922, 2016.

H. Wang and L. Zhang. Identification of two-phase flow regimes based on support vector machine and electrical capacitance tomography. *Measurement Science and Technology*, 20(11):114007, 2009.

M. Wang. Electrode models in electrical impedance tomography. *Journal of Zhejiang University-SCIENCE A*, 6(12):1386–1393, 2005.

Q. Wang, M. Wang, K. Wei, and C. Qiu. Visualization of gas–oil–water flow in horizontal pipeline using dual-modality electrical tomographic systems. *IEEE Sensors Journal*, 17 (24):8146–8156, 2017.

P. Wiedemann, A. Döß, E. Schleicher, and U. Hampel. Fuzzy flow pattern identification in horizontal air-water two-phase flow based on wire-mesh sensor data. *International Journal of Multiphase Flow*, 117:153–162, 2019.

J. Wtorek, A. Bujnowski, and H. Sahli. Influence of electrode size on a Jacobian properties. 2004.

W. Yan, S. Hong, and R. Chaoshi. Optimum design of electrode structure and parameters in electrical impedance tomography. *Physiological measurement*, 27(3):291, 2006.

T. J. Yorkey, J. G. Webster, and W. J. Tompkins. Comparing reconstruction algorithms for electrical impedance tomography. *IEEE Transactions on Biomedical Engineering*, (11): 843–852, 1987.